Towards Understanding Surface Wetness and Corrosion Response of Mild Steel in Marine Atmospheres

---

A Dissertation

Presented to

the faculty of the School of Engineering and Applied Science

University of Virginia

---

in partial fulfillment

of the requirements for the degree

Doctor of Philosophy

by

Eric John Schindelholz

May

2014

APPROVAL SHEET

The dissertation
is submitted in partial fulfillment of the requirements
for the degree of
Doctor of Philosophy

Eric Schindelholz
AUTHOR

The dissertation has been read and approved by the examining committee:

Robert Kelly
Advisor

Giovanni Zangari

Elizabeth Opila

James Burns

William Keene

Accepted for the School of Engineering and Applied Science:

Dean, School of Engineering and Applied Science

May
2014

This dissertation is dedicated to my late grandmother, Barbara Schindelholz.

Executive Summary

Atmospheric corrosion is often approximated as a discontinuous process reliant on the availability of electrolyte to provide ionic conduction between the anode and cathode sites. A critical question is, when can a surface be considered wet enough for corrosion to proceed at a considerable rate? This question has been the subject of many studies since the beginning of corrosion as a modern scientific discipline and has led to the development of the time of wetness (TOW) concept. Time of wetness is a measured estimate of the fraction of time a metal surface remains wet during exposure. It is extensively utilized as an input parameter in corrosion service life prediction models and structural health monitoring applications. Although the basic concept and importance of TOW in governing corrosion is generally agreed upon, what is meant by "wet" has remained ambiguous and practical determination of this parameter has widely varied throughout its history of use. One of the issues limiting advancement of this concept is the lack of information on the relationship between corrosion response and the hygroscopic nature of contaminants that develop on a surface as a result of deposition of and reaction with atmospheric particles. This information is of particular importance in environments where aerosol deposition is known to drive corrosion, such as in the case of marine (saline) atmospheres where sea salt aerosol (SSA) is the dominant pollutant.

The objective of this work was to 1) elucidate the relationship between relative humidity, the hygroscopic behavior of sea salt simulants and the corrosion response of mild steel contaminated with them, and 2) use this information to assess the accuracy and appropriateness of current TOW determination methods for marine environments. The particular case of mild steel contaminated with of sea salt aerosol proxies (NaCl, $MgCl_2$, and artificial seawater (ASW)) at the initial stages of corrosion was examined.

The approach to this problem was twofold. First, the hygroscopic behavior of sea salt simulants and expected chemistries resulting from corrosion under these simulants was characterized. Second, the effect of RH on corrosion response (attack morphology and corrosion rate) of mild steel contaminated with these simulants was quantified. From this two-pronged approach, an understanding of the interrelationship between the state of electrolyte available on the surface and the corrosion response as a function of RH was developed. To carry out these tasks two novel methods were developed for production and study of salt microparticles on the same size order as coarse mode marine aerosols (>1 μm). One, based on inkjet printing technology, enabled controlled and high-throughput loading of microparticles. The other, an interdigitated electrode impedance sensing method, allowed characterization of the hygroscopic behavior of these particles.

The results raise the question as to whether surfaces contaminated with SSA ever dry in natural ambient conditions (in terms of corrosion being possible). For ASW, major aqueous-solid (deliquescence) phase transitions occurred at ~10% RH, attributed to a metastable hydrated Mg-Cl phase, and the deposits remained significantly conductive down to <2% RH, even for 24 h, likely due to trapping of supersaturated brine under salt crusts. Translation of these findings to the outdoor climate, where humidity levels below 2% RH are rare, suggests that brine associated with sea salt contaminants may always be present in quantities sufficient to enable corrosion.

Regardless of whether a surface ever truly dries, the findings challenge the commonly utilized humidity thresholds for estimations of TOW on SSA contaminated surfaces. These include the ISO 9223 threshold of 80% RH and use of the deliquescence RH (DRH) of sea salt constituents, such as those for NaCl (76%RH) and $MgCl_2.6H_2O$ (33%). Corrosion can initiate by adsorbed water on NaCl crystals down to 33%RH, and proceed at rates comparable to that at and above the DRH of NaCl (76%) at humidity levels down to 53% due to development of hygroscopic corrosion chemistry. Corrosion can be sustained down to at least 11%RH under $MgCl_2$ deposits, possibly due to trapped fluid or deliquesced electrolyte, which is well below the DRH of $MgCl_2.6H_2O$ (33%). Under ASW, corrosion was detectable down to 23% RH. No substantial inflection in the trends of corrosion loss as a function of RH were notable at the observed or predicted phase transitions in any of these cases.

Similarly, conductance-based TOW sensing methods were demonstrated to inadequately capture the full wetting contribution of hygroscopic atmospheric particles during field deployment. This was due to electrode spacing of typical TOW sensors being far greater than the expected aerosol sizes deposited on the sensors. Using the microelectrode sensing method developed in this work that, it was demonstrated that, provided great enough sensitivity, conductance varies across the entire RH range for ASW. Although phase transitions marked distinct transitions in conductance versus RH trends for these salts on the microelectrode sensors, these changes could not be used to distinguish between significant and insignificant corrosion taking place. Therefore, a wet-dry threshold based on conductance alone, as is used for current methods, is not a sufficient indicator of the presence of electrolyte that can sustain considerable corrosion.

Given the uncertainties associated with current time of wetness (TOW) determination methods and in light of these findings, the conservative assumption that, under conditions where SSA is present, electrolyte sufficient to enable corrosion is always present on mild steel surfaces in ambient outdoor environments may be most appropriate (i.e., TOW is unity). A simple alternative approach for dose-response corrosion models that utilize TOW as an input parameter is to account for a time above a critical relative humidity where corrosion becomes considerable, which in this case was between 33% and 53% RH. Further work is suggested to test the universality of these findings in cases of varying salt loadings, diurnal humidity and temperature transients, and exposure times more representative of structures exposed to outdoor conditions. The experimental framework developed provides one means of doing so in either field or more rigorously controlled lab conditions.

Acknowledgements

I would like to express my sincere gratitude to Prof. Robert Kelly. I will always be indebted to you for the opportunities you provided, your knowledge, support and friendship.

A special thank you to those at two research institutions at which I was fortunate to intern during my studies. Drs. Tadashi Shinohara, Hideki Katayama and Akira Tahara at the Japan National Institute of Materials Science and Drs. Ivan Cole and Tim Muster at the Commonwealth Scientific and Industrial Research Organization are gratefully acknowledged. Thank you for being such gracious hosts, great teachers and kind friends.

I would like to acknowledge all the members of the Center for Electrochemical Science and Engineering, from whom I have learned so much. A very special thank you goes to Bailey Risteen for her dedication to this work and patience over the past three years. It has been a privilege to work with her. Thank you to Richard White and Lok-kun Tsui for their technical expertise and assistance. Also, I would like to thank Prof. William Keene and John Maben for the numerous and insightful discussions and providing IC analysis.

Instrumentation at Ohio State University and Penn State University were utilized for portions of this work. Profs. Rudy Buchheit and Gerald Frankel at OSU and Dr. Josh Stapleton at the PSU Materials Characterization Laboratory are gratefully acknowledged.

Lastly, I would like to thank my wonderful (future) wife Mara for her support, encouragement and patience. I am looking forward to the next chapter of our lives.

Table of Contents

List of Tables

List of Figures

1 Introduction

In the atmospheric environment, aqueous corrosion is often approximated as a discontinuous process reliant on the availability of electrolyte to provide ionic conduction between the cathode and anode sites for it to proceed. A critical question in atmospheric corrosion is when can a surface be considered wet enough for corrosion to occur at a considerable rate? This question has been the subject of many studies since the beginning of corrosion as a modern scientific discipline and has led to the development of the time of wetness (TOW) concept.

Time of wetness is a measured estimate of the fraction of time a metal surface remains wet during exposure. It is extensively utilized as an input parameter in corrosion service life prediction models and structural health monitoring applications, and treated as an on-off switch for corrosion. Although the basic concept and importance of TOW in governing corrosion is generally agreed upon, what is meant by “wet” has remained ambiguous and practical determination of this parameter has widely varied throughout its history of use. Furthermore, current determination methods do not fully capture the water sorption behavior of deposited atmospheric particles.

One of the issues limiting advancement of this topic is the lack of information on the relationship between corrosion response and the hygroscopic nature of contaminants that develop on a surface as a result of deposition of and reaction with atmospheric particles. This gap is of particular importance in environments where aerosol deposition is known to drive corrosion, such as in the case of marine (saline) atmospheres where sea salt aerosol (SSA) is the dominant pollutant. Lack of information on this subject also limits a more comprehensive mechanistic understanding of corrosion processes associated with atmospheric particles.

1.1 Objectives

The objective of this work was to 1) elucidate the relationship between relative humidity (RH), the hygroscopic behavior of sea salt simulants and the corrosion response of mild steel contaminated with them, and 2) use this information to assess the accuracy and appropriateness of current TOW determination methods for marine environments. The driving question behind this work, is under what relative humidity range and time frame can electrolyte be expected to be present and corrosion rates significant for low carbon steel contaminated with sea salt simulants?

1.2 Approach

The approach to this problem was twofold. First, the hygroscopic behavior of sea salt simulants and expected chemistries resulting from corrosion under these simulants was characterized. Second, the effect of RH on corrosion response (attack morphology and corrosion rate) of mild steel contaminated with these simulants was quantified. From this, an understanding of the interrelationship between the state of electrolyte available on the surface and the corrosion response as a function of RH was developed. In turn this information was utilized to assess the accuracy of current TOW estimation methods in the case of steel in marine environments and suggest paths for improvement. Given the prohibitive complexity of natural atmospheric environments, the majority of this work was carried out under simplified and rigorously controlled laboratory conditions. To carry out these tasks two novel methods were developed for production and study of salt microparticles on the same size order as coarse mode marine aerosols (>1 μm). One, based on inkjet printing technology, enabled controlled and high-throughput loading of microparticles. The other, an interdigitated electrode impedance sensing method, was developed to characterize hygroscopic behavior of these particles.

1.3 Overview

The work is organized into three chapters (CH 2-4), each of which is comprised of two self-contained sections. Each section is a manuscript in its entirety that has either been published or in preparation for publication. Chapter 2 is comprised of a review of the current state of TOW in atmospheric corrosion along with relevant wetting and drying phenomena. Following this is a comparative field study of common TOW determination methods that pinpoints some of the accuracy issues related to them. The knowledge gaps identified in the review and performance issues elucidated by the field study served to solidify the stated objectives above and guide design of the laboratory experiments discussed in the remainder of the dissertation.

Chapter 3 details the two methods that were developed for both rigorous production and study salt of hygroscopic behavior of salt microparticles on the size order of natural, coarse-mode aerosols. The first section demonstrates the use of an inkjet printing method for controlled, high-throughput loading of aqueous salt droplets on substrates. The positive results of this proof-of-concept study led to the design and construction of a custom inkjet printer housed in a humidity-controlled chamber, which is detailed in the second section. The second section describes an electrical impedance method for measurement of deliquescence (solid to liquid) and efflorescence (liquid to solid) phase transitions of hygroscopic salt particles. These methods served as the basis of the experimental approach utilized in the work reported in the last chapter.

Chapter 4 addresses the objectives posed above. In the first section, the hygroscopic behavior of NaCl and expected corrosion chemistries are related to the corrosion behavior of steel as a function of RH. The understanding developed on this single salt system served as basis from which to extend this work to $MgCl_2$, which is thought to be the active corrosion stimulating component of SSA at low humidity, and further extends it to artificial seawater (ASW), which is more representative of the complex chemistry of SSA (second section). The results were used assess accuracy and appropriateness of current TOW determination methods. The interrelationship between the various topics covered and the structure of this dissertation in terms of understanding the relationship between state of an atmospherically exposed surface and its corrosion response is given in Figure 1.1.

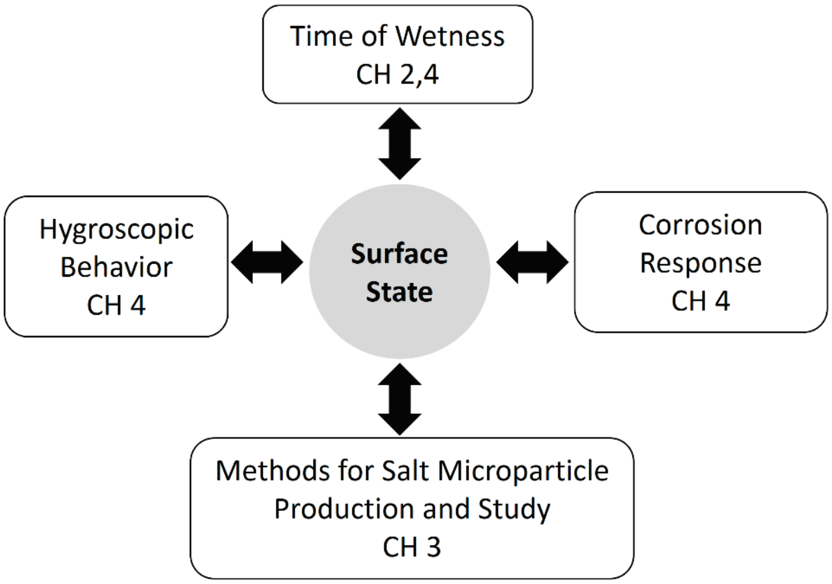

Figure 1.1 Topics covered in this dissertation as they relate to understanding the surface state and corrosion response of an atmospherically exposed metallic surface.

This dissertation is comprised of the following manuscripts:

Schindelholz, E.; Kelly, R. G., Wetting phenomena and time of wetness in atmospheric corrosion: a review. Corrosion Reviews 2012, 30 (5-6), 135-207.

Schindelholz, E.; Kelly, R. G.; Cole, I. S.; Ganther, W. D.; Muster, T. H., Comparability and accuracy of time of wetness sensing methods relevant for atmospheric corrosion. Corrosion Science 2013, 67, 233-241.

Schindelholz, E.; Kelly, R. G., Application of inkjet printing for depositing salt prior to atmospheric corrosion testing. Electrochemical and Solid-State Letters 2010, 13 (10), C29-C31.

Schindelholz, E.; Tsui, L.; Kelly, R.G., Hygroscopic particle behavior studied by interdigitated array microelectrode impedance sensors. Journal of Physical Chemistry A, 2014, 118 (1), 167-177.

Schindelholz, E.; Risteen, B.E.; Kelly, R.G, Effect of RH on corrosion of steel under sea salt aerosol proxies I: NaCl. Submitted, Journal of The Electrochemical Society.

Schindelholz, E.; Risteen, B.E.; Kelly, R.G, Effect of RH on corrosion of steel under sea salt aerosol proxies II: $MgCl_2$, Seawater. Submitted, Journal of The Electrochemical Society.

2 Background

This chapter is comprised of a review of the current state of TOW in atmospheric corrosion along with relevant wetting and drying phenomena. Following this is a comparative field study of common TOW determination methods that pinpoints some of the accuracy issues related to them. The knowledge gaps identified in the review and performance issues elucidated by the field study served to solidify the stated objectives above and guide design of the laboratory experiments discussed in the remainder of the dissertation.

2.1 Wetting Phenomena and Time of Wetness in Atmospheric Corrosion

The concept of Time of Wetness (TOW) is extensively used in the atmospheric corrosion disciplines for such purposes as corrosion prognostics and environmental corrosivity classification. Time of wetness can generally be defined as the amount of time a metal surface remains wet during atmospheric exposure. Although the basic concept and importance of TOW in governing atmospheric corrosion is generally agreed upon, what is meant by “wet” has generally remained ambiguous and its practical determination has been widely varied throughout its history.

The objective of this review is to demystify TOW in terms of definition and measurement and identify issues that inhibit this parameter from providing deeper insight into the effect wetness duration has on atmospheric corrosion. Specifically, this paper summarizes the current state of TOW determination methods along with the parallel concept leaf wetness used in environmental science. Furthermore, wetting and drying phenomena associated with atmospheric corrosion and thought to control TOW are overviewed. From this framework, current issues and limitations of TOW are identified and avenues for further improvement suggested.

2.1.1 Introduction

In order for atmospheric corrosion to occur, a metal surface must be wet by a sufficiently conductive liquid. It follows then that the amount of time a surface remains wet in the environment is a measure of the amount of time corrosion may be possible. This period is often referred to as time of wetness (TOW), a concept widely utilized in determining the extent of corrosion that occurs during atmospheric exposure.

At first glance this concept appears elementary and straightforward, but determining what is meant by "wet" and how to measure it has been the subject of scores of investigations in the field of corrosion over the past sixty years. As a result, numerous practical and theoretical definitions for TOW have been developed. Theoretical definitions have proven to be too general or too simplistic, whereas practical ones are often based on the limits of the particular moisture sensing method used. More than a handful of practical definitions have been used by various investigators over the years. The published data generated from different definitions cannot, generally, be directly compared to each other nor, in many cases, is it entirely clear how to interpret these data. These issues inhibit a deeper understanding on the effect of wetness duration in atmospheric corrosion as well as efforts to develop predictive equations for atmospheric corrosion rates based on measurable environmental parameters.

The objectives of this paper are three-fold, and the paper is thus divided into the same number of parts. The first objective is to provide an overview of wetting and drying phenomena associated with atmospheric corrosion, which is the topic of Part I. The second objective is to summarize the current state of the TOW concept and practical determination methods along with the parallel concept of leaf wetness used in the environmental sciences, Part II. The final objective, and Part III, is to globally address the issues and limitations of current TOW methods and identify avenues for further improvement.

2.1.2 Part I: Wetting and Drying Phenomena

Metal surfaces exposed to atmospheric environments are subject to a number of different wetting and drying phenomena that can control the initiation, propagation, and cessation of corrosion activity. During atmospheric corrosion, the electrolyte is in the form of a thin film, drops, or both. The shape, thickness, and composition of the electrolyte are dynamic and influenced by reactions between the metal and the environment, particulate deposition, weather, and other parameters. The electrolyte, in turn, controls corrosion mechanisms and rate, as will be discussed later in the report. It becomes clear, then, why it is important to understand what exactly a wet surface is and the modes by which surfaces wet and dry in the normal atmosphere.

This section starts by covering the basic theory of wettability in terms of surface energy balance. Experimental observations important to wettability of metal surfaces are then overviewed. This overview is followed by a summary of the modes of transfer of water to and from a surface. Modes of delivery of water to a surface include direct deposition and sorption. Water is transported away from a surface by evaporation and dewetting.

2.1.2.1 Wettability

Wettability in the context of this paper is the ability of a liquid to maintain contact with a solid surface. When a drop of water is in contact with a solid surface a triple interface is formed between the solid, liquid and gas phases, Figure 2.1. There is a surface tension γ

particular to each interface. The surface tension between the liquid and gas phases is γ_{GL}, or simply γ, while that between the solid and gas is γ_{SG} and between the solid and liquid is γ_{SL}. The angle created by the edge of a liquid drop in contact with a solid is termed the contact angle, θ. The Young-Dupré equation relates the vector tensions of these interfaces for an ideal solid surface (i.e., flat, smooth and homogenous) and a liquid drop in equilibrium:

$$\gamma_{SG} = \gamma_{SL} + \gamma_{GL} \cos\theta \qquad 2.1$$

When a droplet is first placed on a solid surface, however, these forces are not in equilibrium:

$$F_h = \gamma_{SG} - \gamma_{SL} - \gamma_{GL} \cos\theta' \qquad 2.2$$

where F_h is the net force per unit length of the triple interface and θ' is the instantaneous angle.

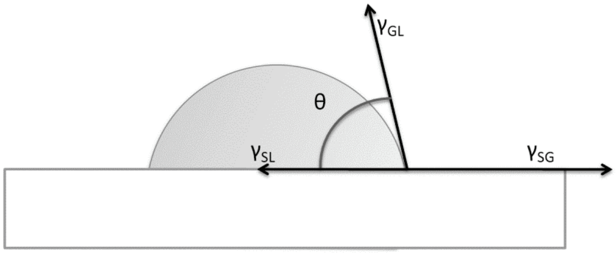

Figure 2.1. A triple phase interface for a liquid drop on a solid substrate illustrating applicable force vectors and contact angle.

The position of the triple interface (i.e., edge of droplet) will move until equilibrium is established, when F_h=0 and θ'=θ. The contact angle can diminish to zero due to movement of the line of contact causing complete spreading of the liquid. Spreading is controlled by the difference between the surface energy of the dry solid and the wetted solid, and is defined as the spreading parameter S:

$$S = \gamma_{SG} - (\gamma_{SL} + \gamma_{GL}) \qquad 2.3$$

If S is positive then the liquid spreads completely, as just discussed. The liquid is then said to perfectly wet the solid. If S is negative, the drop only partially wets the solid ($\theta > 90^o$).

In reality surfaces are rarely perfectly smooth, homogenous and flat, presenting a more complicated picture. A drop on the surface of a non-ideal solid can often exhibit contact angle hysteresis. Two angles are used to describe drops on these surfaces, the advancing angle and the receding angle. The advancing angle is the maximum contact angle that can be sustained by a drop up until the line of contact moves, and the receding angle is the minimum before movement. The difference between the two is the hysteresis. Contact angle hysteresis can be used as a measure of surface roughness and cleanliness. Generally, the smaller the difference, the smoother, cleaner and/or more homogeneous the surface is [1].

In addition to affecting hysteresis, surface roughness can enhance the wetting property of a material. For example clean metal surfaces, which are hydrophilic, can be roughened to increase their wettability (i.e., decrease their contact angle with water). Likewise, roughening a hydrophobic surface decreases its wettability. The lotus plant, for example has a naturally rough hydrophobic leaf surface that causes water to bead up into nearly spherical drops when it is placed on a dry leaf [2]. With hydrophobic, rough surfaces, air in the interstices of the surface can become trapped under the droplet, called the Cassie state. A drop can also fill the surface interstices, termed the Wenzel state. These states are named after the two investigators who modeled them [3].

The shape of liquid drops on a solid are also affected by its surface state and, when they are large enough, gravity. Small drops with radii less than the capillary length

L_c of the liquid, take on the shape of hemispherical caps on ideal surfaces. The capillary length is defined:

$$L_c = \sqrt{\frac{\gamma_{GL}}{\rho g}} \qquad 2.4$$

where ρ is the density of liquid and g the acceleration of gravity. The capillary length for pure water at standard temperature and pressure is around 3 mm. Drops with radii greatly exceeding L_c will be forced to spread and plateau at the top due to gravity, forming a puddle of thickness *e*. The thickness of the puddle e can be determined in terms of L_c and the contact angle:

$$e = 2\,\mathrm{L_c}\sin\left(\frac{\theta}{2}\right) \qquad 2.5$$

Defects or impurities on the surface can also affect the shape of a drop or puddle by pinning the line of contact. This forces the drop to stretch or warp.

Solid surfaces, even hydrophobic ones, can be forced to wet. This phenomenon is commonly witnessed during periods of heavy rain when surfaces are covered with water, but dewet immediately when the rain stops. Another example is the act of painting a surface. Forced wetting occurs due to the relative motion between the liquid and the solid. The viscosity of the liquid that is moving relative to a solid causes it to be dragged by the solid and form a film.

WETTABILITY OF CLEAN AND CORRODED METAL

It is a common theoretical conjecture that a clean metal surface, due to its high surface energy, will completely wet (i.e., θ=0) by water. Observed angles in the literature reported for “clean” surfaces, however, range from zero to non-wetting values [4-9]. For example, Zhang et al. (9) report high contact angles on clean pure copper surfaces, but do not state how the metal surfaces were cleaned nor comment on their degree of cleanliness. It is possible that the surfaces examined in that study were actually contaminated. Contamination by carbonaceous compounds, which are ubiquitous in the environment may be one reason for the observation of such high contact angles [10]. Some investigators have taken involved steps to prevent contamination and have reported contact angles less than 10 degrees for pure copper [11]. Others, such as Erb [12], who have also been careful to prevent contamination, have nonetheless reported high contact angles for copper and other metals.

The debate over whether certain clean metals are completely wettable appears to be ongoing. In reality, metals exposed to the natural atmosphere can be assumed to have contaminated, heterogeneous surfaces that change with time due to corrosion and deposition processes. Although studies on the wetting phenomena of corroding, atmospherically exposed metals are sparse in the literature, some enlightening work has been done in this area.

A corroded or contaminated metal surface may be hydrophobic or hydrophilic in nature or exhibit a heterogeneous mix of both qualities. For example, Muster et al. [7] report on the hydrophobic nature of zinc oxide films resulting from zinc exposed to the atmosphere. They also discuss how wettability affects the atmospheric corrosion behavior of a metal, focusing mainly on precipitation and deliquescence events, which will be discussed later in this paper. Cole et al. [13] carried out a study that examined changes in the surface energy of Al-Zn coated steel samples during exposure to various relative humidity (RH) laboratory environments. They found the surface energy of their samples generally increased during exposure. Min and Webb [6] report on a study in which aluminum and copper fin stocks used for cooling coils were treated after manufacture by exposing to boiling distilled water for 20 minute intervals. They reported increased wettability of the material after treatment (from around 60°advancing angle to around 0°), likely due to the formation of a hydroxylated layer on the metal.

CAPILLARY ACTION

In addition to spreading on a surface, if porosity exists, liquid may be wicked into the pores via capillary action. Capillary action refers to the movement of liquid through crevices or pores in an object and is driven by a balance between surface tension forces and gravity. The flow of liquid through a capillary ceases either by saturating it or by hydrostatic pressure. The latter, for the case a vertical capillary, can be described in terms of fill height, h, by:

$$h = \frac{2\gamma_{GL}cos\theta}{\rho gr} \qquad 2.6$$

where ρ is the density of the liquid, g is gravitational acceleration and r is the radius of the capillary. Capillary action plays an important role in the transport of water into or through corrosion films or corroded metal surfaces and also significantly affects drying time due to minimization of the liquid-air interface [14-16].

PRECURSOR FILMS AND SECONDARY SPREADING

Thus far, the discussion has focused on wetting at the macroscopic scale. Thin fluid films have been shown to exist in front of static and moving macroscopic lines of contact at the liquid-solid-air interface. Thin films of water and simple, non-polar fluids on glass and silica surfaces have been observed and studied by a number of investigators [17-22]. For example, Garoff et al. [20] examined the structure of static precursor water films on silicate glass partially submerged in water and in a high humidity helium atmosphere. They found a thin film (<100 Å) formed within ten minutes of submersion, which emanated beyond the meniscus by 1-2mm and terminated to a much thinner film characteristic of a glass surface in contact with water only.

Although films of this sort have not been directly examined in the corrosion field, a similar and possibly related phenomena termed secondary spreading has been reported. The spreading of a front of microdroplets from drops of aqueous halide solutions on polished metal surfaces has been observed at high humidity levels. This type of behavior is exemplified in Figure 2.2. Neufeld et al. [23] examined sodium chloride on zinc surfaces and found spreading correlated to corrosion activity. They hypothesized that corrosion chemistry was causing gradients in the interfacial energies and, in turn, spreading. Chen et al. [24-25] further examined this phenomenon on zinc and copper surfaces and came to similar conclusions.

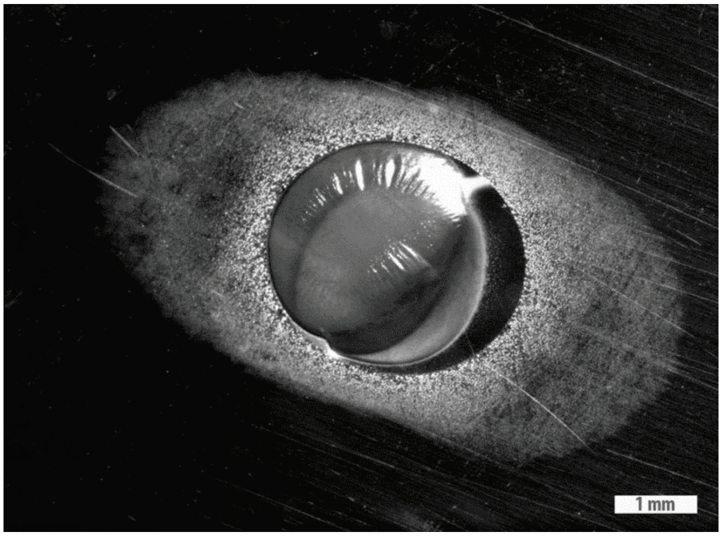

Figure 2.2. Secondary film present (bright haze) surrounding an aqueous NaCl drop on plain carbon steel after exposure for 5 h at 80 % and 23 ° C.

2.1.2.2 Modes of Wetting

This section examines how electrolyte develops on or is transported to and from a surface in the atmospheric environment. Electrolyte can form on or arrive at a metal surface by two main modes- direct deposition or sorption. Surfaces can dry via evaporation and dewetting. The following is a summary of these mechanisms along with associated governing meteorological phenomena. The discussion is given in the context of their influence on corrosion behavior, and, in turn, the effect of corrosion on wetting characteristics.

DIRECT DEPOSITION

Direct deposition of moisture onto a surface can be divided into three classes of pathways- dry deposition of particles, occult deposition of cloud and fog water, and precipitation. These modes will be briefly overviewed here in the context of atmospheric corrosion.

Dry Deposition

In the absence of surface clouds, fog, and precipitation, atmospheric aerosols of varying moisture content deposit onto surfaces via the combined influences of gravitational sedimentation, impaction, and diffusion. Sedimentation is a process whereby the weight of an aerosol causes deposition onto horizontal surfaces. Impaction occurs when an aerosol has enough momentum to defy the flow of an airstream deflecting around an object and impact on its surface. Deposition velocities of particles vary as functions of size and composition, wind-velocity, and the nature of the surface to which the particles deposit. Under moderate wind conditions, settling and impaction are the dominant pathway for size fractions typically larger than around a few microns in diameter, and diffusion is the dominant pathway for smaller fractions [26].

The dry-deposition of particles over all size distributions cannot be reliably quantified by direct measurement. Typically, deposition fluxes are modeled based on measurements of size-resolved concentrations in air, associated meteorological conditions, and the nature of the surface [27-28]. Cole and colleagues have carried out a significant amount of work in this area with a particular focus on relating deposition to corrosion behavior. Specifically, they developed models of the production and deposition of marine aerosols on metal surfaces in coastal environments [29-33].

Marine aerosols are of particular interest in the corrosion field, and for this reason their production, distribution and behavior are briefly discussed here. These aerosols typically range in diameter from a few nanometers to a hundred microns. The larger size fractions, greater than around 0.1 um, are mechanically generated by ocean wave action with production often highly dependent on wind speed [34]. This fraction often comprises 95% of the total aerosol mass but only 5 -10% of the particle number [35]. Aerosols on the lower end of the size range are usually formed from gas-to-particle conversion of non-sea salt sulphate and organic species [36]. The composition of fresh marine aerosol, like all aerosols, evolves via interactions with reactive trace gases. The hygroscopic state is regulated by composition, size, relative humidity, and temperature. Marine aerosols are deliquesced when first emitted and, because humidity levels over the ocean seldom fall below the crystallization RH of marine aerosols, they often remain deliquesced over their atmospheric lifetimes in coastal environments [37].

Occult Deposition from Clouds and Fog

Cloud and fog droplets (liquid or frozen) deposit on surfaces via settling and impaction, a process known as occult deposition. Droplet sizes are often parameterized based on liquid water content (LWC), with typical diameters from 1 to 50 um [38-39]. Deposition velocities of cloud and fog aerosols vary as functions of size, wind velocity, and the nature of the surface to which the particles deposit. Several approaches are used to estimate occult fluxes including (1) models based on LWC, meteorological conditions, time of immersion, and the nature of the surface; (2) measurement of deposition on surrogate surfaces; (3) throughfall rates measured under forest canopies; and (4) water mass-balance calculations for measured watersheds.

Cloud and fog droplets form when hygroscopic cloud condensation nuclei (CCN) are exposed to supersaturated conditions. For a given size and composition, each CCN is associated with a critical supersaturation above which it will spontaneously grow into a cloud or fog droplet and below which it will remain in a stable state. These droplets scavenge soluble gases and aerosols from the surrounding air and also grow via condensation of additional water and coagulation with other cloud droplets. Because air parcels pass through clouds, most CCNs experience multiple cycles of activation into cloud droplets followed by evaporation [38].

Fog, like precipitation, can accumulate and interact with other atmospheric aerosols. In polluted urban environments fog is often more acidic than other forms of precipitation. The lower pH is due to the high efficiency of the small drops in scavenging atmospheric gases and the concentration of the aerosols as the fog droplets evaporate during their atmospheric lifetime [40].

Precipitation

Precipitation includes rain, snow, sleet and hail. Rain is generated when cloud droplets grow to a precipitable size, around 1mm, via water vapor condensation, drop coalescence, and ice processes [26]. Their shape and size are generally dictated by the competing forces of surface tension, gravity, and velocity pressure while they are falling. Falling drops also can collide and coalesce with each other. At ground level, raindrops tend to range from 0.1-9mm in mean diameter [41]. The composition of raindrops is largely governed by the composition of hygroscopic CCN from which they form along with secondary dissolved gasses. Although rain carries contaminants to ground level surfaces, a process termed wet deposition, it also tends to wash them off as will be discussed under the topic of run-off.

Rain, depending on its volume or flux, can cause forced wetting of a hydrophobic surface as mentioned earlier. This effect is easily observed on freshly painted surfaces, where a sheet of water covers the surface during hard rain but often retracts (i.e., dewets) immediately when the rain stops. During light rain, the surface may not completely wet, resulting in discrete drops of water. The geometry and location of the drops or sheet of water can play an important role on the corrosion mechanisms and rate.

SORPTION

In addition to direct deposition onto a surface, electrolyte can also form on a surface via sorption of water vapor. The major modes under which this occurs are adsorption, dew condensation, capillary condensation, and deliquescence. Electrolyte formation via sorption modes is governed by temperature and water activity along with surface geometry and composition

Adsorption at the Metal-Air Interface

Adsorption is the enrichment of one or more components at an interface. In the case of electrolyte formation in metallic corrosion, we are concerned with the adsorption of water on the surface of the metal. Water can either adsorb in molecular form or disassociated form, depending on structural conditions and material make-up of the surface. Disassociated components can be comprised of atomic hydrogen, oxygen, and hydroxyls (OH-).

Disassociation is spontaneous for many common metals, such as iron and copper, under standard conditions. Within a fraction of a second of being exposed to air, hydroxyl groups will form on the surface of these metals [42-43], Figure 2.3. There are some metals that have not been reported to disassociate water under standard conditions, including gold [44].

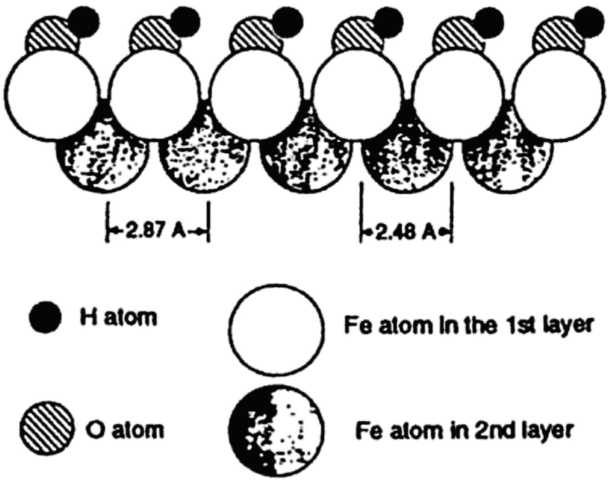

Figure 2.3. Disassociation of water onto a Fe (100) surface [104]. Copyright permission obtained from Copyright Clearance Center.

The adsorption mechanism for those metals or specific sites on a metal surface that associatively adsorb water can be described by the Lewis acid-base model. In this case, the water acts as the electron donor (Lewis base) to the metal (Lewis acid). Electron deficient sites are therefore preferred for adsorption.

Hydroxylated metal surfaces can adsorb molecular water through hydrogen bonding. The adhesive strength between the water and hydroxylated sites and the cohesive bond strength between water molecules is similar. The result is often the formation of clusters of adsorbed water molecules during the first stages of adsorption rather than thin films. Clustering is accentuated by the heterogeneity of the surface [45].

The first layer of large clusters or films of adsorbed water is immobile and has been observed to have an ice-like configuration, the geometry of which is influenced by the underlying metal structure. The second and third layers are slightly more mobile and often randomly oriented. Layers greater than three act similar to bulk water [43, 44, 46].

In reality, other species are also adsorbed on the metal surface, such as oxygen, carbon dioxide, and hydrogen. These absorbed species can affect the adsorption characteristics and surface chemistry of the metal. For example, the adsorption of electronegative species, such as oxygen molecules can increase the Lewis acidity of the surface metal atoms. Another example is the adsorption of anions such as chloride ions (Cl-) by clean gold causing it to transition from a hydrophobic state to a hydrophilic one [47].

The amount of water adsorbed on a metal surface is dependent upon the partial pressure of water in the environment to which it is exposed and temperature. Generally, the higher the relative humidity the greater the amount of adsorbed water on the surface [46, 48-56]. Figure 2.4 illustrates this. Given adsorption is an activated process, temperature can be expected to have an effect as demonstrated by a number of studies of water sorption on gold surfaces [54, 57-59].

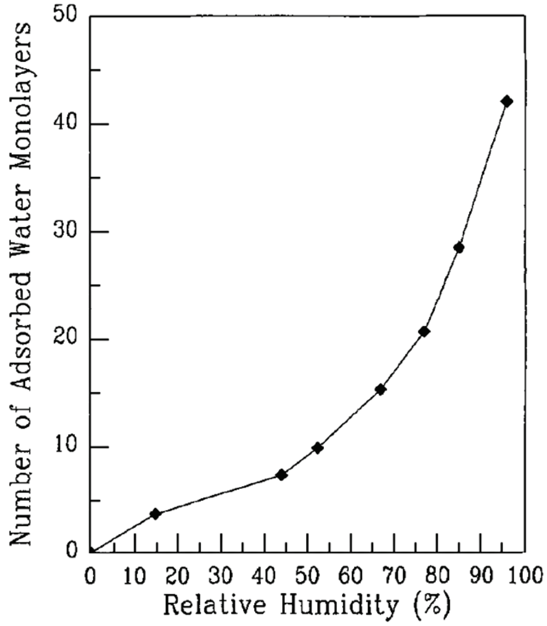

Figure 2.4. Water adsorption onto gold versus RH [105]. Copyright permission obtained from Copyright Clearance Center.

Dew Condensation

An adsorption process well established to significantly contribute to TOW is dew condensation. Condensation of this type can be in liquid form, referred to simply as dew, or in solid form as frost. It occurs when the water vapor partial pressure in the air adjacent to the surface is higher than the water vapor saturation pressure on the surface due to temperature differences between the two.

It is important, at this point, to formally define relative humidity and introduce surface relative humidity (SRH) as a means of describing this phenomenon. Relative humidity is, by definition, water activity expressed as a percentage:

$$RH = \frac{p_{H_2O}}{p_{H_2O,sat}(T_{amb})} * 100\% \qquad 2.7$$

where P_{H2O} is the partial pressure of water in the ambient air, $P_{H2O,sat}$ is the saturated vapor pressure of pure water at the temperature of the ambient air, T_{amb}. At an RH of 100%, liquid water condenses (i.e., water activity is one). Relative humidity at a surface can be further defined as:

$$SRH = RH \cdot \frac{P_{H_2O,sat}(T_{amb})}{P_{sat}(T_{surf})} * 100\% \qquad 2.8$$

where $P_{sat}(T_{surf})$ is the saturated vapor pressure of the aqueous solution that forms on a surface at the surface temperature T_{surf}. Dewing events are generally defined as instances where surfaces are sufficiently cooler than the ambient atmosphere for SRH to be at or greater than 100%, taking P_{sat} as the saturated vapor pressure of pure water. As will be demonstrated in the following sections, condensation often occurs in the natural environment below 100% SRH due to the effects of hygroscopic surface contaminants and surface geometry.

Dew formation on outdoor unsheltered surfaces is a process that usually occurs on a diurnal basis due to cyclic heating and cooling. During the day a metal surface exposed to the sun will absorb solar radiation and at night will be subject to the effect of undercooling. Surfaces located outdoors at night radiate heat to a clear sky and become colder than the ambient air temperature. This behavior seems at first glance to be counterintuitive but can be explained in terms of classic blackbody radiation theory [60]. The extent of undercooling and its likelihood to occur depends on a number of conditions. These conditions include the sky temperature, presence of clouds (reflectivity), view of other surfaces at different temperatures (e.g., ground), the temperature of adjacent objects (e.g., a sample rack), wind velocity and orientation.

Early work carried out by Sereda [61] and Grossman [62] on the dewing behavior of metal panels exposed in the field provides an empirical view of this subject in the context of corrosion. Sereda carried out a study of the macroscopic characteristics of dew formation on metal samples exposed outdoors. He used time-lapse cameras triggered by moisture sensors to study the condensation of moisture on zinc and various steels prepared in different manners. He found the nature of the moisture deposit to vary widely from various size droplets to films depending on the mode of preparation. When the specimens were free of detectable moisture, he recorded undercooling values as low as 5°F for corroded steel and 2°F on clear nights for clean steel during a monitoring period of around five weeks. Dew formation caused the temperature of the samples to approach air temperature. Grossman carried out exposure studies of insulated steel panels in Miami, Florida during a two month period in the fall and observed undercooling on detectibly dry surfaces to as much as 8°C with an average of 2-6° below ambient air temperature as early as twilight. Wind was reported to reduce the temperature difference by a number of degrees. It is important to note that panels were insulated on all sides with only the faces exposed. Additionally, in these studies, the dew effect was convoluted with deliquescence due to contamination by the outdoor environment.

Tens of models exist for the prediction of undercooling and dew formation of metal surfaces in outdoor environments. In the field of corrosion, a number of investigators have created such models for flat exposed metal panels. Dean and Reiser [63] developed a model to predict undercooling for a horizontal panel exposed to a cloudless night sky based on convective heat transfer. This model assumes no radiative heat exchange between the panel and the ground or another adjacent object (the panel is insulated save for the face). The model does not account for heat transfer due to condensation, so is applicable only to predict undercooling up to the point of initial dew formation. Cole and Patterson [64] developed heat transfer models to examine nighttime undercooling and daytime heating behavior. The models take into account radiative heat transfer to or from the ground, evaporation, and other variables. Through these models, they found that cloud cover and wind speed largely govern undercooling. Heating during the daytime is governed to a large degree by plate wetness and cloud cover. Under most conditions, undercooling was less than 4°C under clear and cloudy skies, with or without a breeze. Their model was within 1°C for average values they recorded in the field under similar conditions. One important point about all of these models is that they do not account for the enhanced hygroscopicity of surfaces contaminated with deliquescent particles and corrosion products.

Other studies have examined the phenomenological aspects of dew formation on the microscopic scale with relation to corrosion. This includes, Xu et al. [65] who carried out dew formation on metal plates under a metalloscope in the laboratory. They found surfaces contaminated with dust or salt formed dew more readily than clean surfaces. Wang and Kido [66] examined the formation of nanometer-size dew droplets on SUS304 steel and their effect on corrosion using atomic force microscopy.

Capillary Condensation

Liquid can condense in nanoscopic pores and crevices at RH levels much below those required for flat surfaces. This is due to the Gibbs-Thomson effect as described by the Kelvin Equation:

$$\ln \frac{P_v}{P_o} = -\frac{2H\gamma_{GL}V_t}{RT} \qquad 2.9$$

Where P_v is the equilibrium vapor pressure in a pore below a meniscus separating liquid and vapor phases, P_o is the vapor pressure of the ambient environment, H is the mean curvature of the meniscus, V_t is the liquid molar volume, R is the ideal gas constant, and T, the temperature. The equation states that the vapor pressure below a concave meniscus is less than that in equilibrium with a planar liquid surface. Assumptions made by Equation 9 include ideal gas behavior, equilibrium pressure, and the radius of curvature is equal to the capillary radius r. Often a hemispherical curvature is assumed, H=1/r, Figure 2.5.

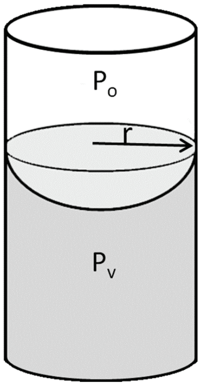

Figure 2.5. Illustration of capillary condensation in a pore. P_o is the vapor pressure above the meniscus, P_v the pressure below it, and r the radius of the pore.

According to the Kelvin equation, when a vapor of certain pressure is brought into contact with a solid, it should condense in all pores or crevices less than the critical radius, as shown in Figure 2.6. The applicability of this model for water in pores less than four nanometers is disputed in the literature [67-69].

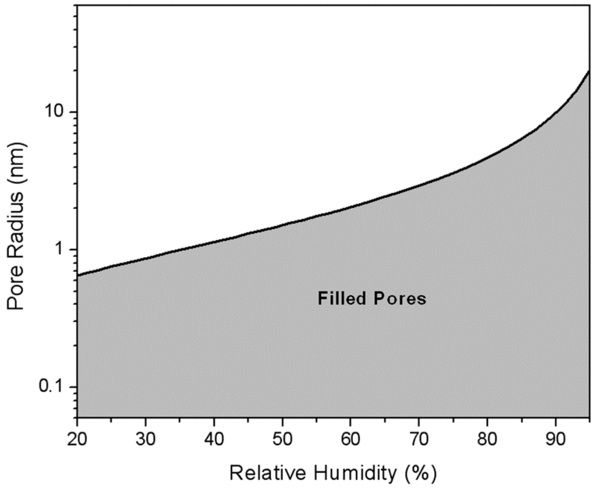

Figure 2.6. Critical pore radius for capillary condensation predicted to occur for pure water using the Kelvin equation at 25 ° C and assuming a hemispherical meniscus.

In terms of TOW, it is important to consider not only the morphology of a bare metal substrate but also condensation-inducing geometries formed by surface contaminants. For example, gas adsorption experiments on steel rusts indicate pores down to single nanometer diameters, well within the effective size range for capillary condensation to occur [70-73]. Points of contact between solid contaminants and the metal surface can also induce capillary condensation. Askey et al. [74] found polished carbon steel coated with 45 μm diameter silica spheres, simulating fly ash particles, corroded considerably compared to control samples after one week of exposure to lab air down to the minimum RH investigated of 65%. This observation may be evidence for the effect of contaminant geometry on TOW, be it insoluble particles or rust. Further information, however, on the direct effect of capillary condensation on corrosion is lacking in the literature.

Capillaries have also been shown to depress the freezing point of condensed water due to lower vapor pressure [75-77]. Freezing point depression can be described by coupling with the Kelvin equation with the Clausius-Clapeyron relation:

$$\frac{1}{r} = \frac{\Delta H_{fus} \Delta T}{2V\gamma_{SL}T_m} \qquad 2.10$$

Where ΔH_{fus} is the enthalpy of fusion, V the molar volume, T_m the melting point, and ΔT the temperature depression before T_m. Nowalk and Christenson [76] found experimental agreement with the above model down to at least -7°C (9nm pores) when examining water condensed between two mica sheets. Capillary freezing point depression likely plays an important role in subzero corrosion and will be discussed in the context of TOW definitions in Part II.

Deliquescence

Deliquescence is the absorption of water vapor by a soluble salt to form a liquid electrolyte. It occurs due to the vapor pressure of a saturated aqueous salt solution being less than that of the saturated vapor pressure of pure water. Deliquescence of a hygroscopic species deposited on a metal surface can cause initiation and support of the corrosion process at humidity levels below that required for adsorption-induced wetting of a clean surface. The fundamentals of deliquescence will be briefly overviewed here. Deliquescence will also be discussed in the context of atmospheric corrosion.

Deliquescent chemical species are present on atmospheric metal surfaces due to deposition from or reaction with the surrounding environment. Deliquescence occurs at a specific RH point, the deliquescence relative humidity (DRH). This is the point where the vapor pressure above a saturated deliquescent salt solution is the same as that of the ambient air. The DRH values for pure constituents of tropospheric aerosols represent a broad RH range, as shown in Table 2.1. The deliquescence point is a function of temperature, as shown in Figure 2.7, along with particle shape and size, [78-80].

Table 2.1. Experimentally determined deliquescence and efflorescence points for common aerosol components at or around 25°C. *N/A denotes behavior that was not measured or observed in the cited references.

Compound	**Chem. Formula**	**Deliquescence RH (%)**	**Efflorescence RH (%)***	**Reference**
Halides	HCl	liquid	liquid	
	$CaCl_2$	20	N/A	(Cohen, Flagan, & Seinfeld, 1987)
	$MgCl_2$	33	N/A	(Tang, 1979)
	NaBr	45-58	N/A	(Cohen*, et al.*, 1987)
	NaCl	75	42-45	(Orr, Hurd, & Corbett, 1958; Tang, 1979)
	NH_4Cl	80	70	(Cohen*, et al.*, 1987; He, Cheng, Zhu, Wang, & Zhang, 2009)
	KBr	80-82	N/A	(Cohen*, et al.*, 1987)
	KCl	84-85	48	(Freney, Martin, & Buseck, 2009; Tang, 1979)
Nitrates	HNO_3	liquid	liquid	
	$Ca(NO_3)_2$	18	N/A	(Tang & Fung, 1997)
	NH_4NO_3	60-61	< 30	(Lightstone, Onasch, Imre, & Oatis, 2000; Tang, 1979)
	$NaNO_3$	75	35	(Tang & Fung, 1997)
	KNO_3	93	N/A	(Freney*, et al.*, 2009)
Sulfates	H_2SO_4	liquid	liquid	
	NH_4HSO_4	39	N/A	(Cziczo, Nowak, Hu, & Abbatt; Tang, 1979)
	$2NH_4NO_3 \cdot (NH_4)_2SO_4$	56	N/A	(Tang, 1979)
	$(NH4)_3H(SO4)_2$	69	N/A	(Tang, 1979)
	$(NH_4)_2SO_4$	80	30-40	(Cziczo, Nowak, Hu, & Abbatt; Orr*, et al.*, 1958; Tang, 1979)
	Na_2SO_4	80	N/A	(Koloutsou-Vakakis & Rood, 1994)
	$MgSO_4$	85	N/A	(Ha & Chan, 1999)
	K_2SO_4	96	60	(Freney*, et al.*, 2009)

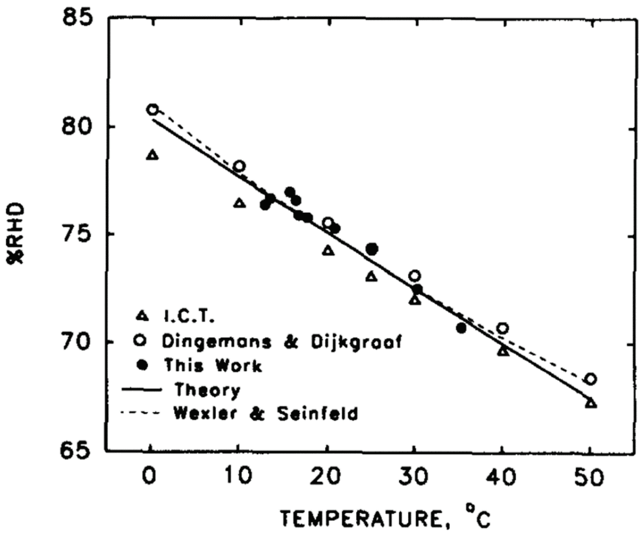

Figure 2.7. Deliquescence RH as a function of temperature for $NaNO_3$ particles [80]. Copyright permission obtained from Copyright Clearance Center.

It is important to note here that a hysteresis exists between the deliquescence point and crystallization point (efflorescence) of a salt during drying, as seen in Figure 8. This behavior is due to the energy barrier associated with nucleation and growth of the solid during drying. Although the efflorescence points of common halide salts have not to date been successfully theoretically predicted, values for certain salts have been experimentally determined, some of which are summarized in Table 2.1.

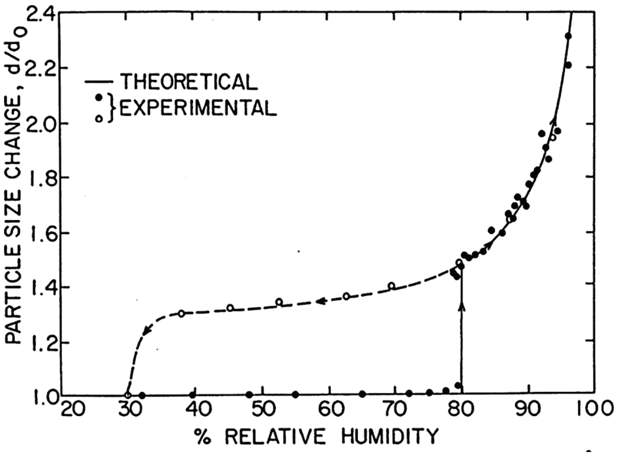

Figure 2.8. Particle size change of $(NH_4)_2SO_4$ particles with respect to relative humidity. The steep slope in the growth regime (arrows towards high RH) at ~80% is the deliquescence point, while the drop at ~30% during evaporation (arrows towards low RH) is the efflorescence point of the salt [88]. Copyright permission obtained from Copyright Clearance Center.

Pure salts are rare in the natural atmosphere, and surface contaminants can be more accurately represented as mixed salts. The deliquescence point of a salt mixture, the mutual deliquescence RH (MDRH), is lower than that of their pure salt components, as shown in Figure 2.9. A number of thermodynamic deliquescence models have been developed in the atmospheric sciences and other fields for estimating the water content of mixed and pure salt systems [81-85]. These models have been shown to agree reasonably well with experimental results [86-89]. In the context of corrosion, Pablan, Yang and coworkers have utilized mixed salt models to examine the deliquescence behavior of particulate matter in nuclear waste repositories [90-92].

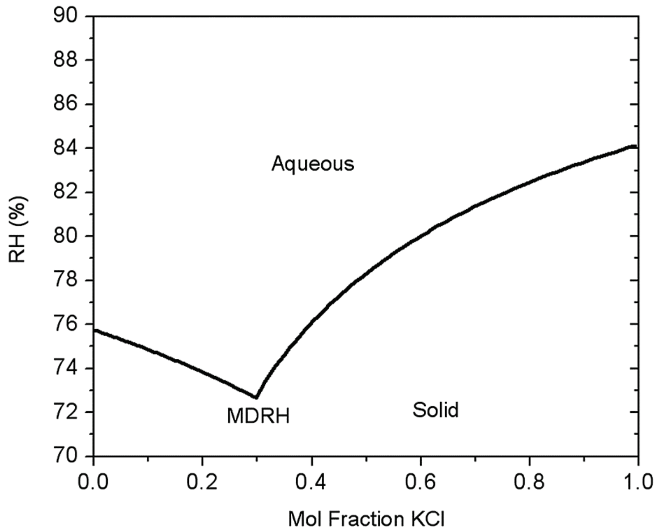

Figure 2.9. Deliquescence behavior of mixed NaCl and KCl constructed using Analyzer Studio strong electrolyte modeling software (OLI Systems).

The majority of work to date on atmospheric corrosion has focused on the effect of single, soluble inorganic salts on TOW. Halides salts, such as NaCl, have been given specific attention because they are commonly found in corrosive marine atmospheric environments as major components of sea salt aerosols. Corrosion at or above the DRH of these inorganic salts has been well documented, but only a few studies have examined or considered the possibility of corrosion below DRH. Lyon and Cai [93] along with Wang and Kido [66] found evidence for corrosion only at and above the deliquescence points of NaCl and KCl when exposing polished carbon steel and iron surfaces with these contaminants to RH levels from well below the DRH to 100%RH. Yang et al. [92], on the other hand, found corrosion on carbon steel to occur under these salts far below their deliquescence points, attributing this to adsorbed water on the salt particles. Nishikata et al. [94] exposed stainless steel covered with aqueous $MgCl_2$ droplets to drying conditions and detected a cease in corrosion activity and corresponding large jump in electrolyte resistance when humidity levels reached the deliquescent point of the $MgCl_2$. These conflicting results, specifically between the two studies that examined carbon steel, may be due to the detection limits of the various methods used to determine wetness or corrosion, a topic that will be discussed in Part 2. The corrosion chemistry and corrosion products may have also influenced wetting and drying behavior in these studies.

Corrosion chemistry and corrosion products likely have a significant effect on the drying of electrolytes and deliquescence. For example, a mixture of deliquescent corrosion products and halide salts, such as ferrous chloride (54% DRH [95]) and sodium chloride, would be expected to have a much lower DRH than the pure salts alone. Such considerations have received little attention in atmospheric corrosion studies, where the study of corrosion by single salts has dominated, and the role of corrosion products on TOW has been largely ignored.

2.1.2.3 Modes of Drying

Drying can occur by evaporation and dewetting. The main difference between evaporation and dewetting is that evaporation is driven by vapor pressure gradients whereas dewetting is primarily driven by interfacial forces. Run-off is a special form of dewetting and will also be discussed.

EVAPORATION

Evaporation is driven by the difference in the water vapor pressure of a solution and the water vapor pressure in the air above that solution, as given by Dalton's law of evaporation:

$$E = b(P_s - P_o) \qquad 2.11$$

Where E is the evaporation rate, P_s is the saturation water vapor pressure of the surface, and P_o is the water vapor pressure of the surrounding air. The rate coefficient b is a function of a multitude of factors including heat, the available amount of water, and the vapor pressure gradient between the surface and the bulk air, many of which are well summarized by [96].

Evaporation can also be viewed in terms of a surface energy balance:

$$R_n + L + Q + G + S = 0 \qquad 2.12$$

where R_n is the flux of net all-wave radiation into the surface, L is the latent heat of vaporization of water, Q is the flux of sensible heat, G is the heat flux at the lower boundary of the surface, and S heat storage capacity of the solid, as illustrated in Figure 2.10. By convention, these terms can be either positive or negative depending on whether energy is being transferred to or from the surface respectively.

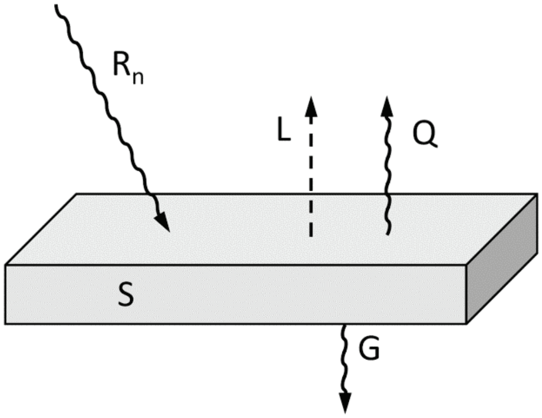

Figure 2.10. Illustration of surface energy balance showing an influx of net all-wave radiation. The scenario depicted here is typical for a boldly exposed wet surface heated by the sun.

Models based on energy balance and Dalton’s law are commonly used in the fields of environmental science and meteorology to predict the evaporation from bodies of water, vegetation canopies, and soils. More pertinent to atmospheric corrosion are those developed in other fields that are used to predict evaporation of thin films or droplets of water from solid surfaces [97-99]. Published studies on evaporation mechanisms or models particular to corrosion are sparse. The work of Cole and coworkers is a pertinent exception and discussed here.

Cole et al. [100] developed and tested a model for the evaporation of drops of sodium chloride solution covering a metal surface under slow mass transfer conditions (i.e., indoor or sheltered conditions). The model they developed was derived from Greiner and Winter's [97] model for the evaporation of water into air from a flat plate of finite thickness assuming laminar boundary layers. It is based on Dalton's law with the rate coefficient accounting for changes in solution vapor pressure as the drop dried along with air velocity and drop geometry. Cole and Patterson [64] further expanded this work to include radiation flux associated with open outdoor exposure, as discussed in the earlier section on dew condensation. Their results exemplify the strong influence that R_n and L in Equation 2.12 have on evaporation from boldly exposed outdoor surfaces. This work also illustrates the dramatic diurnal variance in surface temperature and, hence, SRH, with respect to relatively unvarying ambient RH and temperature that can occur during periods of clear sky and low wind.

Many more studies have been conducted on the effects of evaporation on corrosion than on predicting evaporation. As will be discussed further in Part II of this paper, the thickness and geometry of the electrolyte layer has a strong effect on corrosion behavior.

DEWETTING

Dewetting is the spontaneous withdrawal of a liquid film from a non-wetting surface. This phenomenon can be observed when water is poured on a horizontal surface of a freshly waxed car. The pouring water causes forced wetting to occur, but that is followed by spontaneous dewetting via withdrawal and break-up of the film. Dewetting can be described as a balance of interfacial, gravitational g and long range molecular forces P(e). The free energy F of a film on solid can be described by:

$$F = \gamma_{SL} + \gamma_{GL} + \frac{1}{2}\rho g e^2 + \mathrm{P(e)} \qquad 2.13$$

Where ρ is the density of the liquid and e is the film thickness. A Maxwell double tangent construction of F(e) with the interfacial energy of a dry solid reveals two wetting modes, as depicted in Figure 2.11. The modes are defined by the curvature of F below e_c, which is the equilibrium puddle thickness e in Equation 2.13. The first mode (metastable), where F has positive curvature, is characteristic of thick films. In this mode gravity is a dominant force and long-range forces are negligible. Thick film dewetting occurs by nucleation and growth of dry zones. The second mode (unstable), negative curvature, is characteristic of thin films (on the order of a few nanometers) where long-range forces govern dewetting and gravity is negligible. When dewetting occurs the film breaks up into a polygonal array of small droplets [1].

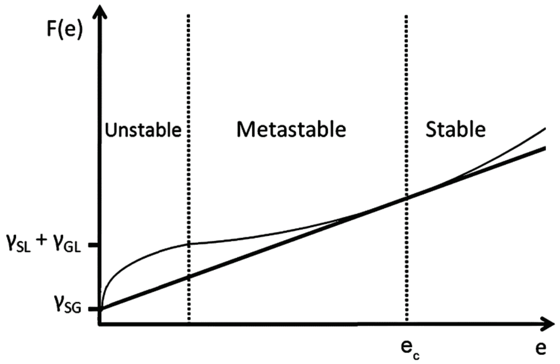

Figure 2.11. Double tangent construction of the free energy of a film as a function of film thickness as per Equation 2.13. The boundary between the stable and unstable region represents the critical film thickness, below which dewetting can occur. Dewetting by nucleation and growth of a dry region occurs in the metastable region. Spinodal decomposition occurs in the unstable region.

In reality, films are not always of consistent thickness and they are rarely composed of a pure liquid. Kheshgi and Scriven [101] examined, via modeling, the dewetting of ordinarily stable thick films due to disturbances which can cause localized thinning or surface tension gradients. They found convex solid surfaces can cause local thinning of a film due to capillary pressure differences; the sharper the surface (i.e., higher curvature), the greater the difference in capillary pressure. Surface tension gradients are also present due to impurities on a solid surface, the heterogeneous nature of the surface itself, or chemical concentration gradients in the liquid.

RUNOFF

Runoff is a special case of dewetting where a macroscopic water film or drop leaves a tilted surface altogether due to the force of gravity. The sticking ability of the water film or drop depends on the wettability of the substrate and contact angle hysteresis at the triple phase boundary. A wealth of work has been carried out to relate these parameters, as reviewed by [102] and [103]. In general, the sticking behavior of drops has been shown to be described by:

$$F_r = \gamma_{GL} R k (\cos\theta_R - \cos\theta_A) \qquad 2.14$$

Where F_r is the dimensionless retention force, R is the radius of contour of a drop, θ_R and θ_A are the receding and advancing angles respectively, and k is a scale factor for the retention force that depends on assumptions for the shape of a drop and contact angle variation along a drop, including the effects of tilt angle [104].

Muster et al. [7] utilized this model, assuming shapes of hemispherical caps, to examine the effect different zinc oxides have on wetness duration after rain events, as seen in Figure 2.12. Their results suggest that oxides can have a significant effect on runoff, which has implications for the ability of the surface to not only retain electrolyte but also the wash-off ability of the surface. This type of modeling could prove important in understanding drying phenomena related to TOW determinations or examining the effects of sample tilt on outdoor exposures.

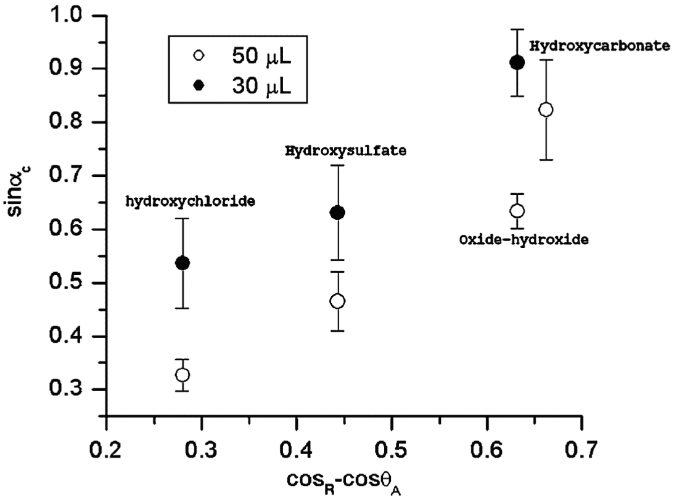

Figure 2.12. Correlation between the dynamic contact angle of oxide coated zinc plates and the predicted plate tilt-angle α *c* required for runoff of 30 and 50 μ l droplet [7]. Copyright permission obtained from Copyright Clearance Center.

Run-off from a surface tends to wash off chemistry that has accumulated on a surface by dry deposition. Cole et al. [105] conducted a study on the effect of rain on the retention of salt on zinc test panels exposed to unsheltered marine coastal conditions. Through surface resistance measurements, they found the panels to wet at higher RH values subsequent to periods of rain as compared to after rain. This effect was attributed to the rain removing hygroscopic salts from the surface of the panels. It is not always true that rain results in the net removal of impurities from a surface. The net effect is guided by a number of factors, including surface geometry and orientation along with length of rain period and flux [106].

2.1.3 Part II: Time of Wetness

Time of wetness, in the broadest sense, is simply a measure of surface wetness duration. Although a seemingly simple concept, what is meant by “wet” and how to measure it has been the subject of scores of investigations over the last sixty years. As a result, numerous practical and theoretical definitions for TOW have been developed. Theoretical definitions have proven to be too general or too simplistic, while practical ones are often based on the limits of particular moisture sensing methods they accompany. Investigators have used more than a handful of practical definitions over the years. The published data generated from different definitions cannot, for the most part, be directly compared to each other. This is in part due to the complexity of the wetting phenomena discussed in Part I.

Part II is divided into three major sections. It is appropriate to spend some time examining the concept of wetness and theoretical definitions for TOW over the history of modern atmospheric corrosion science, which is the emphasis of the first section. Considering the historical context and general TOW definitions, it then becomes more apparent how many practical definitions and accompanying measurement techniques and models were devised. An overview of the practical definitions and associated sensing techniques and models in current use are discussed in the second section. Sensing techniques that are used to detect wetness, but not necessarily for field-based TOW determinations, are also discussed in section two. Other scientific disciplines are interested in surface wetness duration related to atmospheric exposure as well. Most applicable to corrosion science is the concept of leaf wetness in the environmental sciences. This concept is discussed in section three along with related practical definitions, sensing techniques, and models.

2.1.3.1 Early Atmospheric Corrosion Research and Time of Wetness

The study of atmospheric corrosion as a modern scientific discipline began in the early 20th century. Vernon, an early pioneer in the field, carried out a number of studies in the 1930s that examined the effects of humidity and pollutants on corrosion rate [107-109]. He was one of the first to demonstrate the corrosion-accelerating effect of sulfur dioxide in humid environments. Vernon, along with Wilkinson and Patterson [110] and Hudson [111], developed the concept of critical humidity, which is the relative humidity value above which corrosion rate becomes significant. Vernon [107] found critical humidity to usually occur around 60-70% RH in the presence of small amounts of pollution.

U.R. Evans [112] summarized the developments and understanding of corrosion science of the first half of the 20th century in *The Corrosion and Oxidation of Metals*. Regarding atmospheric corrosion, Evans agreed with Vernon’s definition of critical humidity and added that the critical humidity is marked by the point at which a hygroscopic body on the surface is able accumulate water.

Evans divided atmospheric corrosion into three categories based on critical humidity -dry, damp, and wet. Dry corrosion was that which occurred below the critical humidity. Damp corrosion, he stated, occurred above the critical humidity up to the saturation point of water vapor in the air and requires the presence of gaseous or solid pollution. He defined wet corrosion as that which occurs when rain or liquid water is present on the surface.

The work of Tomashov [113] was also important in advancing the understanding of atmospheric corrosion. Tomashov demonstrated that atmospheric corrosion rate is dependent on the amount of moisture on a metal surface. He predicted the effects of electrolyte thickness on corrosion processes whereby oxygen reduction is the primary cathodic reaction, a phenomenon later well demonstrated by Stratmann [114]. He also stated that, “corrosion activity can be best and most fully characterized by length of time the moisture film remains on the surface...”

By the mid-1960s it was well recognized that the time a metal surface remained wet strongly correlated with corrosion rate in atmospheric exposures [61, 115-119]. This has come to be known as the time of wetness (TOW). The TOW concept is now utilized for environmental corrosivity classification, empirical modeling, structural health monitoring, and mechanistic atmospheric corrosion studies. Numerous authors have put forth general theoretical definitions for TOW. For example, Leygraf and Graedel [43] defined it as the “time during which a corrosion stimulating liquid film exists on the surface.” Schweitzer [120] stated that it is the “length of time during which the metal surface is covered by a film of water that renders significant atmospheric corrosion possible.” The definition in ISO 9223 [121] reads as follows, “TOW is the period during which a metallic surface is covered by adsorptive and/or liquid films of electrolyte that are capable of causing atmospheric corrosion.”

As with most TOW definitions in the literature, an important yet subtle difference exists concerning how “wetness” is defined which is exemplified in those given above. The definitions of Leygraf and Graedel and ISO 9223 infer that only an electrolyte need be present on a surface for it to be considered wet. That given by Schweitzer suggests that the electrolyte must also be capable of causing significant corrosion. Defining a surface as wet when an electrolyte is present requires either a measure or prediction of when an electrolyte is present on a surface. The constraint that corrosion must also be significant requires the additional knowledge of the electrochemical response of a surface. This subtlety is one of the major sources for the diversity of practical definitions and associated determination methods overviewed in the next section.

2.1.3.2 Practical Definitions and Sensing

Although the basic concept and importance of TOW in understanding atmospheric corrosion is generally agreed upon, its practical determination is widely varied. More than a dozen practical definitions and accompanying measurement methods have been developed over the last fifty years. The difficulty in applying these definitions lies in determining what is meant by "wet" and being able to accurately capture the complex wetting phenomena overviewed in Part I.

Practical definitions can be categorized by the way in which TOW is treated-either as an environmental parameter or as a surface parameter. As an environmental parameter, TOW is estimated in terms of climatic conditions. As a surface parameter, it is determined by measuring the moisture on an actual surface. Both methods will be overviewed and critiqued in the remainder of this section. Additionally, laboratory methods used to sense surface wetness on metals but have not been explicitly used for TOW determinations will be discussed.

ENVIRONMENTAL PARAMETER

As an environmental parameter, TOW is estimated from meteorological conditions. Temperature and RH of the ambient environment are often utilized to provide indication of surface wetness. This definition of TOW is based on the idea that, above a certain humidity threshold, an electrolyte capable of causing corrosion forms due to sorption of water by the metal surface and contaminants on it. Inarguably, the most commonly used practical definition for TOW is that given by ISO 9223, which defines it as the total time when the relative humidity (RH) of the ambient environment is greater than or equal to 80% at temperatures above 0°C.

A number of limitations of the ISO definition have been pointed out in the literature and even in the ISO 9223 standard itself. One major issue is that, by definition, precipitation and dewing events are excluded. With regard to the latter, temperature differences between the ambient air and the surface can cause quite large deviations between the RH of the surface and the surrounding air, as discussed in Part I. It has also been shown in Part I that many atmospheric contaminants deliquesce at humidity levels far below 80%. A study by Cole et al. [122] clearly shows wetness measured on resistance-type sensors (discussed below) occurring well below the 80% threshold at a number of field sites monitored throughout Asia and Australia. Some of the data from that study are recast here to illustrate the point, Figure 2.13.

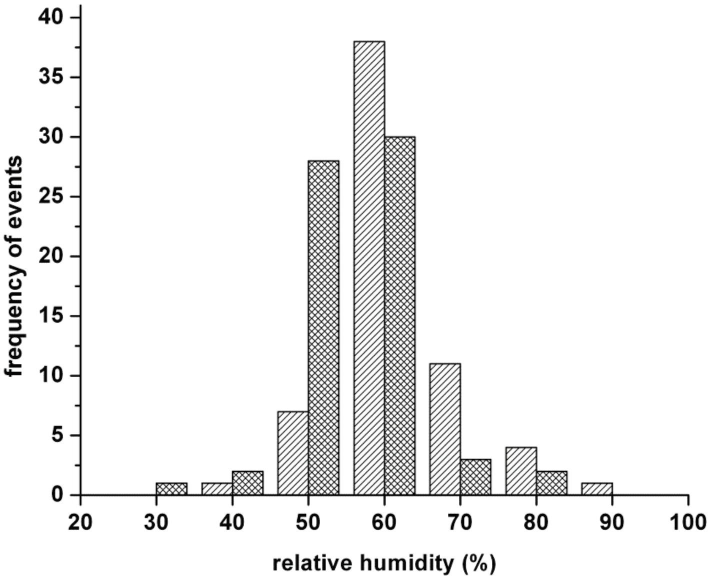

Figure 2.13. Frequency of wetting and drying events recorded using a resistance-type wetness sensor compared to ambient RH at a coastal site in Thailand over an exposure period of one month. The diagonal slashed bars represent wetting events and the crosshatched bars are drying events [122]. Copyright permission obtained from Copyright Clearance Center.

The ISO definition excludes the presence of surface wetness at temperatures below 0°C, although it is well known that liquid water and aqueous electrolytes can exist at subzero temperatures due to depressed vapor pressures as discussed in Part I. Studies examining subzero corrosion in the literature indicate that corrosion does occur, albeit usually at a slower rate than above zero given similar conditions otherwise [123-125]. Mikhailov et al. [123] provide a review of the subject and discuss exposure studies carried out in Antarctica and other cold climates in relation to TOW. In general they found that TOW evaluated in terms of the ISO definition was inconsistent with the corrosion rates seen in extremely cold environments. For example, the results of a year-long exposure study at the Mirnyi coastal station in Antarctica found ISO TOW to be 75hrs for the year, but the average corrosion loss of carbon steel was found to be 7.7 μm equivalent depth, implying a penetration rate of 36 mpy (0.9 mm/yr) if corrosion only occurred during those 75 hours.

Variants of the ISO definition have been proposed with lower RH thresholds and greater temperature ranges to address these shortfalls [70, 122]. These definitions are not standardized nor widely used, and vary between practitioners. Although these variants likely provide a better estimate of wetness duration, comprehensive comparisons between actual wetness conditions of surfaces of interest and these definitional thresholds are lacking.

SURFACE PARAMETER

Another means of estimating TOW is to measure moisture on an actual surface exposed to the atmosphere. This measurement can be approached in one of two ways, either by measuring the moisture on a sensor that serves as a surrogate for a surface of interest, or by measuring moisture directly on the surface of interest itself, such as a structural component or a corrosion test panel. Both approaches will be discussed here.

Indirect Sensing

Indirect methods are by far the most commonly used estimate of TOW when it is treated as a surface parameter. The majority of the sensors used for these methods consist of a set of metal electrodes separated by an insulating material. Deposited moisture that bridges the insulating gap between the electrodes causes a change in electrical properties which is then measured. Time of wetness is then defined as the time during which a certain voltage, current, or impedance threshold is exceeded. Wet-dry thresholds are often established from the baseline response of clean sensors at low humidity levels. A variety of electrical sensor designs and measurement methods are seen in practice which can be classified as galvanic, resistance, or impedance sensing. Quartz crystal microbalances have also been used to measure mass changes associated with moisture sorption events and will be discussed in this section as well.

GALVANIC CORROSION SENSING

Galvanic corrosion sensing relies on a measurable corrosion potential or current that develops between electrodes of different composition due to the presence of moisture. Tomashov and coworkers [126] were some of the first to use galvanic sensors consisting of alternating electrodes of iron or copper coupled with zinc or aluminum to monitor surface moisture. Current that developed between the electrodes due to electrolyte bridging was measured in their studies with a galvanometer. Shortly after, Sereda [61, 119, 127] reported on the development and use of various electrode materials and sensor configurations, including the use of platinum strips on a zinc plate to measure TOW.

Sereda et al. [125] later reported on the development and testing of a small sensor consisting of a pair of interdigitated electrodes of gold and copper or gold and zinc on a fiberglass backing. The electrodes were spaced 100 – 200 μm apart Figure 2.14**.** The sensor was defined as wet when the measured voltage exceeded a certain threshold. Threshold voltages were on the order of 0.1 or 0.01V depending on the type of metals used for the sensor. Although not explicitly stated, the thresholds appear to have been established from baseline readings of clean sensors during initial exposure to outdoor sites. The authors reported that two sensor types were exposed for over one year at various sites across the US and Canada. The temperature of the sensors along with the ambient air temperature and relative humidity were measured during the exposure. One of the findings of interest here is that a simple correlation could not be found between ambient RH and the voltage response of the sensors. The authors suggested this may have been in part due to the difference between surface and ambient relative humidity.

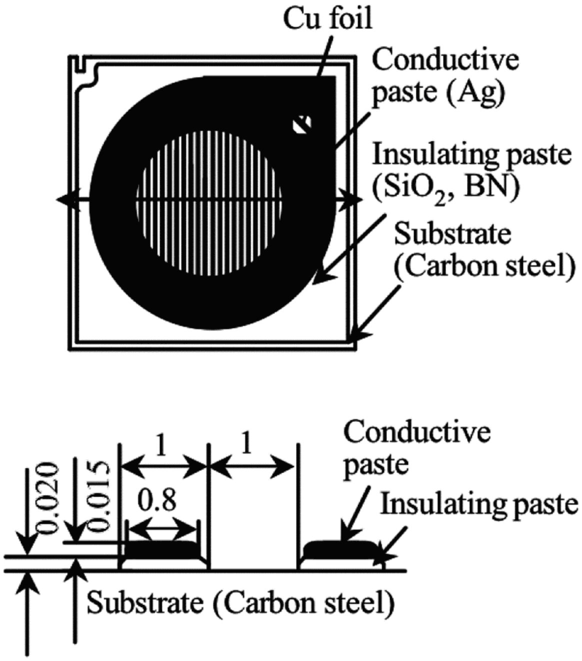

Figure 2.14. Schematic of Shinohara et al.'s ACM sensor [160]. Copyright permission obtained from Copyright Clearance Center.

The ASTM G84-G89 standard [128] for TOW estimation dictates the use of the design described by Sereda et al. [125]. This standard states that new sensors should be "activated" by depositing sodium chloride on their surface followed by exposure to 100%RH conditions in the laboratory. This activation, it explains, promotes the formation of corrosion product. Although not explicitly mentioned in the standard, corrosion products could serve to emulate the wetting behavior of copper and zinc surfaces by capturing some of the sorption contributions they impart, as discussed in Part I. On the other hand, using the activated sensors as indicators for other types of surfaces or environments with low NaCl flux may prove to give an inaccurate estimate of wetness duration.

A number of other sensor designs and measurement methodologies have been developed over the years, a few of which are highlighted here [129-135]. Mansfeld and Kenkel [136] constructed a sensor of alternating electrode plates separated by 6mm thick Mylar spacers and set in an epoxy base. They defined TOW as the time current measured between the electrodes exceeded 0.1μA. A later paper by Mansfeld [137] explains that the threshold was based on the time during which the corrosion current corresponded to a corrosion rate on steel that was considered significant. Also, in this paper, Mansfeld pointed out that many TOW definitions for galvanic-type sensors had been, up to that point, arbitrary. He argued that a better definition for TOW using these sensors was as the time during which a certain corrosion rate is exceeded. The reader is referred to this paper for thorough overview of development efforts and utilization of galvanic sensors prior to the 1980s.

More recently, Shinohara et al. [135] reported on the development and evaluation of a commercial galvanic sensor termed an atmospheric corrosion monitor (ACM). The sensor was constructed of a linear array of silver-epoxy paste applied over a carbon steel substrate, with an epoxy insulator between the two metals, Figure 2.14. They stated that an output of the sensor above 10nA correlated to wetting in their paper, but did not offer an explanation behind the choice of this threshold. They reported on exposing the sensors at two different sites in Japan in outdoor unsheltered and sheltered conditions. The investigators, through correlation with local meteorological data, correlated current output with dewing, drying, and precipitation events as seen in Figure 2.15. Additional performance parameters of these sensors were examined with relation to an impedance sensing method and are discussed in the corresponding section below.

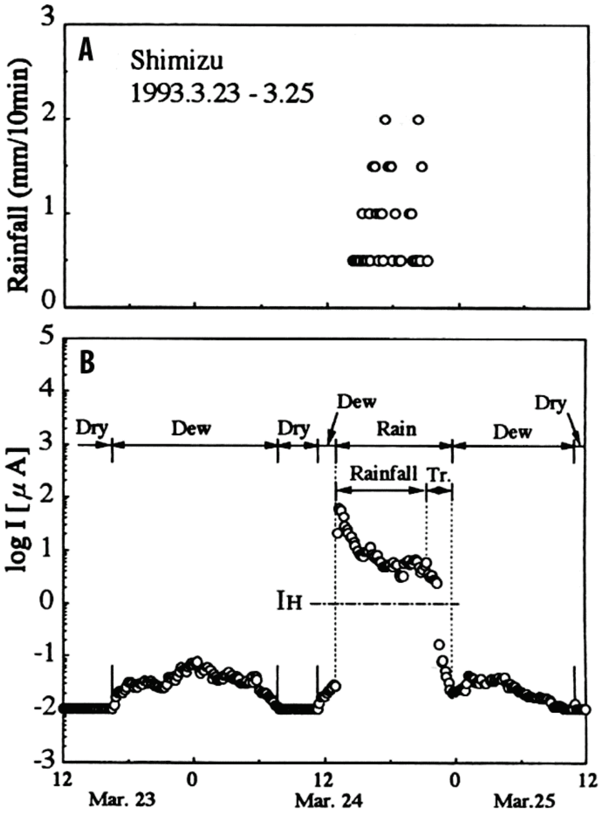

Figure 2.15. Current output of an ACM sensor developed by Shinohara et al. [135] during an outdoor exposure test (B); Rainfall measured during this period (A). Copyright permission obtained from Copyright Clearance Center.

Galvanic sensors, like the other electrode-type sensors discussed in this paper, are able to indicate electrolyte presence from both direct deposition and sorption events. Wetness, in most cases, is defined as the time during which a current threshold or potential that is measurable or deemed significant is exceeded. Because these sensors indicate wetness in terms of corrosion activity, there are instances when a sensor surface could conceivably be wet without indicating as such. For example, if the insulator material between the electrodes is hydrophobic to any degree, electrolyte may not spread across. In this scenario, uncoupled corrosion of the electrodes could occur.

In the same manner, deposited aerosol drops smaller than the electrode spacing of a sensor may not bridge the electrodes. Electrode spacing of those sensors highlighted in the preceding discussion range from several hundred microns to several millimeters compared to, for example, marine aerosol drop diameters which are typically less than a hundred microns. This means that some sensors may not be capturing the wetting contribution of deposited aerosols smaller than their electrode spacing at sites with low deposition velocities and high wash off rates (i.e., low aerosol loading density). Detailed examinations of the relationship between the presence of electrolyte and detection that address these issues are lacking in the literature.

Another issue with these sensors, and all indirect sensors, is that their surface morphology, corrosion product make-up, and electrochemical characteristics are different to some degree from the surfaces for which TOW is being estimated. These differences can affect both the conditions and the rate at which wetting and drying occur. The extent to which these factors affect the accuracy of predicting wetness on a surface of interest has been underexplored.

RESISTANCE SENSING

Resistance sensors are referred to here as those constructed of noble alloy electrodes across which a DC or AC voltage is applied and a corresponding resistance or current is measured. The majority of published work using this type of sensing method for atmospheric corrosion has been carried out by groups in Scandinavia and Australia [105, 138-142].

Norberg [143] developed a sensor based on a design evolved from work carried out by Haagenrud and coworkers [141,144-145] (he sensor is constructed of interdigitated set of gold alloy electrodes with 130μm spacing applied to a sintered alumina backing, Figure 2.16. Alumina was selected to impart thermal conductivity so that the sensors could be placed directly on a surface interest. The standard method utilized in the studies referenced below was to apply 100mV DC with a polarity reversal period of 30 seconds and simultaneously measure the resulting current. The response of clean sensors to RH in the laboratory was characterized by Norberg and an equivalent circuit developed to interpret the output. He also evaluated sensor performance in the field.

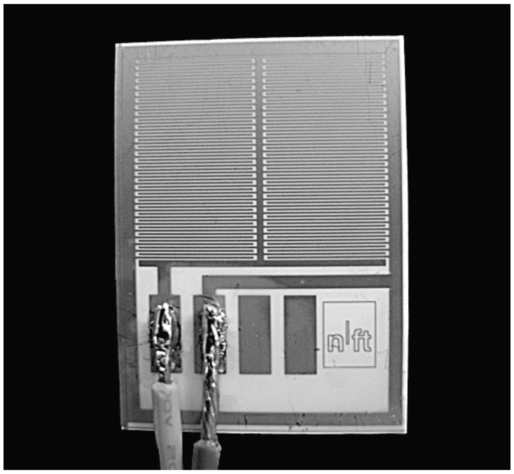

Figure 2.16. Commercial version of moisture sensor (Norwegian Institute for Air Research) developed by Norberg and coworkers [146].

In one study, Norberg [146] mounted sets of 12 sensors on two pieces of coil coated sheet aluminum. The sheets were in turn mounted vertically on the roof of a building in Stockholm for six months. Climatic conditions in the vicinity of these sensors were measured, including humidity, air temperature, wind, and precipitation. Sensor output closely followed trends in relative humidity. Norberg found the relative standard deviation for current output of each set of sensors to be around 10% at any given point in time. He stated that this might be due to differences in surface wetness on each sensor rather than differences in manufacture and set-up. He explained that the deviation could result in large differences in TOW measurements between sensors in cases where the average current is around the threshold current limit chosen for TOW. For this reason, he used 10, 30, and 100nA as thresholds and calculated TOW for each one resulting in TOW of 38, 23, and 1% respectively for the entire exposure period. He did not examine nor speculate as to which best represented actual surface conditions, but his results exemplify the impact of threshold choice on TOW estimations.

This sensor has also been used in a number of exposure studies around Australia and Southeast Asia [105, 122, 138, 139, 140, 142]. Of importance here is the study by Cole et al. [122] where surface chemistry was correlated to the humidity response of these sensors during field exposures. They found that the sensor measurements seemed to capture the deliquescence behavior of the chemistry of the surface solution developed on them. The composition of the surface solution was inferred from analysis of plate wash-off and salt candle solutions placed near the sensors.

The limitations of this sensor and technique are similar to the galvanic sensors, with a few exceptions. This sensor may give a more accurate estimate of surface moisture presence as compared to the galvanic sensors because it does not rely on the occurrence of corrosion. On the other hand, a gold surface may not emulate the typical materials examined during exposure, such as steel or copper, as well as a galvanic sensor might due to lack of corrosion products on its surface and differences in wetting behavior.

IMPEDANCE SENSING

Impedance sensing methods for TOW utilize electrochemical impedance spectroscopy (EIS) techniques to examine electrochemical behavior between separated electrodes. The advantage of using impedance over DC resistance is that both the corrosion activity of the electrodes along with electrolyte resistance between electrodes can be simultaneously monitored.

A research group at the Tokyo Institute of Technology has published numerous studies using specialized EIS sensors to examine corrosion rates and TOW in both laboratory and outdoor settings [94, 147-152]. The laboratory studies published by the Tokyo group focus on corrosion under thin electrolyte films (around 10-1000μm) during wet-dry cycles. The group has examined a number of different metals, electrolyte chemistries, and wet-dry variations. The sensor design utilized consisted of two parallel metal electrodes spaced 0.1mm apart and set in epoxy, Figure 2.17. In these studies, electrolyte was placed as a drop or film on top of the sensor and impedance measured at 10 mhz and 10 Khz frequencies over the course of numerous wet-dry cycles. The 10 mhz frequency was used to determine polarization resistance (R_p) while the 10 Khz frequency was used to determine solution resistance (R_s). Although not specifically defined in the papers reviewed here, their definition for TOW appears to have been the time when R_p^{-1} is determined above zero, as seen in Figure 2.18. The authors recognized that the sample likely still had aqueous solution on its surface even when Rp^{-1} was zero. They postulated that the moisture film would be discontinuous and thus could not to conduct across the electrode gap any better than the epoxy insulator.

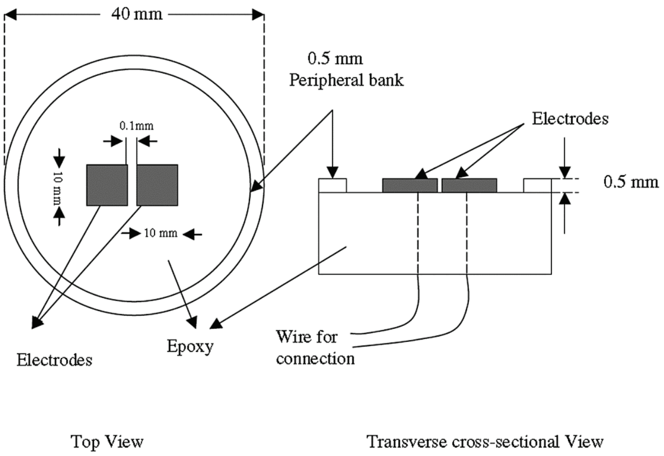

Figure 2.17. Schematic of impedance sensor used by the Tokyo Institute of Technology group. From El-Mahdy [147]. Copyright permission obtained from Copyright Clearance Center.

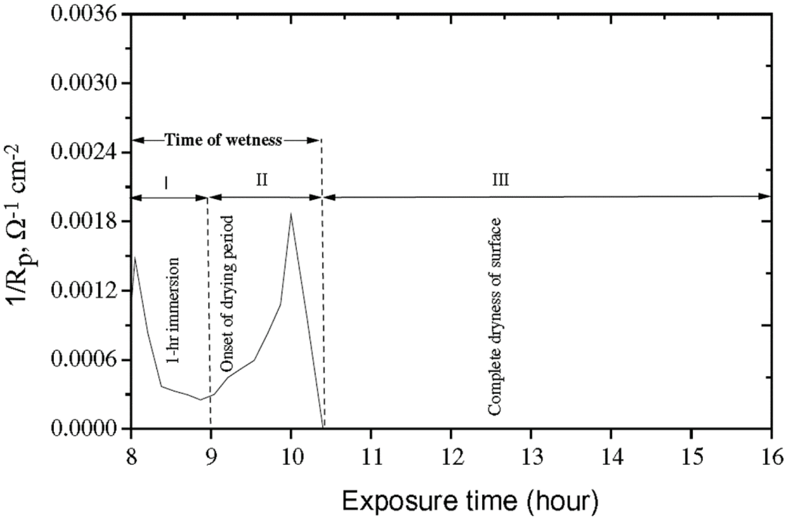

Figure 2.18. Inverse polarization resistance versus time during wet-dry cycling of El-Mahdy's copper impedance sensor. From El-Mahdy [147]. Copyright permission obtained from Copyright Clearance Center.

The group has also published studies on using the same technique with a similar sensor for outdoor atmospheric exposures [147, 153-154]. Nishikata, Suzuki and Tsuru [154] examined corrosion and wetting events of sensors constructed of nickel-bearing carbon steels of varying nickel content during exposure to a marine atmosphere for a period of two years. They defined TOW as the period when R_S was below 10^4 Ω, which was the conductance of the epoxy base. The investigators recognized, as with their lab experiments, that discrete droplets between the electrodes could not be detected. The results of the study show that TOW varied by as much as 20% in some months between sensors with electrodes of different nickel-contents. They postulated that this variance was in part due to different rusts forming on each of the alloys.

A number of other investigators have utilized similar techniques for determining wetting behavior in laboratory and atmospheric environments [134, 155-160]. Of those referenced, two publications [159-160] stand out as important in understanding the interaction of drops and films with the sensor surface. These two studies are summarized and discussed below.

Shitanda et al. [159] constructed a printed circuit board sensor with two silver electrodes arranged in a zigzag pattern. The spacing interval between the electrodes was 1mm. In this publication, the authors reported on the sensor's impedance characteristics at 10 mHz and 10 KHz during deliquescence and drying events. The group placed sodium chloride crystals on the surface of the sensor to achieve a surface density of 15 $mg\cdot cm^{-2}$ and then exposed it in a closed vessel at room temperature and 88% RH until the surface wet. During this period, they took photographs of the sensor surfaces as the water film grew and measured the impedance, Figure 2.19. They used the data to model equivalent circuits for the stages of wetting. The investigators noted that macroscopic water drops only formed on the silver electrodes as opposed to the hydrophobic circuit board during the initial exposure and then coalesced into larger drops which bridged the electrodes during later stages of exposure.

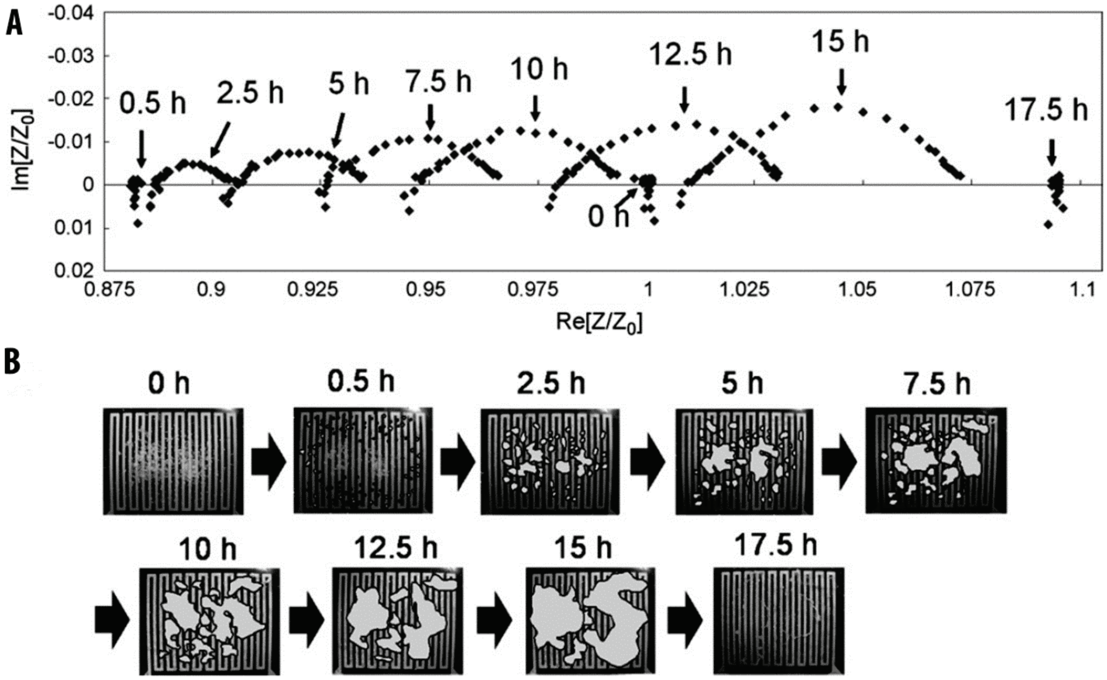

Figure 2.19. (A) Cole - Cole plot of impedance during wetting of NaCl on Shitanda et al.’s [159] sensor during exposure of the initially dry sensor to 88 % RH up to 17.5 hr, at which point the sensor was again dried; (B) enhanced photographic images of the sensor during this period with droplets and puddles outlined. Copyright permission obtained from Copyright Clearance Center.

Katayama et al. [160] carried out a study comparing an impedance sensor and the ACM sensors discussed above. The impedance sensor was constructed of ring and rod carbon steel electrodes. The electrodes were placed in a concentric pattern with a 100 μm gap between them and set in epoxy resin. For the comparison, drops of $MgCl_2$ and NaCl aqueous solutions of various concentrations were placed on both sensors. The sensors were then subjected to stepwise RH cycles between 30-95% with each step in RH held for 12 hours at 298K. The output responses of the sensors were recorded. They found that the impedance sensor was not sensitive to RH changes with low salt density on its surface while the ACM was. Although the investigators did not make conjectures as to why the two sensors responded differently, it may be due to differences in electrode gap size and substrate wettability between the sensors. This study exemplifies the standing issues with electrode-type sensors discussed in the previous sections.

QUARTZ CRYSTAL MICROBALANCE

The quartz crystal microbalance (QCM) has been utilized in many studies to examine water adsorption phenomena on clean and contaminated metal surfaces as discussed in part I of this paper. Forslund, Leygraf and coworkers developed a QCM method for monitoring mass gain associated with wetting, corrosion, and foreign particulate deposition for sheltered outdoor and indoor environments [50, 161-163]. Their method involved placing a QCM into a housing fit with an ambient air filter of 10μm pore size, which they state was necessary to protect the crystals from coarse dust and mechanical damage. The surface of the crystal was coated with copper, silver, or gold depending on the application.

As part of one of their studies, Forslund and Leygraf [162] examined the response of gold QCM sensors to exposure at six outdoor sites. Sensor response indicated irreversible mass gain along with periodic reversible mass gain that correlated with RH fluctuations, Figure 2.20. They attributed the reversible mass gains to sorption of water by the gold surface and deposited contaminants and the irreversible gains to accumulation of contaminants. The method used, they conceded, was subject to error due to long periods of high RH (no dry-out) during exposure and dynamic hysteresis effects as the surfaces changed over time. Nonetheless, the investigators were able to estimate TOW due to adsorbed moisture.

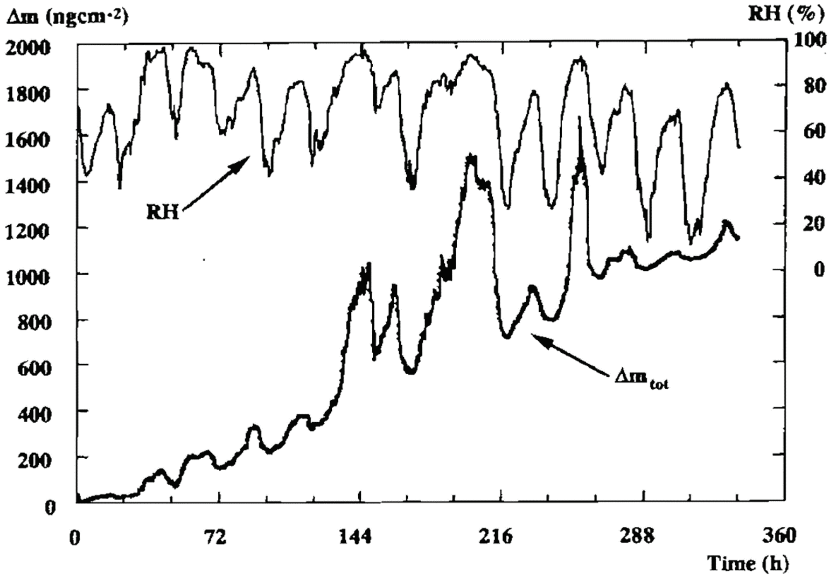

Figure 2.20. Mass variation of an initially clean QCM sensor and ambient RH during exposure to an urban area in Forslund and Leygraf's study [162]. Copyright permission obtained from The Electrochemical Society.

Although QCMs are commonly used for adsorption studies in clean environments, Forslund and Leygraf have demonstrated the utility of these instruments for examining wetting behavior in natural indoor and sheltered outdoor conditions. The high sensitivity of these instruments makes them ideal for TOW determinations exclusively involving adsorption wetting mechanisms. In their work however, the incoming air was filtered. This would have eliminated deposition of larger size fraction aerosols on the sensors, which may have significantly altered its wetting behavior as compared to a bare exposed surface. In addition to mechanical damage, larger deposited particles may cause interpretation issues with measured frequency changes due to the convolution of dampening effects with mass loading as discussed by Zhang, Feng and Sui [164].

Direct Sensing

Methods that have been utilized to directly measure moisture on a surface of interest in the context of corrosion include Kelvin probe potentiometry, scanning force microscopy, and spectroscopy. These methods, for the most part, have been confined to laboratory studies and have not been utilized for routine TOW determination. Nonetheless, they deserve review here as they are all complimentary techniques that could prove useful in detailed studies of the wetting behavior of surfaces.

Kelvin Probe

Kelvin probe (KP) analysis has been utilized to examine atmospheric corrosion under thin electrolyte layers and drops. The advantage of this technique is that electrochemical experiments can be conducted in a non-contact fashion. Although this method is limited to the laboratory, its ability to detect wetting warrants its coverage here. Stratmann [165] was the first investigator to report on using a Kelvin probe for the study of atmospheric corrosion. He demonstrated a linear correlation between potential readings from an ordinary half-cell reference electrode and the Volta potential as measured by the KP. This allowed for KP potential measurements to be correlated to electrochemical potential with reference to the standard hydrogen electrode.

Stratmann and his colleagues carried out experiments using KP to examine corrosion kinetics and wet-dry transition behavior of iron, iron-copper alloys and platinum under thin electrolyte layers [166-170]. In Stratmann and Streckel [168], the investigators reported on the corrosion characteristics of iron and iron copper alloys under repeated wet-dry cycles in a humidity and temperature-controlled chamber. They flooded the sample surfaces with a 100μm thick water layer using a syringe apparatus.

After a certain period of wetness, the samples were dried by changing their temperature with respect to the chamber air temperature. During these exposures, the samples were subjected to varying mixtures of lab air, O_2 and SO_2. Stratmann and Streckel [169] found the potentials of the iron and iron alloy samples would abruptly decrease when first wet and then increase to their maximum potential as they dried, Figure 2.21. Similar potential shifting behavior of steel samples during wet-dry transitions has been reported by a number of other investigators [171-173].

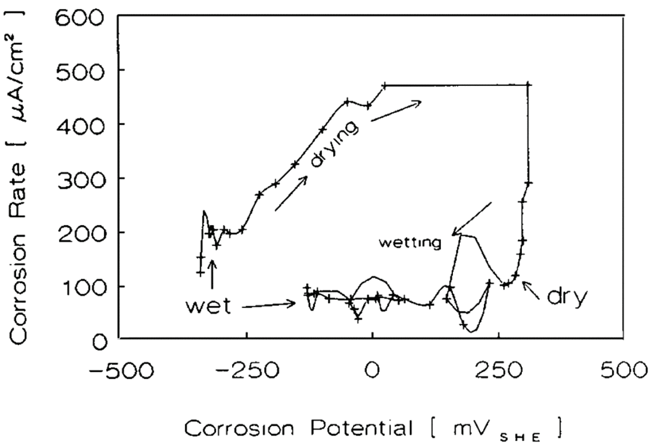

Figure 2.21. Corrosion rate versus corrosion potential measured with a Kelvin probe after placement of a water drop on a polished iron surface exposed to an SO_2 atmosphere for a series of wetting and drying cycles. Arrows indicate the direction of time [169]. Copyright permission obtained from Copyright Clearance Center.

Doi et al. [48] carried out a study on the adsorption-desorption of water on metal surfaces and corresponding work function using an ellipsometer and KP respectively. They measured the thickness of adsorbed water and corresponding Volta potentials on polished and pre-oxidized samples of pure iron, nickel and chromium exposed to RH levels from 0-100%. Although the objective of their study was not to examine the sensitivity limits of their KP method, the results of their paper suggest that the Volta potential measured was sensitive to adsorbed water change down to sub nanometer levels for polished metals, Figure 2.22. Figure 2.22 also exhibits the commonly observed hysteresis between adsorption and desorption.

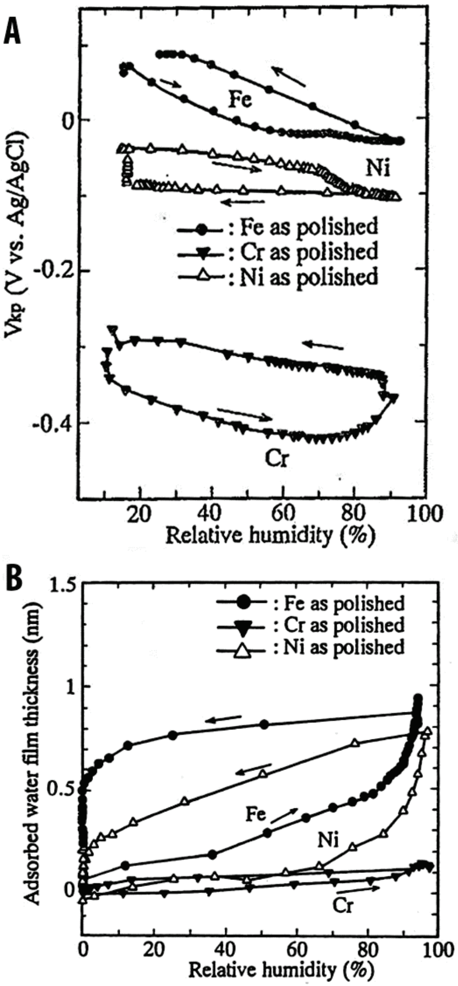

Figure 2.22. (A) Volta potential as measured by a Kelvin probe during exposure of polished alloys to humidity cycles; (B) ellipsometric measurement of water film thickness during the same experiments [48] Copyright permission obtained from Copyright Clearance Center.

The studies summarized above demonstrate that Volta potential measured by a Kelvin probe can be indicative of a wet surface. In most cases, an initial drop in potential correlates to a surface being wet either by direct deposition of an electrolyte or by adsorption. The measured potential appears sensitive to small amounts of surface moisture as reflected in the results of Doi et al. [48]. Although its applicability to field

TOW determinations is questionable, KP appears to be a powerful tool for TOW determinations in the laboratory.

Scanning Force Microscopy

A handful of investigations have been carried out using scanning force microscopy (SFM) to examine sorbed nanoscale water droplets and films on metal surfaces [66, 174-175]. Wang and Kido [66] demonstrated the use of ac non-contact mode SFM to observe adsorption and evaporation phenomena on polished and cleaned SUS304 steel. In their experiment steel samples were first equilibrated to an atmosphere of around 25% RH and then they were placed in a chamber containing the SFM conditioned to 50-60%RH conditions at 25°C. They observed water adsorption and evaporation by means of sample surface profiles for periods of up to around 30 hours, Figure 23. During this time the authors tracked the surface area and volume of the droplets that formed. Although not pontificated upon here, it is interesting to note here the discrepancy between adsorbed water thickness in Figures 2.22 and 2.23. By examining the change in volume over time, the authors were able to distinguish between adsorption and evaporation events.

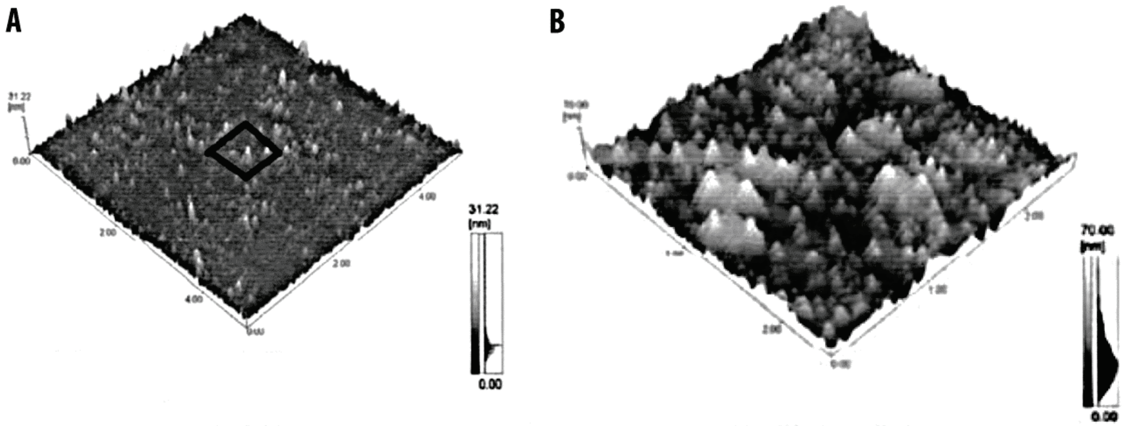

Figure 2.23. SFM surface profiles of SUS304 steel at 25 % RH (A) and 50 % RH (B) at 25 ° C. Scales to the right of the scans indicate peak size distribution and maximum height of peaks: (A) is 31 nm and (B) is 70 nm [66]. Copyright permission obtained from Copyright Clearance Center.

Some studies have reported on the use of SFM in Kelvin force mode, known as Kelvin force microscopy (KFM), to examine not only the profile of nanoscale water but also the Volta potential of surfaces under investigation. Masuda and his collaborators have published a number of papers that report on their observation of corrosion of a variety of metal surfaces under various deposited and sorbed electrolytes of sub-micron thickness [174,176]. Although KFM has been demonstrated to be a functional tool for examining corrosion associated with nanoscopic wetting, Rohwerder and Turcu [177] warned that potential readings acquired by KFM can be heavily influenced by topographical artifacts on the sample and signal contributions from the cantilever of the instrument itself. These effects, they demonstrated, can often lead to inaccurate work function values, including inverted polarity readings.

The use of this technique to characterize nanoscopic amounts of water on a surface may prove useful in addressing the question of what is meant by “wet” in TOW. Along with resolving power, the ability to observe the surface in a wide range of controlled RH atmospheres is the great advantage of this technique. One disadvantage is that surfaces examined must be planar and relatively smooth due to the spacing tolerance required between the cantilever and the surface.

Optical Spectroscopy

A number of optical spectroscopy techniques are routinely utilized to analyze surface moisture in the laboratory environment. Infrared reflection absorption spectroscopy (IRAS) is a method that has been used in studies to monitor atmospheric corrosion behavior during wet-dry cycles [178-180]. In these studies, a small cell with an IR transparent window was used in which a metal sample was subjected to cycles of immersion and drying under various atmospheric conditions. The surface chemistry was monitored using IRAS through the window. The amount of water on the surface was qualitatively monitored by the intensity of the absorption bands in the fingerprint region (300-900cm^{-1}), at 1645 cm^{-1}, and in the 3000-3600cm^{-1} range. The bands correspond to the vibration, stretching, and rotational energies of water molecules in the liquid state. Weissenrieder and Leygraf [181] placed an iron-coated QCM in a similar cell under controlled RH conditions. Through concurrent monitoring of QCM frequency and the intensity of the 3400 cm^{-1} band they found a strong linear correlation between mass and light absorption when altering relative humidity. These results demonstrate not only the complementary nature of the two methods but also the capability of quantitatively measuring adsorbed moisture on a clean surface.

The potential for using spectroscopy methods to monitor TOW in the field has also been demonstrated. Ganther et al. [140] developed a reflectance type TOW prototype sensor. The sensor consisted of an infrared transmitter and receiver mounted opposite to each other at 20° angles to a clean and smooth metal surface. Water present on the surface caused scattering and reduction in received transmittance. A background reflectance value was established on the dry metal surface. The metal was then deemed wet when the reflectance was less than the background value. They tested this sensor on a galvanized steel plate subjected to temperature cycles that induced dewing events to examine the relationship between the output and the plate temperature. The authors concluded that transmittance values qualitatively followed dewing events.

The investigators also deployed a reflectance sensor and one of Norberg's resistance sensors on a stainless steel plate placed under sheltered exposure in suburban Melbourne. The authors did not mention the period of time of this test. They did, however, show comparative outputs for a 5 day period during light rain, Figure 2.24. The authors stated that, although the two sensor outputs follow each other closely, the IR sensor exhibited more sensitivity because it did not abruptly change from wet to dry values during evaporation relative to the resistance sensor. They also stated that this sensor would be suitable for use on any surface that will specularly reflect infrared light, precluding those covered in thick corrosion product. They also noted that sunlight would interfere with the sensor.

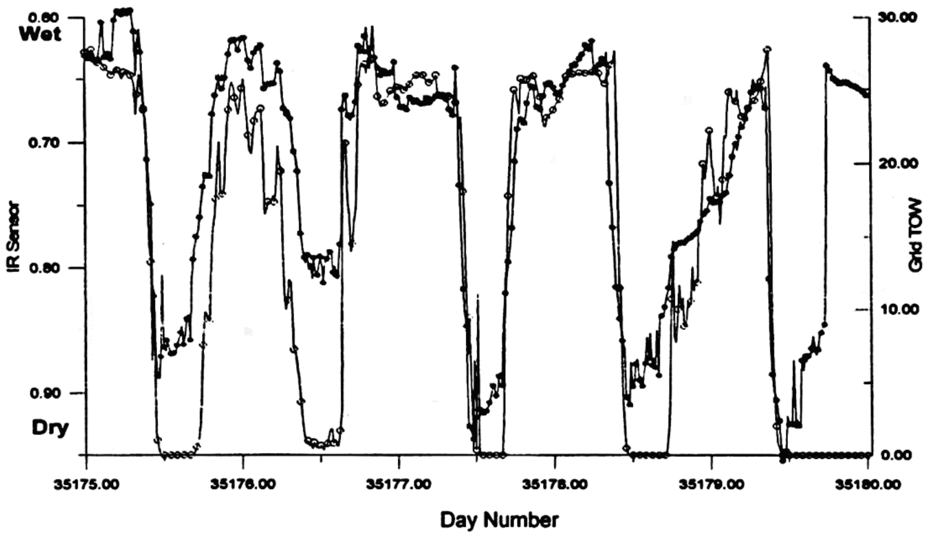

Figure 2.24. Comparison of IR TOW sensor output (closed circles) and Norberg's sensor (open circles) during a sheltered outdoor exposure [140]. Copyright permission obtained from Australasian Corrosion Association.

In general, both of the reflectance spectroscopy and IRAS methods offer the advantage of being non-contact direct surface moisture measurements. IRAS has been demonstrated to be a quantitative measure of sorbed water on clean surfaces provided calibration. The feasibility of quantitative assessment of sorbed water on contaminated surfaces (e.g., corroded) is less clear from work to date. The same holds true for Ganther et al.*'s* reflectance method.

Thus far, all of the methods discussed in this paper were primarily designed and utilized to determine wetness on boldly exposed surfaces. Cooper [182] reported on the development of a sensing technique to detect wetness in occluded spaces, specifically aircraft lap joints. The sensing method involved the deployment of long period grating optical fibers coated with a hydrophilic polymer. The polymer would swell when wet by bulk electrolyte (a visible layer) on the surface causing a decrease in its refractive index and an increase in the spectral loss wavelength.

2.1.3.3 Leaf Wetness in Environmental Science

Plant pathologists and other environmental scientists use the term “leaf wetness” to describe surface moisture in a plant canopy. Moisture influences the initiation and development of many plant diseases. Wetting mechanisms for plants are much the same as those discussed in part I of the paper with the addition of wetting by guttation, a form of plant “perspiration”. It is important to note, however, that most plant leaves are more hydrophobic than clean or corroded metal surfaces. The main wetting mechanisms of interest for a plant canopy are usually precipitation and dew. As with corrosion science, a widely used practical definition for leaf wetness is absent in the literature. Leaf wetness is treated either as an environmental or surface parameter in much the same manner as is found in corrosion science. As a surface parameter, leaf wetness is most commonly defined by the instrumentation used to measure it as pointed out by Magarey et al. [183]. The following is a summary and short discussion of the sensors and models present in the literature that have applicability to atmospheric corrosion.

RESISTANCE SENSORS

The most commonly utilized surface moisture sensors in environmental science today are of the resistance type. There are several commercial sensors available on the market and in wide use. These methods either measure resistance directly on a plant surface or indirectly by emulating a plant surface. Given their similarity to sensors used in atmospheric corrosion reviewed above, indirect sensors will be discussed in more detail.

Indirect sensors are placed adjacent to the foliage to be estimated such that they act as an artificial leaf. As with resistance-type corrosion sensors, wetness is usually defined as any resistance lower than a baseline resistance measured on a clean, dry sensor. A design by Gillespie and Kidd [184] has been utilized in a number of published studies since its inception. It is often mentioned as being one of the most common wetness sensors used in environmental science and referred to as a leaf sensor [185-189]. Gillespie and Kidd's leaf sensor design [184] consists of two interdigitated copper electrodes on a printed circuit board. The electrodes are spaced 1 mm apart. A popular commercial version of this design is the Model 237 Leaf Wetness Sensor (Campbell Scientific) which features gold-plated electrodes, Figure 2.25.

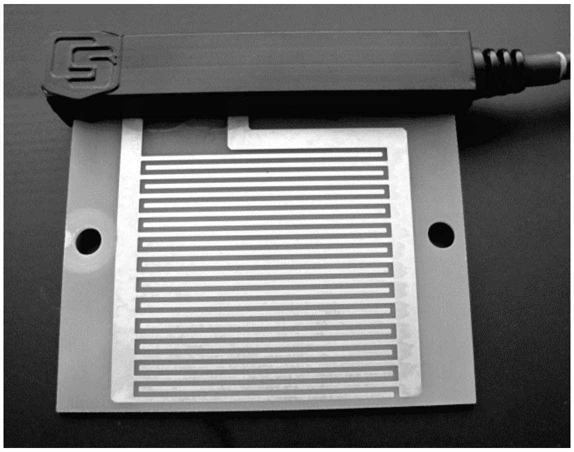

Figure 2.25. Model 237 leaf wetness sensor (Campbell Scientific).

Indirect sensors are often painted with latex to mimic the thermal characteristics of leaves and increase their moisture sensitivity. Davis and Hughes [190] were one of the first to introduce the idea of painting resistance sensors to increase their moisture sensitivity. The thickness and color of paint layers has been shown to have a significant effect on both moisture ingress and thermal emissivity [184]. A number of comparisons have been made between the field performance of both painted and unpainted leaf sensors since these studies, two of which will be discussed here [186-188].

Lau et al. [186] examined the response of a dozen latex painted and bare leaf sensors deployed at various orientations amongst tomato plants and compared sensor response to visual observation of dewing on the plants. They found that, unlike their painted counterparts, unpainted sensor response was dependent on deployment angle and lagged behind the visually observed onset of dewing in many cases. They attributed the favorable performance of painted sensors to the increase in wettability the paint imparted but also its effect on thermal emissivity during dewing.

Sentelhas et al. [188] compared the dew onset detected by unpainted and painted Campbell leaf sensors to dew point depression less than 2°C, which was defined as an indication of dew presence. Six unpainted leaf sensors were deployed in a cotton plant canopy along with local RH and temperature sensors. The sensors were exposed for a period of 20 days, then painted with white latex and redeployed for another 20. The investigators compared the relative standard deviation (RSD) of the mean daily resistance values measured on the six sensors. They found that the RSD was on average 67% for the unpainted sensors and 9% for the painted sensors. They also compared wetness duration as indicated by the sensors to the number of hours of dew point depression under 2°C as determined by temperature and RH, as seen in Figure 2.26. Their results clearly show a stronger correlation of painted sensors to the dew point measurements. Referencing this data along with that of Gillespie and Kidd [184], Lau et al. [186], and other published studies, the authors concluded that the Campbell leaf sensor should be painted to increase the precision and accuracy of leaf wetness estimations. They also noted, with regard to moisture sensitivity, that sensors with smaller electrode gaps may eliminate the need to paint wetness sensors.

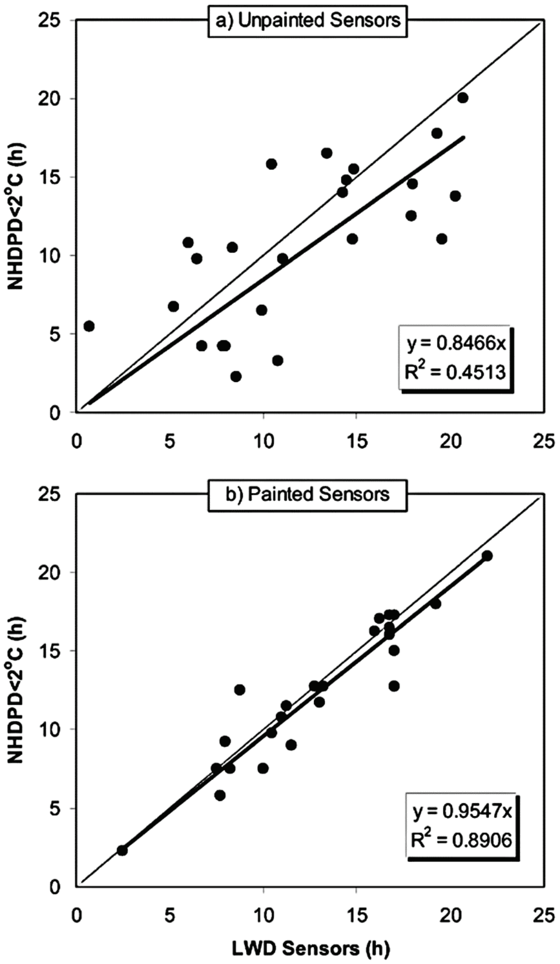

Figure 2.26. Relationship between measured leaf wetness duration (mean of six sensors) and predicted dew point depression (NHPD < 2C) for unpainted (A) and painted (B) sensors [188]. Copyright permission obtained from Copyright Clearance Center.

Although metal and plant surfaces often exhibit different wetting behavior (e.g., hydrophobic vs. hydrophilic), it may be beneficial to examine the use of coated resistance-type sensors for TOW determinations in corrosion science. Judging from results of the studies summarized above, coatings may enhance the sensitivity and precision of wetness duration estimates. Coated sensors would be especially relevant for the emulation of painted metal surfaces. It would be important however to ensure that the coating on the sensor emulates the sorption behavior of the metal surface of interest.

OPTICAL SPECTROSCOPY

Heusinkveld et al. [191] developed a field deployable instrument for detecting moisture on a leaf or upper soil layer (<2mm) based on spectral reflectance spectroscopy. Moisture was detected by scanning a surface and taking a ratio of a frequency band absorbed by free water and a water insensitive frequency. The instrument provided its own source of modulated light so as not to be affected by natural light conditions.

The investigators reported on testing the instrument both in laboratory and field conditions on soil and plant surfaces. In one laboratory experiment, they measured the reflectance of fresh grass leaves as they dried while simultaneously measuring their mass. They found a strong linear correlation between reflectance and mass change as seen in Figure 2.27. Field testing was carried out on a sand crust and plant leaves in a desert dune environment for a period of approximately a week with a scan area of around 20 cm^2 and from a distance of around 30 cm. During this time, water content of the scanned soil was gravimetrically measured. A leaf resistance sensor coated with latex paint mounted near the soil surface was also utilized. Their results indicate similar trends between different measurement methodologies, Figure 2.28.

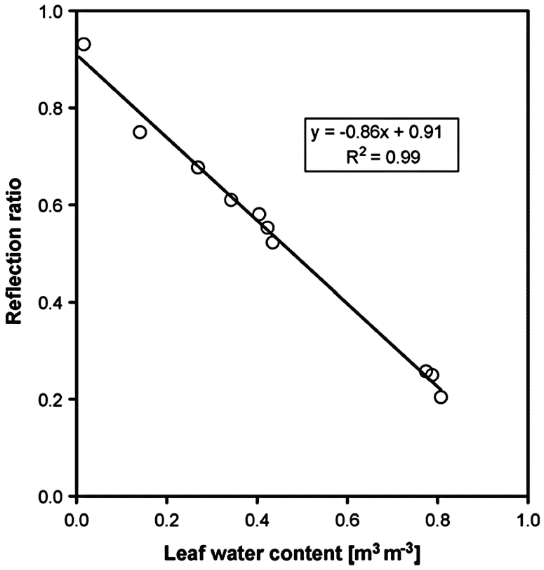

Figure 2.27. Comparison of optical wetness sensor output vs. mass change over drying time for fresh grass leaves [191]. Copyright permission obtained from Copyright Clearance Center.

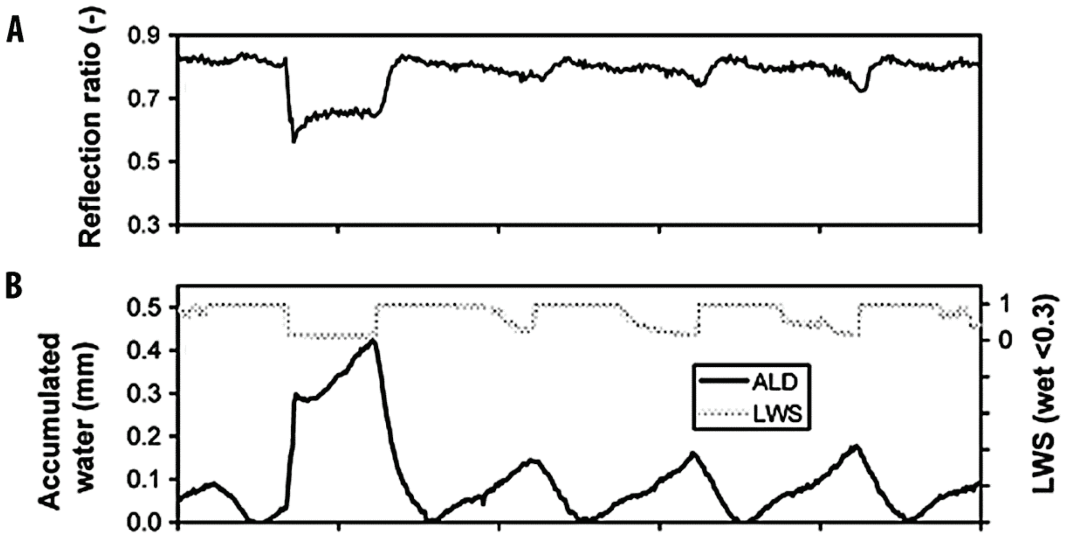

Figure 2.28. Comparison of wetness measurements on the surface of a sand dune slope during October 15 – 19 2000. (A) Optical wetness sensor response; (B) weighing lysimeter and leaf wetness sensor output [191]. Copyright permission obtained from Copyright Clearance Center.

This type of instrument is similar in function to the one developed by Ganther et al. [140] discussed earlier in this report. It has many of the same advantages of Ganther et al.'s sensor in that it is a non-contact method that directly measures the surface of interest. It also has the additional advantages of not being affected by natural light conditions. The authors conceded that specular reflection in soils and leaves, caused by surface droplets of certain geometry or orientation could cause misreading. Nonetheless, this type of instrument may prove of utility for the direct determination of TOW in outdoor corrosion exposures.

MODELS

Both empirical and theoretical models have been developed for predicting leaf wetness, the majority of which focus on dewing events. Models range in scale from individual drops to canopies. Empirical models develop relationships between observed meteorological variables and measured leaf wetness. Meteorological inputs include temperature, wind speed, RH, solar radiation and dew point temperature. Data from weather stations or micrometeorological measurements (measurements near the plants) are used, including leaf wetness determined by visual inspection or resistance sensors. Over the past 20 years, many artificial neural network models have been developed [192-194]. As pointed out by Kim and coworkers, empirical models have the disadvantage of being site and plant specific [195-196].

Most theoretical models are based on the concept of surface energy balance and water budgets as water condenses and evaporates from the plant surface. A highly referenced model of this sort was published by Pedro and Gillespie [197-198]. It simulates dew duration on a single leaf using standard meteorological data. The authors demonstrated that the model was able to predict dew formation within around an hour of visible appearance during field experiments. As with dewing models developed for corrosion TOW, models of this type often do not account for more complex parameters such as ground moisture content and surface contaminants.

Relative humidity thresholds have also been used to determine leaf wetness but have oftentimes been found not sufficiently accurate for reasons similar to those discussed above [194]. Despite this, many investigators have reported satisfactory estimations for surface wetness duration using RH [199-200].

2.1.4 Part III: Summary and Conclusions

Part III focuses on global issues and limitations of current TOW determination methods and definitions and proposes potential pathways to for improvement. Before directly addressing these matters it is appropriate here to briefly summarize some important points in the preceding text.

In Part I, wettability of an atmospherically exposed surface was described in terms of the surface energy balance model. This description included discussion of the macroscopic contact angle, hydrophobic and hydrophilic surfaces, drop geometry, and puddling. Numerous investigators have demonstrated that wetting phenomena on the submicron scale can deviate from that observed on the macroscopic scale. An example of this phenomenon is the presence of nanoscopic precursor films emanating from triple phase boundaries. A phenomenon in which microdroplets appear and spread from deliquesced halide salt droplets on corroding transition metals was also discussed and may be related to the precursor film formation.

Part I also overviewed the normal modes by which water is transferred to and from a surface in indoor and outdoor atmospheric conditions. Water can be directly deposited onto a surface by means of dry deposition of aerosols, occult deposition from clouds and fog, and precipitation events. It can also be sorbed by the surface itself or contaminants on it to create an electrolyte capable of supporting corrosion. Water is transported away from a surface by evaporation, dewetting and runoff.

Part II focused on the concept of time of wetness along with practical definitions and accompanying sensing methods and models. This included a discussion on methods used to predict or detect wetness in the field of corrosion and in the environmental sciences. The capabilities and limitations of the practical definitions and determination methods were critically examined, establishing a foundation for identifying general issues with TOW that are addressed in Part III.

2.1.4.1 Summary of Issues with TOW

The variety of determination methods exemplified in Part II are for the most part complimentary. Yet, estimates made using these methods are not directly comparable. The actual meaning of TOW is ambiguous or overlooked in many cases. Clarification is needed as to what is meant by "wet" and when a surface of interest can be considered wet. The former subject concerns the theoretical definition of TOW while the latter involves practical determination. Issues with the TOW concept and practical definitions will be addressed under these categories.

WHAT IS WET?

The theoretical definitions discussed in Part II of this paper generally state that TOW is the time when a metal surface is wet in the atmosphere. A subtle, yet important, difference was noted in the manner in which a surface is defined as "wet" in these definitions. Some definitions imply wet is the condition whereby a sufficiently conducting electrolyte is present on the surface, so as to complete the electrochemical cell. Others define it as the condition whereby an electrolyte is present and significant corrosion takes place.

This difference has a strong impact on how TOW is determined. Defining a surface as wet when an electrolyte is present requires either a measure of electrolyte presence or knowledge of the climatological parameters and wetting behavior of the surface. The constraint that corrosion must also be significant requires a measure or knowledge of electrochemical response of the surface. The term “significant” must also be defined.

In both cases, however, there is also the question of how much electrolyte must be present on the surface to consider it wet. Can a surface be considered wet if a few raindrops cover a thousandth of its total area? Certainly, corrosion would be possible in the vicinity of the drops. A similar question could be asked about a surface being wet by nanoscopic amounts of electrolyte. Defining TOW in terms of significant corrosion taking place could address this issue. Although the answers to these questions prove rather philosophical in nature, the importance of the issue nonetheless stands and is integral to constructing a robust definition for TOW.

WHEN IS WET?

Numerous practical definitions and accompanying methods have been developed over the last sixty years to estimate when a surface is wet. Issues with these methods will be discussed here under the categories of TOW as an environmental parameter and as a surface parameter. The manner in which time is accounted for in TOW determinations will also be addressed.

Environmental Parameter

Practical definitions that treat TOW as an environmental parameter estimate it by means of climatological variables such as RH and temperature. The most widely used definition of this type is that given by ISO 9223, which defines it as the period during which the RH of the ambient atmosphere is above 80% and the temperature above 0°C. In Part II, this definition was shown to be inaccurate in many cases in terms of estimating conditions of actual surface wetness, due to lack of fully accounting for the wetting and drying modes discussed in Part I. Conditions unaccounted for by this definition include direct deposition events, water sorption by surface contaminants below 80%RH, and the presence of electrolyte at subzero temperatures. Additionally, this estimate does not account for the difference between surface RH and ambient RH, which has been demonstrated to significantly impact wetness duration. Variants of the ISO definition have been proposed that account for some of these shortfalls. None, however, comprehensively account for the wetting and drying modes that control wetness duration. This situation is in part due to the lack of available information on some of these modes in the context of atmospheric corrosion. Specifically, the contribution of surface contaminants to electrolyte formation and duration has not been satisfactorily characterized.

Contaminants on the surface that can be expected to significantly contribute to wetness duration include corrosion products and deliquescent aerosol particles, as discussed in Part I. In the atmospheric sciences substantial effort has gone into characterizing and modeling the wetting behaviors of natural aerosol constituents. The hygroscopic models developed could serve to provide a more reasonable estimate of the presence and amount of electrolyte contributed by deposited aerosols as a function of chemically resolved loading amounts, RH, and temperature. They do, however, lack the ability to predict the deliquescence/efflorescence hysteresis of deposited aerosols and do not account for the effects of corrosion chemistry and corrosion products. These phenomena remain largely unexplored in the context of atmospheric corrosion, but their effect on wetness duration is likely significant and could be incorporated into these models.

The aforementioned knowledge gaps concerning the contribution of contaminants to expected wetting and drying modes hinder the advancement of TOW as an environmental parameter. It is suggested that future work focus on characterizing and modeling the wetting behavior of the surface.

Surface Specific Parameter

An alternate way of approaching TOW is to determine the amount of time a specific type of surface may be wet using either indirect or direct sensing methods. One advantage these methods have over the environmental approach is that surface moisture or corrosion rate can be measured without complete knowledge of the complex wetting behavior of a surface. As with environmental methods, the challenge lays in capturing all of the modes by which a surface can wet and dry. These methods can be broken down into either indirect or direct determinations, with each defined by the type of instrumentation utilized. The following discussion will follow this structure.

Indirect

Indirect methods are by far the most commonly used estimate of TOW as a surface parameter. They utilize sensors that measure wetness on their surface as an estimate for the presence of moisture on a surface of interest, such as a structural component or a corrosion test panel. They are deployed in proximity to or on the surface of interest. Galvanic, resistance, and impedance corrosion sensors along with quartz crystal microbalances comprise the indirect-type sensors used in corrosion science. Resistance sensors are also commonly used in environmental science for determining leaf wetness.

All of these sensor types, with the exception of the QCM, consist of an interdigitated or parallel array of metal electrodes separated by an insulating material. Deposited moisture that bridges the insulator gap between the electrodes causes a measurable change in electrical properties. Time of wetness is then defined as time during which a certain voltage, current, or impedance threshold is exceeded. Threshold definitions are often established from the baseline response of the clean sensors at low humidity levels. A major difference between galvanic and resistance sensing methods is that the former uses reactive electrodes whereby wet is often defined in terms of corrosion behavior (i.e., galvanic current) and the latter uses noble electrodes, defining wet simply as the presence of sufficiently conductive electrolyte. Impedance-based techniques are a sort of hybrid between the two types in the sense that both electrolyte resistance and corrosion rate can be estimated. QCM sensors have been used to determine estimate water sorption-induced mass change.

Indirect measurement techniques, in general, can capture the major wetting and drying modes common to atmospheric corrosion. The surfaces of electrode-type sensors, however, are often quite different than the metal surfaces they are estimating. These differences include thermal transport and emissivity characteristics, affecting condensation and evaporation, and wetting characteristics, affecting wetness detection and duration.

The wettability of a TOW sensor may have a profound effect on wetness detection and duration. Work carried out on leaf wetness sensors used in the environmental sciences has shown this to be the case, as discussed in Part II. This is due to the output of these sensors relying on a sufficiently conductive electrolyte film or droplet to bridge the insulator gap between the electrodes. The leaf wetness sensors examined had a fairly hydrophobic insulator that appears to have been preventing electrode bridging, meaning the sensors were reading dry when they were indeed wet. The solution for this problem was to coat these sensors with latex paint, causing spreading of the electrolyte. The issue of electrolyte bridging has received little attention in the corrosion literature with respect to sensor accuracy. Of specific importance is the effect of electrode spacing on detection of the wetting behavior of hygroscopic deposited aerosols with characteristic sizes less than that of the spacing. At sites with low aerosol deposition velocity and high wash-off rates, deposited particles may not be bridge the electrodes and, thus, their wetting contribution would be unaccounted for.

Contaminants govern wetting by sorption modes and also corrosion response. Thus, it is important that a sensor surface has contaminant levels and composition similar to the surface of interest. Although both the sensor surface and surface of interest are subjected to similar contaminants from the atmosphere, their retention and reaction with those contaminants can be expected to be dissimilar. With respect to retention, a porous, hydrophilic surface, such as rusted steel, may retain more surface contaminants than a flat hydrophobic sensor surface during periods of wash-off. The reaction of sensor electrodes will cause both changes in chemistry and the appearance of corrosion product, which can affect wetting duration. With this in mind, a resistance-type sensor constructed of noble metals may not be a good surrogate for determining the TOW of a corroded surface. Comparisons between the wetting characteristics of sensors and the surfaces they are estimating are lacking.

It is suggested that the accuracy and comparability of common sensing methods be explored in order to correctly interpret their output and to optimize these methods. Direct comparison between the wetting characteristics of the sensors and surface of interest in terms of wetness duration would be a good first step. Achieving this, again, requires a better understanding of the contribution of corrosion products and chemistry along with deposited hygroscopic aerosols to wetness duration. This understanding may lead, as it did for those in the environmental sciences, to surface treatments that better mimic the wetting behavior of corroding metal surfaces. Additionally, the limits of detection of these sensors in the presence of microscopic amounts of electrolyte (e.g., deposited aerosols) should be explored with respect to how contaminant loading and electrolyte geometry relate to output.

The QCM methods have the advantage of being able to emulate the surface of interest by coating the sensors with material of the same composition. Additionally, their sensitivity to small mass changes allow for determination of aerosol deposition flux and water sorption. Conversely, their mechanical fragility, the dampening effects of large deposited particles or precipitation droplets, and the convoluting effects of temperature change on output have limited their applicability to field applications. These methods appear more suitable to monitoring sorption-induced wetness in sheltered exposure of laboratory conditions rather than boldly exposed field use.

Direct

Direct measurement methods that have been used to examine metal surface wetness include Kelvin probe potential measurements, scanning force microscopy and optical spectroscopy. One advantage of using direct measurement methods is that the modes by which wetting and drying occur become virtually inconsequential for wetness determination. All of these methods, with the exception of the spectroscopy techniques developed by Ganther et al. [140] and Cooper [182], have been used exclusively in laboratory settings due to the fragility and sensitivity of the instruments involved.

Direct determination methods have also been developed and utilized in the environmental sciences. Although some of the methods cannot be applied to detecting wetness on metal, an instrument recently developed, based on IRAS, was used for outdoor wetness determinations on soil and plant surfaces [191]. This technology appears to be applicable to atmospheric corrosion and extending the work in this area to metal surfaces may prove fruitful.

2.1.5 Conclusions

Wetting phenomena associated with atmospheric corrosion along with time of wetness definitions and determination methods were overviewed in this paper. Additionally, the concept of leaf wetness used in the environmental sciences was discussed in relation to TOW. Lastly, issues and limitations of TOW were identified and avenues for further improvement suggested. The resulting key conclusions are summarized here.

Both theoretical and practical definitions for TOW are varied in the literature. Theoretical definitions generally define “wet” in terms of the presence of electrolyte on a surface or as an event during which significant corrosion takes place. The manner in which wet is defined has often been ambiguous in practical determinations of TOW.

Practical determination methods can be categorized by the way in which TOW is treated – as an environmental parameter or a surface parameter. Current environmental definitions do not comprehensively capture the wetting and drying modes that are thought to control wetness duration. As a result, many environmental definitions, such as that given by ISO 9223, are poor predictors of actual surface wetness with respect to electrolyte presence. In particular, these definitions oversimplify the wetting behavior of deposited surface contaminants. They also do not account for the expected significant impact of corrosion chemistry and products on wetness duration. This is in part due to the lack of available information on this subject. Hygroscopic aerosol models developed in the atmospheric sciences tailored to account for the influence of corrosion processes could be utilized to provide a more reasonable estimate of electrolyte presence in terms of contaminant chemistry, temperature, and humidity.

Practical determination methods that treat TOW as a surface parameter have often been based on detection limits of the sensing method rather than actual surface conditions. Comprehensive comparisons of sensor output with actual sensor conditions and the surface of interest are lacking in the literature for the indirect methods overviewed here. Such comparisons would yield information on sensor accuracy along with differences in wetting characteristics between the two surfaces.

A number of direct methods for measuring moisture on a surface of interest were overviewed. Most of the methods utilized for corrosion research, however, have been confined to the laboratory due to fragility, complexity and cost. One great advantage direct measurements have over the indirect methods is the fact that the modes by which wetting and drying occur become virtually inconsequential for wetness determination. Spectroscopy techniques developed in the environmental sciences for directly detecting surface moisture on plant and soil surfaces may be applicable to atmospheric corrosion and extending the work in this area to metal surfaces may prove fruitful.

2.1.6 References

1. Gennes, P.-G. Capillarity and wetting phenomena : Drops, bubbles, pearls, waves, New York: Springer, 2004.
2. Tang, X., Dong, J., & Li, X. A comparison of spreading behaviors of silwet l-77 on dry and wet lotus leaves. J. Colloid Interface Sci. 2008; 325,1: 223-227.
3. Barnes, G. T., & Gentle, I. R. Interfacial science : An introduction, New York: Oxford University Press, 2005.
4. Erb, R. A. Wettability of metals under continuous condensing conditions. J. Phys. Chem. 2002a; 69,4: 1306-1309.
5. Horsthemke, A., & Schroder, J. J. The wettability of industrial surfaces: Contact angle measurements and thermodynamic analysis. Chem. Eng. Process. 1985; 19,5: 277-285.
6. Min, J., & Webb, R. L. Long-term wetting and corrosion characteristics of hot water treated aluminum and copper fin stocks. Int J Refrig 2002; 25,8: 1054-1061.
7. Muster, T. H., Neufeld, A. K., & Cole, I. S. The protective nature of passivation films on zinc: Wetting and surface energy. Corros. Sci. 2004; 46,9: 2337-2354.
8. Schrader, M. E. Wettability of clean metal surfaces. J. Colloid Interface Sci. 1984; 100,2: 372-380.
9. Zhang, X., He, W., Odnevall Wallinder, I., Pan, J., & Leygraf, C. Determination of instantaneous corrosion rates and runoff rates of copper from naturally patinated copper during continuous rain events. Corros. Sci. 2002; 44,9: 2131-2151.
10. Strein, E., & Allred, D. Eliminating carbon contamination on oxidized si surfaces using a vuv excimer lamp. Thin Solid Films 2008; 517,3: 1011-1015.
11. Trevoy, D. J., & Johnson, H. The water wettability of metal surfaces. J. Phys. Chem. 2002; 62,7: 833-837.
12. Erb, R. A. Wettability of metals under continuous condensing conditions. J. Phys. Chem. 2002b; 69,4: 1306-1309.

13. Cole, I. S., Balatbat, J., & Neufeld, A. K. Changes in surface energy and wettability of metal surfaces exposed to controlled and actual environments: Implications for models of corrosion. 13th International Corrosion Conference Proceedings 1996; I: 17.
14. Matsuoka, H., Matsunaga, Y., Mitsumoto, S., & Seki, H. Copper corrosion and capillary action in humid atmospheres. Boshoku gijutsu 1987; 36,11: 625-630.
15. Pizzolato, P. J., Larkin, B. K., & Fatino, C. C.Evaluation of the mechanism of corrosion in capillaries, United States:1964.
16. Smith, T. A capillary model for stress-corrosion cracking of metals in fluid media. Corros. Sci. 1972; 12,1: 45-56.
17. Abraham, D. B., Cuerno, R., & Moro, E. Microscopic model for thin film spreading. Phys. Rev. Lett. 2002; 88,20: 206101-206101-206104.
18. Bascomb, W. D., Cottington, R. L., & Singleterry, C. R. Contact angle, wettability and adhesion, Vol. 48, 1964.
19. Burlatsky, S. F., Oshanin, G., Cazabat, A. M., Moreau, M., & Reinhardt, W. P. Spreading of a thin wetting film: Microscopic approach. PhRvE 1996; 54,4: 3832-3845.
20. Garoff, S., Sirota, E. B., Sinha, S. K., & Stanley, H. B. The effects of substrate roughness on ultrathin water films, Vol. 90, AIP, 1989.
21. Lelah, M. D., & Marmur, A. Spreading kinetics of drops on glass. J. Colloid Interface Sci. 1981; 82,2: 518-525.
22. Tanner, L. H. The spreading of silicone oil drops on horizontal surfaces. J. Phys. D (Applied Physics) 1979; 12,9: 1473-1484.
23. Neufeld, A. K., Cole, I. S., Bond, A. M., & Furman, S. A. The initiation mechanism of corrosion of zinc by sodium chloride particle deposition. Corros. Sci. 2002; 44,3: 555-572.
24. Chen, Z. Y., Persson, D., & Leygraf, C. Initial nacl-particle induced atmospheric corrosion of zinc-effect of co2 and so2. Corros. Sci. 2008; 50,1: 111-123.
25. Chen, Z. Y., Persson, D., Nazarov, A., Zakipour, S., Thierry, D., & Leygraf, C. In situ studies of the effect of co2 on the initial nacl-induced atmospheric corrosion of copper. J. Electrochem. Soc. 2005; 152,9: 342-351.
26. Seinfeld, J. H., & Pandis, S. N. Atmospheric chemistry and physics, New York: John Wiley and Sons, 1998.
27. McMahon, T. A., & Denison, P. J. Empirical atmospheric deposition parameters—a survey. Atmos. Environ. (1967) 1979; 13,5: 571-585.
28. Wesely, M. L., & Hicks, B. B. A review of the current status of knowledge on dry deposition. Atmos. Environ. 2000; 34,12-14: 2261-2282.
29. Cole, I. S. Holistic model for atmospheric corrosion part 4: Geographic information system for predicting airborne salinity. Corros. Eng., Sci. Technol. 2004; 39: 89-96.
30. Cole, I. S., Ganther, W. D., Paterson, D. A., King, G. A., Furman, S. A., & Lau, D. Holistic model for atmospheric corrosion. Part 2. Experimental measurement of deposition of marine salts in a number of long range studies. Corros. Eng., Sci. Technol. 2003; 38,4: 259-266.

31. Cole, I. S., & Paterson, D. A. Holistic model for atmospheric corrosion part 5 - factors controlling deposition of salt aerosol on candles, plates and buildings. Corros. Eng., Sci. Technol. 2004; 39,2: 125-130.
32. Cole, I. S., Paterson, D. A., & Ganther, W. D. Holistic model for atmospheric corrosion part 1 - theoretical framework for production, transportation and deposition of marine salts. Corros. Eng., Sci. Technol. 2003; 38,2: 129-134.
33. Cole, I. S., Paterson, D. A., Ganther, W. D., Neufeld, A., Hinton, B., McAdam, G., . . . Purwadaria, S. Holistic model for atmospheric corrosion. Part 3 - effect of natural and man made landforms on deposition of marine salts in australia and south-east asia. Corros. Eng., Sci. Technol. 2003; 38,4: 267-274.
34. O'Dowd, C., Smith, M. H., Consterdine, I. E., & Lowe, J. A. Marine aerosol, sea-salt, and the marine sulphur cycle: A short review. Atmos. Environ. 1997; 31,1: 73-80.
35. Fitzgerald, J. W. Marine aerosols: A review. Atmos. Envron. A-Gen. 1991; 25,3-4: 533-545.
36. O'Dowd, C., & de Leeuw, G. Marine aerosol production: A review of the current knowledge. Philosophical Transactions of the Royal Society A: Mathematical, Physical and Engineering Sciences 2007; 365,1856: 1753-1774.
37. Lewis, E. R., & Schwartz, S. E. Sea salt aerosol production: Mechanisms, methods, measurements, and models - a critical review, Vol. 152, Washington: AGU, 2004.
38. Gultepe, I., Tardif, R., Michaelides, S. C., Cermak, J., Bott, A., Bendix, J., . . . Cober, S. G. Fog research: A review of past achievements and future perspectives. PApGe 2007; 164,6: 1121-1159.
39. Podzimek, J. Droplet concentration and size distribution in haze and fog. StGG 1997; 41,3: 277-296.
40. Graedel, T. E. Corrosion-related aspects of the chemistry and frequency of occurrence of precipitation. J. Electrochem. Soc. 1986; 133,12: 2476-2482.
41. Pruppacher, H. R., & Klett, J. D. Microphysics of clouds and precipitation, 2 ed., Norwell, MA: Kluwer Academic Publishers, 1997.
42. Hung, W.-H., Schwartz, J., & Bernasek, S. L. Sequential oxidation of fe(100) by water adsorption: Formation of an ordered hydroxylated surface. Surf. Sci. 1991; 248,3: 332-342.
43. Leygraf, C., & Graedel, T. Atmospheric corrosion New York: John Wiley and Sons, 2000.
44. Henderson, M. A. The interaction of water with solid surfaces: Fundamental aspects revisited. Surf. Sci. Rep. 2002; 46,1-8: 1-308.
45. Missert, N., & Copeland, R. G. Scanning probe studies of water at aluminum and gold surfaces. Electrochemical Society Proceedings 2005: 658.
46. Lee, S., & Staehle, R. W. Adsorption of water on gold. Corrosion 1996; 52,11: 843-852.
47. Sato, N. Electrochemistry at metal and semiconductor electrodes Amsterdam: Elsevier, 1998.
48. Doi, T., Yamashita, M., & Nagano, H. Water adsorption behavior and kelvin potential change on metal surfaces. J. Jpn. Inst. Met. 1998; 62,1: 64-70.

49. Enikeev, É. K., Loskutov, A. I., Rozenfel'd, I. L., & Alekseev, V. N. Adsorption of water on oxidized surface of metals. Russ. Chem. Bull. 1979; 28,11: 2411-2414.
50. Forslund, M., & Leygraf, C. Quartz crystal microbalance probe developed for outdoor in situ atmospheric corrosivity monitoring. J. Electrochem. Soc. 1996; 143,3: 839-844.
51. Law, B. M. Wetting, adsorption and surface critical phenomena. Prog. Surf. Sci. 2001; 66,6-8: 159-216.
52. Lee, S., & Staehle, R. W. Adsorption of water on copper, nickel, and iron. Corrosion 1997a; 53,1: 33-42.
53. Lee, S., & Staehle, R. W. Adsorption studies of water on copper, nickel, and iron: Assessment of the polarization model. ZMetl 1997b; 88,10: 824-831.
54. Lee, S. K., & Staehle, R. W. Adsorption study of water on gold using the quartz-crystal microbalance technique: Assessment of bet and fhh models of adsorption. ZMetl 1997c; 88,11: 880-886.
55. Nagano, H., Doi, T., & Yamashita, M. Study on water adsorption-desorption on metal surfaces and the early stage of atmospheric corrosion in steels. Mater. Sci. Forum 1998; 289-292,pt 1: 127-134.
56. Tatsuoka, T., Takagi, Y., & Kim, Y. J. Application of scanning kelvin probe for monitoring atmospheric corrosion.editors. Electrochemical society proceedings-2005. Los Angeles, CA, United states: Electrochemical Society Inc., 2005: 511.
57. Dante, J. F., & Kelly, R. G. The evolution of the adsorbed solution layer during atmospheric corrosion and its effects on the corrosion rate of copper. J. Electrochem. Soc. 1993; 140,7: 1890-1897.
58. Sharma, S. P., & Thomas, J. H., III. Adsorption of water vapour on thin-gold electroplate on copper. J. Vac. Sci. Technol. 1977; 14,3: 825-827.
59. Thomas, J. J., & Sharma, S. P. Adsorption and desorption of water on au by the quartz-crystal-oscillator method. J. Vac. Scie Technol., A 1976; 13: 549-551.
60. Hens, H. S., & Leuven, K. U. Applied building physics: Boundary conditions, building performance, and material properties, Berlin: Ernst & Sohn, 2011.
61. Sereda, P. J. Characteristics of moisture deposition on corrosion specimens. Mater Res Stand 1961; 1,9: 719-723.
62. Grossman, P. R. Investigation of atmospheric exposure factors that determine time-of-wetness of outdoor structures Paper presented at the Atmospheric Factors Affecting the Corrosion of Engineering Materials Philadelphia. 1978
63. Dean, S. W., & Reiser, D. B. Time of wetness and dew formation: A model of atmospheric heat transfer. In W. W. Kirk & H. H. Lawson, editors. Atmospheric corrosion. Philadelphia: American Society for Testing and Materials, 1995: 3-10.
64. Cole, I. S., & Paterson, D. A. Mathematical models of dependence of surface temperatures of exposed metal plates on environmental parameters. Corros. Eng., Sci. Technol. 2006; 41,1: 67-76.
65. Xu, N., Zhao, L., Ding, C., Zhang, C., Li, R., & Zhong, Q. Laboratory observation of dew formation at an early stage of atmospheric corrosion of metals. Corros. Sci. 2002; 44,1: 163-170.

66. Wang, R., & Kido, M. Condensation and evaporation behaviors of micro-water droplets on sus304 steel observed using the ac noncontact mode of afm. Mater. Lett. 2003; 57,16-17: 2360-2365.
67. Fisher, L. R., Gamble, R. A., & Middlehurst, J. The kelvin equation and the capillary condensation of water. Natur 1981; 290,5807: 575-576.
68. Kohonen, M. M., & Christenson, H. K. Capillary condensation of water between rinsed mica surfaces. Langmuir 2000; 16,18: 7285-7288.
69. Skinner, L. M., & Sambles, J. R. The kelvin equation: A review. J. Aerosol Sci 1972; 3,3: 199-210.
70. Corvo, F., Mendoza, A. R., Autie, M., & Betancourt, N. Role of water adsorption and salt content in atmospheric corrosion products of steel. Corros. Sci. 1997; 39,4: 815-820.
71. Dillmann, P., Mazaudier, F., & Hœrlé, S. Advances in understanding atmospheric corrosion of iron. I. Rust characterisation of ancient ferrous artefacts exposed to indoor atmospheric corrosion. Corros. Sci. 2004; 46,6: 1401-1429.
72. Ishikawa, T., Kumagai, M., Yasukawa, A., & Kandori, K. Characterization of rust on weathering steel by gas adsorption. Corrosion 2001; 57,4: 346-352.
73. Sarin, P., Snoeyink, V. L., Bebee, J., Kriven, W. M., & Clement, J. A. Physico-chemical characteristics of corrosion scales in old iron pipes. Water Res. 2001; 35,12: 2961-2969.
74. Askey, A., Lyon, S. B., Thompson, G. E., Johnson, J. B., Wood, G. C., Sage, P. W., & Cooke, M. J. The effect of fly-ash particulates on the atmospheric corrosion of zinc and mild steel. Corros. Sci. 1993; 34,7: 1055-1081.
75. Barber, P., Asakawa, T., & Christenson, H. K. What determines the size of liquid capillary condensates below the bulk melting point? J. Phys. Chem. C 2007; 111,5: 2141-2148.
76. Nowak, D., & Christenson, H. K. Capillary condensation of water between mica surfaces above and below zero-effect of surface ions. Langmuir 2009.
77. Nowak, D., Heuberger, M., Zach, M., & Christenson, H. K. Thermodynamic and kinetic supercooling of liquid in a wedge pore. The J. Chem. Phys. 2008; 129,15: 154509-154507.
78. Gao, Y., Yu, L. E., & Chen, S. B. Theoretical investigation of substrate effect on deliquescence relative humidity of nacl particles. J. Phys. Chem. A 2007; 111,4: 633-639.
79. Russell, L. M., & Yi, M. Deliquescence of small particles. J. Chem. Phys. 2002; 116,1: 311-321.
80. Tang, I. N., & Munkelwitz, H. R. Composition and temperature dependence of the deliquescence properties of hygroscopic aerosols. Atmos. Envir. A-Gen. 1993; 27,4: 467-473.
81. Bassett, M., & Seinfeld, J. H. Atmospheric equilibrium model of sulfate and nitrate aerosols. Atmos. Env. (1967) 1983; 17,11: 2237-2252.
82. Clegg, S. L., Brimblecombe, P., & Wexler, A. S. Thermodynamic model of the system$H^{+}{-}NH_4^{+}{-}Na^{+}{-}SO_4^{2-}{-}NO^{3-}{-}Cl^{-}{-}H_2O$ at 298.15 k. J. Phys. Chem. A 1998; 102,12: 2155-2171.

83. Friese, E., & Ebel, A. Temperature dependent thermodynamic model of the system h+−nh4+−na+−so42−−no3−−cl−−h2o. J. Phys. Chem. A. 2010; 114,43: 11595-11631.
84. Nenes, A., Pandis, S. N., & Pilinis, C. Isorropia: A new thermodynamic equilibrium model for multiphase multicomponent inorganic aerosols. Aquat Geochem 1998; 4,1: 123-152.
85. Wexler, A. S., & Seinfeld, J. H. Second-generation inorganic aerosol model. Atmos. Environ. A-Gen 1991; 25,12: 2731-2748.
86. Cruz, C. N., & Pandis, S. N. Deliquescence and hygroscopic growth of mixed inorganic-organic atmospheric aerosol. Environ. Sci. Technol. 2000; 34,20: 4313-4319.
87. Ge, Z., Wexler, A. S., & Johnston, M. V. Deliquescence behavior of multicomponent aerosols. J. Phys. Chem. A. 1998; 102,1: 173-180.
88. Tang, I. N. Deliquescence properties and particle size change of hygroscopic aerosols. Paper presented at the Symposium on Biological Studies of Enbironmental Pollutants: Aerosol Generation and Exposure Facilities, Honolulu, Hawaii. 1979
89. Tang, I. N. Thermodynamic and optical properties of mixed-salt aerosols of atmospheric importance. J. Geophys. Res. 1997; 102,D2: 1883-1893.
90. Pabalan, R. T., Yang, L., & Browning, L. Deliquescence behavior of multicomponent salts: Effects on the drip shield and waste package chemical environmental of the proposed nuclear waste repository at yucca mountain, nevada. Paper presented at the Scientific Basis for Nuclear Waste Management XXV, November 26, 2001 - November 29, 2001, Boston, MA, United states. 2002
91. Yang, L., Pabalan, R., Shukla, P., Juckett, M., He, X., Chiang, K. T., . . . Ahn, T. (2011). *Corrosion of alloy 22 induced by dust deliquescence brines*. Washington, DC: Center for Nuclear Waste Regulatory Analyses.
92. Yang, L., Pabalan, R. T., Browning, L., & Dunn, D. S. Corrosion behavior of carbon steel and stainless steel materials under salt deposits in simulated dry repository environments. Paper presented at the Materials Research Society Symposium: Scientific Basis for Nuclear Waste Management XXVI, December 2, 2002 - December 5, 2002, Boston, MA, United states. 2003
93. Lyon, S. B., & Cai, J. P. A mechanistic study of initial atmospheric corrosion kinetics using electrical resistance sensors. Corros. Sci. 2005; 47,12: 2956-2973.
94. Nishikata, A., Yamashita, Y., Katayama, H., Tsuru, T., Usami, A., Tanabe, K., & Mabuchi, H. Electrochemical impedance study on atmospheric corrosion of steels in a cyclic wet-dry condition. Corros. Sci. 1995; 37,12: 2059-2069.
95. Richardson, G. M., & Malthus, R. S. Salts for static control of humidity at relatively low levels. J Appl Chem 1955; 5,10: 557-567.
96. Black, P. E. Watershed hydrology 2ed., Boca Raton, Fl: CRC Press 1996.
97. Greiner, M., & Winter, R. F. Forced flow evaporation at high mass transfer rates Ger. Chem. Eng. 1978; 1,6: 352-360.
98. Hua, H., & Larson, R. G. Evaporation of a sessile droplet on a substrate. J. Phys. Chem. B 2002; 106,6: 1334-1344.

99. Mori, S., Nakagawa, H., Tanimoto, A., & Sakakibara, M. Heat and mass transfer with a boundary layer flow past a flat plate of finite thickness. Int. J. Heat Mass Transfer 1991; 34,11: 2899-2909.
100. Cole, I. S., Holgate, R., Kao, P., & Ganther, W. The rate of drying of moisture from a metal surface and its implication for time of wetness. Corros. Sci. 1995; 37,3: 455-465.
101. Kheshgi, H. S., & Scriven, L. E. Dewetting: Nucleation and growth of dry regions. Chem. Eng. Sci. 1991; 46,2: 519-526.
102. ElSherbini, A. I., & Jacobi, A. M. Liquid drops on vertical and inclined surfaces: I. An experimental study of drop geometry. J. Colloid Interface Sci. 2004; 273,2: 556-565.
103. Quéré, D. Non-sticking drops. Rep. Prog. Phys. 2005; 68,11: 2495.
104. Dussan V., E. B., & Chow, R. T.-P. On the ability of drops or bubbles to stick to non-horizontal surfaces of solids. J. Fluid Mech. 1983; 137: 1-29.
105. Cole, I. S., Ganther, W. D., & Lau, D. Field studies of surface cleaning and salt retention on openly exposed metal plates. Corros. Eng., Sci. Technol. 2006; 41,4: 310-320.
106. Cole, I. S., Lau, D., Chan, F., & Paterson, D. A. Experimental studies of salts removal from metal surfaces by wind and rain. Corros. Eng., Sci. Technol. 2004; 39,4: 333-338.
107. Vernon, W. H. J. Laboratory study of atmospheric corrosion of metals - 1. Trans. Faraday Soc. 1931; 27,121: 255-277.
108. Vernon, W. H. J. Role of corrosion product in atmospheric corrosion of iron. New York, NY, United States. 1933
109. Vernon, W. H. J., & Whitby, L. Open-air corrosion of copper. Ii. Mineralogical relationships of corrosion products. J. Inst. Met. 1930; 44,2: 389-396.
110. Wilkinson, J. H., & Patterson, W. S. Influence of humidity on atmospheric corrosion of zinc, aluminum, and iron coated with electrolytes. Soc. Chem. Ind. 1941; 60,2: 42-44.
111. Hudson, J. C. Experimental methods for study of corrosion. Soc. Chem. Ind. 1933; 52,12: 69-75.
112. Evans, U. R. The corrosion and oxidation of metals, London: E. Arnold, 1960.
113. Tomashov, N. D. Development of electrochemical theory of metallic corrosion. Corrosion 1964; 20,1: 7-14.
114. Stratmann, M. The atmospheric corrosion of iron — a discussion of the physico-chemical fundamentals of this omnipresent corrosion process invited review. Berichte der Bunsengesellschaft für physikalische Chemie 1990; 94,6: 626-639.
115. Compton, K. G. Factors influencing measurement of corrosion in marine atmosphere. Mat. Prot. 1965; 4,12: 13-14.
116. Ogburn, F., & Myklebust, R. L. Galvanic currents observed during outdoor exposure of iron-nickel cell. Paper presented at the American Electroplaters' Society -- Annual Convention, 1963, Newark, NJ, United States. 1963
117. Opinsky, A. J., Thomson, R. F., & Boegehold, A. L. General motors research corrosion test: Cyclic humidity accelerated corrosion test for sheet steel. American Society for Testing Materials -- Bulletin 1953,187: 47-51.

118. Sereda, P. J. Atmospheric factors affecting the corrosion of steel. Ind. Eng.Chem. 1960a; 52,2: 157-160.
119. Sereda, P. J.Measurement of surface moisture and sulfur dioxide activity at corrosion sites, Philadelphia, PA, United States:1960b.
120. Schweitzer, P. A. Corrosion engineering handbook, New York: CRC Press 2007.
121. ISO. 9223:1992(e) corrosion of metals and alloys- corrosovity of atmospheres-classification, Vol. ISO 9223:1992(E): Geneva, Switzerland: ISO,1992.
122. Cole, I. S., Ganther, W. D., Sinclair, J. D., Lau, D., & Paterson, D. A. A study of the wetting of metal surfaces in order to understand the processes controlling atmospheric corrosion. J. Electrochem. Soc. 2004; 151,12: B627-B635.
123. Mikhailov, A., Strekalov, P., & Panchenko, Y. Atmospheric corrosion of metals in regions of cold and extremely cold climate (a review). Prot. Met 2008; 44,7: 644-659.
124. Morcillo, M., Chico, B., de la Fuente, D., Almeida, E., Joseph, G., Rivero, S., & Rosales, B. Atmospheric corrosion of reference metals in antarctic sites. Cold Reg Sci Technol 2004; 40,3: 165-178.
125. Sereda, P. J., Croll, S.G., Slade, H.F. Measurement of the time-of-wetness by moisture sensors and their calibration. In J. a. E. C. R. S.W. Dean, editors. Atmospheric corrosion of metals, astm, stp 767. American Society for Testing and Materials, 1982: 267-285.
126. Tomashov, N. D., Berukshtis, G. K., & Lokotilov, A. A. Zavodskaja Laboratorija 1956; 22,3: 346-349.
127. Sereda, P. J.Measurement of surface moisture, second progress report Research Paper NO.78 of the Division of Building Research 1959.
128. ASTM. G84: Standard practice for measurement of time-of-wetness on surfaces exposed to wetting conditions as in atmospheric corrosion testing, Vol. G84: West Conshohocken, PA: ASTM International,2005.
129. Agarwala, V. S. Sensors for monitoring corrosion in aircraft systems. Paper presented at the 13th International Corrosion Conference, Melbourne. 1996
130. Ganther, W. D., & Muster, T. Coiled galvanic corrosion sensors for atmospheric corrosion monitoring. Paper presented at the Corrosion & Prevention 2005, Kerrimur. 2005
131. Kučera, V., & Mattsson, E. Electrochemical technique for determination of the instantaneous rate of atmospheric corrosion. In Corrosion in Natural Environments, W.H. Ailor,Dean, S.W., Haynie, F.H., Eds. Philadelphia: ASTM, 1974: 239.
132. Mansfeld, F., & Kenkel, J. V. Electrochemical monitoring of atmospheric corrosion phenomena. Corros. Sci. 1976; 16: 111-122.
133. Motoda, S.-i., Suzuki, Y., Shinohara, T., Kojima, Y., Tsujikawa, S., Oshikawa, W., . . . Izumo, S. Acm (atmospheric corrosion monitor) type corrosion sensor to evaluate corrosivity of marine atmosphere. Zairyo to Kankyo/ Corrosion Engineering 1994; 43,10: 550-556.
134. Oung, J. C., & Shih, H. C. An electrochemical sensor for monitoring the atmospheric-corrosion of iron and steel. Corros. Prevent. and Contr. 1997; 44,6: 173-178.

135. Shinohara, T., Motoda, S., & Oshikawa, W. Evaluation of corrosivity in atmospheric environment by acm (atmospheric corrosion monitor) type corrosion sensor.editors. Switzerland: Trans Tech Publications, 2005: 61-64.
136. Mansfeld, F., & Kenkel, J. V. Electrochemical measurements of time-of-wetness and atmospheric corrosion rates. Corrosion 1977; 33,1: 13-16.
137. Mansfeld, F. Evaluation of electrochemical techniques for monitoring of atmsopheric corrosion phenomena. In F. Mansfeld & U. Bertocci, editors. Electrochemical corrosion testing. American Society for Testing and Materials, 1981: 215-237.
138. Cole, I. S., & Ganther, W. D. Experimental determination of duration of wetness on metal surfaces. Corros. Eng., Sci. Technol. 2008; 43: 156-162.
139. Cole, I. S., & Paterson, D. A. Holistic model for atmospheric corrosion. Part 7 - cleaning of salt from metal surfaces. Corros. Eng., Sci. Technol. 2007; 42,2: 106-111.
140. Ganther, W., Norberg, P., & Cole, I. S. Sensors for measuring factors promoting corrosion within the building envelope. Paper presented at the Proceedings of the 13th International Corrosion Congress Melbourne, Australia. 1996
141. Haagenrud, S., Henriksen, J. F., & Wyzisk. Electrochemical characterization of the nilu/sci atmospheric corrosion monitor. Paper presented at the Corrosion 85, Boston. 1985
142. Norberg, P. Evaluation of a new surface moisture monitoring system. Paper presented at the The Durability of Building Materials and Components, Omiya, Japan. 1993a
143. Norberg, P.Microclimate measurements in the built environment. Phd, Institutionen för byggd miljö,1998.
144. Haagenrud, S., Henriksen, J. F., Danielsen, T., & Rode, A. Technique for measurement of time of wetness. Paper presented at the 3rd International Conference on Durability of Building Materials and Components, Espoo. 1984
145. Haagenrud, S., Kucera, V., & Gullman, J. Atmospheric corrosion testing with electrolytic cells in norway and sweden. Paper presented at the Atmospheric Corrosion. 1982
146. Norberg, P. Evaluation of a new surface moisture monitoring system. In S. Nagataki, T. Nireki & F. Tomosawa, editors. The durability of building materials and components, proceedings of the 6th international conference, omiya, japan. Omiya, Japan: E & FN Spon, 1993b: 637-646.
147. El-Mahdy, G. A., & Kim, K. B. Ac impedance study on the atmospheric corrosion of aluminum under periodic wet-dry conditions. Electrochim. Acta 2004; 49,12: 1937-1948.
148. El-Mahdy, G. A., Nishikata, A., & Tsuru, T. Ac impedance study on corrosion of 55%al-zn alloy-coated steel under thin electrolyte layers. Corros. Sci 2000a; 42,9: 1509-1521.
149. El-Mahdy, G. A., Nishikata, A., & Tsuru, T. Electrochemical corrosion monitoring of galvanized steel under cyclic wet-dry conditions. Corros. Sci. 2000b; 42,1: 183-194.

150. Yadav, A. P., Nishikata, A., & Tsuru, T. Electrochemical impedance study on galvanized steel corrosion under cyclic wet-dry conditions-influence of time of wetness. Corros. Sci. 2004; 46,1: 169-181.
151. Yadav, A. P., Nishikata, A., & Tsuru, T. Evaluation of impedance spectra of zinc and galvanized steel corroding under atmospheric environments. Corros. Eng., Sci. Technol. 2008; 43,1: 23-29.
152. Yadav, A. P., Suzuki, F., Nishikata, A., & Tsuru, T. Investigation of atmospheric corrosion of zn using ac impedance and differential pressure meter. Nieuwpoort, Belgium. 2004
153. Nishikata, A., Kojima, T., & Tsuru, T. Atmospheric corrosion monitoring of weathering steels using ac impedance technique. Proceedings - Electrochemical Society 2005: 102-110.
154. Nishikata, A., Suzuki, F., & Tsuru, T. Corrosion monitoring of nickel-containing steels in marine atmospheric environment. Corros. Sci. 2005; 47,10: 2578-2588.
155. Demo, J., Steiner, A., Friedersdorf, F., & Putic, M. Development of a wireless miniaturized smart sensor network for aircraft corrosion monitoring. Paper presented at the Aerospace Conference, 2010 IEEE. 2010
156. Itagaki, M., Endou, M., Watanabe, K., Katayama, H., Noda, K., & Masuda, H. Corrosion monitoring in marine environments using electrochemical impedance. Proceedings - Electrochemical Society 2005; PV 2004-14: 53-61.
157. Katayama, H., Tay, Y. C., Viloria, A. S., Nishikata, A., & Tsuru, T. Corrosion monitoring of zn and zn-al coated steels under wet-dry cyclic conditions using ac impedance method. Mater. Trans., JIM 1997; 38,12: 1089-1094.
158. Li, S.-x., Dong, J.-h., Han, E.-h., & Ke, W. Evolvement of electrochemical impedance spectra of a bi-electrode cell for carbon steel in the initial stage of wet/dry process. Corr. Sci. Prot. Tech. 2007; 19,3: 167-170.
159. Shitanda, I., Okumura, A., Itagaki, M., Watanabe, K., & Asano, Y. Screen-printed atmospheric corrosion monitoring sensor based on electrochemical impedance spectroscopy. Senor Actuat B-Chem. 2009; 139,2: 292-297.
160. Katayama, H., Endou, M., Masuda, H., Itagaki, M., & Watanabe, K. Corrosion multi-monitoring of carbon steel in coastal area. Los Angeles, CA, United states. 2005
161. Forslund, M., & Leygraf, C. In situ weight gain rates on copper during outdoor exposures. Dependence on airborne pollutants and climatic parameters. J. Electrochem. Soc. 1997a; 144,1: 113-120.
162. Forslund, M., & Leygraf, C. Humidity sorption due to deposited aerosol particles studied in situ outdoors on gold surfaces. J. Electrochem. Soc. 1997b; 144,1: 105-113.
163. Forslund, M., Majoros, J., & Leygraf, C. Sensor system for high resolution in situ atmospheric corrosivity monitoring in field environments. J. Electrochem. Soc. 1997; 144,8: 2637-2642.
164. Zhang, C., Feng, G., & Sui, S. Study on behaviour of QCM sensor in loading variation. Sensor. Actuat. B-Chem. 1997; 40,2-3: 111-115.
165. Stratmann, M. The investigation of the corrosion properties of metals, covered with adsorbed electrolyte layers- a new experimental technique. Corros. Sci. 1987; 27,8: 869-872.

166. Stratmann, M. The investigation of the corrosion properties of metal surfaces covered by condensed or adsorbed layers Paper presented at the 1st international symposium on corrosion of electronic materials and devices. 1991

167. Stratmann, M., & Streckel, H. On the atmospheric corrosion of metals which are covered with thin electrolyte layers i: Verification of the experimental technique. Corros. Sci. 1990a; 30,6-7: 681-696.

168. Stratmann, M., & Streckel, H. On the atmospheric corrosion of metals which are covered with thin electrolyte layers ii: Experimental results. Corros. Sci. 1990b; 30,6-7: 697-714.

169. Stratmann, M., Streckel, H., Kim, K. T., & Crockett, S. On the atmospheric corrosion of metals which are covered with thin electrolyte layers iii: The measurement of polarisation curves on metal surfaces which are covered by thin electrolyte layers. Corros. Sci. 1990; 30,6-7: 715-734.

170. Yee, S., Oriani, R. A., & Stratmann, M. Application of a kelvin microprobe to the corrosion of metals in humid atmospheres. J. Electrochem. Soc. 1991; 138,1: 55-61.

171. Araoka, Nishikata, & Tsuru. Kelvin probe measurement on potential distribution of steels during marine atmospheric rusting process. In D. A. Shifler, P. M. Natishan, T. Tsuru & S. Ito, editors. Corrosion control in saltwater environments. Pennington, New Jersey: Electrochemical Society, 2000: 78-86.

172. Frankel, G. S., Stratmann, M., Rohwerder, M., Michalik, A., Maier, B., Dora, J., & Wicinski, M. Potential control under thin aqueous layers using a kelvin probe. Corros. Sci. 2007; 49,4: 2021-2036.

173. Yamashita, M., Nagano, H., Guillaume, F., & Oriani, R. A. Kelvin probe measurements of the corrosion potential of low-alloy steels in dry-wet cycles. Mater. Sci. Forum 1995; 185-188: 515-524.

174. Masuda, H. Observation of water droplet on various materials by non-contacting afm. J. Jpn. Inst. Met. 1998; 62,2: 173-180.

175. Wadsak, M., Aastrup, T., Odnevall Wallinder, I., Leygraf, C., & Schreiner, M. Multianalytical in situ investigation of the initial atmospheric corrosion of bronze. Corros. Sci. 2002; 44,4: 791-802.

176. Nagashima, N., Masuda, H., & Matsuoka, S. In-situ observation of metal surfaces in aqueous solutions with an electrochemical stm. JSME Int. J. Ser. A 1992; 35,4: 442-448.

177. Rohwerder, M., & Turcu, F. High-resolution kelvin probe microscopy in corrosion science: Scanning kelvin probe force microscopy (skpfm) versus classical scanning kelvin probe (skp). Electrochim. Acta 2007; 53,2: 290-299.

178. Feng, Z., Xueyuan, Z., Persson, D., & Thierry, D. In situ infrared reflection absorption spectroscopy studies of confined zinc surfaces exposed under periodic wet-dry conditions. Electrochem. Solid-State Lett. 2001; 4,5: 19-22.

179. Persson, D., & Leygraf, C. In situ infrared absorption spectroscopy for studies of atmospheric corrosion. J. Electrochem. Soc. 1993; 140,5: 1256-1260.

180. Persson, D., & Leygraf, C. Initial interaction of sulfur dioxide with water covered metal surfaces: An in situ iras study. J. Electrochem. Soc. 1995; 142,5: 1459-1468.

181. Weissenrieder, J., & Leygraf, C. In-situ studies of the initial atmospheric corrosion of iron. In H. E. Townsend, editors. Outdoor atmospheric corrosion. ASTM International, 2002: 127-137.

182. Cooper, K. R., Elster, J., Jones, M., & Kelly, R. G. Optical fiber-based corrosion sensor systems for health monitoring of aging aircraft. 2001 IEEE Autotestcon Proceedings. IEEE Systems Readiness Technology Conference 2001: 847-856.

183. Magarey, R. D., Russo, J. M., Seem, R. C., & Gadoury, D. M. Surface wetness duration under controlled environmental conditions. Agr Forest Meteorol 2005; 128,1/2: 111-122.

184. Gillespie, T., & Kidd, G. E. Sensing duration of leaf moisture retention using electrical impedance grids. Can J Plant Sci 1978,58: 179-187.

185. Armstrong, R., Barthakur, N. N., & Norris, E. A comparative study of three leaf wetness sensors. IJBm 1993; 37,1: 7-10.

186. Lau, Y. F., Gleason, M. L., Zriba, N., Taylor, S. E., & Hinz, P. N. Effects of coating, deployment angle, and compass orientation on performance of electronic wetness sensors during dew periods. Plant Dis. 2000; 84,2: 192-197

187. Sentelhas, P., Gillespie, T., & Santos, E. Leaf wetness duration measurement: Comparison of cylindrical and flat plate sensors under different field conditons. IJBm 2007; 51,4: 265-273.

188. Sentelhas, P. C., Gillespie, T. J., Gleason, M. L., Monteiro, J. E., & Helland, S. T. Operational exposure of leaf wetness sensors. Agr Forest Meteorol 2004; 126,1-2: 59-72.

189. Sentelhas, P. C., Monteiro, J. E. B. A., & Gillespie, T. J. Electronic leaf wetness duration sensor: Why it should be painted. IJBm 2004; 48,4: 202-205.

190. Davis, D., & Hughes, J. A new approach to recording the wetting parameter by the use of electrical resistance sensors. Plant Dis. Rep. 1970; 54: 474-479.

191. Heusinkveld, B. G., Berkowicz, S. M., Jacobs, A. F. G., Hillen, W., & Holtslag, A. A. M. A new remote optical wetness sensor and its applications. Agr. Forest Meteorol. 2008; 148,4: 580-591.

192. Chtioui, Y., Panigrahi, S., & Francl, L. A generalized regression neural network and its application for leaf wetness prediction to forecast plant disease. Chemometrics Intellig. Lab. Syst. 1999; 48,1: 47-58.

193. Dalla Marta, A., De Vincenzi, M., Dietrich, S., & Orlandini, S. Neural network for the estimation of leaf wetness duration: Application to a plasmopara viticola infection forecasting. PCE 2005; 30,1-3: 91-96.

194. Francl, L. J., & Panigrahi, S. Artificial neural network models of wheat leaf wetness. Agr Forest Meteorol 1997; 88,1-4: 57-65.

195. Kim, K. S., Gleason, M. L., & Taylor, S. E. Forecasting site-specific leaf wetness duration for input to disease-warning systems. Plant Dis. 2006; 90,5: 650-656.

196. Kim, K. S., Taylor, S. E., Gleason, M. L., & Koehler, K. J. Model to enhance site-specific estimation of leaf wetness duration. Plant Dis. 2002; 86,2: 179-185.

197. Pedro, M. J., & Gillespie, T. J. Estimating dew duration i: Utilizing micrometeorological data. Agr Meteorol 1982a; 25,283-296.

198. Pedro, M. J., & Gillespie, T. J. Estimating dew duration ii: Utilizing standard weather station data. Agr Meteorol 1982b; 25: 297-310.

199. Papastamati, K., McCartney, H. A., & Bosch, F. v. d. Modelling leaf wetness duration during the rosette stage of oilseed rape. Agr Forest Meteorol 2004; 123,1-2: 69-78.

200. Sentelhas, P. C., Gillespie, T. J., Gleason, M. L., Monteiro, J. E. B. M., Pezzopane, J. R. M., & Pedro Jr, M. J. Evaluation of a penman-monteith approach to provide "reference" and crop canopy leaf wetness duration estimates. Agricultural and Forest Meteorology 2006; 141,2-4: 105-117.

2.2 Comparability and Accuracy of Time of Wetness Sensing Methods Relevant For Atmospheric Corrosion

The performance of three time of wetness (TOW) determination methods during outdoor exposure was examined. Two impedance-based TOW sensor types, RH, and temperature sensors were exposed to coastal marine and laboratory environments for up to three months. The sensor and ISO 9223 methods examined provided incomparable estimates. Inaccuracy of the ISO method originated from a humidity threshold well above the drying point of deposited aerosols and differences between surface and ambient RH. TOW sensor accuracy was linked to electrode configuration. Small electrode spacing was demonstrated to be required to capture the range of wetting events of importance to atmospheric corrosion.

2.2.1 Introduction

This investigation examined the comparability and accuracy of time of wetness (TOW) determinations made using two indirect sensing methods along with the ISO 9223 humidity-based definition during outdoor exposure. Time of wetness is often defined as the fraction of time a metal surface remains wet during atmospheric exposure. Although the basic concept and importance of TOW in governing atmospheric corrosion is generally agreed upon, its practical determination is widely varied.

Practical definitions and associated determination methods represented in literature and practice can be categorized by the way in which TOW is treated- either as an environmental parameter or as a surface parameter. As an environmental parameter, TOW is defined in terms of climatic variables, such as relative humidity (RH) and temperature. A widely used definition of this type is given by ISO 9223, which defines TOW as the time during which the RH of the ambient environment is greater than 80% at temperatures above $0^{o}C$ [1]. This definition is based on the idea that above a certain humidity threshold, corrosion increases substantially due to sorption of water on the surface. The basis for a critical RH of 80% is unclear and this threshold has been shown to be a highly inaccurate estimate for actual surface wetness in certain outdoor environments [2-4].

As a surface parameter, TOW is estimated by measuring moisture on or near a surface of interest. Sensors consisting of arrays of electrodes separated by an insulating gap are commonly used for this purpose. The electrodes of these sensors can be constructed of reactive or noble metals. Corrosion behavior of reactive electrodes, oftentimes set up as galvanic couples, is usually monitored through potential or current measurements as an indicator of wetness [5-8]. Resistance or impedance across sensors constructed of noble electrode is often used a more direct means of indicating the presence or absence of a sufficiently conducting electrolyte [2, 9-12]. Time of wetness is defined as the time during which a voltage, current or resistance/impedance threshold is exceeded. Thresholds are often established as the baseline response of the clean sensors at low humidity. Further information on these methods and particular issues associated with them is presented in a review of TOW by Schindelholz and Kelly [13].

A limitation of all indirect electrode sensors is that the presence of electrolyte can only be detected if it bridges the electrode gap and provides a sufficient amount of conductance. A considerable amount of information is available concerning the response and accuracy of TOW sensors to dewing and precipitation events in natural and laboratory environments [14-17]. In these cases, electrolyte present on the sensor surface had characteristic dimensions greater than that of the electrode spacing. It is conceivable, however, that wet hygroscopic contaminants smaller than the electrode spacing (i.e., deposited aerosols) could be present on the sensors without detection. The accuracy of electrode sensors with regard to detecting the wetting contribution of deposited hygroscopic aerosols in the cases of low RH levels or contaminant loading (small amounts of electrolyte) is unclear.

Another underexplored and overarching issue with the TOW parameter in atmospheric corrosion is the comparability of TOW estimates produced by the dozens of different methods and definitions utilized in practice. Given that multi-site and inter-institutional field data, including TOW measurements, are commonly utilized as critical parameters in atmospheric corrosion modeling and prediction [18-21], an understanding of the comparability of various TOW determination methods is imperative. In a study reported by Morcillo *et al.*, for example, the authors singled out TOW data produced using different determination methods as a likely source of error in their corrosion regression models derived from field data [19].

2.2.2 Experimental

Two indirect TOW sensing methods were utilized for these experiments. The first method was comprised of Wetcorr sensors (Norwegian Institute for Air Research) connected to an astable multivibrator circuit. The Wetcorr sensor, herein referred to as a grid sensor, consists of an interdigitated pair of gold alloy electrodes on a sintered alumina backing, Figure 2.29. The sensing area measures 20 x 20 mm with 130 μm spacing between the electrodes. A similar sensor setup has been used by the authors in past studies [2, 10-12].

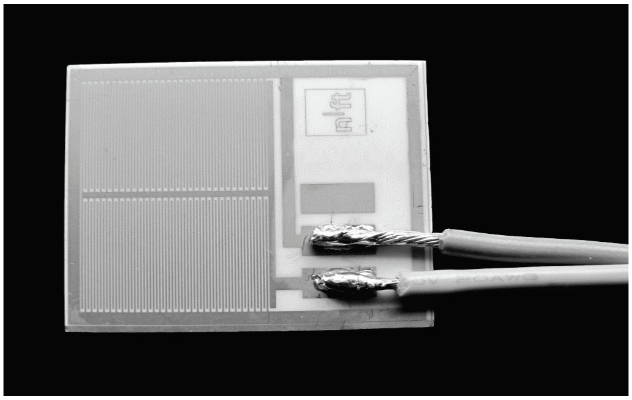

Figure 2.29. Wetcorr sensor (Norwegian Institute for Air Research) used in this study. The longest sides of the sensor measure 30 mm. The lead connections, shown as bare here, were encapsulated in silicone to prevent moisture ingress during the experiments.

The multivibrator was comprised of a 555 timer integrated circuit with a grid sensor connected between the trigger and negative supply of the timer, thus controlling output frequency. In this configuration, an alternating current passed across the sensor fluctuating at the same frequency as the output. Frequency was inversely dependent on impedance between the sensor electrodes and was measured to give wet-dry indication. The circuit output was logged using a Datataker DT80 (Thermo Fisher Scientific).

The grid sensors were defined as being wet above a reading of 0.5 Hz relative to an open circuit (lowest frequency, 0.3Hz) for the purpose of excluding the response of the sensor itself to changes in RH. A new sensor cleaned with deionized (DI) water and organic solvents was subjected to humidity ramps in an environmental chamber (detailed below) between 10% and 95%RH at 23°C to establish this threshold. During these ramps measured frequency exhibited monotonic behavior with respect to RH and peaked to 0.5Hz at 95%. By contrast, subjecting the sensor to condensation conditions (100%RH) produced a frequency of 323 Hz, which is that achieved by short-circuiting the terminals of the circuit (i.e., the highest frequency).

The second method utilized Campbell Scientific 237L leaf wetness sensors connected to a CR1000 data logger manufactured by the same company. The leaf sensor consists of interdigitated gold alloy electrodes deposited on a fiber-reinforced circuit board, Figure 2.30. Its overall sensing area measures 50 x 50 mm with 1 mm electrode spacing. Resistance was measured across the electrodes using a DC half-bridge circuit integrated in the CR1000 as per manufacturer recommendations. The leaf sensor was defined as being wet below a reading of 7.3 MΩ. Not only was this the manufacturer recommended threshold, but also, through the same calibration procedure detailed for the grid sensors above, it was the resistance measured across a clean sensor at 95%RH. Unlike the grid sensors, however, resistance across a clean, new leaf sensor was found to be constant at 7.3MΩ, independent of RH up to 95%. It is important to note that it is common practice in the environmental science community to paint these sensors with a latex paint to increase sensitivity and create a surface more closely resembling the wetting characteristics of leaves [22]. In the present study, painting was not carried out so as to give more comparable results to the grid method. Painting of TOW sensors as such is also not standard practice in the atmospheric corrosion community.

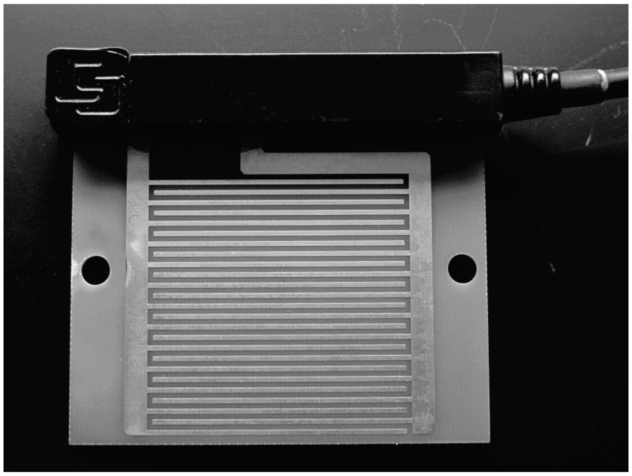

Figure 2.30. L237 (Campbell Scientific) leaf wetness sensor used in this study. The bottom edge of the sensor, as it is picture here, is 76 mm.

Arrays consisting of triplicate sets of each sensor type were subjected to four sequences of outdoor and controlled laboratory exposures, Table 2.2. Outdoor exposure was carried out at a site located in suburban Melbourne, Australia. This location is characterized by light industrial activity and is 3 km west of Port Phillip Bay. Average measured soluble salt deposition (per ISO 9225 wet candle method [23]) for the site is 8 $mg{\cdot}m^{-2}day^{-1}$ [24]. The arrays were mounted approximately 1.5 m from the ground on either an open or sheltered rack, both of which faced North at 45^{o}, Figure 2.31. The roof over the sheltered rack was covered with tarps during the experiments to eliminate diurnal surface heating and cooling of the sensors associated with direct sky exposure. A calibrated HMP 110 RH/temperature probe (Vaisala) mounted in a radiation shield was deployed within two meters of the sensor arrays to characterize the ambient conditions. The manufacturer stated accuracy of the probe was ±3%RH and $\pm 0.2^{o}C$ under the exposure conditions of this study. Type T thermocouples were attached to the top surface of each wetness sensor with a dab of clear and colorless silicon caulking during the last exposure (referred to as “Open 3”) to measure temperature. The RH/temperature probe and thermocouple measurements were taken and logged using a DT80.

Table 2.2. Exposure sequences carried out during this investigation.

Exposure Sequence	**Outdoor Dates (2011)**	**Outdoor Duration (days)**
Open 1	March 22-31	10
Sheltered	April 12-15	4
Open 2	April 18-May6	16
Open 3	May9-Aug7	91

By taking into account the temperature dependence of the saturation pressure of water vapor (P_{sat}), surface temperature along with ambient RH and temperature were used to estimate surface relative humidity RH_s during the outdoor exposures:

$$\mathrm{RH}_s = \mathrm{RH} \cdot \frac{\mathrm{P_{sat,a}}}{\mathrm{P_{sat,s}}} \qquad 2.15$$

where $P_{sat,a}$ and $P_{sat,s}$ are the saturated vapor pressure of water at the temperature of the ambient air and a surface respectively. Saturated vapor pressures were estimated using [25]:

$$P_{sat}(T) = 610.7 \cdot 10^{7.5T/(237.3+T)} \qquad 2.16$$

with pressure in units of Pa and temperature T in units of K. Between outdoor exposures, the sensors were rinsed with DI water. Data were sampled and logged at five minute intervals for all sensors. Precipitation data were collected from an Australian Bureau of Meteorology weather station 5km from the exposure site to aid in interpretation of the results.

Figure 2.31. Exposure site in Highett, Australia used for this study. The rack in the foreground was used for the open exposures and the rack under a roof in the background was used for the sheltered exposures. The distance between the rack and the roof in the shelter structure is approximately one meter.

In all of the exposure sequences except the last, the TOW sensor arrays along with the RH/temperature probe were placed in a Weiss WK480 circulating air environmental chamber within thirty minutes after removal from the marine environment. They were subjected to three consecutive cycles of a humidity profile, save for the first run due to a program error in the chamber, to examine humidity response in a controlled environment. Multiple cycles were carried out to garner information on the repeatability of sensor behavior. The profile consisted of a 4-hour hold at 12%RH, followed by steps to 18,33,53,74 and 94% and back down again in the same manner. The dwell time at each step was 1 hour and the ramp rate between steps was 0.11% per minute. Chamber temperature was held at 23±1°C. Data were sampled and logged at one-minute intervals for all sensors during the chamber exposures.

A 500x Dinolight reflected light, digital microscope (AnMo Electronics Corp.) was placed in the chamber and trained on one of the grid sensors during the lab experiments. Time-lapse video of the surface was taken at the rate of two minutes per frame. The resolution of the resulting images was around one micron per pixel. The video was viewed for visible surface changes related to wetting or drying (e.g., droplet formation, crystallization, etc.). Wetting and drying points were determined as the time at which visible change could first be distinguished (wetting) or no longer observed (drying).

Cleaned gold-coated quartz crystals and polytetraflouroethylene (PTFE) coupons were deployed alongside the sensors during the sheltered outdoor exposure. Two crystals were exposed, each with an area of 154 mm^2. Seventeen Teflon coupons, each measuring 25mm square, were mounted on nylon standoffs. After exposure, the gold surfaces were examined using optical microscopy. The Teflon PTFE coupons were extracted under sonication in 10mL of DI water. Extracts were analyzed by ion chromatography (IC) for Ca^{2+}, Na^{+}, Mg^{2+}, Cl^{-}, and SO_4^{2-}. Data for the samples were corrected based on the averages of the field blanks. The results were compared to the composition of seawater [26] using Mg^{2+} as the reference species following a procedure outlined in Keene *et al.* [27].

2.2.3 Results

Time of wetness estimations calculated for the outdoor exposures are given in Figure 2.32. The ISO definitions (using either ambient or surface RH as the input) consistently gave the lowest estimates followed by the leaf and grid sensors. Although there is considerable difference in TOW values between the methods, values are within five percent amongst replicate sensors. The sheltered exposure is an exception to this and will be discussed in more detail in the next section.

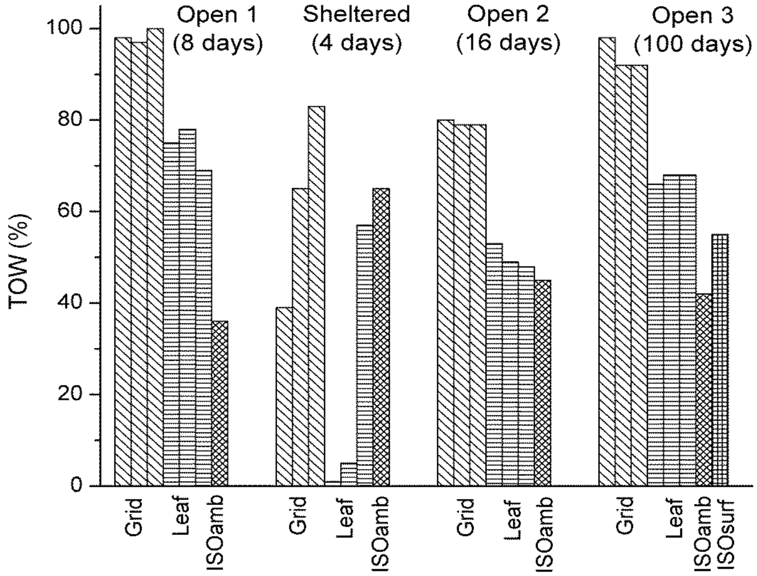

Figure 2.32. Time of wetness estimates calculated for each sensor and using the ISO definition for ambient and average sensor surface RH, labeled ISOamb and ISOsurf respectively, during the outdoor exposures.

The last open exposure, given its length, provided sufficient information to examine the relationship between relative humidity and TOW estimates. Data used for the ISO TOW estimates during the last open exposure are shown in Figure 2.33. It is clear that the sensor surfaces experienced a much broader humidity range than the ambient atmosphere. The average condensation time (RH ≥ 100%) on the surfaces was nearly six times that of the ambient atmosphere and accounted for approximately one quarter of the total exposure time. These results also show that the variability in surface relative humidity amongst the sensors during this exposure was relatively small. The temperature and relative humidity levels at the surface and in the ambient air during a randomly selected 24 hour period, Figure 2.34, reveal this disparity on a diurnal time scale. Sensor response in terms of surface relative humidity for the last exposure is presented in Figure 2.35. This plot was constructed by dividing the average total amount of time a sensor group indicated wet at a particular RH_S range by the total amount of time the sensors spent at that RH_S range during the exposure. The RH_S distribution exhibited in Figure 2.33 was used for this purpose. From this plot, it is apparent that the grid method was responsive to a broader humidity range than leaf method, especially at the lower humidity levels. This led to the generally higher grid TOW estimates given in Figure 2.32.

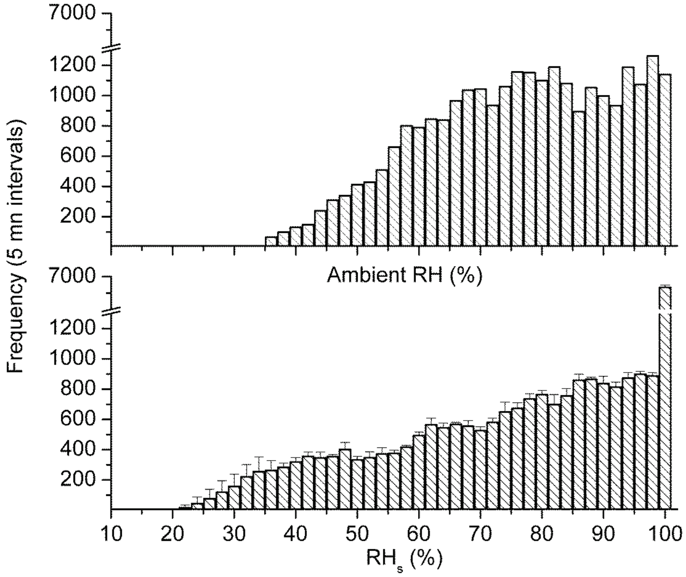

Figure 2.33. Average relative humidity distributions during the 91 day outdoor exposure (Open 3) measured in the ambient air (top) and calculated on the sensor surfaces (bottom). The error bars on the bottom plot indicate standard deviation.

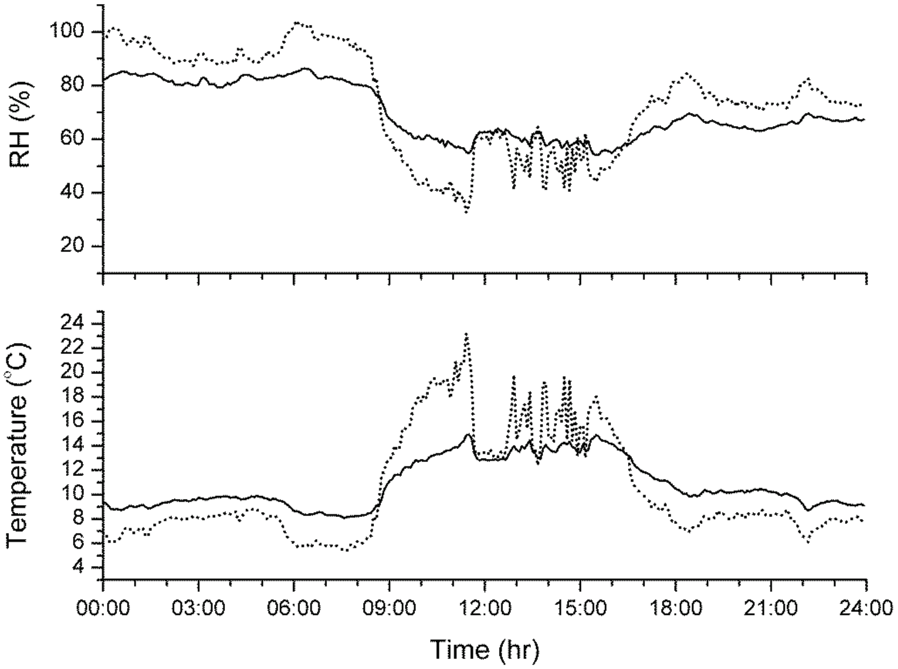

Figure 2.34. Relative humidity (top) and temperature (bottom) measured in the air (solid line) and estimated on the sensor surface (dotted line) during day 60 of the last open exposure. Time 00:00 and 24:00 correspond to midnight local time.

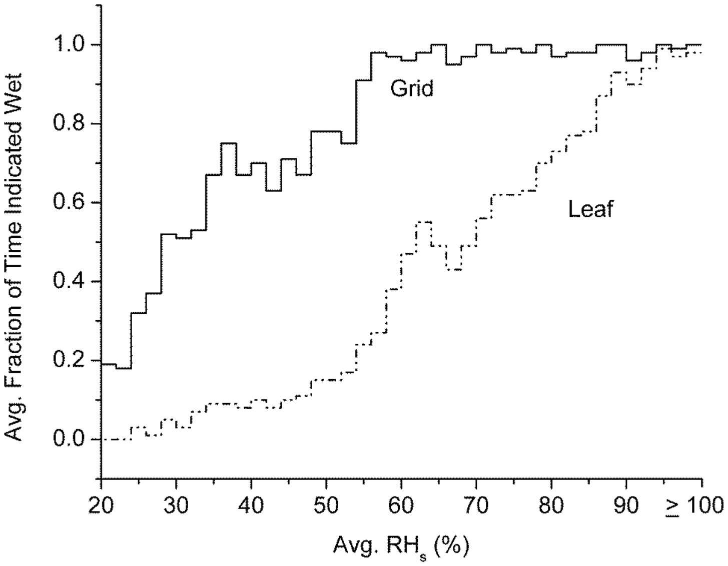

Figure 2.35. The average fraction of time each sensor type indicated wet with respect to the average RH_S during the last open exposure (Open 3).

During the short outdoor exposure sequences, sensor response was examined in relation to surface contaminant characteristics and behavior. Sensor output during these exposures is shown in Figures 2.36- 2.38. It is clear from these figures that sensors of the same type generally responded in unison, with the exception of the sheltered exposure period. During the sheltered exposure, Figure 2.37, the grid sensors responded out of sync during the first 24 hours, with one sensor indicating dry despite ambient RH levels reaching 90%. The response of these sensors, in terms of peak locations, became more concurrent as the exposure progressed. Leaf sensor outputs show a similar but more dramatic disparity. After approximately 30 hours of exposure, and during a period when the RH was not less than 70%, one of the leaf sensors suddenly registered wet and indicated as such for the majority of the remaining exposure. This reading occurred while the other leaf sensors were indicating dry along with the grid sensors at some points. The complimentary response or lack thereof from sensors of the same type during the outdoor exposures was reflected in each of the corresponding subsequent chamber experiments.

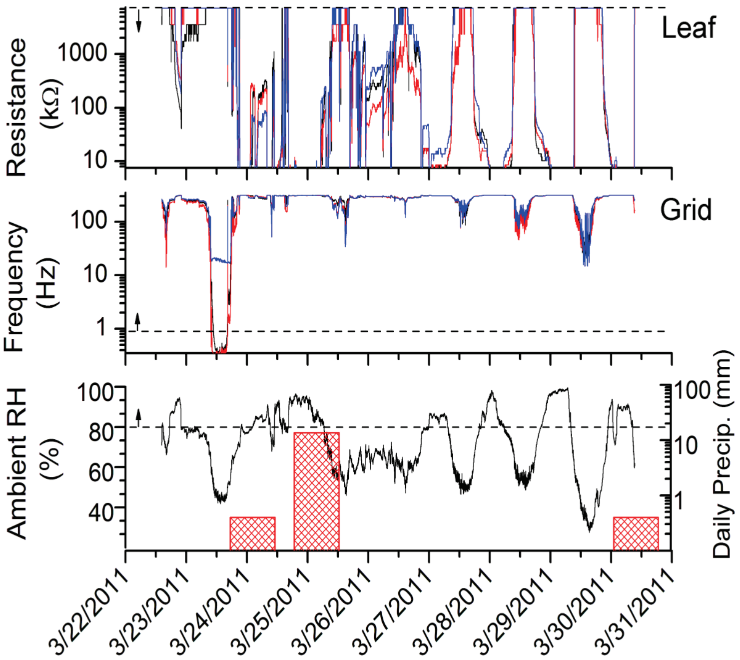

Figure 2.36. Sensor output during the 10 day open exposure (Open 1). Leaf sensor output is on top, followed by grid output, and ambient atmospheric conditions in descending order. Each of the colored lines in the grid and leaf plots represents the output of a single sensor. Dashed lines indicate wet/dry thresholds for each determination method, with arrows pointing towards values indicating wet.

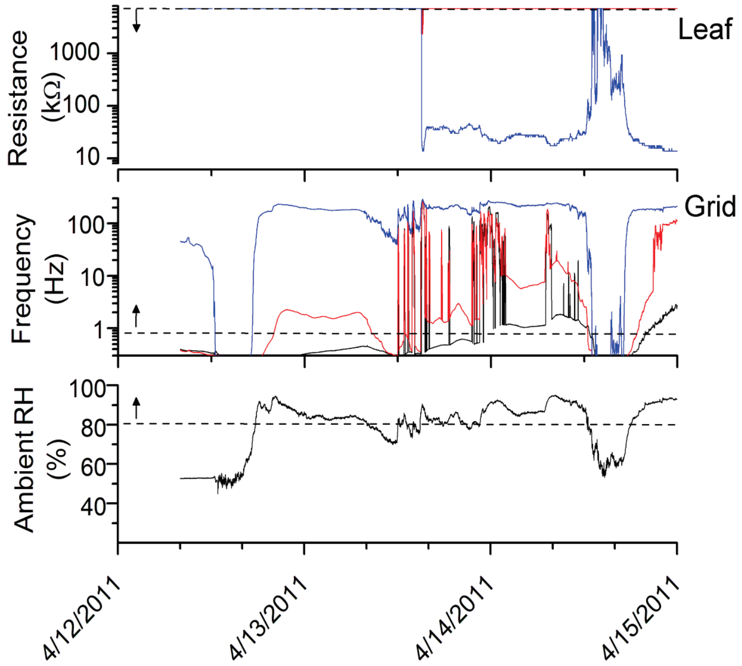

Figure 2.37. Sensor output during the sheltered exposure. Leaf sensor output is on top, followed by grid output, and ambient atmospheric conditions in descending order. Each of the colored lines in the grid and leaf plots represents the output of a single sensor. Dashed lines indicate wet/dry thresholds for each determination method, with arrows pointing towards values indicating wet.

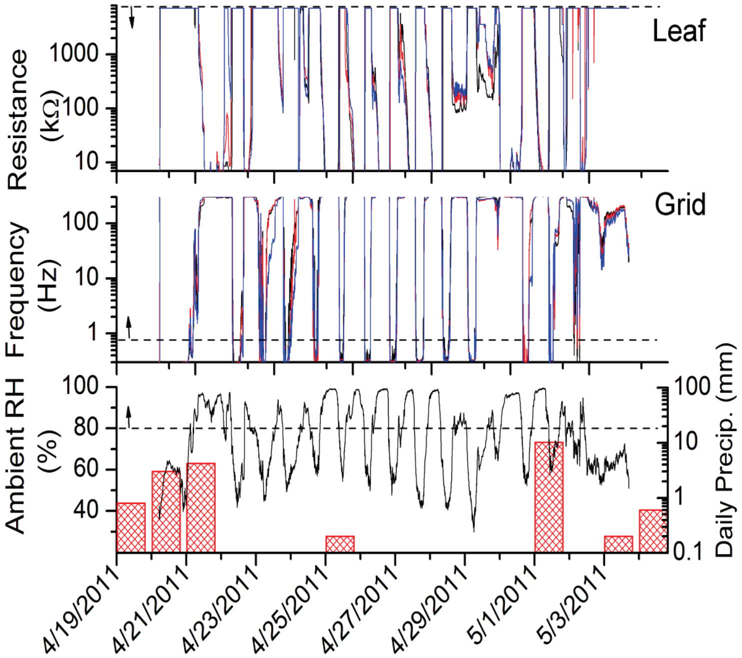

Figure 2.38. Sensor output during the 16 day open exposure (Open 2). Leaf sensor output is on top, followed by grid output, and ambient atmospheric conditions in descending order. Each of the colored lines in the grid and leaf plots represents the output of a single sensor. Dashed lines indicate wet/dry thresholds for each determination method, with arrows pointing towards values indicating wet.

The average wetting and drying points indicated by the sensors and by visual inspection during the chamber experiments are given in Figure 2.39. The range of wetting and drying values associated with each point were no greater than ± 5% RH. A micrograph taken during the chamber experiment after the sheltered exposure evidences the partially wetting nature of the grid sensors by the presence of droplets, Figure 2.40. Droplets were also present on the gold surfaces exposed during the sheltered experiment along with dried deposits, Figure 2.41. Image analysis of one of the gold surfaces was carried out to determine the size and distribution of these drops and deposits, Figure 2.42. Out of the nearly 1400 spots analyzed in a 61mm^2 area, 13 were greater than or equal to the grid sensor electrode spacing of 130μm. All were much below the 1mm leaf sensor spacing. Analyses of extractant solutions from the PTFE coupons subjected to the sheltered exposure produced ion ratios similar to that of seawater with the exception of the calcium component, Table 2.3.

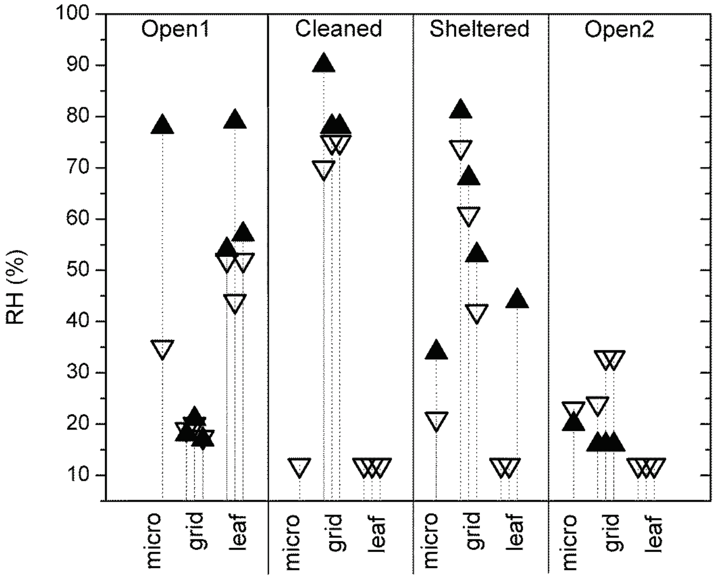

Figure 2.39. Average wetting (closed triangle) and drying (open triangle) points determined for each sensor and time-lapse microscopy (micro) for the humidity chamber experiments. The "cleaned" sensor experiment was carried out following a DI water rinse of the sensors after Open 1.

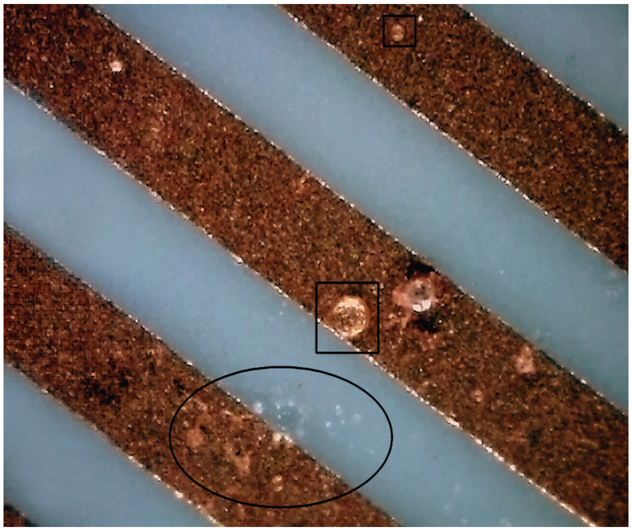

Figure 2.40. Optical micrograph of a grid sensor at 94%RH during the chamber experiment after the sheltered exposure. Electrolyte is in the form of partially wetting droplets (bright round areas). Examples of discrete drops are boxed and a group of drops are circled. Spacing between the electrodes (light stripes) is 130 μm

.

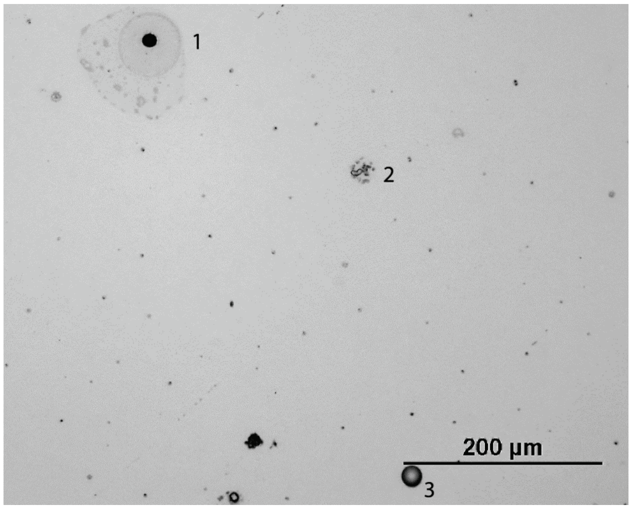

Figure 2.41. Optical micrograph of deposits on a gold surface exposed the duration of the sheltered experiment, showing examples of watermarks (1,2) and a droplet (3) at 45%RH.

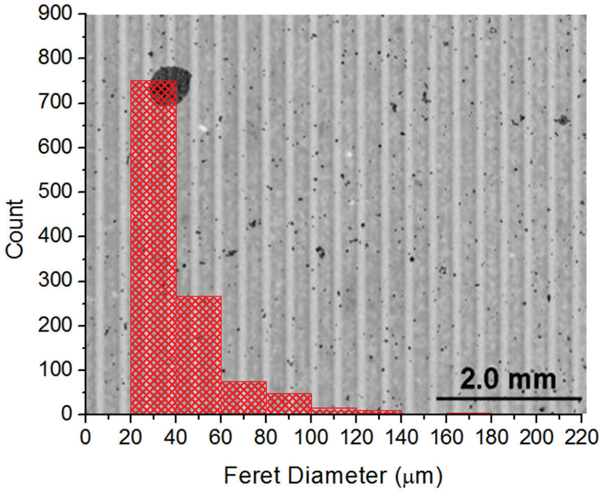

Figure 2.42. Optical micrograph of deposits (black specks) on a gold surface exposed for the duration of the sheltered experiment overlaid with an image of the grid electrode spacing and a particle size histogram. Plot outliers measure 234, 280 and 648 μm. The grid and gold surface images are at the same scale.

Table 2.3. Regression analysis results from IC analysis of Teflon coupon wash-off compared to literature values for seawater [12].

Ratio	**Slope ± SE**	**Wilson**	**% diff from Wilson**
Ca/Mg	$0.541 \pm 5.2 \times 10^{-3}$	0.194	179
Na/Mg	$4.61 \pm 8.5 \times 10^{-6}$	4.41	5
Cl/Mg	$4.85 \pm 2.0 \times 10^{-2}$	5.14	-6
SO4/Mg	$0.543 \pm 1.7 \times 10^{-3}$	0.532	2

2.2.4 Discussion

2.2.4.1 TOW Comparability

The considerable disparity between TOW estimates during the outdoor exposures, Figure 2.32, clearly illustrates that they are highly dependent on determination methodology. The grid sensors in the third open exposure, for example, indicated that they were wet twice as long as the ambient ISO estimate. Results from the third open exposure also show that the choice of ambient RH or surface RH can have considerable impact on the ISO estimate or any humidity-based environmental definition.

The much broader humidity range experienced by the sensor surfaces in the third exposure compared to the ambient environment, Figure 2.33, can be attributed to diurnal heating and cooling. Nighttime undercooling is responsible for the greater amount of condensation time (RH ≥ 100%) that the sensor surfaces experienced. The spread of time spent at the lower end of the RH_s range is due to daytime heating. These effects are reflected in the difference between the surface and ambient temperatures during the diurnal cycle exemplified in Figure 2.34. These results in tandem with the work of others [2, 4, 9] make clear that a more realistic estimate of TOW based on humidity thresholds should utilize surface RH rather than ambient levels for boldly exposed outdoor surfaces.

The difference in TOW estimates between the two sensor methods is attributed to their dissimilar RH response, as illustrated by Figure 2.35. The variability in sensor response and, consequently, TOW estimates could have been due to a number of reasons, including sensitivity of the measurement electronics and the associated TOW definitions, or insufficient electrolyte bridging of electrodes. Results from the short-term experiments are now discussed with the aim of elucidating the effect these factors have on response, and, in turn, comparability.

2.2.4.2 Sensor Response

Leaf and grid sensor output data during the short exposure sequences and subsequent optical microscopic examination of the exposed sensor and gold surfaces indicate that variation in TOW estimates is strongly controlled by electrolyte bridging. Inconsistent sensor output during the sheltered exposure, as compared to the first and second open exposures, is evidence of this. As pointed out in the results section, the responses of the grid sensors were out of sync at the beginning of the exposure but became more concurrent as the exposure progressed. This behavior can be attributed to the slow accumulation of hygroscopic contaminants on the sensor surfaces. The sudden wetting event on one of the leaf sensors during this period while all others indicated dry may have been triggered by accumulating a critical configuration of wet deposits that caused bridging of the electrodes. This would explain the enhanced sensitivity of this sensor to RH change during the subsequent chamber experiment, Figure 2.39.

The commonly muted response of the sensors after wash-off (i.e., rain) periods during the open exposures can also be explained in terms of electrolyte bridging issues. As an example, precipitation during the end of the second open exposure, Figure 2.38, is seen to have caused the leaf sensors to read subsequently dry during the entire last day of exposure and dry up to 95%RH in the later chamber exposure while the grid sensors read wet, Figure 2.39. This effect is likely not only due to electrode spacing, but also to differential washing efficiency between the two types. Directly rinsing the sensors with deionized water after outdoor exposure produced similar behavior in that the leaf sensors read completely dry while the response of the grid sensors was shifted to much higher humidity levels, Figure 2.39.

Microscopic examinations of the exposed sensor and gold surfaces substantiate the notion that intermittent sensor response was controlled by electrolyte bridging. Deliquesced contaminants were found to be in the form of partially wetting droplets, as opposed to bridging electrolyte films, on the grid sensor and gold surfaces, Figures 2.40-2.41. The size distribution of drops and deposits on the exposed gold surface indicates that very few would be able to bridge the grid sensor electrodes and none would bridge the leaf electrodes, Figure 2.42. Given similar distributions on the sensors and the partially wetting behavior of the deliquesced deposits, this observation may explain the lack of response from the two leaf sensors during the sheltered exposure. It is important to note here, however, that the resolution of this analysis is limited to larger coarse mode particles (>20 µm), and one can expect a great number of smaller particles to contribute to wetting as well, as exemplified by Cole, Lau and Paterson [28], Table 2.4.

Table 2.4. An example of deposited coarse-mode sea salt particle size distribution estimated on an ideal surface in the marine environment at 90% RH. Adapted from Cole, Lau, and Patterson [15].

Drop Diameter (µm)	**Frequency**
3.4	0.35
8.5	0.22
17	0.16
34	0.12
85	0.07
170	0.07

To examine the effect of a wider range of particle size distribution and loading density on detection, a theoretical scenario is presented here. Consider an area of 1mm length (leaf electrode spacing) and 170 µm wide (diameter of largest drop in Table 2.4). Assuming equilibrium conditions, the volume of electrolyte over this area can be determined given deliquescent salt loading density and relative humidity. In turn, the volume can be transformed into an equivalent number and size of drops using the distribution in Table 2.4. In an idealized case where all drops are lined up tangentially along the length of this area, detection will occur when the length of the line of drops equals or exceeds the spacing between the electrodes. The time to detection, thus, can be explored as a function of loading density at a certain humidity level.

The results for a case where NaCl is assumed the only contaminant at 90%RH are shown in Figure 2.43. According to Figure 2.43, drops start bridging the grid sensor at loading densities of 1 mg·m^{-2}, while the leaf sensor electrodes are bridged at loadings higher than 7 mg·m^{-2}. The time to detect wetness would be about seven times shorter for the grid as compared to the leaf, given constant deposition velocity. In terms of the Highett site, where it is estimated that 8 mg·m^{-2}day^{-1} salt is deposited [24], it would take a few hours for a cleaned grid sensor to read as wet as opposed to around a day for the leaf sensor. This behavior qualitatively follows that seen in the short exposures discussed above. The experimental results and this analysis show that sensor spacing on the order of that of the grid sensor or smaller would be appropriate for unsheltered conditions at the Highett site for TOW estimation purposes.

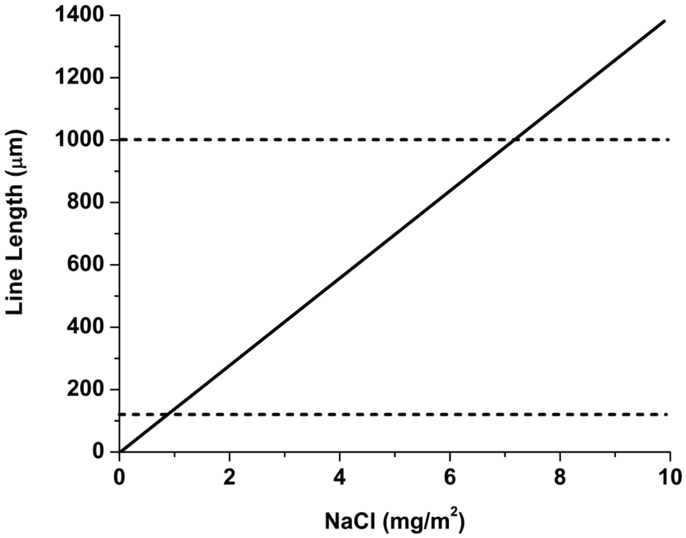

Figure 2.43. Length of line composed of tangentially connected drops as function of NaCl loading density for a 1.00 x 0.170 mm area at 90%RH (solid line). The lower dashed line indicates grid sensor spacing and the upper, leaf sensor spacing.

It is important to point out that the underlying assumptions for the above analysis are highly idealized. It is recognized that increasing the total sensing area (i.e., increasing track length) would probabilistically decrease detection time along with spacing. The analysis also does not account for the presence of fine-mode aerosols (<1 μm diameter). It does, however, bring to light the issue of accurately detecting the wetting contribution of deposited hygroscopic particles.

The discussion above has demonstrated the critical influence of sensor electrode configuration on speed of response, humidity sensitivity, and, in turn, TOW estimates with relation to wetting contributions by hygroscopic aerosols. This issue is one that has received little attention in the literature [13]. At any site with low deposition velocities or high wash-off rates, attention to this matter is imperative for accurate TOW estimations. In all cases, minimizing electrode spacing also minimizes estimation error. A balance, however, must be struck between electrode configuration and robustness and cost limitations of constructing a sensor. The theoretical analysis presented above along with knowledge of deposition velocities, precipitation activity and size distributions of hygroscopic contaminants for a particular site can provide a rough guide for selection of proper electrode spacing.

2.2.4.3 Contaminant Characterization and Behavior

The IC results of the wash-off of surrogate surfaces during the sheltered exposure, Table 2.3, coupled with the coastal marine location of the test site leads to the conclusion that calcium-enriched sea salt was the principle soluble, inorganic contaminant throughout all of the exposures. Calcium enrichment of sea salt is not unique to this site, and it has been established that one common source of excess calcium in marine aerosols is terrestrial dust [29-30].

The grid sensor output and time-lapse micrographs during the RH chamber experiments indicate that the contaminants were wet down to at least 20%RH. Higher contaminant loading densities may have allowed for detection at even lower RH levels. The presence of electrolyte on deposited sea salt aerosols below 20%RH has been reported by a number of investigators and attributed to the low deliquescence and efflorescence points of magnesium and calcium salts [31-33]. The existence of electrolyte at such low humidity levels in marine coastal environments is a phenomenon that deserves further attention. A better understanding of it will aid in developing more realistic humidity thresholds for environmental definitions tailored to such environments.

2.2.5 Conclusions

This investigation examined the comparability of three wetness determination methods for estimating TOW during outdoor exposure. The accuracy of the methods was correlated to actual conditions on the sensors and surrogate surfaces exposed with them. Based on the results of this study, the following conclusions can be drawn:

1. The determination methods utilized in this study did not provide comparable TOW estimates during outdoor exposure for up to three months. This exemplifies the issue that current TOW estimations are a strong property of measurement method and not of location, when, in fact, the opposite should be the case.
2. The comparability and, in turn, accuracy of the wetness sensors utilized was found to be a function of wettability, electrode spacing, aerosol size, and loading density. The grid sensors were more responsive at lower RH levels and lower apparent loading densities of hygroscopic aerosols as compared to the leaf sensors due to finer electrode spacing after periods of wash-off.

3. An idealized theoretical analysis was presented to illustrate the impact of electrode spacing on time to detection for wetness sensors after installation or wash-off events. This analysis could serve as a rough guide for the selection of proper electrode spacing for a particular site, given sensors similar in design to those used here.
4. Utilization of surface RH as opposed to ambient RH for environmental definitions based on humidity thresholds was demonstrated to be a more realistic estimate of surface wetness for boldly exposed outdoor surfaces.
5. Water soluble inorganic surface contaminants at the exposure site were found to consist primarily of sea salt aerosol which remained wet below 20%RH. The 80%RH threshold utilized by the ISO definition was therefore not indicative of the actual wetting conditions. To increase accuracy, environmental TOW definitions must take into account the wetting behavior of sea salt aerosols when utilized for marine environments.

The outcomes of this study have numerous implications for TOW-based structural health monitoring applications and atmospheric corrosion modeling. Utilization of a TOW determination method for health monitoring that inaccurately indicates a surface as dry when indeed it is wet can potentially lead to ignoring active corrosion when it is occurring on a structure. For process-based models, understanding when electrolyte is present and when corrosion can occur is also crucial. Incomparability between TOW methods can be source for error in empirical corrosion models built from multi-site and inter-institutional field data. Although this work has elucidated potential sources of error in current TOW definitions and associated determination methods, a more complete understanding of the wetting behavior of corroded and contaminated surfaces is imperative for their optimization.

2.2.6 References

1. ISO, 9223:1992(E) Corrosion of metals and alloys- Corrosovity of atmospheres- Classification, in, ISO, Geneva, Switzerland, 1992.
2. I.S. Cole, W.D. Ganther, J.D. Sinclair, D. Lau, D.A. Paterson, A study of the wetting of metal surfaces in order to understand the processes controlling atmospheric corrosion, Journal of the Electrochemical Society, 151 (2004) B627-B635.
3. F. Corvo, T. Perez, Y. Martin, J. Reyes, L.R. Dzib, J. Gonzalez-Sanchez, A. Castaneda, Time of wetness in tropical climate: considerations on the estimation of TOW according to ISO 9223 standard, Corrosion Science, 50 (2008) 206-219.
4. L. Veleva, M.A. Alpuche-Aviles, Time of wetness (TOW) and surface temperature characteristics of corroded metals in humid tropical climate, in: H.E. Townsend (Ed.) Outdoor Atmospheric Corrosion, ASTM International, 2002, pp. 48-58.
5. P.J. Sereda, Croll, S.G., Slade, H.F., Measurement of the Time-of-Wetness by moisture sensors and their calibration, in: J.a.E.C.R. S.W. Dean (Ed.) Atmospheric Corrosion of Metals, ASTM, STP 767, American Society fore Testing and Materials, 1982, pp. 267-285.
6. T. Shinohara, S.-I. Motoda, W. Oshikawa, Evaluation of corrosivity of atmosphere by ACM type corrosion sensor, Zairyo to Kankyo/ Corrosion Engineering, 54 (2005) 375-382.
7. F. Mansfeld, J.V. Kenkel, Electrochemical measurements of time-of-wetness and atmospheric corrosion rates, Corrosion, 33 (1977) 13-16.
8. F. Mansfeld, Evaluation of Electrochemical Techniques for Monitoring of Atmsopheric Corrosion Phenomena, in: F. Mansfeld, U. Bertocci (Eds.) Electrochemical Corrosion Testing, American Society for Testing and Materials, 1981, pp. 215-237.
9. P. Norberg, Surface moisture and time of wetness measurements in: J.W. Martin, D.R. Bauer (Eds.) Service Life Prediction Methodology and Metrologies, ACS Symposium Series 805, Amcerican Chemical Society 2001, pp. 23-36.
10. I.S. Cole, W.D. Ganther, D. Lau, Field studies of surface cleaning and salt retention on openly exposed metal plates, Corrosion Engineering, Science and Technology, 41 (2006) 310-320.
11. W. Ganther, P. Norberg, I.S. Cole, Sensors for measuring factors promoting corrosion within the building envelope, in: Proceedings of the 13th International Corrosion Congress Melbourne, Australia, 1996, pp. 411.
12. I.S. Cole, W.D. Ganther, Experimental determination of duration of wetness on metal surfaces, Corrosion Engineering, Science and Technology, 43 (2008) 156-162.

13. E. Schindelholz, R.G. Kelly, wetting phenomena and time of wetness in atmospheric corrosion: a review, Corrosion Reviews doi:10.1515/corrrev-2012-0015 (2012).
14. R.S. Yamasaki, H.F. Slade, P.J. Sereda, determination of time-of-wetness due to condensed moisture, Durability of Building Materials, 1 (1983) 353-361.
15. P.J. Sereda, Characteristics of moisture deposition on corrosion specimens, Materials Research and Standards, 1 (1961) 719-723.
16. I. Shitanda, A. Okumura, M. Itagaki, K. Watanabe, Y. Asano, Screen-printed atmospheric corrosion monitoring sensor based on electrochemical impedance spectroscopy, Sensors and Actuators, B: Chemical, 139 (2009) 292-297.
17. T. Shinohara, S. Tsujikawa, S. Motoda, Y. Suzuki, W. Oshikawa, Evaluation of Corrosivity in Atmospheric Environment by ACM (Atmospheric Corrosion Monitor) Type Corrosion Sensor, in: T. Shoji, T. Shibata (Eds.) International Symposium on Plant Aging and Life Predictions of Corrodible Structures, Sapporo, Japan, May 15-18, 1995, NACE International, Houston, 1997, pp. 453-460.
18. S. Pintos, N.V. Queipo, O. Troconis de Rincón, A. Rincón, M. Morcillo, Artificial neural network modeling of atmospheric corrosion in the MICAT project, Corrosion Science, 42 (2000) 35-52.
19. M. Morcillo, E. Almeida, B. Chico, D. De La Fuente, Analysis of ISO standard 9223 (classification of corrosivity of atmospheres) in the light of information obtained in the Ibero-American Micat project, in, American Society for Testing and Materials, Phoenix, AZ, United states, 2002, pp. 59-72.
20. S.W. Dean, D.B. Reiser, Analysis of long-term atmospheric corrosion results from ISO CORRAG program, in, American Society for Testing and Materials, Phoenix, AZ, United states, 2002, pp. 3-18.
21. D. Knotkova, V. Kucera, S.W. Dean, P. Boschek, Classification of the corrosivity of the atmosphere- standardized classification system and approach for adjustment, in: H.E. Townsend (Ed.) Outdoor Atmospheric Corrosion, ASTM International, 2002, pp. 109.
22. P.C. Sentelhas, J.E.B.A. Monteiro, T.J. Gillespie, Electronic leaf wetness duration sensor: why it should be painted, International Journal of Biometeorology, 48 (2004) 202-205.
23. ISO, ISO 9225: corrosion of metals and alloys- corrosivity of atmospheres - measurement of pollution, in, ISO, Geneva, Switzerland, 1992.
24. W.D. Ganther, T. Muster, Coiled galvanic corrosion sensors for atmospheric corrosion monitoring, in: Corrosion & Prevention 2005, The Australasian Corrosion Association, Kerrimur, 2005, pp. 32:31-11.
25. J.L. Monteith, M.H. Unsworth, Principles of Environmental Physics, 2nd ed., Edward Arnold, London, 1990.
26. T.R. Wilson, Salinity and the major elements of sea water, in: J.P. Riley, G. Skirrow (Eds.) Chemical Oceanography, Academic, Orlando, Fla, 1975, pp. 365-413.
27. W.C. Keene, A.A.P. Pszenny, J.N. Galloway, M.E. Hawley, Sea-Salt Corrections and Interpretation of Constituent Ratios in Marine Precipitation, J. Geophys. Res., 91 (1986) 6647-6658.

28. I.S. Cole, D. Lau, D.A. Paterson, Holistic model for atmospheric corrosion part 6 - from wet aerosol to salt deposit, Corrosion Engineering, Science and Technology, 39 (2004) 209-218.
29. M.O. Andreae, Marine Aerosol Chemistry at Cape Grim, Tasmania, and Townsville, Queensland, J. Geophys. Res., 87 (1982) 8875-8885.
30. T. Suzuki, S. Tsunogai, Origin of calcium in aerosols over the western North Pacific, Journal of Atmospheric Chemistry, 6 (1988) 363-374.
31. I.N. Tang, A.C. Tridico, K.H. Fung, Thermodynamic and optical properties of sea salt aerosols, J. Geophys. Res., 102 (1997) 23269-23275.
32. H.-S. Xiao, J.-L. Dong, L.-Y. Wang, L.-J. Zhao, F. Wang, Y.-H. Zhang, Spatially Resolved Micro-Raman Observation on the Phase Separation of Effloresced Sea Salt Droplets, Environmental Science & Technology, 42 (2008) 8698-8702.
33. D.J. Cziczo, J.B. Nowak, J.H. Hu, J.P.D. Abbatt, Infrared spectroscopy of model tropospheric aerosols as a function of relative humidity: Observation of deliquescence and crystallization, Journal of Geophysical Research, 102 (1997) 18843-18850.

3 Methods Development

This chapter details two methods that were developed for both rigorous production and study salt of hygroscopic behavior of salt microparticles on the size order of coarse-mode aerosols (>1 μm). The first section demonstrates the use of an inkjet printing method for controlled, high-throughput loading of aqueous salt droplets on substrates. The second section describes an electrical impedance method for measurement of deliquescence (solid to liquid) and efflorescence (liquid to solid) phase transitions of hygroscopic salt particles. The inkjet instrument built for this work is also described in this section. These methods and inkjet instrument served as the basis of the experimental approach utilized in the work reported in the last chapter.

3.1 Application of Inkjet Printing for Depositing Salt Prior to Atmospheric Corrosion Testing

This study examined the feasibility of using an unmodified office inkjet printer for precise deposition of soluble salt particles on planar metal samples for atmospheric testing. The density of salt loading achieved in printing solid swathes ranged from 10 – 180 $\mu g \cdot cm^{-2}$ using aqueous 1M and 4M NaCl solutions with 95% confidence intervals $\leq$ 2 μg per print. Printing these solutions on a steel coupon produced particles with a multimodal size distribution and mean Feret's diameters $\leq$ 11 μm. An application of the method for studying the effect of loading density on the atmospheric corrosion of steel is described.

3.1.1 Introduction

This study examined the feasibility of using piezoelectric inkjet printing for rapid, precise and controlled loading of soluble salt particles on metal samples for atmospheric corrosion testing. Loading a metal specimen with well-dispersed particles of salt, such as

NaCl, prior to exposing it to a controlled atmosphere is common practice in materials performance and phenomenological studies in atmospheric corrosion. A frequently used method for depositing salt involves pipetting arrays of microliter-sized drops of salt solution on a sample surface followed by evaporation of the drops. This method tends to be tedious and can suffer from the imprecision of the pipette utilized. More advanced techniques have been developed for depositing salt particles for atmospheric testing, but their use is limited to specific applications [1-2]. The application of inkjet technology for particle deposition can provide a more general alternative to current methods.

Piezoelectric inkjet printing is now commonly utilized in a number of research and industrial fields for processes requiring precision and accuracy in depositing fluid droplets down to femtoliter volumes [3-5]. Many of the industrial processes utilize commercial inkjet systems that can cost upwards of tens of thousands of dollars. A number of investigators, however, have demonstrated the use of modified or unmodified consumer desktop inkjet printers costing hundreds of dollars for research-scale processes [6].

This paper reports on the testing of an unmodified desktop piezoelectric inkjet printer for depositing NaCl particles onto corrosion test samples. The main objective of the study was to characterize the precision of the printing process and the effect of solution concentration and print pattern on particle distribution and loading density. Patterns were created using a drawing program and printed using NaCl solutions onto plastic and metal surfaces. The range of salt loading produced from arrays of solid square elements printed with two different salt solution concentrations was determined. Additionally, the effect of solution concentration on particle size and distribution was observed. As an example application, arrays of varying density NaCl patches were printed onto a steel coupon. The coupon was exposed to high humidity conditions and then examined.

3.1.2 Experimental

3.1.2.1 Printer and Software

An Epson Artisan 50 consumer inkjet printer was chosen for this study due to its low cost (≈100USD). The CD printing feature allowed for loading planar samples up to 12 x 12cm and 4mm thick without modification. The manufacturer specifications state that the printer disperses 5 different controlled drop sizes with the smallest being 1.5 picoliters. Third-party refillable cartridges were installed in the printer for the salt deposition process. All but the black refillable cartridges were rinsed thoroughly, and then filled with ultrapure water (18.2 $M\Omega\cdot cm^{-2}$). A set of black refillable cartridges were rinsed and filled with 1M and 4M NaCl solutions in ultrapure water. Vector drawing software was used to create print patterns and the Epson printer driver was used to control the printer. All prints were carried out in gray scale and using maximum dpi settings.

3.1.2.2 Loading Density

A pattern was constructed that consisted of six $1cm^2$ solid black, 100% opacity box elements, arranged in 2 columns and 3 rows. The pattern was printed onto a set of Parafilm thermoplastic (Pechiney Plastic Packaging Company) coupons adhered to a CD, such that each element of the pattern was laid down on a separate coupon. The pattern was printed five times for each solution concentration, resulting in a total of 60 prints of the individual boxes. An additional set of 30 prints was created to examine the effects of opacity on loading density. The box pattern was modified by varying the opacity levels of each box from 0.1 to 1.0 in the drawing software and printing three replicates at each step. Printing of the modified pattern onto sets of Parafilm coupons was carried out using 1M solution.

The amount of salt on each of the printed coupons was measured by rinsing in ultrapure water and measuring the conductivity of the analyte. The repeatability of the measurement process was examined by carrying out the same measurement 3 times for randomly assigned samples.

3.1.2.3 Particle Size and Distribution

A pattern consisting of a solid swath of 0.4 opacity black was printed using 1M and 4 M NaCl solutions onto a steel coupon and microscopically examined to determine particle size and distribution over the printed surface. An Al29-4C super ferritic stainless steel coupon measuring 2 x 6 cm by 0.2 cm was ground and polished to a 0.1 μm diamond suspension, followed by degreasing in organic solvents and rinsing in ultrapure water. Duplicate prints for each solution concentration were made. Between each printing, the coupon was examined and then cleaned as above. A Jeol 4600F scanning electron microscope was used to examine the coupon in secondary electron imaging modes. Images of five randomly selected areas were captured at 500x magnification and analyzed using the particle analysis modules in Image-J software (NIH).

3.1.2.4 Example Application

Duplicate 3x3 matrices consisting of 1cm^2 block elements were printed on a 1018 carbon steel coupon using 4 M NaCl solution. The mill-finished coupon measured 8 x 9 cm and was degreased in organic solvents followed by rinsing in ultrapure water prior to printing. The opacity of each block in the matrix pattern was varied resulting in a loading gradation of NaCl ranging from 32 to 139 μg-cm^{-2}. After printing, the coupon was exposed to 80% RH at 25^{o}C for 16 hours.

3.1.3 Results and Discussion

3.1.3.1 Loading Density

Loading was found to be affected by solution concentration and pattern opacity. The 1M solid square prints were produced with loading densities of 59 ±1 μg·cm^{-2} NaCl (95% confidence) while the 4M solid squares produced 170 ±2 μg·cm^{-2}. The standard deviations of these print elements was 4 and 6 μg·cm^{-2} respectively. The standard deviation of the analysis method, determined by repeated measurements, was 3 μg per print element, indicating that some of the uncertainty in the loading results may due to the analysis rather than the print process. The results of printing the square pattern at varying opacities revealed a strong linear correlation between opacity and loading density, as seen in Figure 3.1. The results of these experiments indicate that the loading process could be tuned to precisely produce virtually any loading density by varying the print pattern, solution concentration and number of repeated printings.

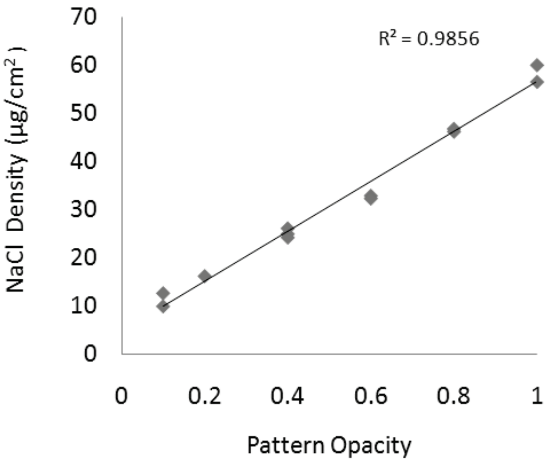

Figure 3.1. Loading density versus opacity of the square block pattern printed with 1 M aqueous NaCl solution.

3.1.3.2 Particle Size and Distribution

The results of the particle analysis indicate that solution concentration affects the size of the particles, as might be expected. A total of 263 particles were counted in the set of images analyzed from the 1M prints and 228 for the 4M prints. Observations of up to 5000x indicated relatively few particles under 0.5 µm diameter, which were not counted. The mean Feret's diameters of the counted particles were found to be 7 µm and 11 µm for the 1M and 4M solutions respectively. The distribution of particle size appears to be multimodal as reflected in Figure 3.2**.** These modes were found to be related to the different controlled drop sizes that the printer was capable of producing.

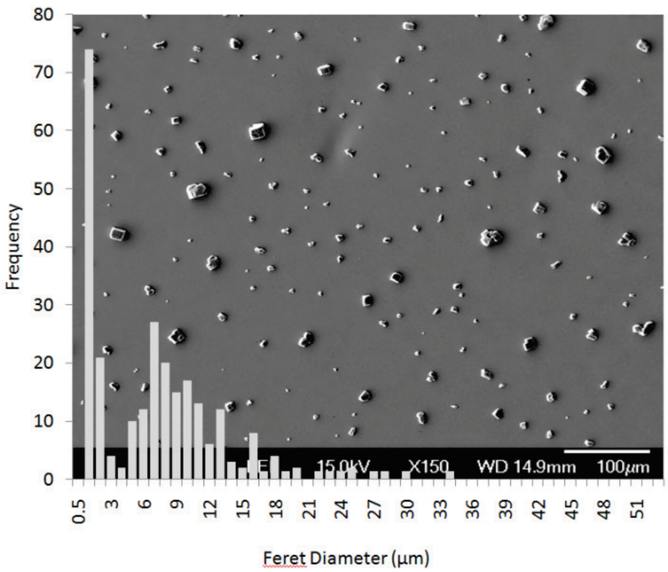

Figure 3.2. A histogram of measured particle sizes for the 1M, 40% opacity prints overlaid on an SEM image of a typical particle field resulting from these prints.

3.1.3.3 Example Application

The printed steel coupon was visually inspected after exposure, Figure 3.3**.** Interestingly, the lower salt density blocks appeared to have corroded more than the higher density blocks, based on rust coverage. This observation counters a common conjecture that the enhanced corrosivity of near-shore marine environments is primarily due to high salt loadings. Given the relatively short time of exposure and qualitative nature of the observation, further investigation is needed to elucidate this matter. Regardless, this application demonstrates the utility of inkjet printing for factorial testing.

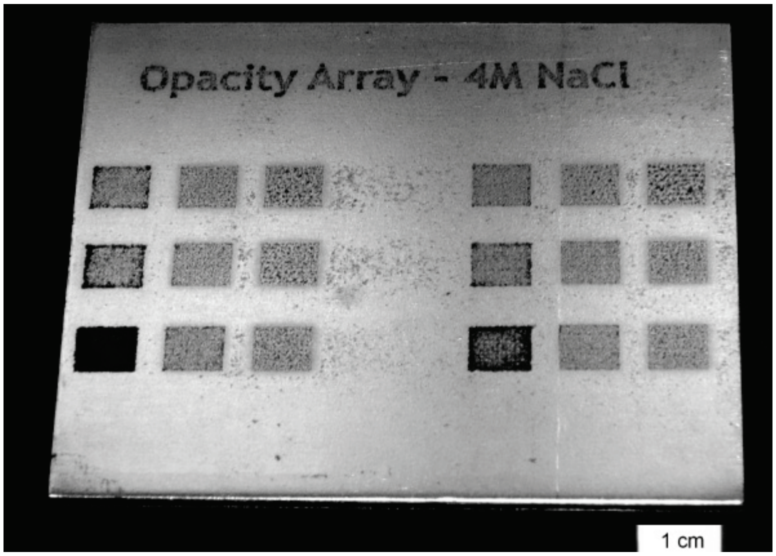

Figure 3.3. Steel coupon with duplicate prints of a NaCl density array after exposure to 80% RH for 16 hours. NaCl loading density increases from bottom to top and left to right, with 32 µg·cm^{-2} in the lower left and 139 µg·cm^{-2} in the upper right.

3.1.4 Conclusions

This study has demonstrated the application of piezoelectric inkjet printing for precise, quick and low-cost loading of NaCl particles on metal substrates for atmospheric testing. The loading densities achieved ranged from 10 - 180 µg·cm^{-2} using 1M and 4M aqueous NaCl solutions with high precision. Results indicate that the loading process could be tuned to produce virtually any density. Solid swathes of 1M and 4M solutions printed on a stainless steel coupon produced salt particles with a multimodal size distribution and mean Feret's diameters of 7 and 11 µm respectively.

The results of this study, although limited to a specific process and set of parameters, have more general applicability. The printer used restricted the maximum size of the substrate to be printed on to the dimensions of a CD. A number of other researchers have reported on the modification of consumer printers similar to the one used here to print on substrates of virtually any dimension [7]. The particles deposited were found to have a multimodal distribution related to the varying drop size put out by the printer. Drop size, hence particle size, could be controlled by modifying the printer or through the use of a commercial research inkjet system [4,7]. Although this study was restricted to NaCl solutions, other types of corrodants or even chemical indicators could be printed on a surface. The speed and precision of the process could be utilized in atmospheric experiments that require numerous replicate samples, such as screening to examine the effect of electrolyte constituents.

3.1.5 References

1. R.P. Frankenthal, R. Lobnig, D.J. Siconolfi and J.D. Sinclair, *J. Vac. Sci. Technol. A, Vac. Surf. Films*, 11, 2274 (1993).
2. H. Masuda, *J. Jpn. Inst. Met.,* 70(9), 780 (2006).
3. S.E. Burns, P. Cain, J. Mills, J. Wang and H. Sirringhaus, *MRS Bull.,* 28(110), 829 (2003).
4. T. Fukushima, K. Nishio and H. Masuda, *Electrochem. Solid-State Lett.,* 13(4), C9 (2010).
5. Y. Hua-Zhong, C. Hanjin and M. Parameswaran, *Sens. Actuators, B,* 123(2), 749 (2007).
6. S. Towne, V. Viswanathan, J. Holbery and P. Rieke, *J. Power Sources*, 171(2), 575 (2007).
7. J. G. Zhou, A. Addison, Z. He and F. Wang, *Mater. Des.*, 26(8), 670 (2005).

3.2 Hygroscopic Particle Behavior Studied by Interdigitated Array Microelectrode Impedance Sensors

The hygroscopic behavior of soluble salts bears importance in many research fields including atmospheric sciences, corrosion, porous building materials, and pharmaceuticals. Several methods have been used to study deliquescence (solid to liquid) and efflorescence (liquid to solid) phase transitions of these salts. In this study, we measured the deliquescence and efflorescence RH values of single salt microparticles deposited on an interdigitated microelectrode sensor via electrical impedance. The salts examined were NaCl, LiCl, NaBr, KCl, and $MgCl_2$. Measured values were in agreement with in-situ optical microscopic observations and, with the exception of $MgCl_2$, literature values. In the case of $MgCl_2$, deliquescence occurred at 33%RH and 12-15%RH, with the latter range being previously unreported. The depressed deliquescence RH was hypothesized to be a result of the formation of a metastable $MgCl_2$ hydrate. Incomplete efflorescence of $MgCl_2$ was also observed after exposure to <1.5%RH for up to 22 hours due to formation of solid shells which trapped fluid. The phenomena elucidated by these results provide explanation for the anomalous water retention and uptake behavior of $MgCl_2$ below 33%RH reported elsewhere in the literature. The results presented in this study validate the use of this method as an alternative or complementary method for study of bulk phase transitions of substrate-deposited particles across a broad RH range. These findings also demonstrate the utility of this method for detection of fluid trapping which cannot be directly ascertained by gravimetric and line-of-sight techniques commonly used in the study of hygroscopic particles.

3.2.1 Introduction

This paper reports on the development and evaluation of an electrical impedance method utilizing interdigitated electrode (IDE) array sensors for the study of the hygroscopic behavior of soluble salt particles. Specifically, the impedance behavior of an IDE sensor loaded with inorganic salt microparticles down to the size range of coarse mode tropospheric aerosols is characterized and deliquescence (solid to liquid) and efflorescence (liquid to solid) phase transitions determined with respect to relative humidity (RH). The hygroscopic behavior of soluble salts bears importance in many fields including pharmaceuticals [1-2], porous building materials [3-4], corrosion [5-7] and atmospheric sciences [8-11]. Regarding the latter, tropospheric aerosols and their constituent chemistries have received extensive attention due to their governance of the chemistry and dynamics of the atmosphere and climate [10, 12-13].

A number of complementary methods have been developed for the study of phase transitions and hygroscopic growth of tropospheric aerosols and other environmental particles. Thorough reviews of the extent of this work have been published [14-16]. In short, gravimetry, optical spectroscopy, microscopy, and particle sizing comprise the general categories of instrumental methods commonly utilized. Gravimetric [8, 17-18] and particle-sizing [19-21] methods are used to track relative mass or dimensional change of particles in response to varying RH. Changes in chemical structure or bonding are utilized as indicators of phase transitions using spectroscopic methods, such as Raman and FTIR spectroscopy [22-24]. Microscopic methods, such as environmental electron microscopy, are used to track morphological changes associated with water uptake and evaporation [25-27]. Variants of many of these general approaches have been developed for the study of single particles or groups of particles both airborne and deposited on a substrate [27-32]. Like all instrumental techniques, each has advantages and disadvantages. For example, although gravimetric and particle-sizing methods enable quantification of water uptake, they generally cannot be used to distinguish between water existing in hydrated compounds and water that has been entrained in partially effloresced solids [8, 18].

Electrical conductance methods have also been utilized for laboratory study of hygroscopic compounds, but use has largely been restricted to macroscopic samples. It is well known that the impedance of many solid insulators decreases with increasing humidity [33, 34]. For ionic solids, water sorption can increase surface conduction by means of ion solvation. Simkovich [35] and later Hucher [36] took advantage of this to characterize the surface sorption of water on NaCl. They did so by monitoring changes in DC resistance measured across electrodes attached to cleaved monolithic crystals of these substances. Through these investigations, they were able to establish the effect of relative humidity on the location and amount of sorbed water for defined orientations. Their findings were subsequently confirmed by other investigators using complementary methods [37-39].

In addition to study of surface sorption phenomena, relative changes in electrical impedance have been utilized for the determination of deliquescence and efflorescence [40-41]. Yang demonstrated the use of single frequency impedance measurements across electrodes bridged by salt-doped filter paper for determination of the deliquescence relative humidity (DRH) of single and mixed inorganic salts [40]. Deliquescence was marked by a large drop in impedance caused by formation of bridging electrolyte.

Determinations using this method were in agreement with theoretical and literature values for the salts examined. The authors, however, conceded a major disadvantage of their approach was that long hold times (up to 24 hours) were necessary to allow for equilibration between changes in humidity due to the effects of the filter paper and the relatively large amount of saturated salt solution used to dope it (500µl). In another study, impedance was measured across 2 µl drops of salt solutions suspended between polished platinum electrodes while varying RH and monitoring with an optical microscope [41]. Using the impedance response coupled with visual appearance, the authors reported efflorescence relative humidity (ERH) and DRH values for several inorganic salts. In all cases the DRH values were at least 10%RH higher than the well-established values for these salts, which the authors attributed to surface roughness of the electrodes. Substantial evidence exists, however, that suggests the surface geometry and particle sizes used in their study likely had little effect on DRH [8, 42]. Given impedance measurements seemed to track with morphological changes, probable alternative causes is insufficient equilibration time between changes in humidity (up to 30min in their case) or possibly inaccurate calibration of the RH sensor utilized.

Nonetheless, these investigators have demonstrated the applicability of electrical impedance methods for the determination of deliquescence and efflorescence. Impedance methods offer convenience in terms of relatively simple instrumentation and have been shown to be highly sensitive to both liquid-solid transformations and detection of small amounts of water associated with effloresced crystals. Like most methods that utilize sequestered particles on substrates, the impedance approaches discussed above allow for coupling of complementary instrumentation, such as optical microscopy, for study of singular particles or identical samples. Another advantage of substrate methods is that it allows for extended exposure of particles to examine the effects of aging or slow drying kinetics, something difficult to achieve in most aerosol-based approaches, which have short residence times [8,29].

Here we report, as extension of the work discussed above, on the development and characterization of an impedance method for determination of DRH and ERH of substrate-deposited microparticles. An interdigitated micro-electrode sensor was employed to measure impedance across these particles. Interdigitated electrode (IDE) sensors are commonly used for moisture sensing applications ranging from RH sensors that detect water uptake of hydrophilic film coatings [43-45] to meteorological dewing and precipitation sensors that detect relatively large droplets of water [5,46-47] To our knowledge, utilization of IDE sensors for laboratory study of hygroscopic particles down to the size range of coarse mode tropospheric aerosols is unique. Aside from extending applicability to study of small environmental particles, reducing particle size also allows for reduction in equilibration times during humidity response and examination of efflorescence behavior. The specific objectives of this work were to: 1. Characterize the impedance behavior of the sensor with respect to the physical state of deposited inorganic salt particles; 2. Evaluate the feasibility and accuracy of this method for determination of DRH and ERH of single salts.

In this study, impedance measurements across a frequency range of 0.2 to10^6 Hz were utilized to evaluate the electrical characteristics of a sensor loaded with NaCl particles and relate humidity response to the physical state of the particles as observed by in-situ optical microscopy. From this, two measurements frequencies were selected which best represented the deliquescence and efflorescence behavior. Deliquescence and efflorescence RH determinations were made by measuring impedance at these two frequencies for NaCl, KCl, NaBr, LiCl and $MgCl_2$ during humidity cycling. Determinations were compared to microscopic observations and literature values. The hygroscopic behavior of $MgCl_2$ was explored in further detail to elucidate its anomalous humidity response and to demonstrate the utility of this method for detection of fluid entrapment resulting from efflorescence.

3.2.2 Experimental Methods

Commercial sensors consisting of an interdigitated pair of platinum electrodes arranged in a comb pattern on a fused quartz substrate were used (ALS Co., Tokyo). Each of the pair had 65 digits which measured 2 mm long by 10 μm wide and 0.1 μm in height. Spacing between the digits was 3 μm. The sensors were cleaned using a heated base piranha solution (3:1:1 ammonium hydroxide, hydrogen peroxide, and water) followed by soaking and rinsing in ultrapure (UP) water (18.2 MΩ·cm, <5 ppb TOC, 0.2 μm particulate filter). Immediately prior to use, the sensors were dried in a stream of 99.99% pure nitrogen gas. These steps were taken to reduce possible contaminants on the sensor surfaces that could potentially alter the hygroscopic behavior of the salt deposits during the experiments. The cleaned sensor surfaces were found to be hydrophobic in nature, with sessile UP water drops deposited on them exhibiting contact angles of approximately 75 degrees.

Saturated salt solutions of NaCl (99.999%), NaBr, KCl and LiCl (>99%) along with $MgCl_2$ (99.995%) were prepared using UP water. A 5 mM solution of NaCl in ethanol (>99.5%) was also prepared. All salts were acquired from Sigma Aldrich. The solutions were passed through a 0.2 µm particulate filter into cleaned borosilicate glass reservoirs after preparation.

Droplets of the saturated salt solutions were deposited onto the sensors inside an environmental chamber using a piezoelectric inkjet print head (Microfab Technologies, Plano, Texas), Figure 3.4. The solution pathway during the printing consisted of PEEK tubing and a 50 µm borosilicate glass capillary which was part of the jet head. Prior to the start of an experiment, 200-300 droplets of approximately 20pL in volume (~35 µm airborne saturated solution diameter, ~100 µm deposited diameter) were deposited onto the sensor area in a square matrix pattern with the aid of a programmable 2-axis stage, Figure 3.4. This particle size was chosen to ensure morphological changes of the particles were readily apparent during the optical microscope observations described later. In one set of experiments involving MgCl$_2$, the inkjet was also used to create a 3µL droplet that completely covered the sensing area.

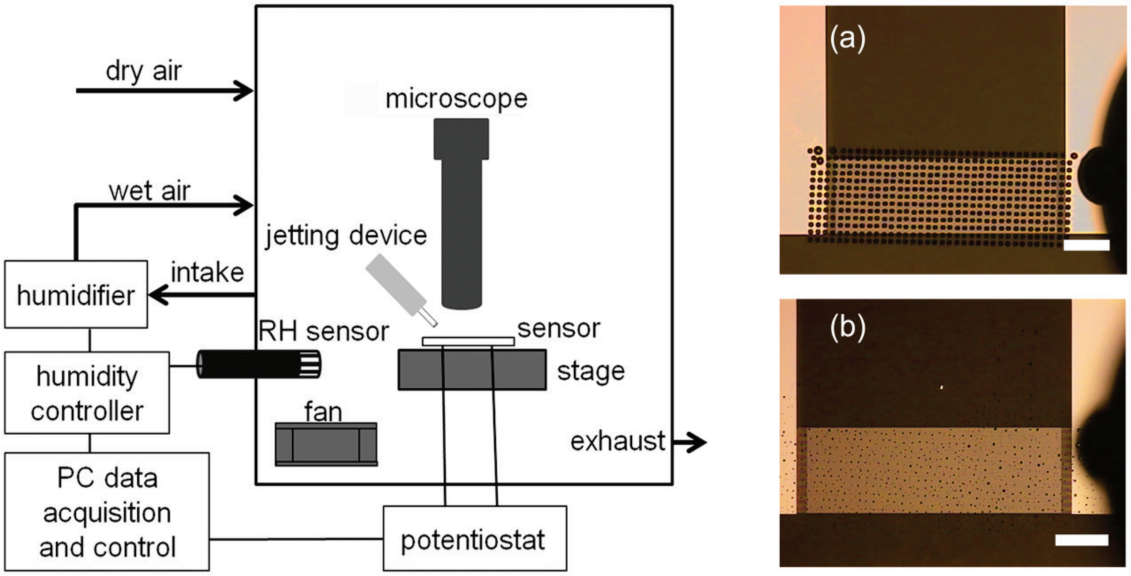

Figure 3.4. Left, schematic of experimental setup used in this study. Right, top-down views of the interdigitated area of the sensor loaded with (a) 100 µm droplets and (b) 1-25 µm NaCl droplets. The profile (black) of the jetting device in the foreground is on the right in these images. Scale bar is 500 µm wide.

An additional experiment was carried out where droplets of the ethanolic NaCl solution were jetted onto the sensor to create much smaller particles representative of the coarse mode tropospheric aerosol size range. When the ethanol had evaporated from the deposits on the sensor and they were rewet to 76%RH (saturated NaCl solution), the resulting droplets ranged in diameter between 1 and 25 μm, with a mode of 15 μm, Figure 3.4b. The NaCl loading density was 8 $\mu g \cdot cm^{-2}$ in this experiment.

Experiments were carried out over a range of RH within a clean environmental chamber. Trace contaminants and water vapor were removed from feed air by filtering through activated charcoal, 4Å molecular sieves, and a 0.01 μm coalescing filter. Clean feed air was pumped through the chamber at 8 $L \cdot min^{-1}$ to maintain slight positive pressure. Humidity was controlled and logged using an ETS5100 programmable humidity control system (Electro-Tech Systems), which was comprised of a PID controller, a calibrated RH sensor and a recirculating air ultrasonic humidifier filled with UP water. The RH sensor had a manufacturer-stated accuracy of ±1.5% RH under the exposure conditions of this study.

Clean and salt-loaded sensors were exposed to humidity ramping in the environmental chamber while measuring impedance and taking optical micrographs. Impedance was measured across the sensors using a two-electrode configuration with a Parstat 2263 potentiostat (Princeton Applied Research). Potentiostatic impedance was measured across a frequency range of 0.2 to 10^6 Hz. An excitation voltage of 20 mV versus open circuit was used. Measurements were taken at four minute intervals during the humidity ramping experiments. Morphology was measured via a digital reflected light optical microscope trained on the sensor. The resolve limit of the microscope was 0.6μm.

Images were taken at four minute intervals during the experiments. All experiments were carried out at ambient lab temperature, 294±1°K.

3.2.3 Results and Discussion

3.2.3.1 Clean Sensor Response

Impedance measurements were carried out across a blank, clean sensor during cycling of the environmental chamber from <1.5%-87%RH. This was done to establish the limits of the potentiostat in its experimental configuration and the baseline RH response of the sensor. A comparison of spectra taken across the RH range indicates little variance in impedance response at all but the lowest frequencies, Figure 3.5. Examination of the measured phase angle as a function of frequency revealed consistent measurement artifacts above 26 kHz and noise below 100 Hz. A plot of Impedance at the highest frequency that lacked significant artifacts (26 kHz) and the lowest frequency (0.2 Hz) versus RH exemplifies the range of noise realized through the humidity cycling experiment and the effect of RH, Figure 3.6. Linear fits to these data show a general drop in low frequency impedance from 0 to 87%RH of $1.49*10^9$ Ω (8% change) and a drop in high frequency impedance of 931 Ω (0.6% change).

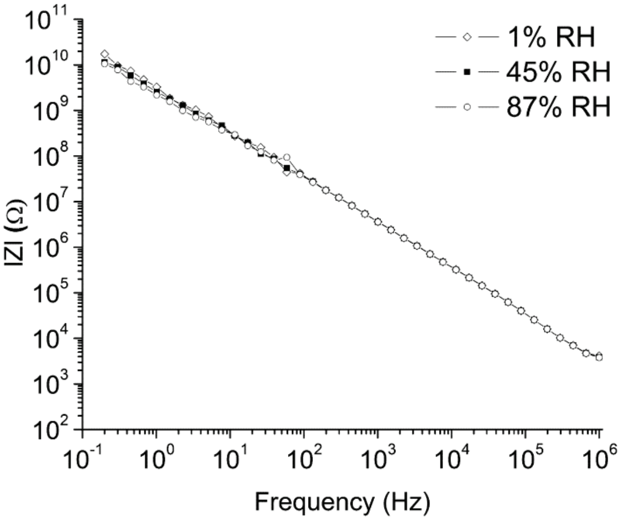

Figure 3.5. Modulus of impedance measured across a blank sensor at several RH points.

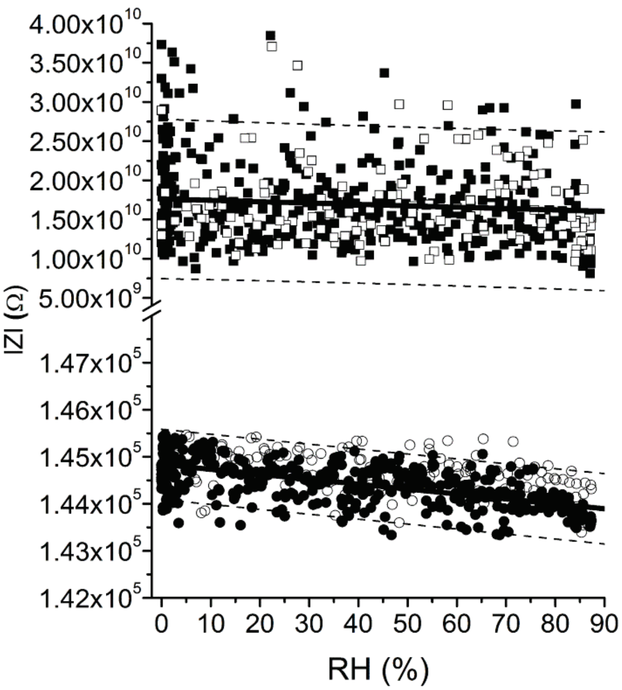

Figure 3.6. Modulus of impedance measured at 0.2Hz (circles) and 26kHz (squares) across a blank, clean sensor during humidity cycling from 0-87%RH. The open symbols indicate impedance during dehumidification and the closed symbols indicate measurements taken during humidification. Linear fits to this data are indicated with solid lines along with the 95% prediction bands (dashed lines) for these fits.

The clean sensor spectra represent the stray impedance of the potentiostat and experimental setup. Noise seen in the spectra below 100 Hz is attributed to electrostatic interference from the surrounding environment. Measurement artifacts above 26 kHz were related to the internal impedance of the instrumentation [48]. The drop in impedance with increased relative humidity was due to water sorption on the sensor surface which allowed a certain amount of conduction between the electrodes. This is a well characterized behavior that is taken advantage of in RH sensor technologies [49]. The lowest frequencies were most sensitive to RH, because they had the highest dynamic range in impedance.

3.2.3.2 NaCl Loaded Sensor Response at 0.2 Hz to 1 MHz

A sensor loaded with ~100 μm diameter NaCl droplets was subjected to a humidity cycle ranging 3-80%RH while measuring impedance and taking time-lapse micrographs. The humidity profile utilized consisted of 1%RH steps each of 30 min duration during dehumidification followed by drying to low RH and then 20 min per 1%RH during humidification around the phase transition points, Figure 3.7. Impedance spectra measured during the dehumidification ramp along with corresponding micrographs are given in Figure 3.8. Impedance at all frequencies remained virtually independent of RH at and above 52% during dehumidification, and only liquid was visible. A jump in impedance was observed when humidity fell between 52 and 50% followed by a much larger jump between 50 and 49% at all frequencies, which corresponded to crystallization of the drops. Real-time observation of this process revealed that transformation time from Figure 3.8 drop to crystal for each of the deposits was only a few seconds. After crystallization, and below 49%RH, impedance at the higher frequencies was the same as that measured across the blank sensor. Impedance at the lower frequencies exhibited a knee region which shifted down the frequency range with decreasing RH until it was indistinguishable from that measured across the blank sensor, below 32%. During humidification, the knee region reappeared and moved to higher frequencies with increasing RH, Figure 3.9. A large drop in impedance at all frequencies was notable between 75 and 77% and corresponded to the visual deliquescence of the drops, Figure 3.9.

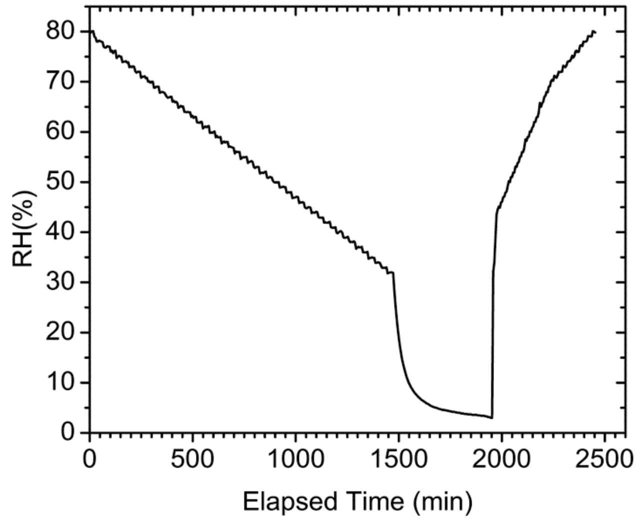

Figure 3.7. Recorded humidity profile during NaCl humidity cycle experiment.

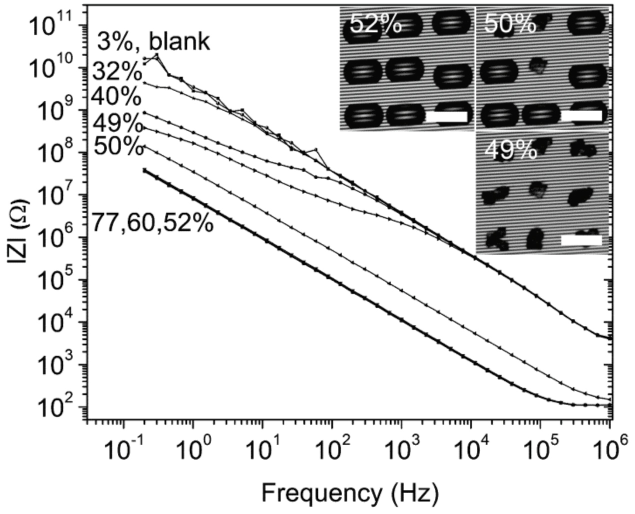

Figure 3.8. Impedance spectra at select RH points measured across a sensor loaded with NaCl particles during the dehumidification ramp. The spectrum labeled “blank” is that of the unloaded sensor at 45%RH. Inset micrographs show the state of the particles during some of these measurements. Scale bars are 150 μm wide.

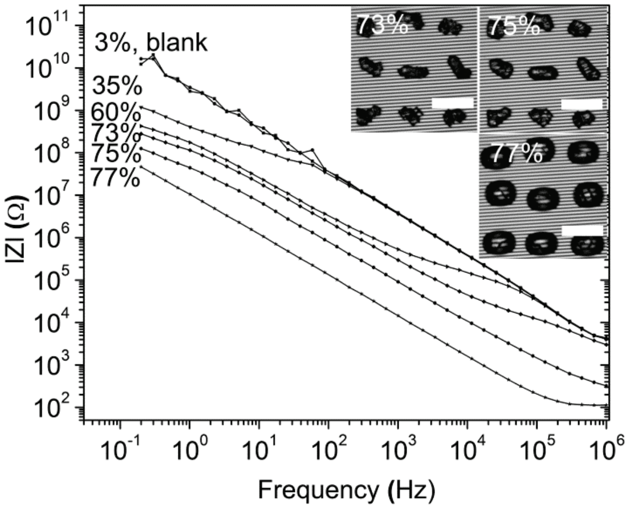

Figure 3.9. Impedance spectra at select RH points measured across a sensor loaded with NaCl particles during the humidification ramp. The spectrum labeled "blank" is that of the unloaded sensor at 45%RH. Inset micrographs show the state of the particles during some of these measurements. Scale bars are 150 μm wide.

These results indicate that this method can be utilized for tracking bulk phase transitions of NaCl particles. The large shifts in |Z| at all frequencies in the spectra correlate with visual observations of deliquescence and efflorescence, which will be discussed in more detail later. From Figures 3.8 and 3.9, it is clear that impedance measured at any single frequency could be used to track these transitions. Measurements at the highest frequencies, however, appear to be more indicative of the transitions as they exhibit the greatest dynamic ranges in impedance, especially during efflorescence.

In addition to phase transitions, the impedance data also qualitatively reflect the state of electrolyte on the surface of, or in conjunction with, the effloresced particles. During humidification but prior to deliquescence, the decreasing impedance observed is attributed to water adsorption and capillary condensation as has been demonstrated by others [35-36]. The characteristic movement of the knee region from lower to higher frequencies during humidification is a reflection of increased shunting of the stray impedance by the increasingly conductive pathways through the electrolyte and across a growing electrolyte/electrode (double layer) interface. Here the stray impedance (blank and 3% spectra in Figure 3.9) is characteristic of an ideal capacitor, where |Z| is inversely proportional to frequency with a slope of negative one. The double layer interface acts as a non-ideal capacitor, as manifested by the presence of negative slopes of less than one in the linear portion of all of the spectra which lay below the stray impedance (spectra >3%RH in Figure 3.9). Non-ideal behavior (i.e., slope not equal to one) of the double layer is commonly observed in electrochemical systems and is often attributed to contributions from electrode geometry and surface heterogeneity [48, 50]. Aside from differences in slope, the decrease in intercept of the linear portions of the spectra in Figure 3.9 reflects the relative increase in the capacitive dispersion of the double layer which is approximately proportional to electrolyte coverage. The large drops in intercept seen between 73 and 77% are largely indicative of significant changes in electrolyte coverage. During dehumidification, Figure 3.8, similar but opposite trends are apparent and reflect decreasing electrolyte coverage and increasing electrolyte resistance subsequent to efflorescence. The relatively small changes in impedance with RH when the particles are in a deliquesced state, 77%, 60%, and 52% curves in Figure 3.8, reflects the comparatively small changes in electrolyte coverage (droplet perimeter remains pinned until efflorescence) and the negligible impact of the expected changes in solution resistance on impedance as it dries.

In the remainder of the paper, normalized |Z| measurements at 0.2 Hz and 26 kHz will be reported and used to track the hygroscopic behavior of the deposited salts. The former measurement frequency was chosen as it was most sensitive to the presence of small amounts of electrolyte, as per the discussion above. The latter measurement frequency was used because it was more indicative of bulk phase transitions and is one of the highest frequencies that did not exhibit instrument artifacts. Measured impedance values were normalized to deconvolute the impedance contribution of the deposited particles from the humidity response of the sensor itself and noise realized during measurements. To normalize the measurements, impedance at 26 kHz was divided by $1.45 \cdot 10^5\ \Omega$ and that measured at 0.2 Hz was divided by $6.00 \cdot 10^9\ \Omega$. These divisors are the lowest values of the prediction bands for the two frequencies achieved during humidity cycling of the blank sensor, Figure 3.6. Thus, any normalized impedance value below unity would indicate significant admittance contribution from the particles themselves.

3.2.3.3 NaCl Loaded Sensor RH Response at 0.2 Hz and 26 kHz

The results of the NaCl experiment presented thus far along with those from replicate experiments using the same and smaller size particles are cast in terms of normalized impedance measured at 0.2 Hz and 26 kHz versus RH, Figure 3.10. In all cases, sharp transitions marking deliquescence and efflorescence at 76-77% and 51-49 %RH respectively are evident. The largest dynamic range in |Z| during both events was realized in the 26 kHz measurements. The deliquescence-efflorescence hysteresis region lies between these two transitional events and is marked by impedance at a minimum baseline and only liquid drops visually present.

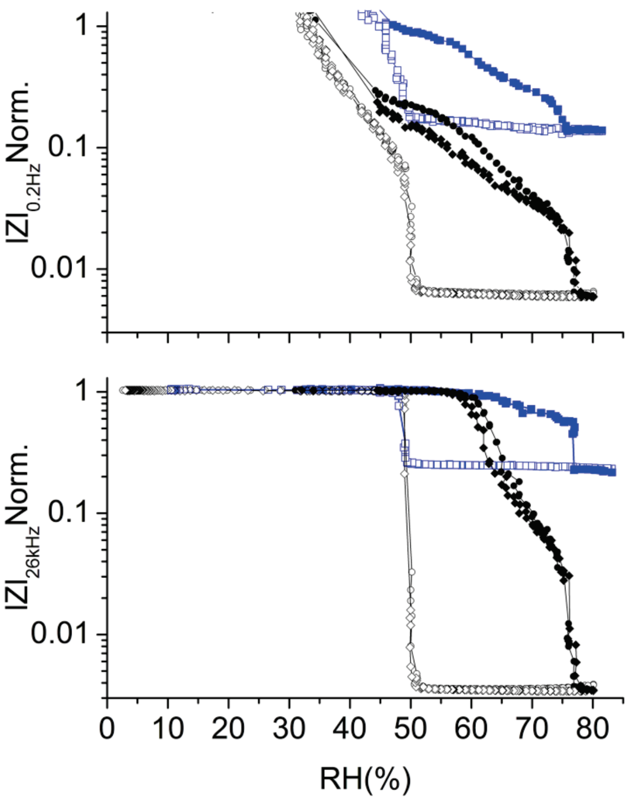

Figure 3.10. Impedance measured at 26 kHz (top) and 0.2 Hz (bottom) as a function of RH during replicate NaCl experiments. The black diamond and circle symbols are for duplicate experiments using a sensor loaded with ~100 µm particles and the blue square symbols are for an experiment using a sensor loaded with 1-25 µm particles. In all cases, the open symbols indicate impedance during dehumidification and the closed symbols indicate measurements taken during humidification.

Closer examination of the impedance behavior during dehumidification for one of the larger particle experiments shows the rise in impedance between 51 and 49%RH, which tracked with visual observation of droplet crystallization, Figure 3.11. A small fraction of the particles in the field of view of the microscope (3 of 38) also crystallized at 52%RH, prior to the large jump in impedance. It is evident that during the 50%RH step, the number of crystallized particles did not level off with time. Increasing the step duration may have allowed all particles to crystalize within this step.

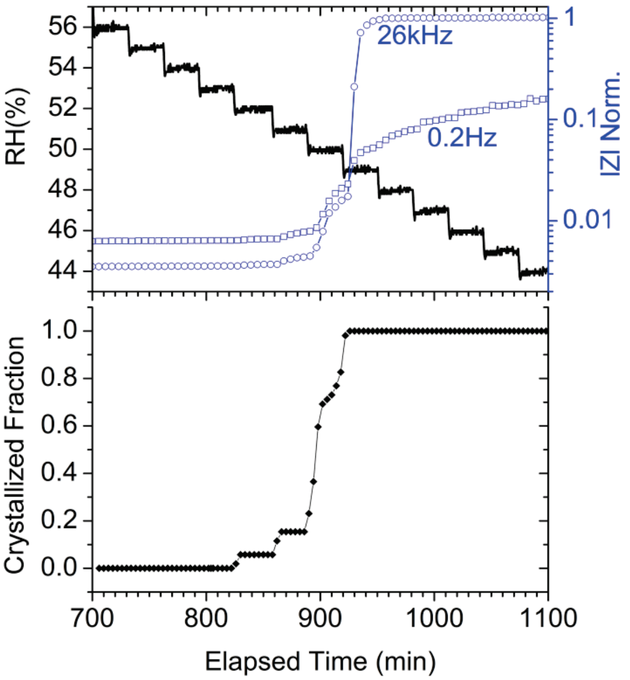

Figure 3.11. Measured impedance response and RH (top) during dehumidification of a sensor loaded with ~100 µm diameter NaCl particles along with fraction of drops crystallized as evidenced by optical micrographs (bottom).

The impedance behavior during humidification in this same experiment is seen in Figure 3.12. The sharp drop between 75% and 77% followed by a flat-line at a relative minimum in |Z| at both frequencies tracked with visual deliquescence. Microscopic examination also indicated that solid-liquid transformation was complete by the end of the 77%RH step. The spread of the impedance drop over this range, as opposed to a sharp drop occurring within in a single RH step, was likely due to either a spike in humidity seen at the onset of the 76% step which caused partial deliquescence or step time that did not allow for adequate equilibration. Despite the same humidity spikes in the experiment carried out with smaller particles, there is a sharp drop to minimum impedance within the 76% step, Figure 3.10, suggesting inadequate equilibration time for the larger deposits.

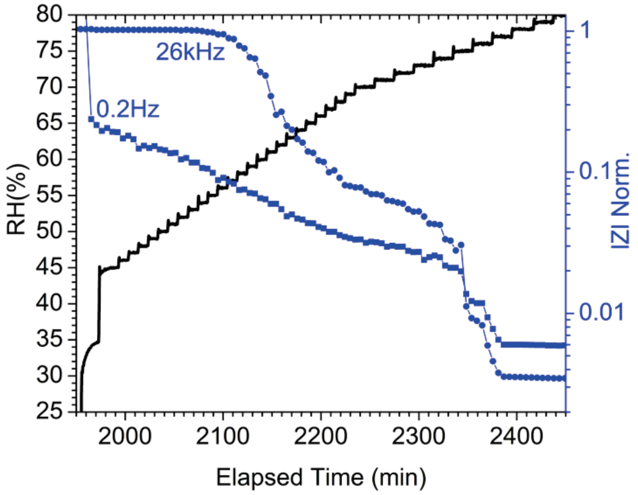

Figure 3.12. Measured impedance response and RH during humidification of a sensor loaded with ~100 µm NaCl particles.

The higher time resolution of the single frequency curves shown in Figures 3.11 and 3.12 also allows for characterization of the state of particles outside of the deliquescence-efflorescence hysteresis humidity region. For example, the rise in impedance at 0.2 Hz in step with decreasing RH after efflorescence occurred likely reflects the evaporation of water from the effloresced particles, Figure 3.11. Likewise, low frequency, and eventually high frequency, impedance gradually decreased in step with RH during humidification, indicating water uptake, Figure 3.12. Interestingly, however, the measured impedance during dehumidification was consistently lower than that measured during humidification for any given RH below 49%, Figure 3.10. This may have been due to trapped electrolyte in crevices or capillaries on the crystal surface or between the crystal and the sensor which slowly evaporated during dehumidification. Water retention of amounts greater than that explained by surface sorption on effloresced NaCl aerosols has been observed by others as well for particles ranging in size from 0.1 to 1 µm diameter [9, 51-52]. The results reported here suggest that fluid trapping is not size exclusive nor confined to suspended aerosols. Nevertheless, these results demonstrate that tracking impedance at both frequencies can be used for quantitative determination of bulk phase transitions and qualitative detection of minute amounts of water associated with effloresced particles.

3.2.3.4 NaBr, KCl, LiCl

Similar experiments were carried out to determine the deliquescence and efflorescence behavior of NaBr, KCl, and LiCl. In these experiments deposited drops of salt solution were subjected to stepped dehumidification ramp at the rate of 30 min/1%RH followed by a 24 hour hold at <1.5%RH and then a stepped humidification ramp at the rate of 20 min/1%RH. The results are given in Figure 3.13. Deliquescence for all salts is marked by the steep drop in $|Z|_{26kHz}$ to the lowest impedance values during dehumidification. Examination of the NaBr and KCl 0.2 Hz curves reveal steep drops also occurring prior to deliquescence. This behavior was found to be repeatable, and, although not further investigated, may be related to the water adsorption phenomena discussed in the previous section. As with the NaCl results, some interparticle variation in efflorescence was visually observed in each of these experiments and is reflected in the impedance curves as a gradual rise prior to a jump of several orders in magnitude during dehumidification in Figure 3.13**.** The ERH range was determined for these salts based on the two endpoints of the steep line, which captured the behavior of the majority of the particles, Figure 3.13. The ERH range along with DRH determined from the impedance data in Figure 3.13 are reported in Table 3.1. The DRH values determined for all of the salts are within ±2%RH of range of reported values, which is within accuracy of the RH sensor utilized. The ERH values were within 4% for those values that could be found in literature. These findings further substantiate the accuracy of this method for determination of bulk phase transitions across a broad RH range.

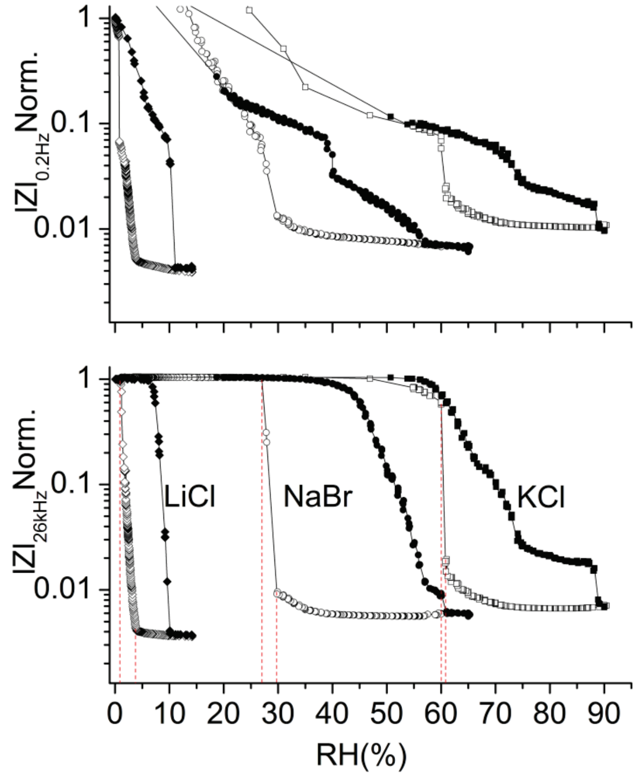

Figure 3.13. Impedance at 0.2 Hz (top) and 26 kHz (bottom) measured across LiCl, NaBr and KCl loaded sensors and as a function of RH. The open symbols indicate measurements during dehumidification and the closed symbols indicate measurements taken during humidification. Dashed lines indicate the ERH ranges determined for each salt.

Table 3.1. Experimental DRH and ERH values compared to literature values

	Obs. DRH	**Lit. DRH**	**Obs. ERH**	**Lit. ERH**
NaCl	76	74-76a-e	50	41-48c,e-g
NaBr	60	58a,c,h,i	27-30	21-30f,h,j
KCl	88	83-86c,k,l	59-61	48-56c,e,m,n
LiCl	10	10-11a,o	1-4	--

[a] Greenspan [53]. [b] Schuttlefield *et al.* [54]. [c] Cohen, Flagan and Seinfeld [18]. [d] Cruz and Pandis [20]. [e] Tang [17]. [f] Wise *et al.* [55]. [g] Cziczo *et al.* [24]. [h] Ghorai and Tivanski [56]. [i] Apelblat [57]. [j] Minambres *et al.* [58]. [k] Tang, Tridico and Fung [59]. [l] Tang and Munkelwitz [60]. [m] Freney, Martin and Buseck [61]. [n] Orr, Hurd and Corbett [62]. [o] Arenas *et al.* [8].

3.2.3.5 $MgCl_2$

Experiments were also carried out to characterize the hygroscopic behavior of $MgCl_2$, but the results did not allow for straightforward DRH and ERH determinations. Although the findings are not wholly understood, their inclusion here provides further insight into the little reported low humidity behavior of $MgCl_2$.

A sensor loaded with $MgCl_2$ particles was subjected to three replicate and consecutive humidity cycles similar to those used for the other salts. The measured impedance and RH during one of these cycles along with corresponding micrographs are shown in Figure 3.14. The measured impedance data for all three experiments in terms relative humidity are given in Figure 3.15. Sharp transitions are notable in $|Z|_{26kHz}$ below 5%RH during dehumidification and between 12 and 18% during humidification for each of these experiments. These transitions corresponded to the appearance of cracked and translucent glass-like solids Figure 3.14 (b) and the dissolution of the majority of them respectively (c). In all experiments, the micrographs revealed that a few of these solids persisted until 33%RH (c) at which point they too dissolved. Remarkably, the location of those deposits that did not deliquesce until 33%RH varied between experiments. In contrast to the behavior of the other salts examined, particle size did not appear to change dramatically during any of these transitions.

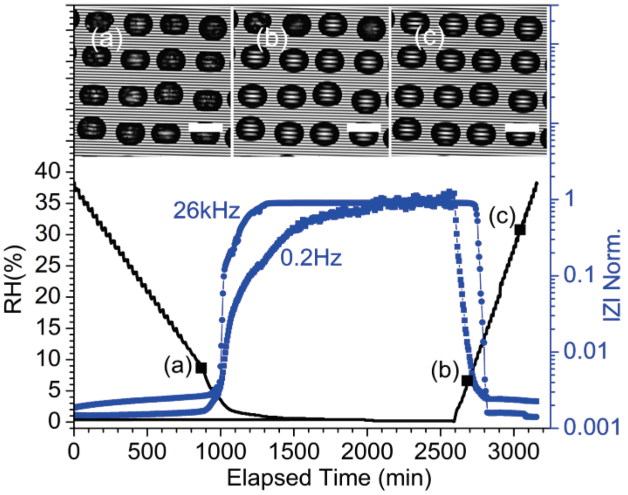

Figure 3.14. Response of sensor loaded with $MgCl_2$ and recorded RH. Inset are micrographs of the loaded sensor prior to efflorescence (a), after efflorescence and prolonged exposure to <1%RH (b), and after deliquescence of the majority of the drops at 15%RH (c). Scale bars are 150μm wide.

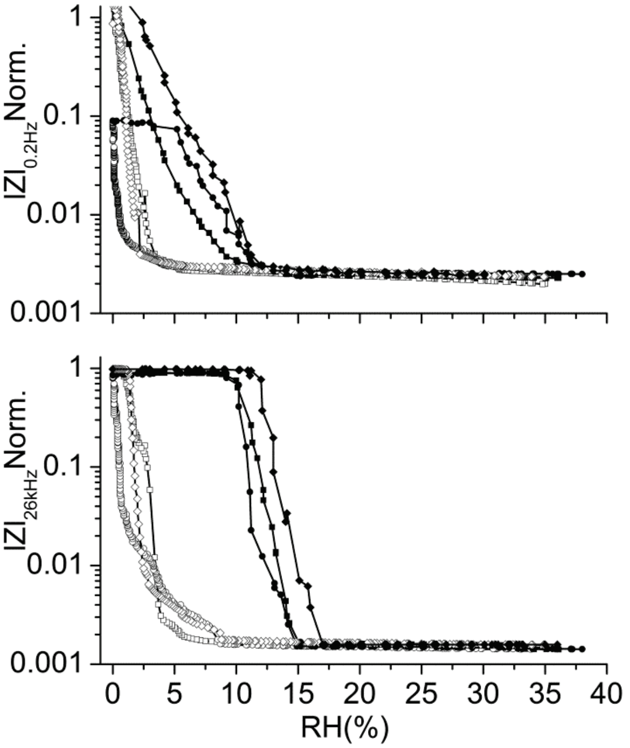

Figure 3.15. Impedance at 0.2 Hz (top) 26 kHz (bottom) measured across an $MgCl_2$ loaded sensor as a function of RH for three consecutive and replicate experiments. The open symbols indicate impedance during dehumidification and the closed symbols indicate measurements taken during humidification.

The high frequency impedance response along with the optical micrographs indicates that the solids that formed either deliquesced at 12-15%RH or at 33%RH. The latter is the well-established DRH of $MgCl_2.6H_2O$ [17,53]. Magnesium chloride is known to form a variety of hydrates with $MgCl_2.6H_2O$ being the thermodynamically favored phase at 270-369K [63]. Those that deliquesced at 12-15%RH may have done so due to contamination or the presence of a metastable hydrate. Contamination is ruled out here because the deliquescence behavior of a particular deposit varied from experiment to experiment, suggesting that neither location-specific contamination nor substrate heterogeneities controlled deliquescence behavior. The formation of non-equilibrium hydrated phase formation in particles which exhibit different DRH than that of the equilibrium phase has been reported for a number of other inorganic and organic salts [8, 18, 64]. In one of the few studies in the literature of the low humidity behavior of $MgCl_2$, Cziczo and coworkers, using FTIR spectroscopy, observed water retention during drying of aerosol particles at <1%RH and uptake during humidification well below 33%RH at 298K [9]. They could not explain this behavior by the formation or presence of the hexahydrate form alone and postulated that it was due to either incomplete efflorescence or formation of a metastable hydrate. Retention of water that cannot be attributed to the hexahydrate form and uptake below 33%RH has been reported by others using gravimetric methods [65-66].

The impedance results of the experiments reported here suggest that, in addition to the anomalous deliquescence behavior, the particles only partially effloresced in at least two of the experiments. This is reflected by $|Z|_{0.2Hz}$ remaining significantly below the stray impedance baseline (unity value of normalized impedance) throughout the experiments, Figure 3.15. The continuous rise in impedance seen in Figure 3.14 at <1.5%RH may have been due to the slow evaporation of electrolyte from the partially effloresced deposits. The immediate drop in low frequency impedance at the onset of humidification may also be indicative of incomplete efflorescence. Cziczo reported that $MgCl_2$ aerosols dried to less <1%RH immediately absorbed water upon subsequent addition of water vapor [9]. They attributed this to the presence of supersaturated liquid with access to the surrounding atmosphere. Low frequency response seen in our data may be indicative of similar behavior.

To examine the drying behavior of $MgCl_2$ in greater detail, two replicate experiments were carried out on a larger size scale. A 3µl drop of solution was jetted onto a sensor that was then subjected to a similar humidity profile. Measured impedance remained well below stray impedance with relatively little variance throughout the experiments, Figure 3.16. Small shifts in impedance at 18%RH and 33%RH correlated to the sudden transition of the drop from transparent to opaque (within 4 min) and visible deliquescence respectively. Impedance was found to rise throughout dehumidification below 18%RH and into humidification up to 33% RH, during which the top of the deposit caved in and nodules grew out of what appeared to be cracks. Prior to reaching 33%RH during humidification in the second experiment, the surface of the deposit was probed with a wire to reveal a thin (~1 mm) shell with liquid underneath.

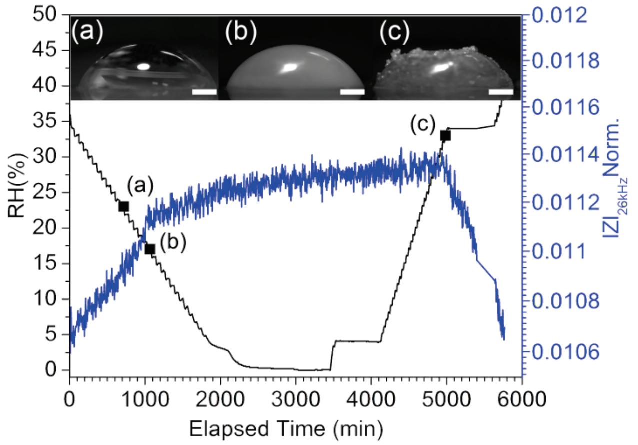

Figure 3.16. Impedance response of sensor loaded with 3 µl $MgCl_2$ drop and recorded RH. Inset are side-view micrographs of the liquid drop (a), immediately after shell formation (b), and just prior to deliquescence(c). Scale bars are 500µm wide.

The results of the experiments discussed above indicate that incomplete efflorescence of $MgCl_2$ deposits was due to the formation of a solid shell structure. The shells that formed trapped the underlying fluid, retarding water evaporation. Evaporation appeared to have occurred through cracks on the surface and capillary pathways through the nodules in the large drops, and likely did the same in the case of the small drops. A number of other inorganic and organic aqueous salt droplets ranging in diameter from 0.1µm to 2 mm, both deposited on substrates and suspended in air, have been reported to form shell structures during evaporation [11, 51, 67-69]. The formation of these structures has been attributed to the preferential nucleation of the solid at the substrate-air-liquid interface [11] or the liquid-air interface in the case of suspended aerosols without solid contaminants [51, 69]. The shell-formation behavior of $MgCl_2$ along with the formation of metastable hydrates would explain the presence of anomalous water retention during drying and uptake during humidification observed by other investigators [9, 66].

Two results in our experiments that are not understood, but worth noting, are (a) the preferential formation of solids that deliquesced at 33%RH on the large drops during drying, and (b) the difference in ERH between the large and small drops. Drop volume and geometry were the only obvious variables that differed between the two. The probability for containing favorable nucleation sites may serve as one plausible explanation for these differences [70-71].

3.2.3.6 Application to Mixed Salts and Environmental Particles

In this work, we have demonstrated the applicability of this method for deposits of single inorganic salts ranging in size from several microns to a few millimeters. This method is also applicable to particles of a smaller size scale and is hypothesized to have more general applicability to both organic and mixed hygroscopic salts. The detection limits of this method are largely constrained by the electrode geometry, particle size and coverage. The size of detectable isolated particles is limited to the dimensions of the electrode gap. Particles smaller than the gap could also be examined provided they are configured in such a way as to provide continuous conductive bridges across the electrodes, as could be achieved by a relatively high particle loading density. In recent years interdigitated electrode sensor geometries have been successfully scaled down for molecular and vapor phase chemical sensing with electrode spacing on the order of 100 nm [72-74], and sensors with gaps down to 1 μm are commercially available. Utilizing sensors with smaller spacing could extend the applicability of this method for study of finer size particles.

As discussed earlier, the impedance measured across a deposit is related to electrode/particle interfacial area (coverage). The effect of coverage on sensitivity is evidenced in a comparison of the results of the small and large NaCl particle experiments in Figure 3.10. Due to the lower salt loading density of the small particle experiment (8 $\mu g \cdot cm^{-2}$ compared to ~100 $\mu g \cdot cm^{-2}$ for the large particles), the dynamic range of impedance is depressed relative to that carried out with larger particles. Although bulk phase transitions can be tracked in both cases, the higher loading density in the large particle experiment shows enhanced sensitivity to the minute amounts of water associated with the effloresced particles at low humidity, Figure 3.10. Increasing loading density or sensing area is one means to enhance sensitivity regardless of particle size. Aside from electrode bridging and coverage, the spatial arrangement of particles is of no significant consequence to impedance response. This characteristic, combined with the robustness of the sensors utilized in this work, similar to glass slides, could allow for a variety of field collection techniques and laboratory deposition methods. Given that a significant fraction of environmental particles, such as tropospheric aerosols, are composed of organic components, it is noted here that impedance response is independent of the chemical nature of the hygroscopic deposits (i.e., organic versus inorganic), reliant only on their producing a sufficiently conductive electrolyte.

Further work is necessary to validate the applicability of this method for study of hygroscopic salt mixtures and complex chemistries associated with natural environmental particles. As discussed in the introduction, Yang et al. have shown that mutual deliquescence relative humidity (MDRH) values can be determined using a two-electrode impedance arrangement [40]. Although the sample geometry and sensor substrates differed between this work and theirs, the fundamental physical effect of bulk phase transitions on impedance variation remains the same and should allow for MDRH determinations using this method. Likewise, efflorescence phase transformations, which have not yet been examined using impedance in complex systems, will likely be detectable, thereby allowing for study of phase segregation behavior during drying of mixed salts. It is important to point out that for a distribution of particle sizes and compositions, as could be expected in natural environmental particles, the inner and interparticle variation in phase behavior may lead to less well defined trends in impedance response to relative humidity than seen in the work presented here.

3.2.4 Conclusions

In this work, an impedance method using interdigitated microelectrode array sensors was developed and evaluated for the determination of efflorescence and deliquescence RH values for a number of inorganic salts. The modulus of impedance measured at any single frequency from 0.2 Hz to 10^6 Hz across the sensors loaded with salt particles was found to be indicative of deliquescence and efflorescence events. Impedance at the highest frequencies exhibited the greatest dynamic range in measured values during phase transitions and the lowest frequencies were most sensitive to the presence of moisture. The DRH points and ERH ranges of NaCl, LiCl, NaBr and KCl were determined from $|Z|$ measured at 26 kHz and were in agreement with *in-situ* optical microscopic observations and literature values. These findings substantiate the accuracy of this method for determination of bulk phase transitions across a broad RH range and extend the applicability of impedance methods for study of hygroscopic microparticles and efflorescence. Future work is planned to extend this method for the study of mixed salts and particles of in the size range of fine-mode aerosols ($<1\mu$m diameter).

The humidity response of $MgCl_2$ was also examined, but the results did not allow for straightforward DRH and ERH determinations. Deliquescence behavior was marked by two RH ranges, whereby some drops deliquesced at the commonly reported 33%RH and others at 12-15%RH, a previously unreported range. It is hypothesized that the lower DRH values reflect the formation of a metastable $MgCl_2$ hydrate. Incomplete efflorescence of the $MgCl_2$ particles was observed even after exposure to <1.5%RH for more than 22 hours. This was due to the formation of solid shells which trapped fluid. The phenomena elucidated by these results provide explanation for the anomalous water retention and uptake behavior of $MgCl_2$ below 33%RH reported by others [9, 66]. These findings also demonstrate the utility of this method as alternative or complementary to detection of fluid trapping which cannot be directly ascertained by gravimetric and line-of-sight methods commonly used in the study of hygroscopic particles.

3.2.5 References

1. Mauer, L. J.; Taylor, L. S. Deliquescence of Pharmaceutical Systems. *Pharm. Dev. Technol.* 2010, *15*, 582-594
2. Chen, D. Hygroscopicity of Pharmaceutical Crystals. Ph.D. Thesis, University of Minnesota, Minneapolis, 2009.
3. Espinosa, R. M.; Franke, L.; Deckelmann, G. Phase Changes of Salts in Porous Materials: Crystallization, Hydration and Deliquescence. *Constr. Build. Mater.* 2008, *22*, 1758-1773.
4. Linnow, K.; Juling, H.; Steiger, M. Investigation of NaCl Deliquescence in Porous Substrates Using RH-XRD. *Environ. Geol.* 2007, *52*, 383-393.
5. Schindelholz, E.; Kelly, R. G. Wetting Phenomena and Time of Wetness in Atmospheric Corrosion: A Review. *Corros. Rev.* 2012, *30*, 135-207.
6. Yang, L.; Pabalan, R. T.; Browning, L. In *Experimental Determination of the Deliquescence Relative Humidity and Conductivity of Multicomponent Salt Mixtures*, Warrendale, PA, USA, Mater. Res. Soc: Warrendale, PA, USA, 2002; pp 135-42.
7. Cole, I. S.; Ganther, W. D.; Sinclair, J. D.; Lau, D.; Paterson, D. A. A Study of the Wetting of Metal Surfaces in Order to Understand the Processes Controlling Atmospheric Corrosion. *J. Electrochem. Soc.* 2004, *151*, B627-B635.

8. Arenas, K. J. L.; Schill, S. R.; Malla, A.; Hudson, P. K. Deliquescence Phase Transition Measurements by Quartz Crystal Microbalance Frequency Shifts. *J. Phys. Chem. A* 2012, *116*, 7658-7667.
9. Cziczo, D. J.; Abbatt, J. P. D. Infrared Observations of the Response of NaCl, $MgCl_2$, NH_4HSO_4, and NH_4NO_3 Aerosols to Changes in Relative Humidity from 298 to 238 K. *J. Phys. Chem. A* 2000, *104*, 2038-2047.
10. Ge, Z.; Wexler, A. S.; Johnston, M. V. Deliquescence Behavior of Multicomponent Aerosols. *J. Phys. Chem. A* 1998, *102*, 173-180.
11. Ciobanu, V. G.; Marcolli, C.; Krieger, U. K.; Zuend, A.; Peter, T. Efflorescence of Ammonium Sulfate and Coated Ammonium Sulfate Particles: Evidence for Surface Nucleation. *J. Phys. Chem. A* 2010, *114*, 9486-9495.
12. O'Dowd, C. D.; Smith, M. H.; Consterdine, I. E.; Lowe, J. A. Marine Aerosol, Sea-Salt, and the Marine Sulphur Cycle: A Short Review. *Atmos. Environ.* 1997, *31*, 73-80.
13. Pilinis, C.; Seinfeld, J. H.; Grosjean, D. Water Content of Atmospheric Aerosols. *Atmos. Environ.* 1989, *23*, 1601-1606.
14. McMurry, P. H. A Review of Atmospheric Aerosol Measurements. *Atmos. Environ.* 2000, *34*, 1959-1999.
15. Li-jun, Z.; et al. Deliquescence and Efflorescence Processes of Aerosol Particles Studied by in Situ Ftir and Raman Spectroscopy. *Chinese J. Chem. Phys.* 2008, *21*, 1.
16. James Davis, E.; Ravindran, P.; Ray, A. K. Single Aerosol Particle Studies. *Adv. Colloid Interface Sci.* 1981, *15*, 1-24.
17. Tang, I. N., Deliquescence Properties and Particle Size Change of Hygroscopic Aerosols. In *Symposium on Biological Studies of Environmental Pollutants: Aerosol Generation and Exposure Facilities*, Honolulu, Hawaii, 1979.
18. Cohen, M. D.; Flagan, R. C.; Seinfeld, J. H. Studies of Concentrated Electrolyte Solutions Using the Electrodynamic Balance. 1. Water Activities for Single-Electrolyte Solutions. *J. Phys. Chem.* 1987, *91*, 4563-4574.
19. Chen, Y. Y.; Grace Lee, W. M. The Effect of Surfactants on the Deliquescence of Sodium Chloride. *J. Environ. Sci. Health. A* 2001, *36*, 229-242.
20. Cruz, C. N.; Pandis, S. N. Deliquescence and Hygroscopic Growth of Mixed Inorganic-Organic Atmospheric Aerosol. *Environ. Sci. Technol.* 2000, *34*, 4313-4319.
21. Chen, Y. Y.; Lee, W. M. Hygroscopic Properties of Inorganic-Salt Aerosol with Surface-Active Organic Compounds. *Chemosphere* 1999, *38*, 2431-2448.
22. Xiao, H.-S.; Dong, J.-L.; Wang, L.-Y.; Zhao, L.-J.; Wang, F.; Zhang, Y.-H. Spatially Resolved Micro-Raman Observation on the Phase Separation of Effloresced Sea Salt Droplets. *Environ. Sci. Technol.* 2008, *42*, 8698-8702.
23. Li, X.-H.; Wang, F.; Lu, P.-D.; Dong, J.-L.; Wang, L.-Y.; Zhang, Y.-H. Confocal Raman Observation of the Efflorescence/Deliquescence Processes of Individual $NaNO_3$ Particles on Quartz. *J. Phys. Chem. B* 2006, *110*, 24993-24998.
24. Cziczo, D. J.; Nowak, J. B.; Hu, J. H.; Abbatt, J. P. D. Infrared Spectroscopy of Model Tropospheric Aerosols as a Function of Relative Humidity: Observation of Deliquescence and Crystallization. *J. Geophys. Res.* 1997, *102*, 18843-18850.

25. Hiranuma, N.; Brooks, S. D.; Auvermann, B. W.; Littleton, R. Using Environmental Scanning Electron Microscopy to Determine the Hygroscopic Properties of Agricultural Aerosols. *Atmos. Environ.* 2008, *42*, 1983-1994.
26. Hoffman, R. C.; Laskin, A.; Finlayson-Pitts, B. J. Sodium Nitrate Particles: Physical and Chemical Properties During Hydration and Dehydration, and Implications for Aged Sea Salt Aerosols. *J. Aerosol Sci* 2004, *35*, 869-887.
27. Ahn, K.-H.; Kim, S.-M.; Jung, H.-J.; Lee, M.-J.; Eom, H.-J.; Maskey, S.; Ro, C.-U. Combined Use of Optical and Electron Microscopic Techniques for the Measurement of Hygroscopic Property, Chemical Composition, and Morphology of Individual Aerosol Particles. *Anal. Chem.* 2010, *82*, 7999-8009.
28. Zhang, Y.; Hu, Y. a.; Ding, F.; Zhao, L. Ftir-Atr Chamber for Observation of Efflorescence and Deliquescence Processes of Naclo4 Aerosol Particles on Znse Substrate. *Chin. Sci. Bull.* 2005, *50*, 2149-2152.
29. Liu, Y.; Yang, Z.; Desyaterik, Y.; Gassman, P. L.; Wang, H.; Laskin, A. Hygroscopic Behavior of Substrate-Deposited Particles Studied by Micro-Ft-Ir Spectroscopy and Complementary Methods of Particle Analysis. *Anal. Chem.* 2008, *80*, 633-642.
30. Widmann, J. F.; Aardahl, C. L.; Davis, E. J. Microparticle Raman Spectroscopy. *Trends in Analytical Chemistry* 1998, *17*, 339-345.
31. Lee, W.-M.; Chou-Yuan, C.; Shou-Lin, H. The Deliquescent Growth of Inorganic-Salt Aerosols Observed by a Combined System of TDMA and Integrated Nephelometer. *J. Aerosol Sci* 1996, *27*, 313-314.
32. Tang, I. N.; Fung, K. H.; Imre, D. G.; Munkelwitz, H. R. Phase Transformation and Metastability of Hygroscopic Microparticles. *Aerosol Sci. Technol.* 1995, *23*, 443-453.
33. Ewing, G. E. Ambient Thin Film Water on Insulator Surfaces. *Chem. Rev.* 2006, *106*, 1511-1526.
34. Das-Gupta, D. K. Electrical Properties of Surfaces of Polymeric Insulators. *Electrical Insulation, IEEE Transactions on* 1992, *27*, 909-923.
35. Simkovich, G. The Surface Conductance of Sodium Chloride Crystals as a Function of Water Vapor Partial Pressure. *J. Phys. Chem.* 1963, *67*, 1001-1004.
36. Hucher, M.; Oberlin, A.; Hocart, R. Adsorption of Water Vapor on the Cleavage Surfaces of Some Alkali Metal Halides. *B. Soc. Fr. Mineral. Cr.* 1967, 320–332.
37. Dai, D. J.; Peters, S. J.; Ewing, G. E. Water Adsorption and Dissociation on NaCl Surfaces. *J. Phys. Chem.* 1995, *99*, 10299-10304.
38. Laux, J. M.; Fister, T. F.; Finlayson-Pitts, B. J.; Hemminger, J. C. X-Ray Photoelectron Spectroscopy Studies of the Effects of Water Vapor on Ultrathin Nitrate Layers on Nacl. *J. Phys. Chem.* 1996, *100*, 19891-19897.
39. Dai, Q.; Hu, J.; Salmeron, M. Adsorption of Water on NaCl (100) Surfaces: Role of Atomic Steps. *J. Phys. Chem. B* 1997, *101*, 1994-1998.
40. Yang, L.; Pabalan, R.; Juckett, M. Deliquescence Relative Humidity Measurements Using an Electrical Conductivity Method. *J. Solution Chem.* 2006, *35*, 583-604.
41. He, K.; Cheng, H.; Zhu, Y.; Wang, L.; Zhang, Y. Measurement of Electric Properties of the Single Supersaturated Aerosol Droplet. *Chin. Sci. Bull.* 2008, *53*, 1773-1776.

42. Gao, Y.; Yu, L. E.; Chen, S. B. Theoretical Investigation of Substrate Effect on Deliquescence Relative Humidity of Nacl Particles. *J. Phys. Chem. A* 2007, *111*, 633-639.
43. Yamazoe, N.; Shimizu, Y. Humidity Sensors: Principles and Applications. *Sens. Actuators B* 1986, *10*, 379-398.
44. Sakai, Y.; Matsuguchi, M.; Hurukawa, T. Humidity Sensor Using Cross-Linked Poly (Chloromethyl Styrene). *Sens. Actuators B* 2000, *66*, 135-138.
45. Lee, C.-W.; Rhee, H.-W.; Gong, M.-S. Humidity Sensor Using Epoxy Resin Containing Quaternary Ammonium Salts. *Sens. Actuators B* 2001, *73*, 124-129.
46. Gillespie, T.; Kidd, G. E. Sensing Duration of Leaf Moisture Retention Using Electrical Impedance Grids. *Can. J. Plant Sci.* 1978, 179-187.
47. Schindelholz, E.; Kelly, R. G.; Cole, I. S.; Ganther, W. D.; Muster, T. H. Comparability and Accuracy of Time of Wetness Sensing Methods Relevant for Atmospheric Corrosion. *Corros. Sci.* 2013, *67*, 233-241.
48. Orazem, M. E.; Tribollet, B., *Electrochemical Impedance Spectroscopy*. Wiley-Interscience: 2011; Vol. 48.
49. Chen, Z.; Lu, C. Humidity Sensors: A Review of Materials and Mechanisms. *Sensor Lett.* 2005, *3*, 274-295.
50. Lukács, Z. The Numerical Evaluation of the Distortion of EIS Data Due to the Distribution of Parameters. *J. Electroanal. Chem.* 1997, *432*, 79-83.
51. Braun, C.; Krieger, U. Two-Dimensional Angular Light-Scattering in Aqueous Nacl Single Aerosol Particles During Deliquescence and Efflorescence. *Opt. Express* 2001, *8*, 314-321.
52. Weis, D. D.; Ewing, G. E. Water Content and Morphology of Sodium Chloride Aerosol Particles. *J. Geohys. Res. D* 1999, *104*, 21275-21285.
53. Greenspan, L. Humidity Fixed Points of Binary Saturated Aqueous Solutions. *J. Res. Natl. Bur. Stand. A* 1977, *81 A*, 89-96.
54. Schuttlefield, J.; Al-Hosney, H.; Zachariah, A.; Grassian, V. H. Attenuated Total Reflection Fourier Transform Infrared Spectroscopy to Investigate Water Uptake and Phase Transitions in Atmospherically Relevant Particles. *Appl. Spectrosc.* 2007, *61*, 283-292.
55. Wise, M. E.; Biskos, G.; Martin, S. T.; Russell, L. M.; Buseck, P. R. Phase Transitions of Single Salt Particles Studied Using a Transmission Electron Microscope with an Environmental Cell. *Aerosol Sci. Technol.* 2005, *39*, 849-856.
56. Ghorai, S.; Tivanski, A. V. Hygroscopic Behavior of Individual Submicrometer Particles Studied by X-Ray Spectromicroscopy. *Anal. Chem.* 2010, *82*, 9289-9298.
57. Apelblat, A. The Vapour Pressures of Saturated Aqueous Lithium Chloride, Sodium Bromide, Sodium Nitrate, Ammonium Nitrate, and Ammonium Chloride at Temperatures from 283 K to 313 K. *J. Chem. Thermodyn.* 1993, *25*, 63-71.
58. Miñambres, L.; Sánchez, M. a. N.; Castaño, F.; Basterretxea, F. J. Infrared Spectroscopic Properties of Sodium Bromide Aerosols. *J. Phys. Chem. A* 2008, *112*, 6601-6608.
59. Tang, I. N.; Tridico, A. C.; Fung, K. H. Thermodynamic and Optical Properties of Sea Salt Aerosols. *J. Geophys. Res.* 1997, *102*, 23269-23275.

60. Tang, I. N.; Munkelwitz, H. R.; Wang, N. Water Activity Measurements with Single Suspended Droplets: The Nacl-H2o and Kcl-H2o Systems. *J. Colloid Interface Sci.* 1986, *114*, 409-415.
61. Freney, E. J.; Martin, S. T.; Buseck, P. R. Deliquescence and Efflorescence of Potassium Salts Relevant to Biomass-Burning Aerosol Particles. *Aerosol Sci. Technol.* 2009, *43*, 799-807.
62. Orr, C.; Hurd, F. K.; Corbett, W. J. Aerosol Size and Relative Humidity. *J. Colloid Sci.* 1958, *13*, 472-482.
63. Sugimoto, K.; Dinnebier, R. E.; Hanson, J. C. Structures of Three Dehydration Products of Bischofite from in Situ Synchrotron Powder Diffraction Data ($MgCl_2.NH_2O$; N = 1, 2, 4). *Acta Crystallogr. B* 2007, *63*, 235-242.
64. Peng, C.; Chan, C. K. The Water Cycles of Water-Soluble Organic Salts of Atmospheric Importance. *Atmos. Environ.* 2001, *35*, 1183-1192.
65. Davila, A.; Duprot, L.; Melchiorri, R.; Janchen, J.; Valea, S. Hygroscopic Salts and the Potential for Life on Mars. *Astrobiology* 2010, *10*, 617-628.
66. Winkler, P. The Growth of Atmospheric Aerosol Particles as a Function of the Relative Humidity. Ii. An Improved Concept of Mixed Nuclei. *J. Aerosol Sci* 1973, *4*, 373-87.
67. Cheng, R. J.; Blanchard, D. C.; Cipriano, R. J. The Formation of Hollow Sea-Salt Particles from the Evaporation of Drops of Seawater. *Atmos. Res.* 1988, *22*, 15-25.
68. Shahidzadeh-Bonn, N.; Rafaï, S.; Bonn, D.; Wegdam, G. Salt Crystallization During Evaporation: Impact of Interfacial Properties. *Langmuir* 2008, *24*, 8599-8605.
69. Colberg, C. A.; Krieger, U. K.; Peter, T. Morphological Investigations of Single Levitated H2so4/Nh3/H2o Aerosol Particles During Deliquescence/Efflorescence Experiments. *J. Phys. Chem. A* 2004, *108*, 2700-2709.
70. Vonnegut, B. Variation with Temperature of the Nucleation Rate of Supercooled Liquid Tin and Water Drops. *J. Colloid Sci.* 1948, *3*, 563-569.
71. Lightstone, J. M.; Onasch, T. B.; Imre, D.; Oatis, S. Deliquescence, Efflorescence, and Water Activity in Ammonium Nitrate and Mixed Ammonium Nitrate/Succinic Acid Microparticles. *J. Phys. Chem. A* 2000, *104*, 9337-9346.
72. Bonanni, A.; Fernández-Cuesta, I.; Borrisé, X.; Pérez-Murano, F.; Alegret, S.; Valle, M. DNA Hybridization Detection by Electrochemical Impedance Spectroscopy Using Interdigitated Gold Nanoelectrodes. *Microchim Acta* 2010, *170*, 275-281.
73. Singh, K.; Whited, A.; Ragineni, Y.; Barrett, T.; King, J.; Solanki, R. 3d Nanogap Interdigitated Electrode Array Biosensors. *Anal Bioanal Chem* 2010, *397*, 1493-1502.
74. Toohey, M. J. Electrodes for Nanodot-Based Gas Sensors. *Sens. Actuators B* 2005, *105*, 232-250.

4 Effect of RH on Corrosion of Steel under Sea Salt Aerosol Proxies

This section is comprised of a two-part series of papers. In the first section, the hygroscopic behavior of NaCl and expected corrosion chemistries are related to the corrosion behavior of steel as a function of RH. The understanding developed on this single salt system served as basis from which to extend this work to $MgCl_2$, which is thought to be the active corrosion stimulating component of SSA at low humidity, and further extends it to artificial seawater (ASW), which is more representative of the complex chemistry of SSA (second section). The results were used assess accuracy and appropriateness of current TOW determination methods.

4.1 Part I: NaCl

This paper is the first of two that examine the relationship between relative humidity, the hygroscopic behavior of sea salt aerosol proxies, and the atmospheric corrosion of mild steel contaminated with them. Here, the association between the deliquescence phase transitions (solid-aqueous) of a single salt, NaCl, and the corrosion response of steel contaminated with this salt is examined. Specific focus is given to mechanisms that allow corrosion below the deliquescence relative humidity of NaCl (76% RH). Mild steel loaded with aqueous NaCl drops or crystals (9 $\mu g \cdot cm^{-2}$) was subjected to isohumidity exposures for up to 30 d. The resulting damage evolution was quantified by optical profilometry. The corrosion chemistry that developed was identified using EDS and Raman spectroscopy. The wetting and drying of simulated corrosion chemistries was characterized by impedance measured across an interdigitated electrode sensor. Taken together, these results show that corrosion can initiate by adsorbed water on NaCl crystals as low as 33% RH. At humidity levels of 53% RH and above, attack proceeded at rates comparable to that observed above the deliquescence RH due to the development of hygroscopic corrosion chemistry. The governing role of the hygroscopic properties of this chemistry on attack rate and morphology is discussed.

4.1.1 Introduction

In atmospheric environments, corrosion is often approximated as a discontinuous process reliant on the availability of electrolyte to provide ionic conduction between cathode and anode sites for it to proceed at a considerable rate. A critical question in atmospheric corrosion is when can a surface be considered wet enough for corrosion to occur at a considerable rate? Indeed, this question has been the subject of many studies since the beginning of atmospheric corrosion as a modern scientific discipline. It has led to the development of a great number of methods which estimate or measure surface wetness as a means of determining when corrosion may be possible or significant (i.e., time of wetness). Great advances have been made in understanding the relationship between the state of the electrolyte on a surface and the corrosion response under the cases of thin films [1-3] and macroscopic drops [4-6] at high humidity levels. Relatively little information is available regarding this relationship under aerosol-size deposits and at lower humidity levels, as could be expected on outdoor surfaces. This paper is the first of two that seek to further the understanding of the relationship between relative humidity, hygroscopic behavior of soluble salts, and the corrosion response of steel surfaces in environments where sea salt aerosol (SSA) is the primary contaminant.

In this paper we test the universality of the contention that the deliquescence point of a single salt contaminant serves as the delineation between a wet and a dry surface as well as significant and insignificant corrosion attack. We do so for the specific case of

NaCl microparticles on mild steel at the initial stages of corrosion under isohumidity conditions. We also explore the role of a number of physical phenomena that could allow for initiation and sustainment of corrosion below the deliquescence point including (1) the presence of adsorbed water associated with NaCl on the steel surface, (2) the existence of supersaturated NaCl brine resulting from crystallization point depression, and (3) the hygroscopicity of the corrosion chemistry produced at the anode and cathode sites. An understanding of the contributions of these phenomena to the atmospheric corrosion of steel should have an impact on the design of accelerated test regimes as well as the interpretation of field exposure data.

4.1.2 Background

Barring events that directly deposit electrolyte onto a surface, such as precipitation, the amount of electrolyte available to a corrosion cell in the atmospheric environment is generally governed by relative humidity and the hygroscopic nature of the surface constituents. Soluble salts on the surface, resulting from the deposition of atmospheric aerosols and gaseous pollutants (hereto referred as primary contaminants), largely contribute to surface wetness. Development of methods to measure or estimate the contribution of these contaminants to surface wetness, under the general concept of time of wetness (TOW), has been the subject of many studies [7] Of particular attention has been the relative humidity at which primary contaminant salts deliquesce, often presumed as the delineation between an adequately wet and a dry surface for corrosion to proceed and the threshold between significant and insignificant corrosion [8-11].

Deliquescence is the bulk phase transformation whereby a solid salt spontaneously absorbs water to form an aqueous electrolyte above a specific RH. The corresponding RH for this transformation is the deliquescence RH (DRH). Above this RH there is a thermodynamic driving force for the salt to form an electrolyte and below it, a solid. The volume of electrolyte created by the deliquescence of a contaminant often far exceeds the amount of water adsorbed on the salt or the substrate alone. This electrolyte in turn provides sufficient conductance necessary to sustain corrosion at a considerable rate. Such reasoning is, in part, the basis of the general supposition that the deliquescence point of a salt serves as the critical humidity threshold which delineates a surface sufficiently wet enough for considerable corrosion to take place from a relatively dry surface for which corrosion is insignificant [7].

The corrosion behavior of metals contaminated with the simple binary salt constituents of sea salt or deicing salts, such as NaCl, at humidity levels at or above the DRH of these salts has been well documented in the laboratory setting [12-15]. The understanding gained from these studies has helped make great advances in the interpretation and prediction of corrosion performance in natural environments and accelerated tests. Natural environments, however, often reach humidity levels well below the deliquescence points of the primary contaminants alone. Relatively few studies have been reported that have directly examined corrosion below the deliquescence point of these salts. Of those that have, conflicting results have been presented as to whether or not corrosion is significant and why. Given that steel continues to be the structural alloy most exposed to saline environments and NaCl is a primary constituent of salts in these environments, we will examine the specific case of NaCl-contaminated steel.

Aqueous corrosion of NaCl-contaminated steel and other alloys is known to take place to some degree below the DRH of NaCl [16-19]. In the 1950s, Preston and Sanyal

[16], and, later, Ericsson [17] reported the initiation and sustainment of corrosion under NaCl crystals down to 58% RH (the lowest RH tested) through isohumidity experiments. Since that time, the possibility for initiation of corrosion under crystalline NaCl particles has received little attention, and, of those that have reported this occurrence ~50% RH appears to be the minimum [20, 21]. Initiation has been speculated to be due to, among other things, the presence of electrolyte trapped between the crystals and the steel substrate by capillary action after drying[17], adsorbed moisture films on the steel[22] or on the salt surfaces themselves[16,20]. Once corrosion has commenced, it has been observed to be sustained down to much lower humidity levels than where it originally initiated [20, 23, 24]. For example, Yang, using a sensor constructed of mild steel, observed corrosion currents between the electrodes, which were covered in rust and NaCl down to 27% RH, the lowest humidity achieved in their test [20]. They hypothesized that low humidity corrosion was due to the presence of hygroscopic iron chloride salts which have been shown to cause corrosion at such low levels [25, 26].

Conflicting results and views, however, are presented in the literature as to whether or not corrosion rates are significant below the DRH of NaCl [16, 20, 21, 24, 27, 28]. Findings of Preston and Sanyal [16] and also Ericsson [17] found that the mass gain of NaCl-inoculated steel coupons exposed just below and just above the DRH (~70% and ~80% RH) to be comparable after 30 days of isohumidity exposure. Additionally, Preston found that mass gain of coupons within this range was nearly an order of magnitude higher than that of coupons exposed at 58% RH, which was the next lowest RH level utilized [16]. These results suggest that corrosion rates are similar around the DRH point, but considerably vary at some point below it. In contrast to these findings, Cai et al. used iron wire electrical resistance sensors inoculated with NaCl particles and found corrosion to be barely detectable at only a few percentage points below the DRH of this salt after 4 days of exposure [27]. Conflicting results such as this are likely due to the detection limits of the method used or factors that convolute the results of indirect measures of corrosion loss.

These discrepancies raise the following questions that have served as motivation for this work: Does the DRH coincide with the RH at and above which corrosion becomes considerable? What other phenomena are in play that could allow for corrosion below the deliquescence point? How do changes in surface chemistry due to corrosion affect the hygroscopic behavior and, in turn, the relationship between corrosion response and RH?

4.1.3 Experimental

Details of the experimental procedures are given in the following sections, but an overview of the approach is warranted. Polished mild steel coupons were loaded with NaCl microparticles in the form of droplets or crystals and were subjected to isohumidity conditions ranging from 0 to 90% RH for up to 30 days. After exposure, surfaces of some sample sets were cleaned and surface profilometry was utilized to characterize attack morphology and quantify volume loss. Other sets of samples were examined in the as-removed state using optical, Raman, and scanning electron microscopy to characterize the effect of relative humidity on the state of the surfaces. Furthermore, the humidity response of NaOH and $FeCl_2$-NaCl deposits was studied using an interdigitated electrode impedance method [29] to characterize hygroscopic chemistries that develop in anodic and cathodic reaction sites, respectively.

4.1.3.1 Samples

Coupons of AISI 1010 plain carbon steel measuring 25 x 25 mm were polished to a 0.01 μm colloidal silica finish. After polishing, they were rinsed with ultrapure (UP) water (18.2 MΩ·cm, <5 ppb TOC) and absolute ethanol (>99.5%), then dried in a stream of zero grade compressed air.

4.1.3.2 Salt Loading

Prior to exposure, salt was deposited onto the coupons using a custom inkjet printer inside a humidity-controlled chamber. Specifically, a near saturated solution of NaCl (99.999%) and UP water was dispensed onto each coupon in a 10 x 10 mm square array pattern of 126 x 126 droplets. The droplets were approximately 1 pL in volume (~14 μm airborne saturated solution diameter), which is representative of the larger size fraction of natural SSA [30]. The resulting salt loading density was measured after printing to be 8.6 ± 0.1 $\mu g \cdot cm^{-2}$ using a wash-off methodology outlined in Schindelholz and Kelly [31]. These loadings, in terms of chloride content are within the range of those reported by Shinohara (10^{-1} to 10^{2} $\mu g \cdot cm^{-2}$) for chloride measured on boldly exposed roofs in coastal marine environments [67]. For one set of samples, here termed the droplet-loaded samples, printing was carried out at 78% RH and 21°C so that the deposits were in the form of droplets at the start of the exposure. On another set, referred to as the crystal-loaded samples, the pattern was printed in the same manner, but onto samples heated on a stage at 60°C. Heating resulted in near instantaneous (<1 s) crystallization of the droplets when they hit the surface with no detectable signs of corrosion. Images of the printed patterns are shown in Figure 4.1. Further details on the inkjet instrument utilized in this study [29] and the use of inkjet printing for corrosion testing [31-33] are reported elsewhere.

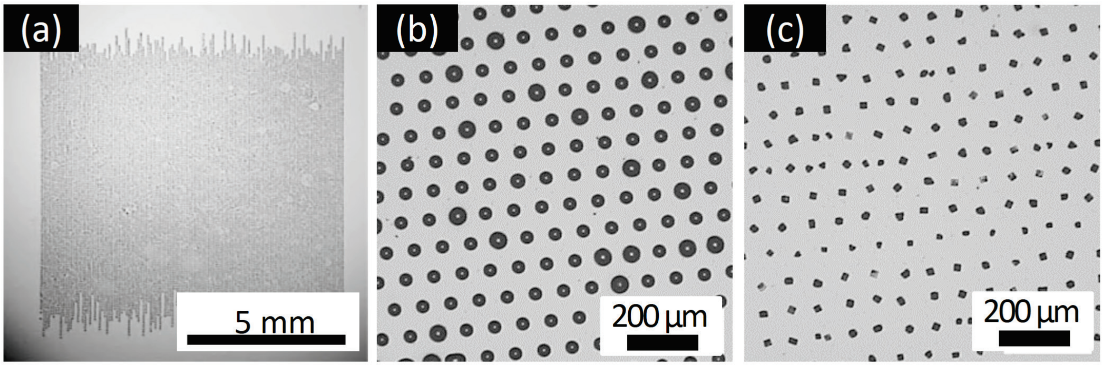

Figure 4.1. (a) printed droplet pattern on steel coupon, (b) detail of droplet pattern immediately after printing, (c) detail of crystal pattern immediately after printing.

4.1.3.3 Isohumidity Exposure

Immediately after printing, the samples were placed in glass containers that contained saturated salt solutions or desiccant to maintain a particular RH, Table 4.1. In order to ensure the deposits on the droplet-loaded coupons stayed wet (deliquesced) at the start of the isohumidity exposures, the containers were filled with humidified zero air to achieve 77-80% RH. Likewise, chambers holding the crystal-loaded coupons were filled with dry (<5% RH) zero air. The zero air was produced using an Environics 7000 Zero Air Generator (USA). Afterwards, the air ports on the chambers were closed and the chambers were left to equilibrate to their RH set point (controlled by the salt solution or desiccant) at 21 ± 2^{o} C. In-situ measurements using a calibrated RH sensor (Vaisala, HMP110) indicated that the atmospheres within the chambers equilibrated to within 1.5% of the expected RH in one hour or less and remained so for the duration of the experiments. Coupons were removed at intervals from the chambers for periods of up to 30 days to assess the corrosion response.

Table 4.1 Solutions or desiccant used to control humidity in chambers. All solutions were prepared from UP water and >99.95% analytical grade salts.

Saturated Solution or Desiccant*	**RH (%)**
$BaCl_2$	90
KCl	85
NaCl	76
$SrCl_2$	71
$CoCl_2$	64
$CaNO_3$	53
$MgCl_2$	33
CH_3CO_2K	23
4Å molecular sieves*	<1.5

As a precautionary measure, sets of cleaned polycarbonate coupons were also placed in the isohumidity chambers during the exposures to monitor possible sources of contamination. After exposure, the coupons were extracted under sonication in UP water and analyzed by ion chromatography for all ionic constituents of the saturated salts used for RH control, with the exception of Ba^{2+}, Sr^{+}, and Co^{2+}, along with formate (a common indoor atmospheric contaminant[34]) following the procedure outlined in Keene et al. [35]. Most of the measured ion loadings were below the limits of detection of our procedure (0.001 $\mu g \cdot cm^{-2}$). Of those that were measurable, we found no significant difference in loading amounts between the samples that had been placed in the chambers and those that had not (blanks). No loadings higher than 0.005 $\mu g \cdot cm^{-2}$ were observed, which is far below the 9 $\mu g \cdot cm^{-2}$ loading density of NaCl on our samples.

4.1.3.4 Post Exposure Analysis

Upon removal from the exposure chambers, samples were either immediately stripped of rust for profilometry measurements or left in as-is condition and, if stored prior to analysis, placed in a vacuum desiccator. Rust was removed by immersing the samples in an aqueous solution of 1M dibasic ammonium citrate heated to 40°C for 1-5 min (dependent on rust amount). This was followed by rinsing with UP water and drying with compressed air. The cleaned coupons were then scanned using a NewView 7300 white light interferometer (Zygo Corp., US). At least three areas within the printed regions of each coupon were scanned, with each area measuring 1x1 mm. An additional scan was carried out in the unprinted (uncorroded) region of each coupon to serve as a reference. Each scan was then analyzed to determine total volume loss and maximum pit depth with respect to the original polished plane of the coupon. The dataset resulting from this analysis consisted of 2-4 coupons per isohumidity set point and exposure period. The manufacturer-stated height resolution of the instrument in the configuration utilized was ~1 nm with a lateral resolution of ~500 nm.

The sample sets left in as-is condition were examined using reflected light optical microscopy, SEM-EDS, and Raman microscopy to characterize changes in surface composition and morphology after exposure. Optical microscopy was carried out using a reflected light microscope installed in the humidity controlled chamber used for printing. An InVia Raman microscope (Renishaw, Illinois) was used for analysis of phase constituents. The instrument was operated with a 458 nm laser, with power on the sample limited to 1 mW with a spot size of ~2 µm. The relative humidity during Raman analyses was less than 50%. A Quanta 650 field emission SEM-EDS (FEI, Oregon) was utilized for analysis in high vacuum, backscattered electron mode using 5-10kV accelerating voltage and working distance of 10 mm.

4.1.3.5 Hygroscopic Behavior of Anolyte and Catholyte Simulants

To study the hygroscopic behavior of chemistries expected to develop at the anodic and cathodic regions of atmospherically corroding steel under NaCl, droplets of these chemistries were subjected to humidity cycling. During the cycling, the impedance across the droplets were measured and optical micrographs were taken. First, aqueous solutions of NaOH and 1:1 (mole basis) $FeCl_2$-NaCl (all >99.99% purity) were prepared with UP water and placed in airtight containers. These solutions were our catholyte and anolyte proxies, respectively. At the start of an experiment, droplets of one of these solutions was jetted onto a clean interdigitated electrode sensor using the same method as above. The sensor (ALS Co., Tokyo) consisted of an interdigitated pair of platinum electrodes (3 μm electrode gap) on a quartz substrate. The droplet-loaded sensor was subjected to cyclic humidity ramping inside the inkjet chamber. During ramping, impedance was measured across the sensor at 0.2 Hz and 26 kHz with an excitation of 20 mV versus open circuit. Additionally, morphological changes were tracked via a reflected light microscope trained on the sensor. Measured impedance values were normalized to deconvolute the impedance contribution of the deposited particles from the humidity response of the sensor itself and noise realized during measurements. This was done by dividing values measured across the salt loaded sensor by values measured across a blank, clean sensor. Thus, any normalized impedance value below unity indicated significant admittance (i.e., conductance) contribution from the particles themselves. The humidity profile consisted of a dehumidification ramp stepped at the rate of 30 min/1% RH followed by a 4-12 h hold at <2% RH and then humidified at 20 min/1 % RH. Three consecutive cycles for each of the solutions. All experiments were carried out at ambient lab temperature, 21 ± 2° C. Further details on the instrumentation and experimental procedure are given by Schindelholz, Tsui and Kelly [29].

4.1.4 Results

4.1.4.1 Effect of RH on Attack Morphology and Volume Loss

Figure 4.2 shows a series of scan profiles and images of surfaces of droplet-loaded coupons after seven days of isohumidity exposure. These images and following descriptions are generally representative of the disparities in attack morphology witnessed with respect to relative humidity, regardless of the exposure times examined or of the original state of the salt deposits (droplet or crystal). In general, corrosion at 33% RH was found to progress radially from a subset of the salt deposits in a fern-like pattern reminiscent of salt creep. Corrosion at 53% RH also clearly emanated from certain salt deposits, but the damage was more filamentary which resulted in discrete pitting. Additionally needle-like crystals formed in areas around the rust formations and between the original NaCl deposits, and can be seen as thin, irregular lines in the 53% optical image. Coupons exposed at 64% RH exhibited the most uniform corrosion attack in that the greatest amount of area was corroded. Above 64% RH, the number density of pits was found to decrease and their size increased substantially with increasing relative humidity. No sign of sustained corrosion attack was detected at 0% and 23% RH.

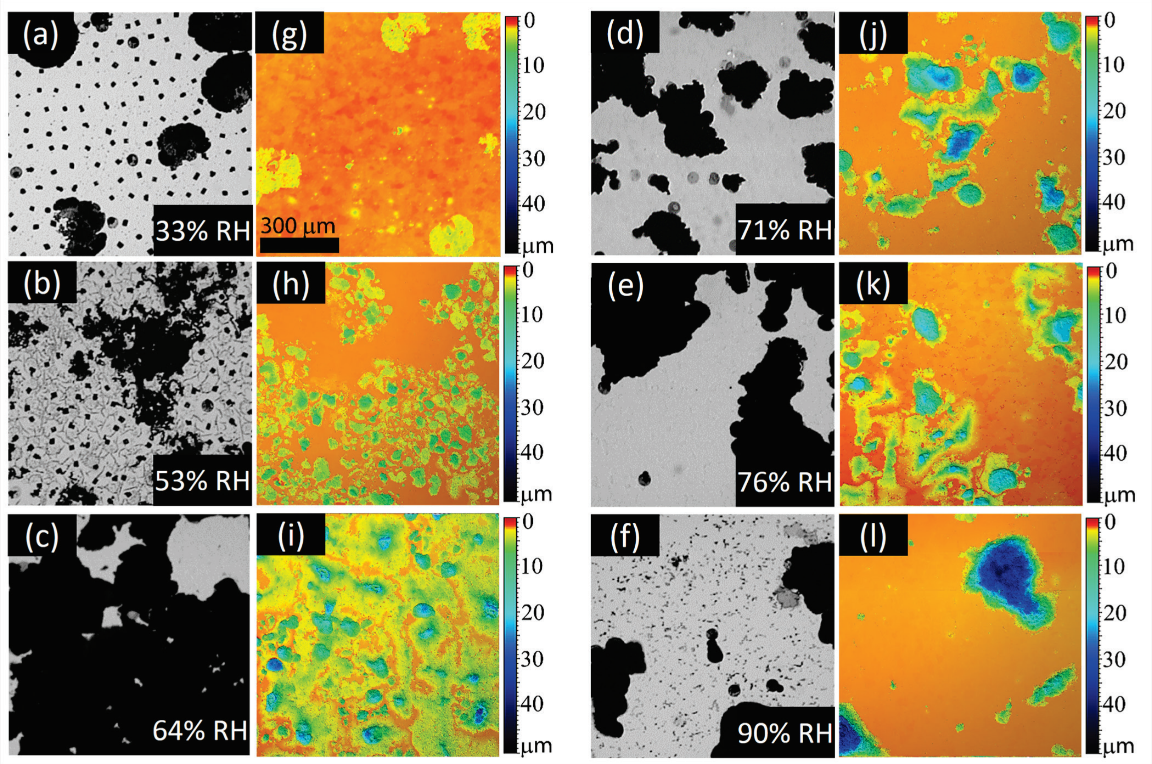

Figure 4.2 Optical micrographs of droplet-loaded coupons after 7 d exposure and before rust removal (a-f); measured surface profiles after removal for the same exposure period (g-l). All images are of the same scale.

As a means of quantitatively comparing attack morphology across the RH range and between droplet-loaded and crystal-loaded samples, the average maximum pit depth was determined for each sample type and humidity level, Figure 4.3. These values were computed by averaging the maximum pit depth found in each of the scans for all samples of a certain type (droplet or crystal) exposed at the same relative humidity. It is notable here that the dispersion reflected by the error bars at 85% and 90% RH at 30 days is due to the low number density of pits compared to the field of view of the profilometry scans, as represented by the 90% profile in Figure 4.2**.** Figure 4.3b demonstrates the fact that crystal-loaded coupons generally witnessed the similar attack trends to the droplet-loaded coupons.

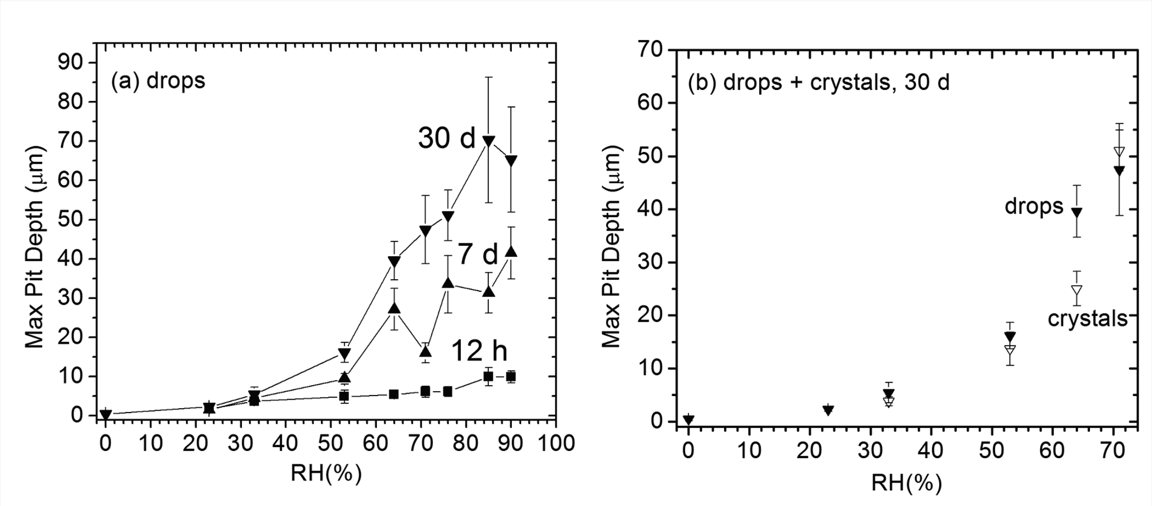

Figure 4.3 Maximum pit depth vs. RH for (a) droplet-loaded samples across entire RH range examined and (b) droplet and crystal-loaded samples below the DRH of NaCl.

The average nominal corrosion depth witnessed by the samples is given in Figure 4.4**.** These values were calculated by dividing the volume loss for each scan by the area of the scan (field of view). Data points which fall below the noise threshold (dashed line) in these plots were not significantly different from measurements taken in the unprinted region of the coupons. Figure 4.4b indicates no significant difference in corrosion loss between the droplet-loaded and crystal-loaded samples after 30 days of exposure.

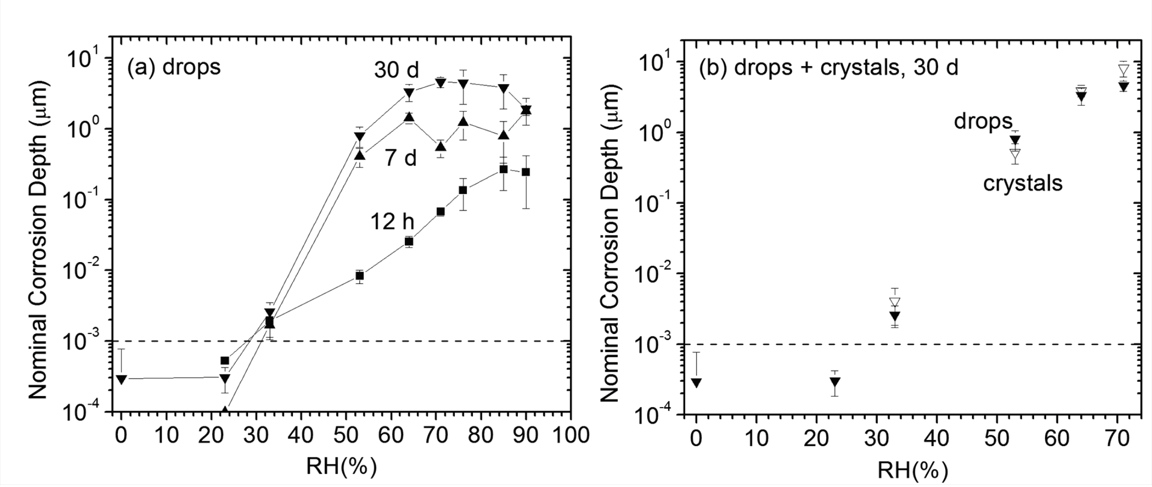

Figure 4.4 Average volume loss divided by scan area (nominal depth) vs. RH for (a) droplet-loaded samples across entire RH range examined and (b) droplet and crystal-loaded samples below the DRH of NaCl. The dashed line represents the upper bound of the 95% confidence interval of volume loss measured on clean areas outside the printed salt pattern.

4.1.4.2 Surface State Immediately After Exposure

Two additional experiments were carried out to elucidate the state of the droplet and crystal-loaded surfaces during the exposures at humidity levels below the deliquescent point of NaCl. In the first experiment, sets of droplet-loaded coupons were placed in the isohumidity chambers for 12 h. After this, they were moved from the chambers into the lab (at 60% RH) and immediately placed in the humidity controlled inkjet chamber (at the same humidity from which they were came) and imaged. The resulting micrographs are shown in Figure 4.5**.** These images show that, after 12 hours, the majority of droplets were in a deliquesced state for 71% RH, less than half were deliquesced at 64% RH with the remainder of the NaCl crystallized, and all had crystallized at 53% RH and below (not shown).

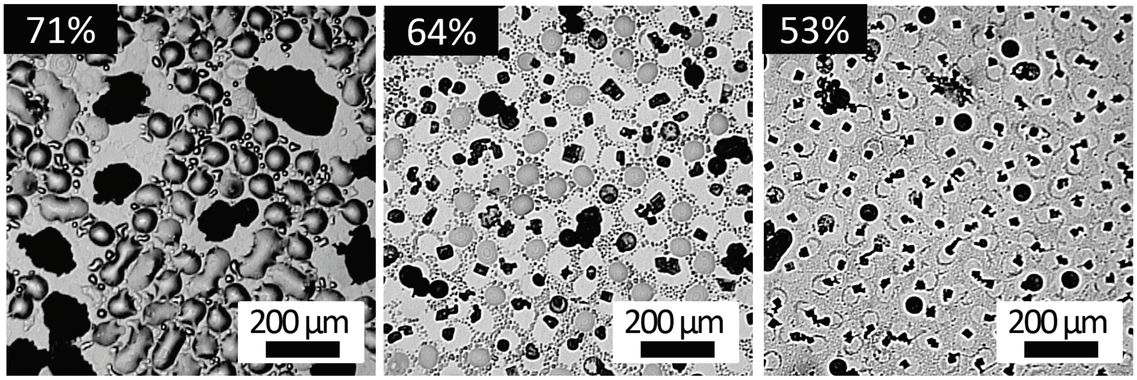

Figure 4.5 Optical micrographs of droplet-loaded coupons immediately after 12 h exposure below the DRH of NaCl. The RH was controlled at the indicated value during the imaging. The black regions are rust formations.

The experiment was repeated using crystal-loaded coupons, except removal occurred after 7 days of exposure. The resulting micrographs are shown in Figure 4.6**.** Examination revealed pools of electrolyte had developed on the surface of the samples exposed at 64% and 71% RH with the original NaCl deposits apparently having partially (64%) or fully (71%) dissolved forming this electrolyte. Although electrolyte was not visible at 53% RH, needle-like crystals had developed between the original NaCl deposits and small crystallites peppered the surface around actively corroding sites. Note that a larger particle size than that used for the profilometry experiments was used in this experiment to ensure proper visualization given the magnification limitations of the microscope utilized. The same behavior was seen for both deposit sizes.

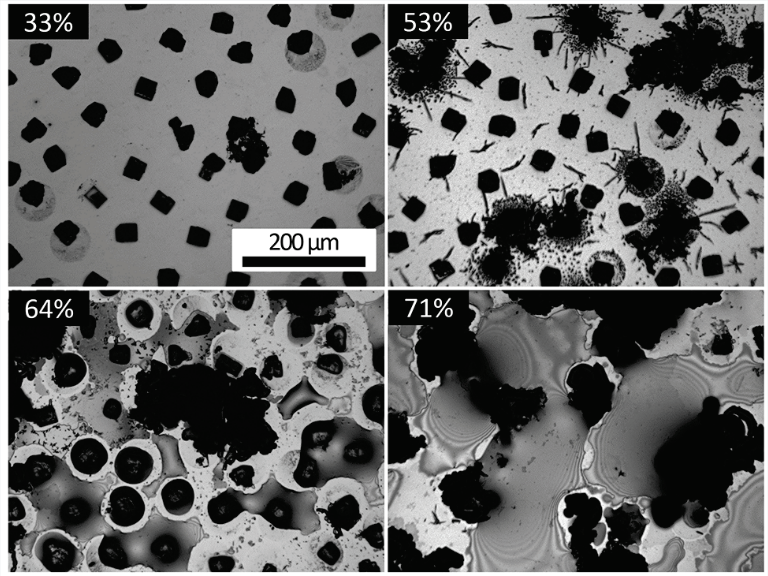

Figure 4.6 Optical micrographs of crystal-loaded coupons immediately after 7 d exposure below the DRH of NaCl. The RH was controlled at the indicated value during the imaging. The black regions are rust formation and electrolyte pools are readily visible in the 64% and 71% images.

4.1.4.3 Ex-situ Surface Analyses

After exposure and optical imaging, the samples from the 7 day crystal experiment described above were examined using SEM-EDS and Raman microscopy. Composite elemental maps of some of these samples are shown in Figure 4.7**.** Importantly, they show that the pools of electrolyte and needle-like crystals seen in Figure 4.6 are Na-O rich and Cl deficient. No evidence of Na-O deposits nor areas exhibiting enrichment of these two elements could be located on the sample exposed at 33% RH. The mottled magenta areas, most notable at the seven o'clock positions with respect to the large NaCl crystals, are artifacts related to shadowing effect from the position of the EDS detector.

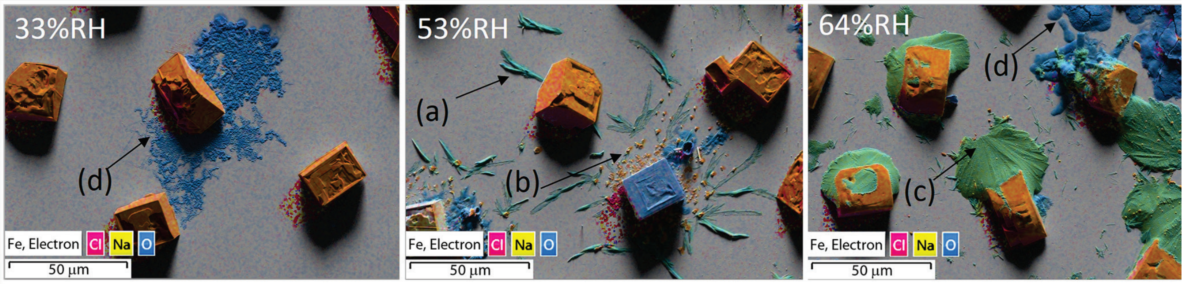

Figure 4.7 Composite SEM-EDS images of crystal-loaded coupons shown in Figure 4.6. The large cubic crystals are the original NaCl deposits (orange). The needles (a) and solidified pools (c) are Na-O rich phases (teal). Small NaCl particles are indicated by (b). The areas exemplified by (d) are rust (blue).

Raman analysis of the Na-0 rich dried pools and needle form phases, represented by (a) and (c) in Figure 4.7, indicates that they are two different compounds, Figure 4.8. Spectra of the dried pools shared all of the major features with the reference $Na_2CO_3.10H_2O$ salt analyzed, with both exhibiting the C-O stretch band at 1079 cm^{-1} which is characteristic of this compound [36]. Raman spectra of the needle-form crystals exhibited strong peaks at 1062 and 1029 cm^{-1}. The 1062 peak is characteristic of the C-O stretch band of $NaHCO_3.Na_2CO_3.2H_2O$ [37]. The other peaks of this spectrum did not match this compound nor could other appropriate matches be located in the literature. Phases similar in appearance and nearly identical in spectral signature, Figure 4.8, were also found in association with the NaOH deposits on the (inert) impedance sensor after humidity cycling.

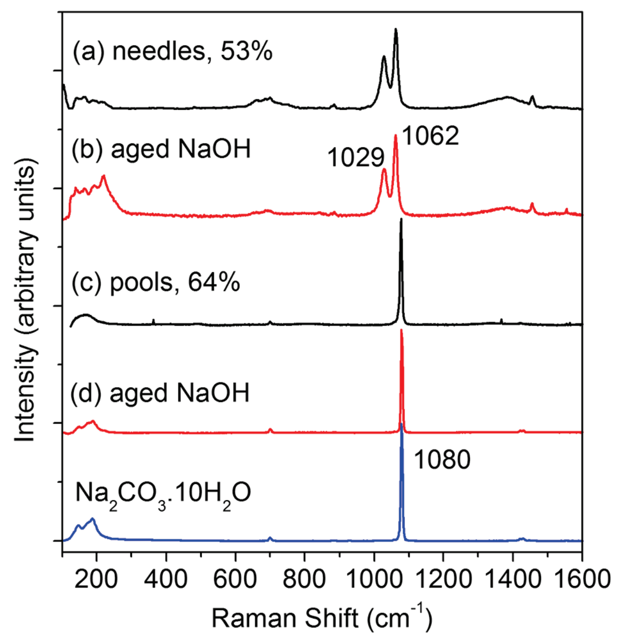

Figure 4.8 Raman spectra of (a) needle-like crystals similar in appearance and location to those labeled in Figure 7 for the 53% coupon; (b) needle-like crystals associated with the NaOH deposits on the interdigitated sensor after humidity cycling; (c) crystallized pools similar in appearance and location to those labeled in Figure 7 for the 64% coupon; (d) persistent solid associated with the NaOH deposits on the sensor during humidity cycling. The bottom spectrum is that of a reference salt.

4.1.4.4 Humidity Cycling of Simulated Anolyte and Catholyte

Drops of NaOH (catholyte simulant) deposited on an interdigitated sensor were subjected to three consecutive humidity ramping cycles as described in the experimental section. At the start of the experiment, when the RH was 80% and within a few minutes after depositing the drops, thin films of secondary droplets spreading from the original NaOH drops became notable, Figure 4.9. This spreading was reminiscent of the spreading behavior of alkaline films (secondary spreading) seen during corrosion of NaCl droplets on steel and other alloys [12, 38]. The typical impedance response, |Z|, noted during humidity cycling is given in Figure 4.10. As exemplified in this figure, two major transition points in |Z| occurred – one at 50 ± 3% RH during dehumidification and the other at 60 ± 4% RH during humidification. These transition points correlated to the visual transformation of a large volume of electrolyte to needle-like crystals, images (a) and (b), and the onset of deliquescence of these crystals respectively, (c) and (d) in Figure 4.10. A certain amount of insoluble solid also persisted during the entirety of the humidity cycling which are seen as the defined features in the puddles of images (a) and (d). Impedance measured at 0.2Hz followed similar trends, but remained at least an order of magnitude below the stray impedance baseline (represented as the unity value of the normalized impedance) throughout the experiment. At humidity levels below the solid-liquid phase transitions, $|Z|_{0.2Hz}$ moved in step with RH down to the lowest RH achieved, indicating significant admittance contribution from the presence of the deposited particles themselves.

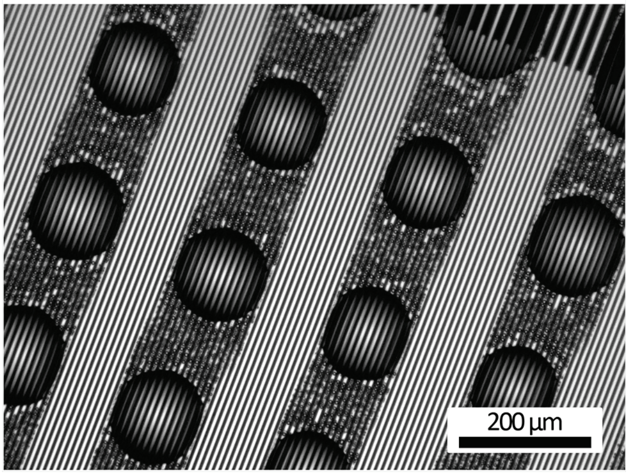

Figure 4.9 Optical micrograph of NaOH drops (catholyte simulant) at 80% RH and 10 min after depositing onto the interdigitated sensor. The wide, dark grey bands apparent between the drops are thin films of secondary droplets that emanated from the main drops after placement.

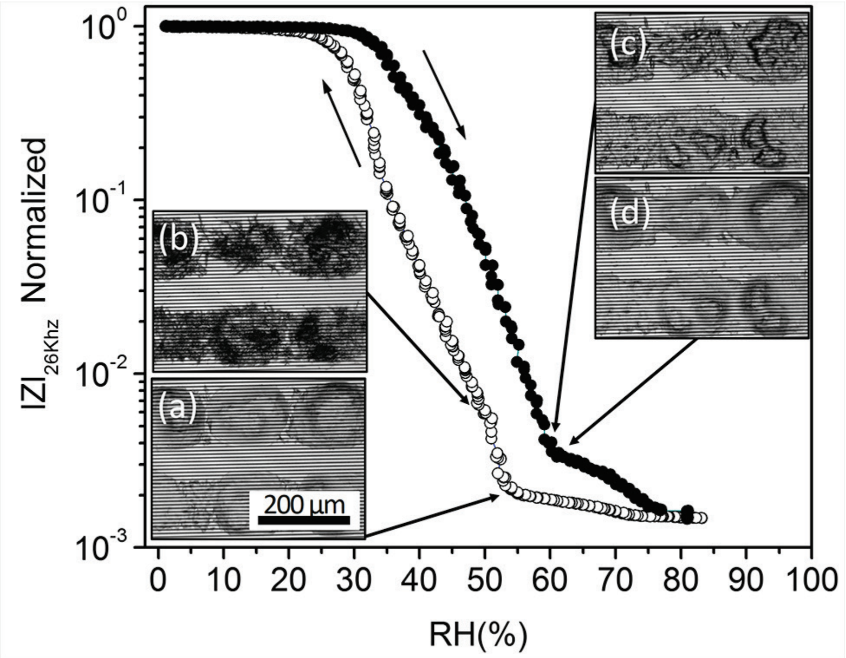

Figure 4.10 Impedance measured across an interdigitated sensor loaded with NaOH drops (catholyte simulant) during humidity cycling. Open circles are measurements taken during dehumidification and closed are those taken during humidification. Inset are micrographs corresponding to (a) beginning of the appearance of needle-like crystals, (b) completion of needle efflorescence, (c) onset of dissolution of needles, and (d) their complete dissolution.

A replicate experiment was carried out to examine the hygroscopic behavior of the anolyte simulant, NaCl-$FeCl_2$ drops. The results of one of the humidity cycles are shown in Figure 4.11, which was typical for all cycles. During dehumidification, impedance rose sharply at 49 ± 2% RH while during humidification it dropped precipitously at 55 ± 2% RH. These transitions correlated with visual shrinkage and transformation of liquid droplets to crystalline-appearing deposits, images (a) and (b), and the formation of droplets respectively, images (c) and (d). The disparity in impedance values between the dehumidification and humidification curves when the droplets were deliquesced in both cases (>60% RH) is representative of the overall increase in impedance measured across the sensor from cycle to cycle during the experiment. This increase correlated with the growth of rust visible in the deposits. As with the NaOH experiment, impedance measured at 0.2 Hz followed similar trends, but remained significantly below the stray impedance baseline throughout the experiment and moved in step with RH at humidity levels below the solid-liquid phase transitions.

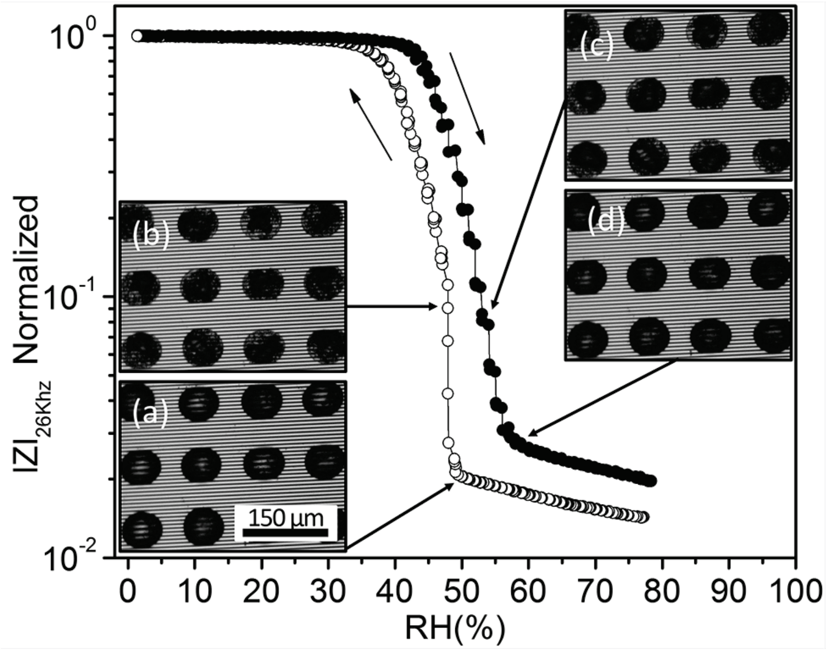

Figure 4.11 Impedance measured across an interdigitated sensor initially loaded with NaCl-FeCl$_2$ drops (anolyte simulant) during humidity cycling. Open circles are measurements taken during dehumidification and closed are those taken during humidification. Inset are micrographs taken (a) just prior to efflorescence of visible electrolyte, (b) after efflorescence, (c) at the onset of visible electrolyte growth and (d) after a major deliquescence event.

4.1.5 Discussion

The results presented here show that the deliquescence point of NaCl in no way represents a critical RH threshold below which corrosion cannot initiate nor be sustained at a considerable rate for mild steel. To illustrate this, the 30 day volume loss data presented in Figure 4.4 were converted to a per annum corrosion rate in Figure 4.12**.** From this figure, it is clear that, although corrosion loss was detectable at 33% RH, the rate of corrosion was negligible at 0.03 µm/year. At ≥53% RH, however, corrosion rates averaged over 300 to 2500 times higher (10 to 75 µm/year). In fact, the corrosion rate at the DRH was not significantly different than at 64% RH. It is also important to point out that the no significant difference in volume loss, and hence corrosion rate, at 30 d was observed between the crystal and the drop samples.

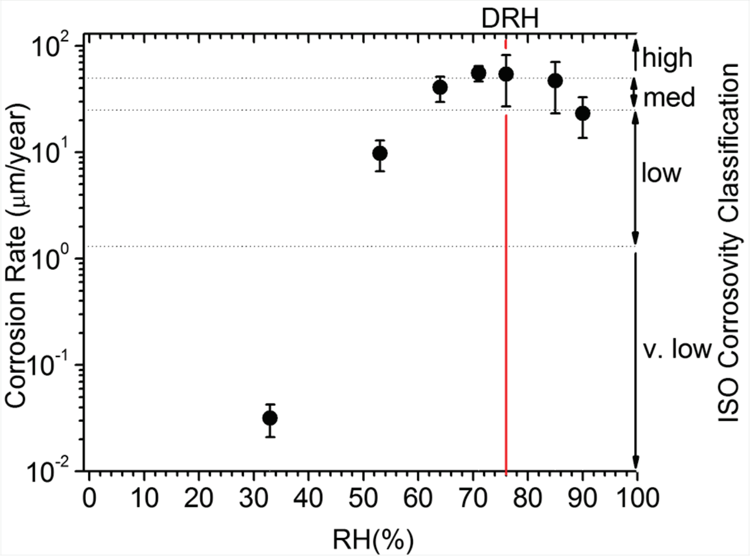

Figure 4.12 30 d volume loss data from droplet-loaded experiments normalized to a per annum corrosion rate and compared to the DRH of NaCl (76%RH) and the ISO 9223 atmospheric corrosivity classifications for steel [66].

The minimum RH at which sustained corrosion was detectable was 33% RH in these experiments, regardless of the initial state of the deposits (i.e., drops or crystals), Figure 4.4. This finding is not unique in the sense that mild steel has been reported to corrode in the presence of NaCl below its DRH (76%) in both the case of drying of droplets and by initiation under crystalline deposits of this salt down to at least 50% RH [16,17,20-22], as discussed earlier. Our findings, however, lower the observed threshold for initiation and sustainment by 20% RH.

In the remainder of the discussion we will focus on relating the hygroscopic behavior of the surface constituents (i.e., NaCl and corrosion chemistries) to the damage experienced by the coupons. In the first section the results will be discussed in the context of phenomena that can initiate and sustain corrosion below the deliquescence point. In the second section we relate this understanding of hygroscopic behavior to the attack morphology witnessed on the steel surfaces.

4.1.5.1 Corrosion below the Deliquescence Point

Corrosion below the deliquescence point of a hygroscopic salt such as NaCl could be initiated or sustained by a number of physical phenomena that permit the presence of electrolyte including (1) the presence of adsorbed water associated with the salt on the steel surface, (2) the existence of supersaturated brine resulting from crystallization point suppression (i.e., deliquescence-efflorescence hysteresis), and (3) the hygroscopicity of the corrosion chemistry. Each of these phenomena is examined here in the context of the present results and their broader impact on the current understanding of wetting and drying behavior of atmospherically exposed surfaces contaminated with hygroscopic species.

Initiation

We attribute the initiation of corrosion under crystalline NaCl deposits to adsorbed water associated with the salt crystals in contact with steel. Preston and Sanyal [16] and Yang [20], who have reported corrosion under crystalline hygroscopic deposits, have speculated this to be the cause, but without further explanation. Here we explore this issue in more detail, with focus on the potential role of adsorbed water on the surface of the NaCl crystallites.

Data available in the literature regarding adsorbed water measured on NaCl crystal surfaces, along with measures of ionic conductance across those surfaces with respect to relative humidity indicate that there may be sufficiently conductive electrolyte available on the surface of crystalline NaCl down to at least 40-50% RH [39-43]. Findings generally indicate that, as humidity increases from 0% RH, water first adsorbs onto surface defect sites or in the form of small 2D islands with partial coverage up to ~40% RH [41]. Between ~40-50% RH, coverage increases rapidly to the point where it exhibits hydrogen bonding properties resembling that of bulk water [43]. Additionally, sharp increases in measured conductance [29,39,42] along with the occurrence of observable restructuring of the surface, such as step movement [40,44], occur at an above this range. These findings together suggest that at and above 40-50% RH solvation and conduction of Na^+ and Cl^- occurs [41, 45]. As an example of this effect, results of impedance measured across an interdigitated electrode sensor loaded with NaCl particles is plotted along with the estimated water coverage of a NaCl (001) face according to Foster and Ewing [43] are given in Figure 4.13**.** It is notable here the impedance data shown in Figure 4.13 was collected from the same particles (in terms of solution used, size, and deposition methodology) as used for this study.

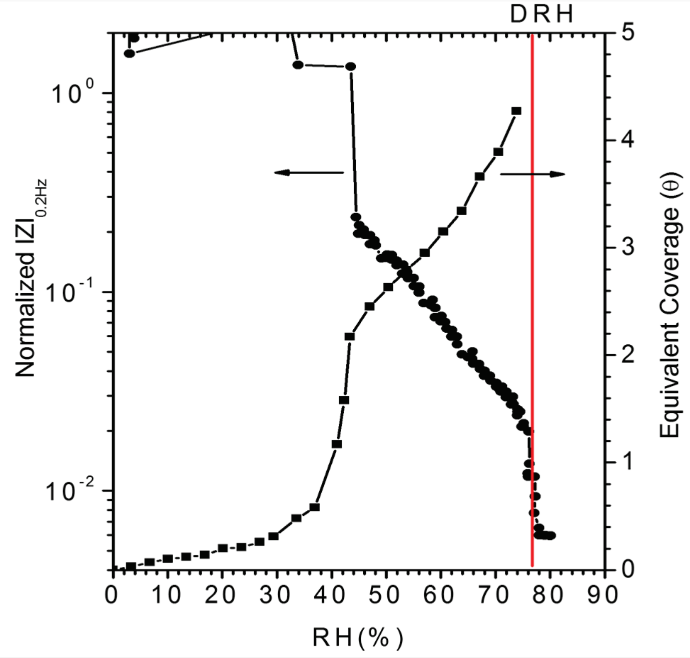

Figure 4.13. Impedance measured across an interdigitated sensor loaded with NaCl crystals during humidification from a related experiment [29] and the estimated equivalent coverage of water sorbed on a NaCl 001 surface as indicated by FTIR spectroscopy [43].

Since the salt is in intimate contact with the metal surface, water adsorption properties of the metallic surface along with potential for capillary condensation must be considered. Water adsorption on many planar metals and oxides is characterized by gradual increase with RH, with approximately one layer of equivalent monolayer coverage near 20% RH increasing to two or five layers by 50% RH [34,46,47]. The first monolayer of water has been demonstrated to be immobile with an ice-like configuration [48]. At two to three monolayers, according to Phipps and Rice [46], ionic mobility will be an order of magnitude less than that of a typical bulk solution. Thus, at ~50% RH there should be sufficient conduction both on the salt and the metal surface for corrosion to be possible. Furthermore, capillary condensation between contact points of the salt and metal surface may allow for the presence of conductive electrolyte well below 40-50% RH [7], which may explain the initiation of corrosion down to 33% RH. Although information is lacking with regard to this phenomenon in the particular case of the NaCl-steel system under examination here, evidence for the development of condensate in the form of small droplets as a result of AFM tip contact with mica surfaces down to 33% RH has been well documented [49].

Sustainment

Although it appears that adsorbed water can initiate corrosion under hygroscopic crystals, it does not seem probable that the amount of available adsorbed water alone would be sufficient to sustain corrosion at the rates observed down to 53% RH in our study. Two probable possibilities are examined here- the existence of supersaturated brines below the deliquescence point and the development of hygroscopic corrosion chemistries.

Deliquescence-Efflorescence Hysteresis

In the case of dehumidification of deliquesced droplets, one probable explanation for sustainment of corrosion below the DRH is lack of droplet drying due to kinetic limitations of crystallization (efflorescence) [8]. This phenomena, termed deliquescence-efflorescence hysteresis, is commonly observed in single component microdroplets of aqueous salt solutions either in aerosol form or sequestered on inert substrates [7]. In these cases, crystallization of the supersaturated solutions occurs at a well-defined relative humidity point or range during dehumidification, termed the efflorescence relative humidity (ERH). In previous work, we had shown that NaCl droplets on the inert interdigitated sensor, of the same size and solution as used for our isohumidity experiments here, effloresced at 50%, even after exposing to humidity levels below the DRH for up to 12 hours [29]. The NaCl droplets on the steel coupons during our isohumidity experiments, however, exhibited a greater dispersion of efflorescence relative humidity points, after 12 hours of exposure, as evidenced in Figure 4.5. All droplets remained in deliquesced state at 71% RH, with less than half deliquesced at 64% and all drops had crystallized by 53% RH and below. The large inter-droplet ERH variability on the steel surfaces compared to that observed on the impedance sensor may be due to surface heterogeneities that act as favorable nucleation sites, such as rust, or the change in chemistry in these droplets due to corrosion. Nonetheless, these results show that although useful as a guide in determining RH range in which deliquesced electrolyte may be present during drying, the ERH of single salt microdroplets on clean, inert surfaces or in aerosol form, may not strictly translate to its behavior on a reactive surface. Furthermore, results from the isohumidity experiments where the deposits were initially effloresced indicate that hysteresis is not a necessary condition for sustainment of considerable corrosion below the deliquescence point, Figure 4.4.

Hygroscopic Behavior of Corrosion Chemistry

Within the time frame of our experiments, optical examination and profilometry results reveal that corrosion is localized (i.e., pitting). Thus, one could expect the development of distinct electrolyte compositions at the anodic sites (anolyte) and the cathodic sites (catholyte). The catholyte would be expected to be an alkaline electrolyte, which develops from cathodic reduction of dissolved oxygen [12, 15, 21]. The anolyte would be a Fe-Cl rich acidic electrolyte, which develops as a result of the dissolution and subsequent hydrolysis of iron [50-52]. Sustainment of significant corrosion below the deliquescence point in both crystal and droplet cases can be largely attributed to the development of hygroscopic catholyte and anolyte chemistries. A schematic interpretation of the evolution of the surface chemistry for the specific case of corrosion initiation under crystals in our experiments is given in Figure 4.14, which will be referenced in the discussion below.

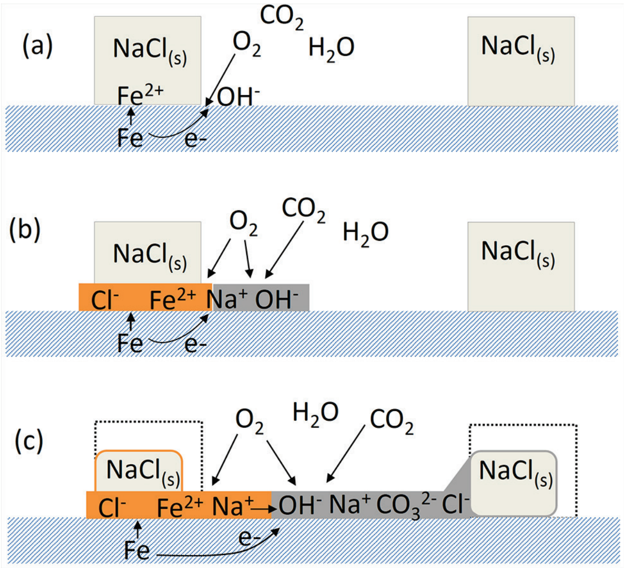

Figure 4.14. Schematic interpretation of the development of corrosion chemistry associated with NaCl crystals on a mild steel substrate below 76%RH. Upon initiation of corrosion (a), discrete chemistries develop at the anodic (orange) and cathodic (grey) sites (b), the extent to which is dependent on time and humidity level. At higher RH and longer times (c), as seen in Figure 4.6 for 64% and 71%, puddles of catholyte develop on the surface that can substantially dissolve the NaCl crystals.

Catholyte

Ex-situ analysis of the electrolyte pools that developed on coupons exposed at ≥64% RH and the needle-form crystals which developed on those at 53% RH indicate chemistries consistent with the formation of an alkaline electrolyte at cathodic sites. This production of hydroxyl ions from the aqueous reduction of dissolved oxygen would cause the migration of Cl^- ions away from the cathode sites, and Na^+ ions towards them to maintain electroneutrality. This leads to a sodium-rich, chloride-poor alkaline solution [12, 15], as illustrated in Figure 4.14. In the presence of air, as is the case in our experiments, carbonation of this catholyte occurs [38, 53]. When dried, such an electrolyte would be expected to produce exactly the solids observed in the pools and needles, Figure 4.8. It should be noted that development of sodium-rich alkaline films emanating from aqueous NaCl droplets under which corrosion is taking place, termed secondary spreading, has been reported by a numerous researchers for a variety of alloy systems above the DRH, including mild steel [12,38,54,55]. To our knowledge, this is the first reported instance of such phenomena occurring substantially below the DRH.

The deliquescence behavior of the catholyte is critical to the corrosion below the DRH. As shown in Figure 4.10, a large volume of the simulated catholyte (NaOH) retains its aqueous form down to 50% RH at which point the formation of needle-form crystals was observed. Although this major phase transition event takes place in this RH range, one could expect some amount of electrolyte to be present down to at least the deliquescence point of NaOH, 6% RH [56], provided its production rate at the cathodic site exceeds that of its conversion rate to carbonate solution. Evidence for such a low RH with conducting electrolyte can be found in the significant admittance observed for aged NaOH deposits on the sensor down to <6% RH. The occurrence of corrosion down to 33% RH is also evidential of some form of catholyte, although not directly detectable. On the opposite end of the RH spectrum, $Na_2CO_3.10H_2O$ has a DRH of 90% [57], and was found both on steel samples exposed above 64% RH after drying to near 0% and on the impedance sensors throughout humidity cycling. In summary, due to the transient nature of the catholyte chemistry a single DRH point cannot be expected, but it is reasonable to expect some form of conductive catholyte present across nearly the entire RH range provided active corrosion is occurring.

Anolyte

The aqueous chemistry that forms at the anodic sites associated with the NaCl deposits is expected to be composed in large part of Fe^{2+}, Na^+, Cl^-, and H^+, forming an acidic ferrous chloride solution. Both $FeCl_2.4H_2O$ and $FeCl_2.2H_2O$ are known to precipitate out of such anolyte solutions in corrosion pits on steel under NaCl deposits as a result of atmospheric exposure [4, 51, 58]. The DRH of the four hydrate salt has been reported to be 55 to 59% RH at room temperature [26, 59, 60]. Information on the DRH of $FeCl_2.2H_2O$ is lacking, but upon humidification of this salt from near 0% RH, it has been observed to convert to the four hydrate at ~15% RH [26]. Both Turgoose [26] and, later, Watkinson [61] reported active corrosion of iron in contact with $FeCl_2.4H_2O$ crystals down to 20% RH, albeit at a slow rate. Watkinson attributed the corrosion under the solid salt to waters of hydration. An alternative explanation in light of the discussion above is that corrosion was initiated by unbound, adsorbed water. Watkinson also proposed that the deliquescence point of the four hydrate salt serves as a threshold between insignificant and significant corrosion rates of $FeCl_2$-contaminated iron, although no evidence was provided [62]. Nonetheless, their results show that, although corrosion was detectable in our study only down to 33% RH, a considerable presence of such phases may sustain corrosion at even lower humidity levels.

Humidity cycling of the Fe-Cl-Na deposits, our anolyte simulant, on the impedance sensor in this study indicated major and repeated liquid solid phase transitions between 47% and 57% RH, which are in the range of the DRH of $FeCl_2.4H_2O$ and also the ERH of NaCl. This result confirms that above ~50% RH, deliquesced anolyte will be present. Formation of insoluble precipitate formed in these deposits as would be expected due to oxidation of Fe^{2+} forming FeOOH polymorphs [63]. The significant admittance contribution of the deposits on the sensor in step with RH down to <2% RH is likely indicative of some amount of water present allowing for ionic conduction. The state of this water, whether as trapped brine [29] or adsorbate on the salt surfaces, cannot be distinguished.

The large disparity in corrosion rate observed between 33% and 53% RH in this study is hypothesized to be due to the major liquid-solid phase transitions of the anolyte and catholyte. Both the measured and expected transitions for these chemistries center around the ~50% RH mark. These transitions would be expected to largely shut down the electrochemical reactions by reducing the area available for their occurrence along with minimizing the ability for solvation and transport of ions between the anode and cathode. Although both the anolyte and catholyte simulants exhibited significant admittance down to low RH, it is proposed that the hygroscopic behavior of the anolyte is what governs corrosion below the DRH of NaCl. Comparison of Figures 4.10 and 4.11 show that although both simulants exhibit transitions in impedance near 50% RH, the transitions of the anolyte are more abrupt with decreasing RH than the catholyte. For example, by an RH of 40%, the impedance across of the anolyte is nearly 0.7 times that of the stray impedance baseline (unity) whereas the impedance of the catholyte is only 0.03 of the baseline. The catholyte does not reach 0.7 of the baseline until < 30% RH, likely due to the presence of deliquesced NaOH as discussed above.

4.1.5.2 Relationship between Hygroscopic Behavior and Attack Morphology

The distinct differences in attack morphology seen with respect to relative humidity may also be related to the major phase transitions of the anolyte and catholyte and their effect on the separation of anodic and cathodic reactions. The attack morphology observed on the coupons at ≤53% is characterized by localized shallow pitting with rust patterns similar in appearance to salt creep formations [64]. The morphology transitions to more sparse and deep pits at ≥64% RH, Figures 4.2 and 4.3. The disparity is most evident after the 30 day exposures. This change in morphology is in line with the idea that the maximum pit size is controlled by ohmic drop between the cathodic and anodic sites and the cathodic current available to sustain a pit [65]. If areal coverage of catholyte (secondary spreading) relates to cathodic current, minimizing this area would minimize the pit size and cause shallower pits. The spatial frequency of pitting would be higher as the individual salt crystals would not interact. At high humidity levels, corrosion is truly localized with the development of sparse and deep pits.

4.1.6 Conclusions

Steel surfaces loaded with NaCl particles were subjected to isohumidity exposures for up to 30 d. The resulting attack and corrosion chemistry that developed were characterized. The wetting and drying behavior of simulated corrosion chemistries was studied using an impedance sensing method. Taken together, these results allow the following conclusions to be drawn:

1. The deliquescence RH of NaCl (76%) does not serve as a RH threshold for either the corrosion loss rate or the attack morphology versus RH trends. The minimum RH at which detectable corrosion was sustained under NaCl deposits was 33% RH. The largest inflection in corrosion loss versus RH occurred between 33 and 53% RH, where rates went from 0.3 to 10 μm/y (30 d normalized), respectively. At times greater than 7 d, rates from 53% to 71% RH were comparable to those at

76% to 90%. These findings were observed regardless of whether the NaCl deposits were initially crystalline or deliquesced (droplet) form.

2. The initiation of corrosion under crystalline NaCl deposits well below their DRH can be explained in terms of the presence of adsorbed water associated with the salt crystals in contact with the steel. There is likely sufficiently conductive electrolyte available on the NaCl crystals to initiate corrosion down to at least 40-50% RH, and capillary condensation between the NaCl and steel surfaces may account for corrosion down to 33% RH.
3. Sustainment of corrosion at considerable rates down to 53%RH and the large change in attack morphology between 33% and 53% is attributed to the hygroscopic behavior of the chemistry that developed at the anode and cathode sites. Impedance measurements across simulants of these corrosion chemistries, air-aged $FeCl_2$-NaCl and NaOH, respectively, indicated major liquid-solid transitions (i.e., wet and dry) at ~50% RH. Drying below this level may largely shut down electrochemical reactions by minimizing the ability for solvation of ferrous ions at the anode and transport of ions between the anode and cathode.
4. An increase in the degree of localized corrosion with increasing RH was observed above 33% RH and rationalized in terms of the changes in the amount of cathode area (and hence cathode current) available, as indicated by the increasing coverage of an alkaline catholyte film that was spread between actively corroding sites.

4.1.7 References

1. G. A. El-Mahdy, A. Nishikata and T. Tsuru, *Corros. Sci.*, **42**, 1509 (2000).
2. M. Stratmann and H. Streckel, *Corros. Sci.*, **30**, 681 (1990).

3. T. Tsuru, A. Nishikata and J. Wang, *Mater. Sci. Eng., A*, **198**, 161 (1995).
4. S. Li and L. H. Hihara, *J. Electrochem. Soc.*, **159**, C147 (2012).
5. E. Dubuisson, P. Lavie, F. Dalard, J.-P. Caire and S. Szunerits, *Corros. Sci.*, **49**, 910 (2007).
6. C. Chen and F. Mansfeld, *Corros. Sci.*, **39**, 409 (1997).
7. E. Schindelholz and R. G. Kelly, *Corros. Rev.*, **30**, 135 (2012).
8. I. S. Cole, W. D. Ganther, J. D. Sinclair, D. Lau and D. A. Paterson, *J. Electrochem. Soc.*, **151**, B627 (2004).
9. S. B. Lyon and J. P. Cai, *Corros. Sci.*, **47**, 2956 (2005).
10. P. R. Roberge, in *Uhlig's Corrosion Handbook*, 3 ed., R. Revie Editor, p. 299, John Wiley & Sons, Hoboken, New Jersey (2011).
11. M. Apted, R. Arthur, F. King, D. Langmuir and J. Kessler, *JOM*, **57**, 43 (2005).
12. J. Zhang, J. Wang and Y. Wang, *Corrosion*, **61**, 1167 (2005).
13. S. X. Li and L. H. Hihara, *Corros. Eng. Sci. Technol.*, **45**, 49 (2010).
14. J. Wang and Y. Wang, *Corrosion*, **61**, 264 (2005).
15. J. Weissenrieder and C. Leygraf, *J. Electrochem. Soc.*, **151**, B165 (2004).
16. R. S. Preston and B. Sanyal, *J. Appl. Chem.*, **6**, 26 (1956).
17. R. Ericsson, *Mater. Corros.*, **29**, 400 (1978).
18. Z. Y. Chen, S. Zakipour, D. Persson and C. Leygraf, *Corrosion*, **60**, 479 (2004).
19. D. Liang, H. Allen, G. Frankel, Z. Chen, R. Kelly, Y. Wu and B. Wyslouzil, *J. Electrochem. Soc.*, **157**, C146 (2010).
20. L. Yang, R. T. Pabalan, L. Browning and D. S. Dunn, in *Materials Research Society Symposium: Scientific Basis for Nuclear Waste Management XXVI, December 2, 2002 - December 5, 2002*, p. 791, Materials Research Society Symposium - Proceedings, Boston, MA, United states (2003).
21. J. Forsberg, J. Hedberg, C. Leygraf, J. Nordgren and L.-C. Duda, *J. Electrochem. Soc.*, **157**, C110 (2010).
22. C. Li, Y. Ma, Y. Li and F. Wang, *Corros. Sci.*, **52**, 3677 (2010).
23. D. Fyfe, in *Corrosion*, L. L. Shreir, R. A. Jarman and G. T. Burstein Editors, p. 2.26 Butterworth Heinemann, Oxford, England (1994).
24. F. Mansfeld, *Mater. Corros.*, **30**, 38 (1979).
25. D. Thickett, The effect of RH on archaeological iron deterioration, in *Archaeological Metal Finds- From Excavation to Exhibition, October 11-13th 2006*, ICOM-CC subworking group AIAE, Mannheim, Germany (2006).
26. S. Turgoose, *Studies in Conservation*, 97 (1982).
27. J. Cai, R. A. Cottis and S. B. Lyon, *Corros. Sci.*, **41**, 2001 (1999).
28. I. S. Cole, *Corros. Eng. Sci. Technol.*, **39**, 89 (2004).
29. E. Schindelholz, L.-k. Tsui and R. G. Kelly, *J. Phys. Chem. A*, **118**, 167 (2013).
30. C. O'Dowd and G. de Leeuw, *Philosophical Transactions of the Royal Society A: Mathematical, Physical and Engineering Sciences*, **365**, 1753 (2007).
31. E. Schindelholz and R. G. Kelly, *Electrochem. Solid-State Lett.*, **13**, C29 (2010).
32. N. S. Azmat, K. D. Ralston, B. C. Muddle and I. S. Cole, *Corros. Sci.*, **53**, 3534 (2011).
33. N. Mi, M. Ghahari, T. Rayment and A. J. Davenport, *Corros. Sci.*, **53**, 3114 (2011).

34. C. Leygraf and T. Graedel, *Atmospheric Corrosion* John Wiley and Sons, New York (2000).
35. W. C. Keene, M. S. Long, A. A. P. Pszenny, R. Sander, J. R. Maben, A. J. Wall, T. L. O'Halloran, A. Kerkweg, E. V. Fischer and O. Schrems, *Atmos. Chem. Phys.*, **9**, 7361 (2009).
36. J. F. Widmann, C. L. Aardahl and E. J. Davis, *TrAC, Trends Anal. Chem.*, **17**, 339 (1998).
37. M. Steinberg and K. Schofield, *Combust. Flame*, **129**, 453 (2002).
38. Z. Y. Chen, D. Persson and C. Leygraf, *Corros. Sci.*, **50**, 111 (2008).
39. M. Hucher, A. Oberlin and R. Hocart, *B. Soc. Fr. Mineral. Cr.*, 320 (1967).
40. H. Shindo, M. Ohashi, K. Baba and A. Seo, *Surf. Sci.*, **357–358**, 111 (1996).
41. B. Finlayson-Pitts, *Chem. Rev.*, **103**, 4801 (2003).
42. G. Simkovich, *J. Phys. Chem.*, **67**, 1001 (1963).
43. M. C. Foster and G. E. Ewing, *J. Chem. Phys.*, **112**, 6817 (2000).
44. A. Verdaguer, G. Sacha, H. Bluhm and M. Salmeron, *Chem. Rev.*, **106**, 1478 (2006).
45. D. Wales and G. Ewing, in *Intermolecular Forces and Clusters II*, p. 1, Springer Berlin / Heidelberg (2005).
46. P. B. Phipps and W. D. Rice, in *Corrosion Chemistry*, p. 235, American Chemical Society (1979).
47. S. Lee and R. W. Staehle, *Corrosion*, **53**, 33 (1997).
48. M. A. Henderson, *Surf. Sci. Rep.*, **46**, 1 (2002).
49. L. Xu, A. Lio, J. Hu, D. F. Ogletree and M. Salmeron, *J. Phys. Chem. B*, **102**, 540 (1998).
50. A. Turnbull, *Corros. Sci.*, **23**, 833 (1983).
51. L. S. Selwyn, P. J. Sirois and V. Argyropoulos, *Studies in Conservation*, **44**, 217 (1999).
52. M. R. Gilberg and N. J. Seeley, *Studies in Conservation*, **26**, 50 (1981).
53. A. K. Neufeld, I. S. Cole, A. M. Bond and S. A. Furman, *Corros. Sci.*, **44**, 555 (2002).
54. Z. Y. Chen, D. Persson, A. Nazarov, S. Zakipour, D. Thierry and C. Leygraf, *J. Electrochem. Soc.*, **152**, 342 (2005).
55. R. Jia, C. Yan and F. Wang, *J. Mater. Sci. Technol.*, 225 (2009).
56. P. W. Winston and D. H. Bates, *Ecology*, **41**, 232 (1960).
57. A. Arnold and K. Zehnder, in *The conservation of wall paintings*, p. 103, London (1991).
58. N. Mi, Synchrotron x-ray studies of atmospheric pitting corrosion of stainless steel, in *School of Metallurgy and Materials*, p. 184, University of Birmingham (2013).
59. G. M. Richardson and R. S. Malthus, *J. Appl. Chem.*, **5**, 557 (1955).
60. E. McCafferty, *J. Electrochem. Soc.*, **128**, 39 (1981).
61. D. Watkinson and M. T. Lewis, *Studies in Conservation*, **50**, 241 (2005).
62. D. Watkinson and M. Lewis, in *Metal 04: Proceedings of the International Conference on Metals Conservation*, p. 4 (2004).
63. S. Oh, S. Kwon, J. Lee, J. Yoo and W. Choo, *Corrosion*, **58**, 498 (2002).
64. W. J. P. van Enckevort and J. H. Los, *Crystal Growth & Design*, **13**, 1838 (2013).

65. Z. Y. Chen, F. Cui and R. G. Kelly, *J. Electrochem. Soc.*, **155**, C360 (2008).
66. ISO, 9223:1992(E) Corrosion of metals and alloys- Corrosovity of atmospheres-Classification, in, ISO, Geneva, Switzerland (1992).
67. T. Shinohara, S.-I. Motoda and W. Oshikawa, *Zairyo to Kankyo/ Corrosion Engineering*, **54**, 375 (2005).

4.2 Part II: $MgCl_2$, Seawater

This paper is the second of two that seek to elucidate the relationship between the hygroscopic behavior of sea salt aerosol proxies and the humidity-induced corrosion response of mild steel contaminated with them. In this work, artificial seawater (ASW) and $MgCl_2$ were examined. The wetting and drying behavior of ASW was characterized by impedance measurements across an interdigitated electrode sensor. Mild steel loaded with ASW and $MgCl_2$ microparticles was subjected to isohumidity exposures for up to 30 days. The resulting damage evolution was quantified by optical profilometry. The corrosion chemistry that developed was identified using EDS and Raman spectroscopy. Together, the results bring into question whether surfaces contaminated with sea salt aerosol ever truly dry in ambient outdoor environments. Sustained corrosion was detectable down to 11% RH for $MgCl_2$ and 23% RH for ASW, with significant admittance of ASW deposits at <2% RH even after 24 h, likely due to fluid trapping under a solid salt crust. Trends in corrosion loss versus RH were not directly reflective of the major liquid-solid phase transitions observed or predicted for ASW or $MgCl_2$ alone. In light of these findings, common time of wetness determination methods are contended to be fatally flawed as quantitative indicators of electrolyte presence and corrosion rate.

4.2.1 Introduction

This paper is the second of two that seek to further the understanding of the relationship between relative humidity, the hygroscopic behavior of soluble salts, and the corrosion response of mild steel surfaces contaminated with them. Part 1 considered NaCl as a proxy for sea salt aerosol (SSA) in order develop an understanding of a single salt system as the basis for examining more challenging and relevant environments

[1].This paper extends the single salt work to $MgCl_2$, often considered the dominating component of SSA with respect to low humidity (<50% RH) corrosion [2-4] and further extends the work to artificial seawater (ASW), which is comprised of the inorganic components of natural sea salt. The aims of this study were to: (1) quantitatively characterize the relationship between solid-liquid phase transitions of these salts and the corrosion response of steel contaminated with them in terms of RH, and (2) establish the RH and time frame under which there is sufficient electrolyte to cause corrosion. The understanding developed is used to assess the accuracy and appropriateness of the time of wetness parameter for describing corrosion of SSA-contaminated surfaces. The impact of these results on the design of accelerated test regimes and the interpretation of field exposure data are also discussed.

To achieve these objectives, both the hygroscopic behavior of these sea salt proxies and the corrosion behavior associated with them were studied. The hygroscopic behavior of ASW microparticles was characterized using an interdigitated electrode (IDE) sensing method. Major solid-liquid transitions were identified. The phases associated with these transitions were identified by ex-situ analyses of the dried seawater deposits. The corrosion behavior of mild steel contaminated with microparticles of ASW and $MgCl_2$ (separately) was investigated as a function of RH. Both the attack morphology and volume loss rates were quantified. As with the sensor experiments, the dried salts on the corroded steel were characterized; the type and spatial distribution of the minerals were used to better understand the location and nature of the electrochemical reactions. Taken together, the results from the sensor experiments and the steel coupons allow relationships to be drawn between the hygroscopic behavior of these surface contaminants and the corrosion response.

4.2.2 Background

Laboratory studies of aerosols produced from natural and artificial seawater provide a general understanding of their hygroscopic behavior, but their physical state at low humidity levels is not well understood. The hygroscopic behavior of soluble salts can be characterized by the bulk liquid-solid phase transitions that occur- deliquescence and efflorescence. Deliquescence is the absorption of water vapor by a solid salt to form a liquid electrolyte, a process that occurs at or above a specific RH value, the deliquescence RH (DRH). The DRH is the point at which the water vapor pressure above a saturated solution of the salt is equal to that of the ambient air. The relative humidity at which a deliquesced solution crystallizes is known as the efflorescence relative humidity (ERH). Some amount of hysteresis is usually observed between the DRH and the ERH [5]. This hysteresis is due to the energy barrier associated with nucleation of the solid during drying, analogous to the hysteresis that occurs when a liquid cools below its melting temperature prior to solidification (i.e., undercooling). Table 4.2 gives the DRH and observed ERH values of the thermodynamically predicted major constituents of evaporated seawater and their relative amounts. Being the primary component of sea salt, the phase transitions of NaCl dominate its hygroscopic behavior [6]. Below the ERH of NaCl, the hygroscopic behavior of natural and artificial seawater is governed by magnesium-rich constituents [7, 8], which are thought to be why retention of water (5 - 15 wt%) has been observed down to <1% RH during drying at room temperature [6, 9, 10]. The physical state of this water has been ascribed to the presence of hydrated salts or trapped supersaturated brines composed of Mg^{2+} and Cl^- or SO_4^{2-}[6,8,10,11].

Table 4.2 Predicted major constituents of evaporated seawater and corresponding DRH and observed ERH at room temperature.

Constituent	Mass %	DRH (%)	ERH (%)
NaCl	90[a]	76[b]	40 – 55[b-e]
$MgCl_2.6H_2O$	3 – 4[a]	33[f]	--
$MgSO_4.H_2O$	3 - 4[a]	85[f]	--
$KMgCl_3.6H_2O$	2[a]	59[d]	40 - 50[d]
$CaSO_4$	2[a]	--	80 – 90[d,g]

[a]Harvie, Moller and Weare (1984) [53]. [b]Tang (1979) [54]. [c]Zeng *et al.* (2013) [49]. [d]Xiao *et al.* (2008) [8]. [e]Liu *et al.* (2008) [7]. [f]Ha and Chan (1999) [55]. [g]Qian *et al.* (2012) [56].

The effect of RH on the corrosion response of metal surfaces contaminated with natural and artificial sea salt is often described in terms of the deliquescence behavior of NaCl and $MgCl_2.6H_2O$, but results from Part 1 and the information above bring into question the relative importance of the deliquescence behavior of these salts with regard to corrosion response. In Part 1, we demonstrated that considerable corrosion could initiate and be sustained under NaCl crystals down to 33% RH, which is well below its DRH (76%). For sea salt, the DRH of $MgCl_2.6H_2O$ (33%) is often used as a guidepost threshold between wet and dry and significant and insignificant corrosion taking place [2, 12-14]. Indeed, corrosion has been readily observed on plain carbon and stainless steels contaminated with sea salt and $MgCl_2$ down to 33% RH [2, 3, 15]. Few investigators have either explicitly examined or reported the possibility for corrosion to occur below this limit. Of those that have pursued such studies, Mayazumi, Tani and Arai reported sustained stress corrosion cracking of 316F stainless steel under synthetic seawater deposits down to 15% RH [16]. Most recently, Wang found that particles of a $MgCl_2$-based multicomponent salt mixture similar in composition to seawater sustained observable corrosion of AA2024-T3 down to ~20% RH for up to 4 h [17]. Of interest here is whether the retained water in sea salt at such low humidity levels is capable of sustaining corrosion on mild steel and how the phase transitions of NaCl and $MgCl_2$ correlate to corrosion response.

4.2.3 Experimental

Details of the experimental procedures are given in the following sections, but an overview is provided here. Polished mild steel coupons were loaded with either $MgCl_2$ or artificial seawater droplets and subjected to isohumidity conditions ranging from <2% to 90% RH for periods of up to 30 days. After exposure, surfaces of a subset of samples were cleaned and surface profilometry was utilized to characterize attack morphology and quantify volume loss. Other subsets were examined in-situ during humidity exposure or ex-situ in the as-removed state using optical, Raman, and scanning electron microscopy to characterize the effect of RH on the state of the surfaces. Furthermore, the hygroscopic behavior of seawater deposits was studied using an IDE impedance sensing method. The methods, materials, and instruments utilized in this study were the same as those used in Part 1, to which the reader is referred to for further details.

4.2.3.1 Corrosion Exposures

Coupons of AISI 1010 plain carbon steel measuring 25 x 25 mm were polished to a 0.01 μm colloidal silica finish. After polishing, they were rinsed with ultrapure (UP) water and absolute ethanol (>99.5%), then dried in a stream of zero grade compressed air.

Prior to exposure, aqueous droplets of either a near saturated aqueous solution of $MgCl_2$ (>99.99% purity) or ASTM D1141 artificial seawater (ASW) [18] were dispensed onto each coupon using a custom inkjet printer [19] in the same 10 x 10 mm square array pattern as described in Part 1. The in-air diameter of the droplets dispensed was 35 μm for ASW and 15 μm for $MgCl_2$, which is representative of the larger size fraction of natural SSA [20]. The resulting salt loading densities were 15.7 ± 0.1 $\mu g \cdot cm^{-2}$ for ASW and 7.9 ± 0.1 $\mu g \cdot cm^{-2}$ for $MgCl_2$. These loadings, in terms of total chloride content, are within the range of soluble chloride loadings measured on boldly exposed metal surfaces in coastal marine environments (10^{-1} to 10^{2} $\mu g \cdot cm^{-2}$) [21,22].

Additionally, on one set of ASW coupons, the square array pattern was deposited 20 times over in the same location, resulting in a loading density of ~314 $\mu g \cdot cm^{-2}$. Loading was carried out at 80% RH for ASW and 50% RH for $MgCl_2$ such that both remained in mostly or fully deliquesced state, respectively.

Immediately after loading, sets of samples were either placed in isohumidity chambers or left in the humidity controlled inkjet environmental chamber for in-situ examination. Those placed in isohumidity chambers were exposed for up to 30 d at 21 ± 2°C. To ensure the deposits remained in an aqueous state at the start of the isohumidity exposures, the chambers were initially filled with humidified zero air to achieve approximately 50% or 80% RH for $MgCl_2$ or ASW, respectively. Other sets of samples were left in the humidity controlled inkjet environmental chamber after printing and subjected to various humidity profiles while monitoring morphological changes of the deposits using a reflected light optical microscope. Further details on these procedures and the experimental setup are given in Part 1.

After humidity exposure, samples were either immediately stripped of rust before being scanned using an optical profilometer, or left in the as-is condition for ex-situ analysis. Rust removal consisted of immersing samples in an aqueous solution of diammonium citrate at 40°C for 1-5 min. The cleaned coupons were scanned using a NewView 7300 white light profilometer (Zygo Corp., US). At least three areas (1 x 1 mm each) within the printed area and one outside the printed area of each coupon were scanned. Each scan was analyzed for total volume loss and maximum pit depth with respect to the original polished plane of the coupon. The resulting dataset consisted of at least 2 coupons per isohumidity set point and exposure period. The sample sets left in the as-removed condition were examined using reflected light optical microscopy, SEM-EDS and Raman microscopy, using the same methods as in Part 1.

4.2.3.2 Hygroscopic Behavior of ASW on Sensor

The hygroscopic behavior of ASW was investigated using an IDE impedance sensing method [19] along with time-lapse optical microscopy. At the start of the experiment, droplets of ASW were jetted onto an interdigitated Pt-electrode sensor (3 μm electrode spacing) in the inkjet environmental chamber. The droplet-loaded sensor was subjected to cyclic humidity ramping inside the chamber. The humidity profile used in the experiment consisted of a dehumidification ramp at a stepped rate of 1% RH/30 min from 85% followed by a 24 h hold at <2% RH, and then a humidification ramp at 1% RH/20 min returning to final RH of 85%.The salt-loaded sensor was subjected to this profile for three consecutive cycles at 21 ± 2°C. During ramping, impedance was measured across the sensor at both 0.2 Hz and 26 kHz with an excitation of 20 mV around the open circuit potential. Measured impedance values were normalized to deconvolute the impedance contribution of the deposited particles from the humidity response of the sensor itself and noise realized during measurements. Normalization was achieved by dividing impedance values measured across the salt-loaded sensor by values measured across a blank, clean sensor at 85% RH.[19] Thus, any normalized impedance value below unity indicated a significant admittance (i.e., conductance) contribution from the particles themselves. Micrographs of the deposits on the sensor were taken using a reflected light optical microscope during cycling. Areal coverage of the deposits was calculated from the micrograph series using a thresholding procedure in ImageJ software (NIH, US). Further details on the instrumentation and experimental procedure are given by Schindelholz, Tsui and Kelly [19].

After humidity cycling, the deposits on the sensors along with ASW deposits on a clean, undoped silicon wafer were examined using SEM-EDS to characterize the compositions, morphologies, and typical arrangement of the dried deposits. Analysis was carried out in high vacuum, backscattered electron mode using a 15 kV accelerating voltage at a working distance of 10 mm. The Si wafer was utilized because it allowed for analysis of the oxygen content of the phases, which was otherwise convoluted by the SiO_2 substrate of the impedance sensor. The wafer would be expected to have a very thin SiO_2 film, but its contribution was negligible for accelerating voltage used and thickness of deposits examined here (>>1 μm). The compositions of segregated phases on the wafer were compared to dried aqueous droplets of references salts also placed on the wafer. The reference salts were $MgCl_2$, $MgSO_4$, and $CaSO_4$ (>99.9% purity).

4.2.4 Results

4.2.4.1 Humidity Cycling of ASW on IDE Sensor

Measurements during humidity cycling of the ASW-loaded sensor indicate four major transitions in particle coverage and impedance and show significant admittance by the particles throughout the experiments. The impedance measured across the sensor during one of these humidity cycles is given in Figure 4.15. This figure also shows the corresponding areal coverage of the particles along with images of the particles near the transitions. It is notable that transitions occur in impedance and coverage at the same RH. Two major transition points occurred during dehumidification- one at 49 ± 2% RH and the other at 9 ± 1% RH. Likewise, the two major transitions during humidification were at 11 ± 2% RH and 74 ± 2% RH. The transition points at 49% and 74% corresponded to the formation of large block-like crystals (micrographs a and b) and their dissolution (f), respectively. The transition points at 9% and 11% reflect shrinkage (c) and growth (d and e) around these block-like crystal cores. Throughout the humidity cycling, the ASW particles imparted significant admittance across the sensor, even after holding at <2% RH for 24 h, as seen in Figure 1 where $|Z|_{0.2Hz}$ remains below unity. The morphological changes and impedance behavior described above were nearly identical for all three humidity cycles.

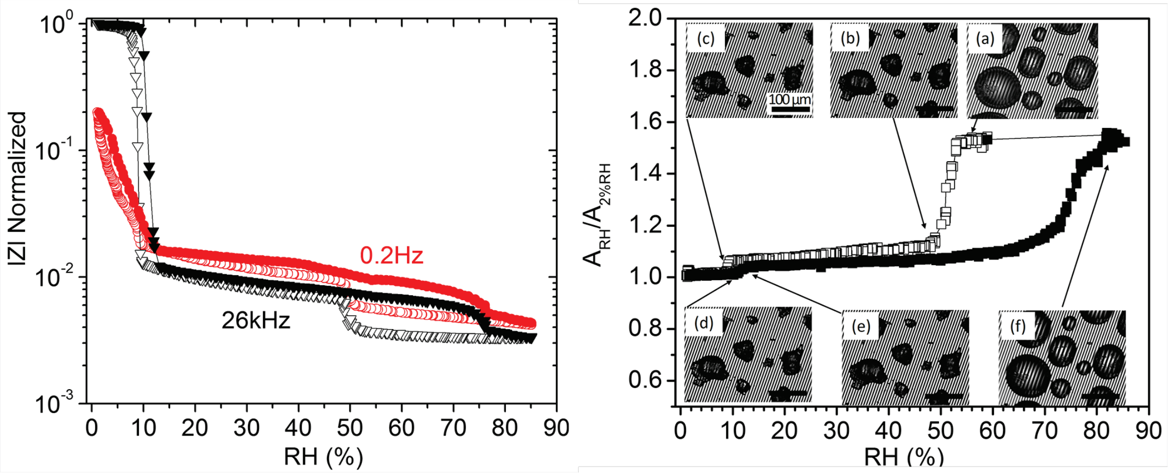

Figure 4.15 Left, impedance measured across an IDE sensor loaded with ASW at two frequencies during humidity cycling. Right, corresponding areal coverage, A, of particles as determined from optical micrographs, some of which are inset to illustrate major transitions. Open symbols are measurements taken during dehumidification and closed are those taken during humidification.

4.2.4.2 Phase Segregation of Dried ASW on Sensor

After humidity cycling, the particles on the sensor along with those examined on a clean silicon wafer were examined using SEM-EDS. A composite elemental map along with EDS spectra of one of the dried deposits on the wafer is given in Figure 4.16, which is representative of the phase compositions, morphologies, and typical arrangement of the dried deposits on the sensor. The dried deposits generally consisted of a large NaCl particle at the core (a) with a number of discrete phases around its perimeter (b-e). Of these, a Mg-Cl-O phase (c), similar in composition to the $MgCl_2$ reference salt, was seemingly largest in volume fraction. K-Mg-Cl rich phases (b) were often found in association with the Mg-Cl-O phase. Nodular, pillar, or needle-shaped phases of nearly the same composition as $CaSO_4$ (d) were commonly found surrounding the perimeter of the NaCl core, but not necessarily in contact with it. The location and appearance of these deposits correlated to those solids that were visually present throughout the humidity cycling. A distinct Mg-S-O phase (e) was also commonly noted around the perimeter of the NaCl core, but was relatively small in size fraction.

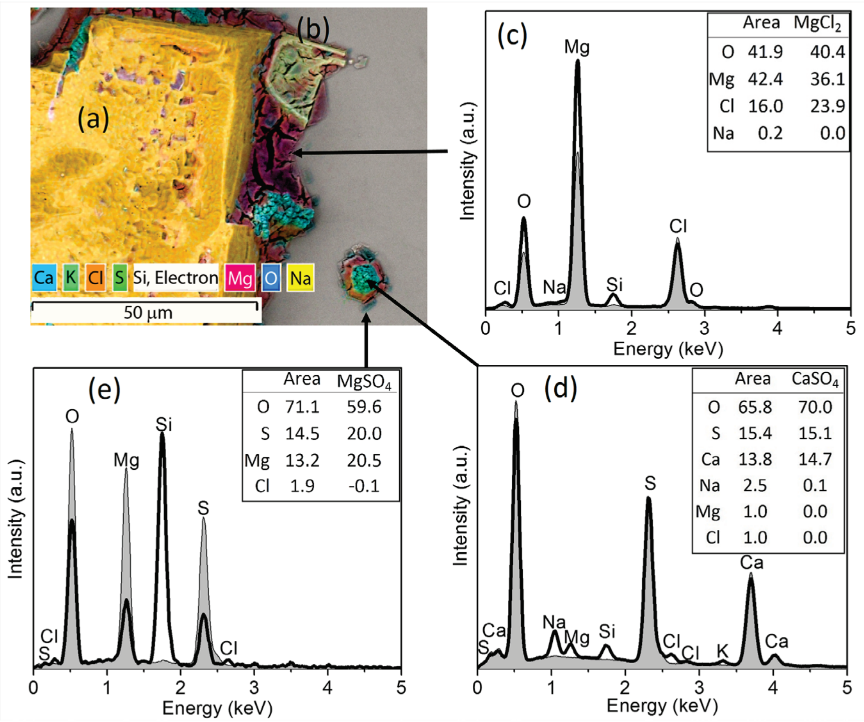

Figure 4.16 Composite SEM-EDS image of a dried ASW particle on an Si wafer along with EDS spectra of indicated areas (heavy black line) compared to spectra taken of reference salts of similar composition (filled grey). The values reported in the tables are those greater than 0.1 At. % for the area indicated. Area (a) indicates the large NaCl core crystal (orange) and (b) indicates a K-Mg-Cl rich phase (light grey). Area (c) is an Mg-Cl rich phase (purple), (d) is Ca-S-O rich (green), and (e) is an Mg-S-O rich phase (blue).

4.2.4.3 MgCl$_2$-induced Corrosion of Steel

Isohumidity exposures of MgCl$_2$ on steel indicated that sustained corrosion occurred down to at least 11% RH and attack became more severe with increasing RH and time. Figure 4.17 shows a series of surface profiles and optical micrographs of the coupons after the 7 d exposure. Corrosion at 11% RH and 23% RH was generally confined to areas directly underneath a subset of the MgCl$_2$ deposits. At 33% RH, coupons exhibited radial spreading of shallow attack from circular pits under a fraction of the original droplets. At 53% RH, pitting was less confined to original droplet area and more uniform in nature (numerous pits covering more area). Attack at 75% RH and 90%

was similar in appearance to that at 53%, but relatively deeper and sparser. These morphology trends held across all exposure durations. The average maximum pit depth, Figure 4.18, generally increased monotonically with time and RH, with the exception of 75% and 90% RH exposures at longer times. These values were computed by averaging the maximum pit depth found in each of the scans for all samples exposed at the same relative humidity. A similar trend is seen in the overall volume loss, given in Figure 4.19 as the nominal corrosion depth. These values were calculated by dividing the volume loss for each scan by the area of the scan (field of view). Data points which fall below the noise threshold (dashed line) in this plot were not significantly different from measurements taken in the unprinted region of the coupons.

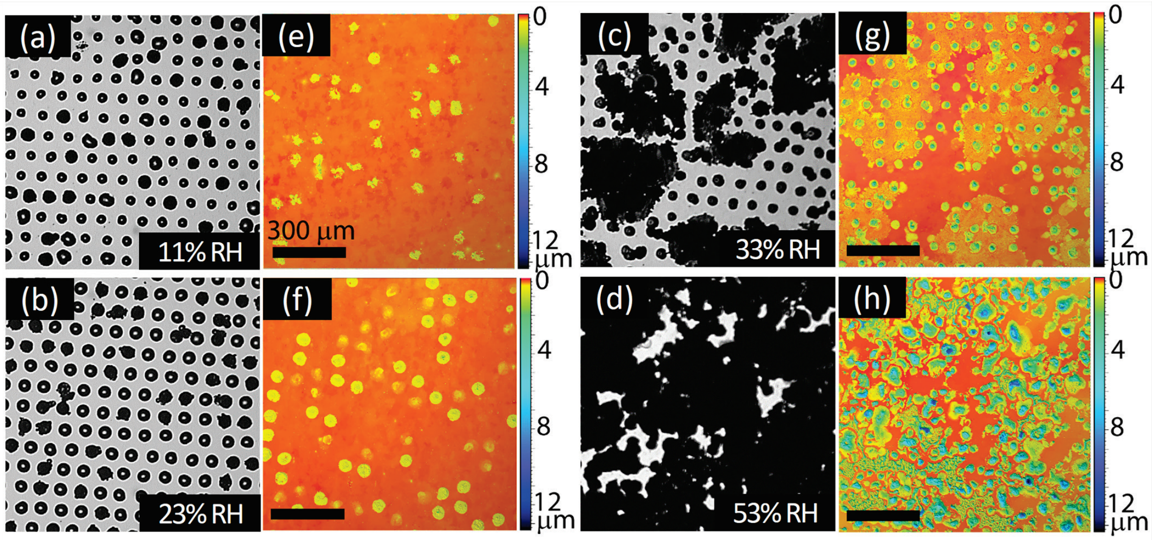

Figure 4.17 Optical micrographs of $MgCl_2$-loaded coupons (8 $\mu g \cdot cm^{-2}$) after 7 d of exposure at the humidity indicated and before rust removal (a-d). Measured surface profiles after rust removal for the same exposure period are also shown (e-h). All images are the same scale.

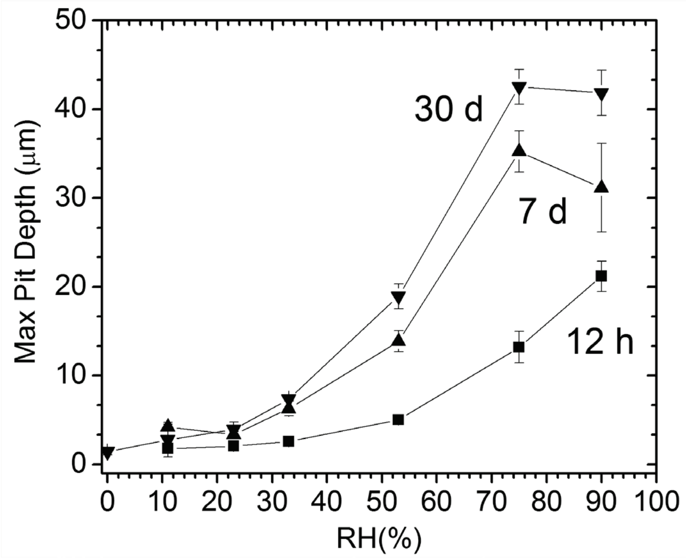

Figure 4.18 Maximum pit depth vs. RH for $MgCl_2$-loaded steel coupons (8 μg·cm^{-2}).

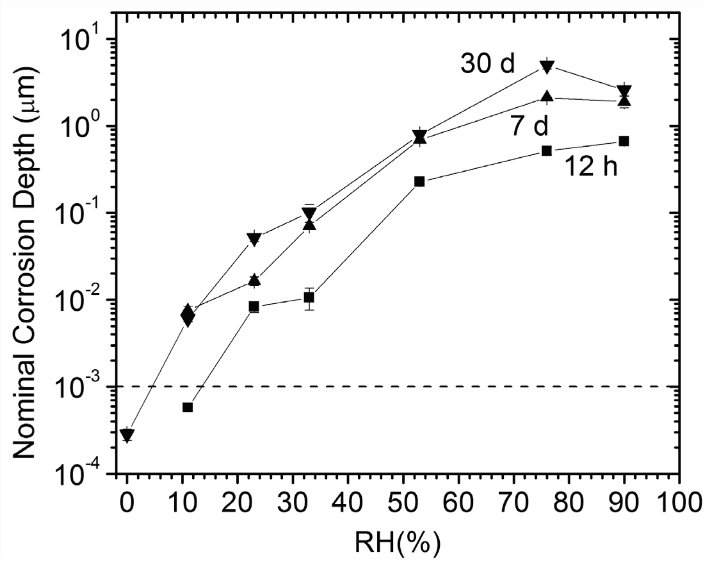

Figure 4.19 Average volume loss divided by scan area (nominal depth) vs. RH for $MgCl_2$-loaded steel coupons (8 μg·cm^{-2}). The dashed line represents the upper bound of the 95% confidence interval of volume loss measured on clean areas outside the printed salt pattern.

An additional experiment was carried out in the inkjet environmental chamber to characterize the state of the $MgCl_2$ deposits on the steel coupons during exposure at humidity levels below the deliquescence point of $MgCl_2.6H_2O$ (33% RH). This experiment was performed in order to simulate the drying conditions in the isohumidity exposure chambers at 23% and 11% RH and to examine the effect of the steel substrate on deliquescence behavior upon humidification. A coupon was loaded with $MgCl_2$ in the same manner as the isohumidity experiments and, afterwards, was kept in the humidity-controlled inkjet environmental chamber with a microscope trained on it. After loading at 50% RH, the humidity was lowered to 23% RH for 12 h, and then held at 11% for another 12 h. The appearance of the deposits after 12 h at 23% and then at 11% RH remained the same, with some deposits in deliquesced state and others in the form of a shriveled, dark appearance due to corrosion, Figure 4.20. Following this exposure, the coupon was subjected to a dehumidification ramp down to < 2% RH and humidification to 40% RH which is above the DRH of $MgCl_2.6H_2O$. This ramping was carried out at the rates used for the ASW humidity cycling experiments. Further dehumidification from 11% RH, Figure 4.20 (a), caused the remaining droplets to form shell-like, transparent solids near 7% RH (b). During the humidification ramp, the majority of these shell-like solids deliquesced at 11% RH (c) and portions of the dark, shriveled deposits started to grow at 33% RH, as exemplified by the arrow in (d).

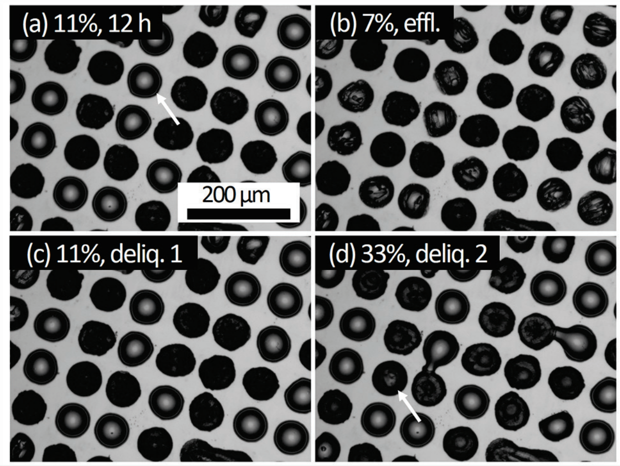

Figure 4.20 Optical micrographs of $MgCl_2$ deposits on steel during dehumidification (a, b) and humidification (c, d). The RH during imaging is given by the indicated values. The dark deposits are droplets under which considerable rust formation occurred. (a) was taken after 12 h exposure at 11% RH and the clear droplets in this image, as exemplified by arrow, partially effloresced upon reaching 7% RH, (b). The lower (c, d) images were taken after two different deliquescence events. The arrow in (d) indicates a deposit where deliquescence took place near 33% RH.

4.2.4.4 ASW-induced Corrosion of Steel

Isohumidity exposure of steel coupons loaded with 16 $\mu g \cdot cm^{-2}$ ASW exhibited sustained corrosion detectable down to 33% RH and trends in attack morphology that shared traits with those coupons loaded with $MgCl_2$ and NaCl [1]. Figure 4.21 shows a series of surface profiles and optical micrographs of the ASW coupons after the 7 d exposure. Corrosion at 33% RH was shallow and confined to areas under the original deposits or was in the form of radial attack reminiscent of that which occurred under the $MgCl_2$ deposits at the same humidity level, Figure 4.17. Attack at 53% RH and above exhibited similar trends as those seen for the NaCl-loaded coupons in Part 1. As with $MgCl_2$ and NaCl, the ASW maximum pit depth generally increased monotonically with RH with a drop-off in slope occurring at >76% RH at longer times, Figure 4.22**.** A similar trend is seen in the overall volume loss, given in Figure 4.23 as the nominal corrosion depth.

Additional isohumidity exposures were carried out at 23% and 11% RH using a loading density 20x higher than that reported above (320 μg·cm^{-2}) to examine the effect of loading on low humidity corrosion rate. Sustained corrosion was detectable down to 23% but not 11% RH, Figure 4.24. Attack occurred directly under the original deposits.

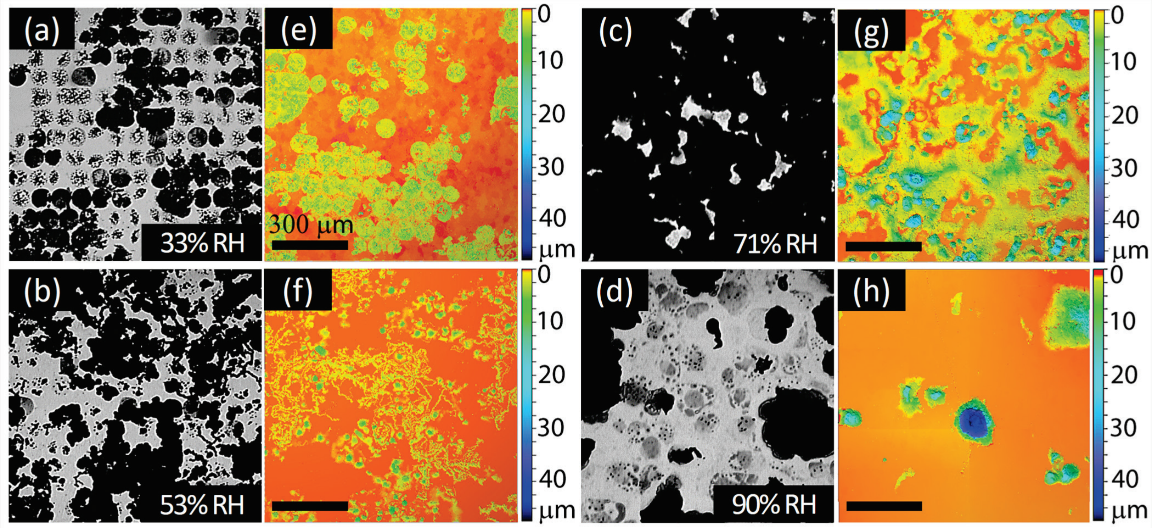

Figure 4.21 Optical micrographs of ASW-loaded coupons (16 μg·cm^{-2}) after 7 d of exposure at the humidity indicated and before rust removal (a-d). Measured surface profiles after rust removal for the same exposure period are also shown (e-h). All images are the same scale.

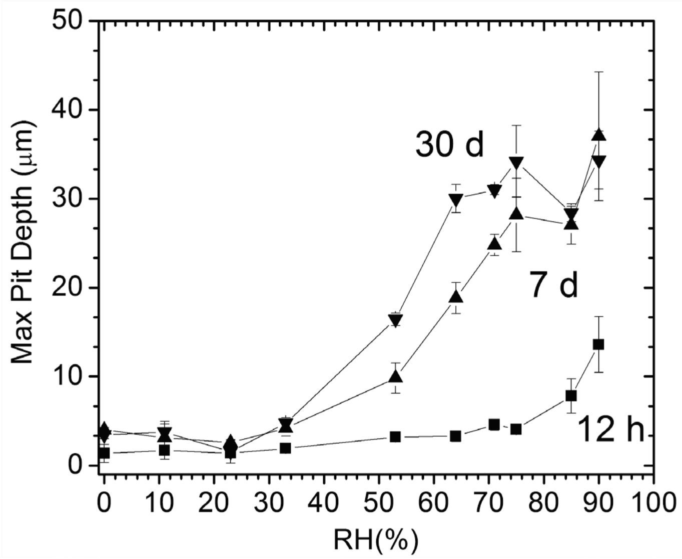

Figure 4.22 Maximum pit depth vs. RH for ASW-loaded steel coupons (16 μg·cm^{-2}).

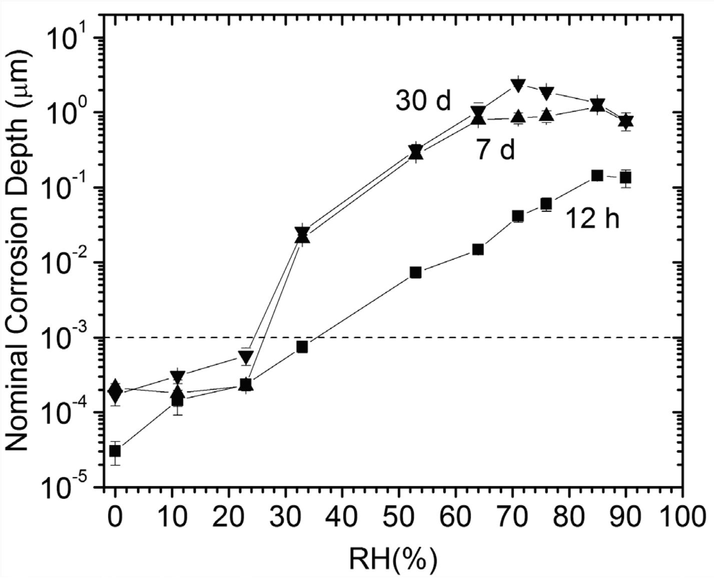

Figure 4.23 Average volume loss divided by scan area (nominal depth) vs. RH for ASW-loaded steel coupons (16 μg·cm^{-2}). The dashed line represents the upper bound of the 95% confidence interval of volume loss measured on clean areas outside the printed salt pattern.

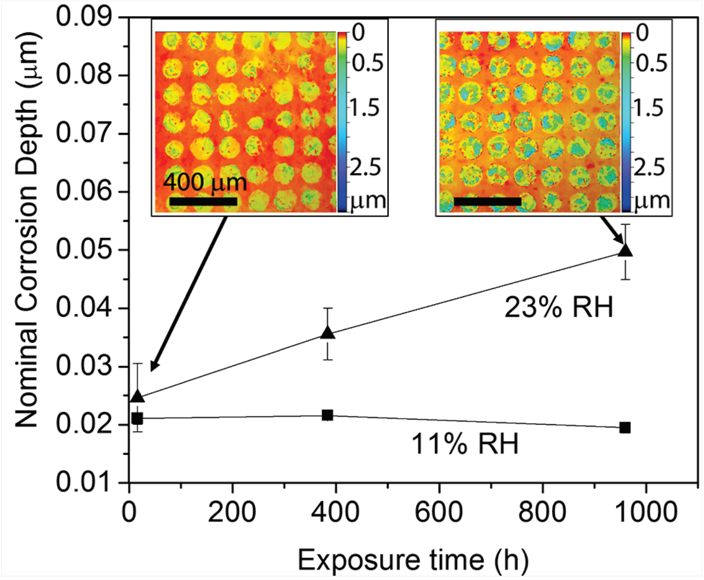

Figure 4.24 Average volume loss divided by the scan area (nominal depth) vs. RH for steel coupons loaded with ASW (314 μg·cm^{-2}) at 12 h, 7 d and 40 d. Measured profiles at 23% RH after 12 h and 40 d are inset.

As with $MgCl_2$, in-situ experiments were carried out on ASW deposits under an optical microscope to characterize the state of the surface during isohumidity exposure at humidity levels below the deliquescence point of $MgCl_2.6H_2O$ and NaCl. It was found that the hygroscopic behavior of ASW on the reactive steel surface was different from that observed on the inert sensor surface in instances where corrosion had occurred. This difference was observed in the first experiment in which sets of ASW-loaded coupons (16 μg·cm^{-2}) were exposed in the environmental chamber at 71%, 64% and 53% RH for 12 h. In all cases, corrosion was observed to occur under only a subset of droplets, which darkened within a few minutes after loading the droplets. At 71% RH, deposits stayed in droplet form, but droplets under which no corrosion occurred slowly shrank over the course of the 12 h leaving behind seemingly no trace of NaCl crystals in their place, Figure 4.25 (b). At 64% RH and 53% RH, NaCl crystals dropped out of solution in all of the deposits over the course of the 12 h exposure, as exemplified by Figure 4.25 (d). This behavior is in contrast to the ASW droplets on the sensor which remained at humidity levels below the DRH of NaCl for 13 h prior to immediate NaCl dropout once the humidity ramp reached ~50% RH.

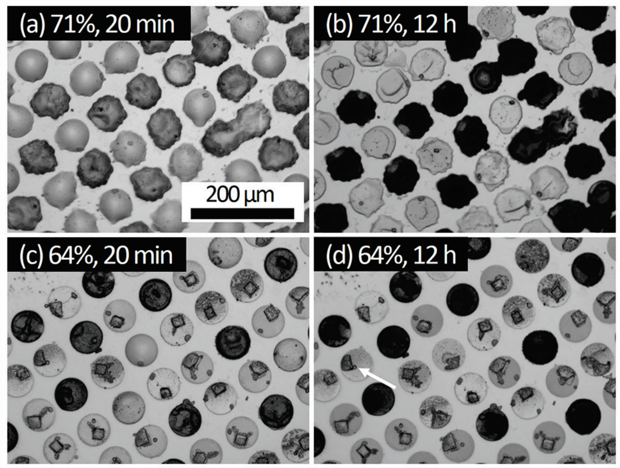

Figure 4.25 Optical micrographs of ASW droplets on steel held at 71% RH (a, b) and 64% (c, d) for up to 12 h after depositing. The elapsed exposure time after depositing is indicated by the micrograph labels. The dark deposits are droplets under which considerable rust formation occurred. The arrow in (d) exemplifies a NaCl core crystal that formed upon shrinkage of a droplet.

In the second experiment, a coupon with the high ASW loading pattern (320 $\mu g \cdot cm^{-2}$) was subjected to the same low humidity profile as described for $MgCl_2$ above. As with $MgCl_2$ on the steel and ASW on the sensor, the appearance of deposits after 12 h at 23% and then 11% RH remained relatively unchanged. A small amount of what appeared to be electrolyte was present at the edges of some of the deposits during this period. Further dehumidification caused rapid shrinkage of these areas upon reaching 9% RH, with no noticeable change occurring below this humidity level. During humidification, the first visible change occurred at 12% RH, exhibiting regrowth of the same areas, with little noticeable change after that up to 38% RH. The shrinkage and growth events at ~10% RH were similar to that seen for ASW on the sensor. Experiments were also carried out using the low ASW loading pattern, but such changes were not detectable, likely due to limits of resolution of the microscope.

4.2.4.5 Ex-situ Analyses of ASW and $MgCl_2$ on Steel

After exposure and optical imaging, steel samples from the 7 d ASW experiments and $MgCl_2$ that were left as-is (no rust removal) were examined using SEM-EDS and Raman microscopy. Dried ASW deposits that induced minimal corrosion exhibited phases similar in composition and spatial distribution to those seen on the sensor and Si substrate. This is exemplified in a comparison of areas (a) and (c) in Figure 4.16 and Figure 4.26. The extent to which these phases and the arrangement was seen was dependent upon the amount of corrosion that occurred in association with the deposits, Figure 4.26 (b). Also seen in Figure 4.26 are Na-Cl-O rich deposits that were present between the rust and the ASW particles, area (d), which was typical for coupons exposed at ≥53% RH. These deposits shared the morphological and compositional characteristics of phases that developed on NaCl-loaded coupons exposed at the same humidity levels in Part 1, except that trace amounts of other ionic constituents of ASW (Mg, Ca, K, S) were also present, Figure 4.26. No evidence of Na-O deposits could be located on the ASW loaded coupons at ≤33% RH; nor was any elemental enrichment of this sort detectable on areas of the surface outside of the salt or rust deposits on the $MgCl_2$-loaded coupons.

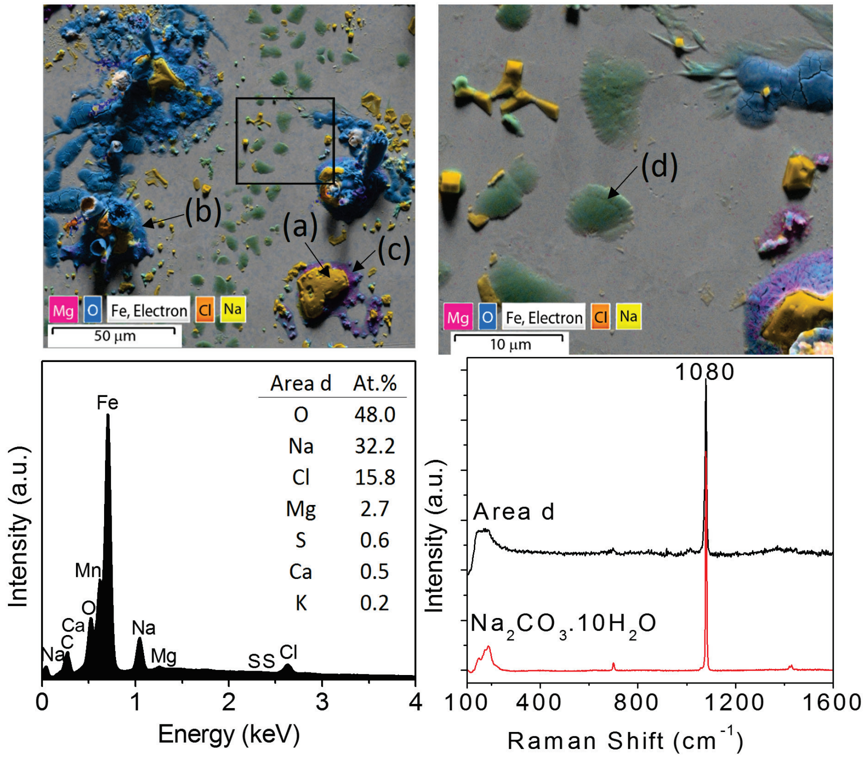

Area d	At.%
O	48.0
Na	32.2
Cl	15.8
Mg	2.7
S	0.6
Ca	0.5
K	0.2

Figure 4.26 Upper left, composite SEM-EDS image taken of an ASW-loaded steel coupon (16 µg·cm^{-2}) after 4 d exposure at 53% RH. (a) and (c) indicate a NaCl core crystal (orange) and Mg-Cl-O rich areas (purple), respectively, of a dried droplet where little corrosion occurred. Area (b) points to rust formations (blue) over ASW deposits. Upper right, detail of the boxed area in the left image showing Na-O rich deposits (green), as exemplified by (d). Lower left, EDS spectrum of area (d) in the upper image. Lower right, Raman spectrum of a deposit similar to that of (d) compared to that of a reference salt.

4.2.5 Discussion

In this work, the hygroscopic behavior of $MgCl_2$ and ASW were characterized and linked to the corrosion response of steel under atmospheric conditions. The hygroscopic behavior was determined via impedance measurements of salts deposited onto an IDE sensor. The hysteresis of the RH behavior was quantified and related to the deliquescence and efflorescence RH values from the literature. The dried salts were further characterized using EDS and Raman microscopy to identify the minerals formed in order to better understand the hygroscopic behavior. The corrosion behavior of steel with salts deposited on its surface was also investigated as a function of RH. Both the morphology and damage evolution rates were quantified. As with the IDEs, the dried salts on the corroded steel were characterized, allowing the use of the type and spatial distribution of the minerals to better understand the location and nature of the electrochemical reactions.

The present work dramatically challenges the view of the fraction of time that a surface can be considered sufficiently wet to support corrosion reactions. The use of a salt DRH as the delineation of the RH above which sustained corrosion is possible is shown to be inappropriate and, in some cases, highly inaccurate. In addition, the use of the standard definition of TOW as a quantitative indicator of corrosion rate or potential for significant corrosion is shown to be fatally flawed. Corrosion was found possible well below the DRH of salts that serve as proxies for the ubiquitous sea salt aerosols, with evidence of significant admittance (conductance) in ASW deposits at <2% RH even after 24 h, likely due to fluid trapping under a solid salt crust. In addition, sustained corrosion occurred at humidity levels as low as 23% RH under ASW and down to at least 11% RH under $MgCl_2$. The rate of volume loss generally increased with increasing RH, with the large increase in loss between 33% and 53% RH. The remainder of the discussion explains the hygroscopic behavior observed on inert and steel surfaces, the corrosion response of steel to this behavior, highlighting the importance of the effects of the corrosion chemistry, and finally ties these observations into a more complete understanding of the true time of wetness of actual surfaces.

4.2.5.1 Hygroscopic Behavior of ASW

The major liquid-solid transitions of the sensor-deposited ASW particles during humidity cycling are associated with NaCl and $MgCl_2$, as demonstrated by the combination of impedance and optical measurements along with identification of the phases in the dried particles. The large transitions at ~50% RH during dehumidification and 76% RH during humidification, Figure 4.15, are characteristic of the efflorescence and deliquescence behavior of both pure NaCl [7,19] as well as NaCl in synthetic and natural sea salt, Table 4.2

The analogous transitions seen near 10% RH in Figure 4.15 are attributed to the phase transitions of $MgCl_2.xH_2O$. Transitions within a few percent of these values also occurred during humidity cycling of sensors loaded with pure $MgCl_2$ droplets in our previous work [19]. Furthermore, an Mg-Cl-O rich phase was found in large quantities in areas consistent with the shrink-growth seen during humidity cycling, Figure 4.16. $MgCl_2$ is known to form a variety of hydrates, with the thermodynamically favored form at 0° to $96^{\circ}C$ being the hexahydrate ($MgCl_2.6H_2O$), which has a DRH of 33% [23]. Given that the transitions witnessed here were well below 33% RH, it is reasonable to postulate that a metastable hydrate with a lower DRH formed. Non-equilibrium hydrated phases with different DRH than the equilibrium form have been reported to occur for a number of other organic and inorganic salts [24-26].

Although major phase transitions occurred down to 9% RH during dehumidification, the ASW particles retained significant conductance even after holding for 24 h at <2% RH, which is indicative of the presence of some form of electrolyte. The low humidity admittance is most evident in the $|Z|_{0.2Hz}$ curve Figure 4.15, which remains significantly below that measured across a clean, unloaded sensor (unity value of normalized impedance). The continual rise in $|Z|_{0.2Hz}$ when the RH was held constant at <2% RH and its movement in step with RH immediately upon subsequent humidification demonstrates that this admittance is governed by water availability. This behavior, again, was seen for deposits of pure $MgCl_2$ in our previous work [19]. In that case, we found the slowly rising impedance measured upon holding at <2% RH reflected the evaporation of fluid trapped under partially effloresced deposits. The fluid trapping occurred due to the formation of solid shells at the electrolyte-air interface of the drops during efflorescence. Given the apparent controlling behavior of $MgCl_2$ on ASW particle conductance at low humidity in our current experiments, it is not unreasonable to propose that similar fluid trapping also occurs with ASW. This reasoning is consistent with reports of anomalous retention of water in both natural and artificial seawater particles and solvated Mg^{2+} at similar low humidity levels [8, 10]. The implications of this in terms of time of wetness and the limitation of these findings with regard to natural environment will be discussed in the following sections.

Visual observations of ASW and $MgCl_2$ droplets deposited on steel and subjected to different RH levels, Figure 4.20 and Figure 4.25, indicate that the efflorescence behavior on corroded surfaces deviates from that seen on inert surfaces, such as our sensors. These differences are attributed to the dramatic changes in surface chemistry resulting from corrosion that cause efflorescence to occur nearer to the DRH points of a particular salt, as was examined in more detail in part 1. As with the case of NaCl in Part 1, the results of the isohumidity corrosion experiments presented in this paper further demonstrate that considerable corrosion can be sustained below the DRH of salts.

4.2.5.2 Effect of RH on Corrosion Response

The minimum RH at which sustained corrosion was detectable under ASW deposits was 23%, but some of the results suggest that corrosion may be sustained at even lower humidity levels. This is exemplified in Figure 4.27 where 30 d volume loss results have been normalized to a per annum corrosion rate. The fact that a higher loading density (314 $\mu g \cdot cm^{-2}$) was required to detect corrosion down to this level, as opposed to the lower loading density (16 $\mu g \cdot cm^{-2}$) where the minimum was 33% RH, indicates that corrosion rate is dependent on the loading level and detection limits of the examination methodology. This result is reasonable given the comparatively minute amount of electrolyte available at these low humidity levels. If the presence of Mg-Cl rich electrolyte is what is largely enabling corrosion at these low levels, then the results for the $MgCl_2$ experiments, where this electrolyte is in relative excess, support this and suggest that corrosion is possible down to 11% RH, and likely even lower.

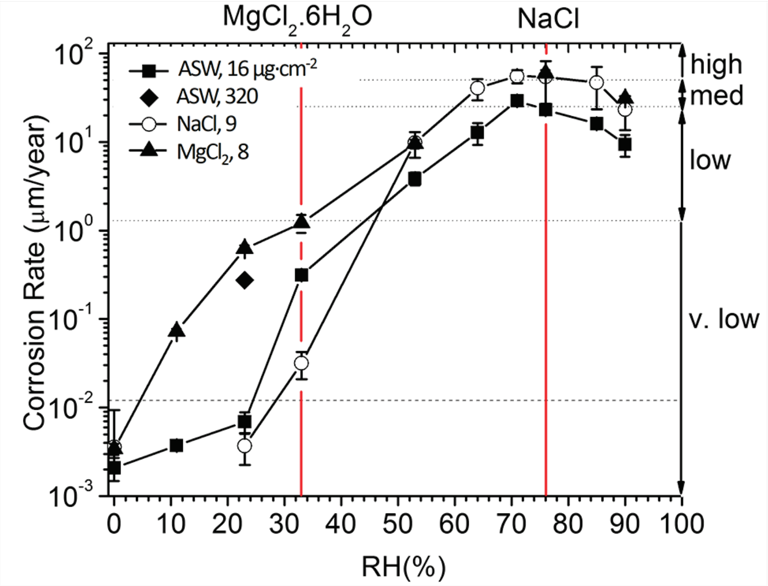

Figure 4.27 30 d volume loss data from all isohumidity exposures normalized to a per annum corrosion rate and compared to the DRH of NaCl (76%) and $MgCl_2.6H_2O$ (33%) along with the ISO 9223 atmospheric corrosivity classifications for steel [35]. The loading density of salt associated with each of these exposures is given in the legend. The lowest dashed line represents the upper bound of the 95% confidence interval of volume loss measured on clean areas outside the printed salt pattern.

A large inflection in corrosion loss trends with respect to RH for ASW loaded coupons for longer times occurred between 33% and 53% RH, which is not directly relatable to the phase transitions reported above, Figure 4.23. This observation is in line with conclusions drawn by Evans and Taylor [27] and Duly [28] who also reported corrosion to become considerable within this range based on results of isohumidity experiments similar to those in our study. Both groups tracked corrosion in terms of mass loss of polished mild steel coupons contaminated with natural sea salt at various exposure periods, although the loadings utilized in their work are not mentioned. Our 7 d results are compared to Evans and Taylor's results in Figure 4.28 to illustrate this point. Mass loss is proportionally equivalent to volume loss (or normalized corrosion depth) permitting direct comparison of trends in this way. The trends are complimentary with regard to the inflection between 33% and 53%. Evans and Taylor's data further suggest that, in their own words, “The corrosion rate becomes serious when the relative humidity exceeds about 40% RH.” This range does not correspond to any of the observed major phase transitions of ASW on the impedance sensor or the steel. Nor are such inflections in loss notable at the DRH or observed ERH of singular salts of $MgCl_2$ or NaCl on steel.

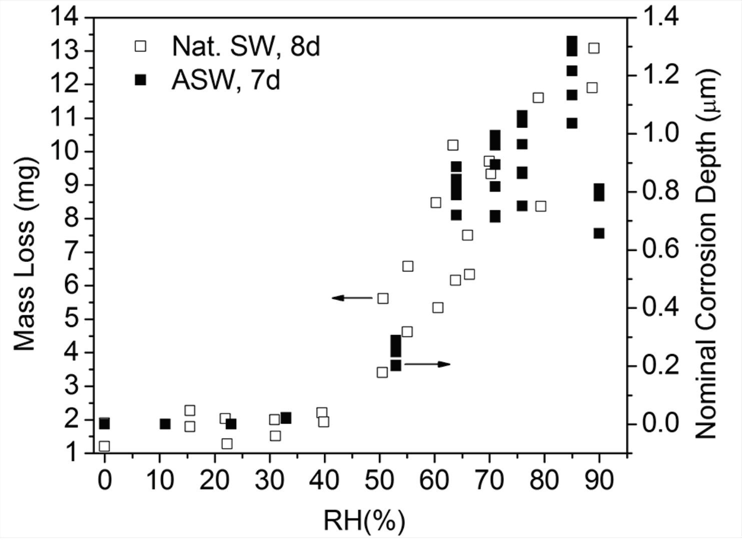

Figure 4.28 Comparison of mass loss data from Evans and Taylor’s 8 d isohumidity exposure of natural seawater contaminated mild steel [27] with volume loss (nominal depth) from our 7 d exposure using artificial seawater.

Distinct differences in attack morphology and surface state of the ASW contaminated steel are also apparent between 33% and 53% RH. An inflection of maximum pit depth as a function of RH occurs in this range, Figure 4.22. This sharp change reflects the transition from shallow pitting radiating from deposits at 33% RH to more discrete pits and filiform-type corrosion at 53%. These two humidity levels also delineate the bound on the presence of sodium carbonate rich catholyte that developed between the deposits at ≥53% RH, Figure 4.26, and none detectable outside the rust covered areas at ≤33% RH. All of these trends are similar to that reported for NaCl alone, Part 1.

For NaCl, we postulated that these distinctions were due to the governance of the hygroscopic behavior of the corrosion chemistry, and this may also be the case for ASW. In part 1, we found that simulants of corrosion chemistry expected to develop under NaCl exhibited major deliquescence-efflorescence transitions at ~50% RH. The simulants were $FeCl_2$-NaCl (anolyte) and NaOH (catholyte). Although the corrosion chemistry under ASW is inherently more complex than under NaCl alone, it is still dominated by Na and Cl and may be expected to exhibit similar behavior. Regarding the catholyte, the major sodium carbonate phase found on ASW-loaded coupons at 53% RH and above, Figure 4.26, was nearly identical to that found on the NaCl-loaded coupons and the NaOH-loaded sensors after exposure in Part 1. The chemistry of the anodic sites (anolyte) is expected to be dominated by Fe^{2+} and Cl^-, and, accordingly, the hygroscopic behavior of $FeCl_2$ [29, 30]. Therefore, if the hygroscopic behavior of these simulants is of any indication, the anodic and cathodic sites would be expected to largely shut down between 33% and 53% RH. However, this does not mean that electrolyte capable of causing corrosion is absent below this threshold nor that corrosion stops. The less well-defined distinction in attack with RH seen for $MgCl_2$ alone may be due to the distinctly different corrosion chemistry detailed elsewhere [31, 32].

4.2.5.3 Implications for TOW

Although our experiments do not exactly replicate of the conditions witnessed in natural environments, they do provide a point from which to assess the accuracy and appropriateness of current TOW determination methods. In particular, the results presented here and in Part 1, coupled with literature findings [5,33], bring into question whether steel surfaces contaminated with SSA can ever be considered dry in outdoor atmospheres. Furthermore, we argue that common humidity-based and moisture-sensing methods for determination of TOW are inappropriate for steel contaminated with the examined salt aerosols.

Our results raise the question as to whether surfaces contaminated with SSA ever truly dry in natural ambient conditions (in terms of corrosion being possible). Major phase transitions of ASW occurred at ~10% RH, attributed to a metastable hydrated Mg-Cl phase, and the ASW deposits remained significantly conductive down to <2% RH, even for 24 hours, likely due to fluid trapping. To put these findings into perspective, the hourly mean RH levels measured during the driest month of the year in the Yuma desert [34] (one of the hottest and driest in North America), are given Figure 4.29. Also shown in the figure are hypothetical[33] RH profiles over surfaces subjected to daytime solar heating. In only the cases of the heated surfaces, would the RH dip below the 10% transitions and in no cases do the profiles achieve <2%. Of course, SSA is not commonly the dominant surface contaminant in desert environments, but these conditions can be considered a very conservative lower bound of expected humidity in natural outdoor conditions. This example also raises the issue of surface heating, which could allow for drying of the brines we found to be persistent during our room temperature experiments. Further work is needed to examine the effect of heating on the hygroscopic behavior of SSA to provide a conclusive answer to this question.

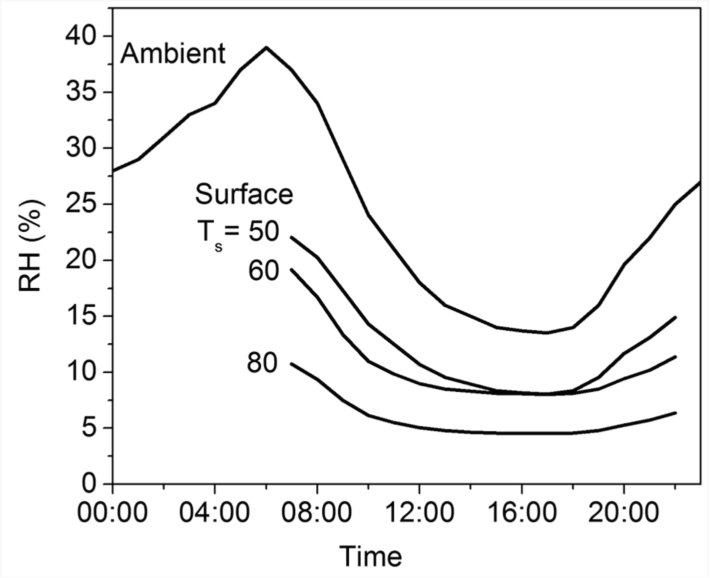

Figure 4.29 Mean measured hourly ambient RH during the month of July (1973 to 1986) for Yuma, Arizona [34]. The "Surface" curves are hypothetical values for RH above a surface heated to T_s °C given the ambient air temperature is 40°C.

Regardless of whether a surface ever truly dries, our findings challenge the commonly utilized humidity based thresholds for estimations of TOW on SSA contaminated surfaces. These include the ISO 9223 threshold of 80% RH [35] and use of the DRH of sea salt components [12, 36], including that of $MgCl_2.6H_2O$ (33%). In Part 1, we demonstrated that corrosion can initiate by adsorbed water on NaCl crystals down to 33%RH, and proceed at rates comparable to that at and above the DRH of NaCl (76%) at humidity levels down to 53% due to development of hygroscopic corrosion chemistry. Here we found corrosion can be sustained down to at least 11%RH under $MgCl_2$ deposits, possibly due to trapped fluid or deliquesced electrolyte, which is well below the DRH of $MgCl_2.6H_2O$ (33%). Under ASW, corrosion was detectable down to 23% RH. No substantial inflection in the trends of corrosion loss as a function of RH was notable at the observed or predicted phase transitions in any of these cases. Considering that these deliquescence points proved relatively insignificant under simple sea salt proxies in highly controlled conditions, it is doubtful that such delineation will be witnessed in the natural environment where surface chemistry and RH-T transients are much more complex.

Similarly, the accuracy of electrode-based TOW sensing methods is questionable with regard to their ability to fully capture the wetting contribution of hygroscopic atmospheric particles during field deployment. These methods typically utilize sensors composed of electrodes separated by an insulating gap, similar in construction and function to the sensors utilized in this work. Time of wetness is defined as the time during which a voltage, current or resistance/impedance threshold is exceeded [5]. Thresholds are often established as the baseline response of the clean sensors at low humidity. In previous work we have shown that the humidity at which conductance-based sensors read wet was highly dependent on loading and coverage of contaminants, and not exclusively their hygroscopic behavior [33]. This limitation was due to electrode spacing of typical TOW sensors being far greater than the expected aerosol sizes deposited on the sensors. In other work [19] and here we optimized sensitivity by maximizing particle coverage across electrodes, minimizing the spacing of the interdigitated electrodes and choosing measurement frequencies that allow for measurement of changes at high impedances. By doing so, we were able to demonstrate that, provided great enough sensitivity, impedance varies with RH across the entire RH range for ASW. This result is unsurprising given the findings of Simkovich [37] who measured changes in conductance down to less than 5% RH across electrodes attached to singular macroscopic crystals of NaCl due to the presence of adsorbed water. Later, Hucher [38] reported a similar observations for other simple binary salts below their deliquescence point. Although phase transitions mark distinct transitions in conductance versus RH trends for these salts, these changes could not be used to distinguish between significant and insignificant corrosion taking place. Where then can a wet-dry threshold be defined in terms of conductance alone? There appears to be no satisfactory, universally applicable answer to this question. This is not to say conductance based sensors are of no utility in field conditions. They still, importantly, provide a qualitative measure of the relative amount of contaminant loading and electrolyte coverage, both of which can affect corrosion response. Although more representative of actual surface conditions on a corroding surface, galvanic-based corrosion sensors suffer from the same conduction and bridging issues as unreactive sensors [5].

This work coupled with our previous work [33] demonstrates that the TOW parameter is a strong function of measurement method, and, as indicator of electrolyte presence or significant corrosion, is fatally flawed. Nonetheless, correlations are often drawn between TOW and corrosion rates observed in the field, usually in the form of dose-response models [36, 39, 40]. Utilized as an independent variable in these models, it is important to recognize that TOW represents a convolution of multiple disparate parameters, such as RH, temperature, salt type and loading. The weighting of each is inherent to the specific TOW determination method itself.

Given the uncertainties associated with current TOW determination methods in light of this discussion and the likelihood for electrolyte presence even down to extremely low humidity levels, the conservative assumption that, under conditions where SSA are present, electrolyte sufficient to enable corrosion is always present on mild steel surfaces may be more appropriate (i.e., TOW is unity). A simple alternative approach is to account for a time above which a critical relative humidity (CRH) is exceeded, where corrosion is considered significant [41, 42]. Significant can be defined here as the point which large inflection in corrosion loss occurs with respect to RH, which for our work and others [27, 28] was between 33 and 53%. We postulated that this range is due to the governance not of the chemistry of SSA itself, but the corrosion chemistry that develops. Further work is necessary to examine the extent of independence of this CRH range with respect conditions more representative of natural environments.

4.2.5.4 Application and Limitations of Findings to Field Conditions

As with all laboratory experiments, there are a number of limitations that should be kept in mind regarding the direct application of these results to the natural environment where SSAs are the primary contaminant. Differences in expected chemistry between natural SSA and ASW, salt loading, the transient nature of RH and temperature along with exposure time are discussed.

The seawater mixture used here (ASTM D1141) is most representative of the inorganic constituents of natural seawater, and, in turn, that of freshly emitted coarse mode SSA (≥2.5 μm diameter) which typically are the dominant salt contaminant on surfaces near surf beaches (<2 km) [33, 43]. It is not representative of their organic content, which, for coarse mode aerosol, has been measured to range from that of natural seawater, ~1 ppm total organic content [44], to up to 0.6 mass fraction [45]. It is also not representative of finer, aged aerosols (typically <2.5 μm) which can be transported tens to hundreds of km inland [46], and, in part, due to their longer atmospheric lifetime (hours to days), can exhibit drastically altered chemistry (e.g., acidification, halogen depletion) [47]. Although understanding the interaction of aged SSA with metallic surfaces is of great importance [46, 48], we chose to examine ASW, due to the availability of information regarding the hygroscopic behavior of natural and artificial seawater and its relation to corrosion.

Despite these differences, our results suggest that ASW produces similar behavior to that of natural seawater. The general hygroscopic behavior of ASW was found to be in general agreement with that reported for freshly emitted aerosols composed of natural seawater [6, 8, 49]. Also, corrosion loss trends were similar to those reported by Evans and Taylor [27] who used natural seawater in their experiments. Furthermore, the similarity in attack trends between ASW and NaCl and changes in surface chemistry bring into question the relative importance of accounting for differences between ASW and freshly emitted, coarse mode SSA chemistry in lab experiments for mild steel that seek to emulate field conditions, especially at later stages of exposure where considerable rust has formed.

Regarding the corrosion experiments, the static contaminant loadings here and in part 1 are within the range reported for surfaces exposed at coastal marine sites [21,22,50], but they are not representative of the transient conditions witnessed in many outdoor environments. In the outdoor environment, contaminant loading on boldly exposed surfaces is subject to the competing effects of continuous aerosol deposition and wash-off by precipitation [22]. Surfaces sheltered from the sky may witness continuous deposition of contaminants. One question of importance is, do the trends in attack morphology and corrosion loss as a function of RH reported in this work hold across the range of expected loading densities on outdoor surfaces? If this is the case, one potential utility of this is that RH could be utilized to tune the desired type and amount of attack in accelerated testing experiments.

The conditions utilized in this work do not fully represent the temperature range or diurnal humidity cycling of surfaces exposed in outdoor environments. In our work, temperature was held constant at 21°C. Surfaces in outdoor environments, of course, can experience a wide range of temperatures, which are both seasonal and diurnal in nature, as discussed in the previous section. Temperature can affect both deliquescence and efflorescence behavior, the extent to which is dependent on the salt as well as electrochemical kinetics. Information on the temperature dependence of the hygroscopic behavior of sea salt is scant, but available information on its primary components, NaCl and $MgCl_2$ (hexahydrate) suggests that it may be minimal. Regarding deliquescence, predictions using concentrated electrolyte modeling software, StreamAnalyzer (OLI Systems, US) following the procedures of Yang *et al.* [51] for NaCl show the DRH to vary by only one percent from 0° to 90°C, which is in close agreement with experimental findings [52]. The DRH of $MgCl_2.6H_2O$ for the same temperature range decreases from 34% to 27% RH. Concerning efflorescence, the ERH of substrate-deposited NaCl along with others salts, has been reported to be independent of temperature from 0° to 27°C [52]. This, of course, does not take into account kinetic hindrances to drying (e.g., metastable hydrates and fluid trapping).

With regard to corrosion response, our experiments were carried out under isohumidity conditions. The question remains as to whether these trends in corrosion response still hold under transient conditions and longer exposure periods. In this regard, the findings presented here are more relevant to storage environments or occluded spaces sheltered from the effects of diurnal cycling.

Although a number of unanswered questions remain, the results provided here add to the foundational data under rigorously controlled conditions from which to understand more complicated environments. The experimental approach developed in this work provides one means to further explore them.

4.2.6 Conclusions

In this work the hygroscopic behavior of artificial seawater and $MgCl_2$ particles were characterized and linked to the humidity-induced corrosion response of mild steel contaminated with them. The following conclusions were drawn:

1. Humidity cycling of ASW on an interdigitated electrode sensor indicated liquid-solid phase transitions occurred at ~10% RH, with evidence of significant conductance down to <2%, even after 24 h. This low humidity behavior is postulated to be due to the formation metastable $MgCl_2$ hydrates and fluid trapping under a solid salt crust, respectively.
2. Trends in corrosion loss versus RH were not directly reflective of the major liquid-solid phase transitions observed or predicted for ASW or $MgCl_2$ alone. The minimum RH where sustained corrosion was detectable was 11% for $MgCl_2$ and 23% for ASW. Trends observed for ASW-loaded steel generally followed those of NaCl-loaded steel in Part 1. A large inflection in loss occurred between 33% and 53% RH, where rates went from 0.3 to 4 µm/y (30 d normalized). As in Part 1, this inflection was attributed to the governance of the hygroscopic behavior of

the corrosion chemistry that developed rather than that of the initial salt contaminant.

3. Given the uncertainties associated with current time of wetness (TOW) determination methods and in light of these findings, the conservative assumption that, under conditions where SSA is present, electrolyte sufficient to enable corrosion is always present on steel surfaces may be most appropriate (i.e., TOW is unity). A simple alternative approach for dose-response models that utilize TOW as an input parameter is to account for a time above a critical relative humidity where corrosion becomes considerable, which in this case was between 33% and 53% RH.
4. Further work is suggested to test the universality of these findings in cases of varying salt loadings, diurnal humidity and temperature transients, and exposure times more representative of structures exposed to outdoor conditions. The experimental framework developed provides one means of doing so in either field or more rigorously controlled lab conditions.

4.2.7 References

1. E. Schindelholz, B. E. Risteen and R. G. Kelly, in preparation, (2014).
2. K. Noda, M. Yamamoto, H. Masuda and T. Kodama, in *Corrosion and Corrosion Control in Saltwater Environments: Proceedings of the International Symposium*, p. 144 (2000).
3. Y. Tsutsumi, A. Nishikata and T. Tsuru, *Corros. Sci.*, **49**, 1394 (2007).
4. N. Mi, M. Ghahari, T. Rayment and A. J. Davenport, *Corros. Sci.*, **53**, 3114 (2011).
5. E. Schindelholz and R. G. Kelly, *Corros. Rev.*, **30**, 135 (2012).
6. I. N. Tang, A. C. Tridico and K. H. Fung, *J. Geophys. Res.*, **102**, 23269 (1997).
7. Y. Liu, Z. Yang, Y. Desyaterik, P. L. Gassman, H. Wang and A. Laskin, *Anal. Chem.*, **80**, 633 (2008).
8. H.-S. Xiao, J.-L. Dong, L.-Y. Wang, L.-J. Zhao, F. Wang and Y.-H. Zhang, *Environ. Sci. Technol.*, **42**, 8698 (2008).
9. A. A. Frossard and L. M. Russell, *Environ. Sci. Technol.*, **46**, 13326 (2012).

10. D. J. Cziczo, J. B. Nowak, J. H. Hu and J. P. D. Abbatt, *J. Geophys. Res.*, **102**, 18843 (1997).
11. L.-J. Zhao, Y.-H. Zhang, Z.-F. Wei, H. Cheng and X.-H. Li, *J. Phys. Chem. A*, **110**, 951 (2006).
12. I. S. Cole, W. D. Ganther, J. D. Sinclair, D. Lau and D. A. Paterson, *J. Electrochem. Soc.*, **151**, B627 (2004).
13. P. R. Roberge, in *Uhlig's Corrosion Handbook*, 3 ed., R. Revie Editor, p. 299, John Wiley & Sons, Hoboken, New Jersey (2011).
14. A. Nishikata, Y. Tsutsumi and T. Tsuru, Corrosion monitoring of stainless steels in marine atmospheric environment, in *Corrosion and Electrochemistry of Advanced Materials*, S. Fujimoto, E. Akiyama and H. Habazaki Editors, p. 652, Electrochemical Society, Los Angeles, CA, United states (2005).
15. T. Prosek, A. Iversen, C. Taxén and D. Thierry, *Corrosion*, **65**, 105 (2009).
16. M. Mayuzumi, J. Tani and T. Arai, *Nucl. Eng. Des.*, **238**, 1227 (2008).
17. B.-b. Wang, Z.-y. Wang, W. Han, C. Wang and W. Ke, *T. NonFerr. Metal Soc.*, **23**, 1199 (2013).
18. ASTM, ASTM Standard D1141, in *Standard Practice for the Preperation of Substitute Ocean Water*, ASTM International, West Conshohocken, PA (2013).
19. E. Schindelholz, L.-k. Tsui and R. G. Kelly, *J. Phys. Chem. A*, **118**, 167 (2013).
20. C. O'Dowd and G. de Leeuw, *Philosophical Transactions of the Royal Society A: Mathematical, Physical and Engineering Sciences*, **365**, 1753 (2007).
21. T. Shinohara, S.-I. Motoda and W. Oshikawa, *Zairyo to Kankyo/ Corrosion Engineering*, **54**, 375 (2005).
22. I. S. Cole, W. D. Ganther and D. Lau, *Corros. Eng. Sci. Technol.*, **41**, 310 (2006).
23. K. Sugimoto, R. E. Dinnebier and J. C. Hanson, *Acta Crystallogr. B*, **63**, 235 (2007).
24. K. J. L. Arenas, S. R. Schill, A. Malla and P. K. Hudson, *J. Phys. Chem. A*, **116**, 7658 (2012).
25. M. D. Cohen, R. C. Flagan and J. H. Seinfeld, *J. Phys. Chem.*, **91**, 4563 (1987).
26. C. Peng and C. K. Chan, *Atmos. Environ.*, **35**, 1183 (2001).
27. U. R. Evans and C. A. J. Taylor, *Br. Corros. J.*, **9**, 26 (1974).
28. S. Duly, *Journal of the Society of Chemical Industry*, **69**, 304 (1950).
29. P. Zhang, G. Chen, B. Guo and S. K. Cheng, *Advanced Materials Research*, **152**, 353 (2011).
30. M. R. Gilberg and N. J. Seeley, *Stud. Conserv.*, **26**, 50 (1981).
31. H. Masuda, *Corrosion*, **57**, 99 (2001).
32. J. Zhang, J. Wang and Y. Wang, *Corrosion*, **61**, 1167 (2005).
33. E. Schindelholz, R. G. Kelly, I. S. Cole, W. D. Ganther and T. H. Muster, *Corros. Sci.*, **67**, 233 (2013).
34. D. A. Stewart, Low Relative Humidity in the Atmosphere, in, p. 55, U.S. Army Missle Command, Redstone Aresenal, Alabama (1989).
35. ISO, 9223:1992(E) Corrosion of metals and alloys- Corrosovity of atmospheres-Classification, in, ISO, Geneva, Switzerland (1992).
36. W. D. Ganther, I. S. Cole, A. M. Helal, W. Chan, D. A. Paterson, G. Trinidad, P. Corrigan, R. Mohamed, N. Sabah and A. Al-Mazrouei, *Mater. Corros.*, 1066 (2010).

37. G. Simkovich, *J. Phys. Chem.*, **67**, 1001 (1963).
38. M. Hucher, A. Oberlin and R. Hocart, *B. Soc. Fr. Mineral. Cr.*, 320 (1967).
39. P. R. Roberge, R. D. Klassen and P. W. Haberecht, *Materials & Design*, **23**, 321 (2002).
40. J. Tidblad, *Atmos. Environ.*, **55**, 1 (2012).
41. W. H. J. Vernon, *Faraday Society -Transactions*, **27**, 255 (1931).
42. F. Mansfeld, *Mater. Corros.*, **30**, 38 (1979).
43. I. S. Cole, D. A. Paterson and W. D. Ganther, *Corrosion Engineering Science and Technology*, **38**, 129 (2003).
44. T. R. Crompton, *Analysis of seawater*, Butterworths, London (1989).
45. B. Gantt and N. Meskhidze, *Atmos. Chem. Phys.*, **13**, 3979 (2013).
46. I. S. Cole, N. S. Azmat, A. Kanta and M. Venkatraman, *Int. Mater. Rev.*, **54**, 117 (2009).
47. W. C. Keene, R. Sander, A. A. P. Pszenny, R. Vogt, P. J. Crutzen and J. N. Galloway, *J. Aerosol Sci*, **29**, 339 (1998).
48. N. S. Azmat, K. D. Ralston, B. C. Muddle and I. S. Cole, *Corros. Sci.*, **53**, 1604 (2011).
49. J. Zeng, G. Zhang, S. Long, K. Liu, L. Cao, L. Bao and Y. Li, *Surf. Interface Anal.*, **45**, 930 (2013).
50. M. E. Boan, A. Rodríguez, C. Abreu and C. Echeverría, *Corrosion*, **69**, 1217 (2013).
51. L. Yang, R. Pabalan and M. Juckett, *J. Solution Chem.*, **35**, 583 (2006).
52. G. Zeng, J. Kelley, J. D. Kish and Y. Liu, *J. Phys. Chem. A* (2014).
53. C. E. Harvie, N. Møller and J. H. Weare, *Geochim. Cosmochim. Acta*, **48**, 723 (1984).
54. I. N. Tang, Deliquescence properties and particle size change of hygroscopic aerosols, in *Symposium on Biological Studies of Environmental Pollutants: Aerosol Generation and Exposure Facilities*, Honolulu, Hawaii (1979).
55. Z. Ha and C. K. Chan, *Aerosol Sci. Technol.*, **31**, 154 (1999).
56. Z. Qian, F. Wang, Y. Zheng, J. Yu and Y. Zhang, *Chin. Sci. Bull.*, **57**, 591 (2012).

5 Conclusions

This dissertation examined the relationship between relative humidity, the hygroscopic behavior of NaCl, $MgCl_2$ and artificial seawater (ASW) microparticles and the corrosion response of mild steel contaminated with them. The following summarizes the major outcomes and conclusions of this work:

1. Two novel experimental methods were developed to carry out this work. First, an inkjet aerosol deposition method and instrument were developed for rigorously controlled, high-throughput loading of particle of the same size scale as coarse mode atmospheric aerosols (>1 μm) onto substrates. The precision and accuracy of this method in terms of control of droplet size, placement and loading density is unparalleled by current methods utilized for study of atmospheric corrosion. It has been demonstrated here as a tool for high-throughput assay-type studies that utilize replicate samples, but can also be used for study of particle-substrate interactions on a singular particle basis.
2. Second, an impedance sensing method using finely spaced, interdigitated microelectrode array sensors was developed and validated for study of the hygroscopic state of substrate-deposited salt microparticles. Of importance to atmospheric corrosion, this method allows for interrogation of relative admittance (i.e., conductance) of microparticles, a property that cannot be directly ascertained by other common methods. The technique was validated using a number of inorganic single salts and particle sizes ranging 1 to 100 μm diameter with regard to deliquescence (liquid-solid) and efflorescence (solid-liquid) phase transitions.

3. The deliquescence RH of NaCl (76%) does not serve as a RH threshold for either the corrosion loss rate or the attack morphology versus RH trends. The minimum RH at which detectable corrosion was sustained under NaCl deposits was 33% RH. The largest inflection in corrosion loss versus RH occurred between 33 and 53% RH, where, for a salt loading of 9 µg·cm-2, rates went from 0.3 to 10 µm/y (30 d normalized), respectively. At times greater than 7 d, rates from 53% to 71% RH were comparable to those at 76% to 90%. These findings were observed regardless of whether the NaCl deposits were initially crystalline or in deliquesced (droplet) form.
4. The initiation of corrosion under crystalline NaCl deposits well below their DRH can be explained in terms of the presence of adsorbed water associated with the salt crystals in contact with the steel. There is likely sufficiently conductive electrolyte available on the NaCl crystals to initiate corrosion down to at least 40-50% RH, and capillary condensation between the NaCl and steel surfaces may account for corrosion down to 33% RH.
5. Sustainment of corrosion at considerable rates down to 53%RH under NaCl and the large change in attack morphology between 33% and 53% is attributed to the hygroscopic behavior of the chemistry that developed at the anode and cathode sites. Impedance measurements across simulants of these corrosion chemistries, air-aged $FeCl_2$-NaCl and NaOH, respectively, indicated major liquid-solid transitions (i.e., wet and dry) at ~50% RH. Drying below this level may largely shut down electrochemical reactions by minimizing the ability for solvation of ferrous ions at the anode and transport of ions between the anode and cathode.

6. Trends in corrosion loss versus RH were also not directly reflective of the major liquid-solid phase transitions observed or predicted for ASW or $MgCl_2$ alone. The minimum RH where sustained corrosion was detectable was 11% for $MgCl_2$ and 23% for ASW. Trends observed for ASW-loaded steel generally followed those of NaCl-loaded steel, which is likely due to NaCl being the dominant constituent of ASW (90 wt%). A large inflection in loss occurred between 33% and 53% RH, where rates went from 0.3 to 4 μm/y (30 d normalized) for a salt loading of 16 μg·cm-2. As with NaCl, this inflection was attributed to the governance of the hygroscopic behavior of the corrosion chemistry that developed rather than that of the initial salt contaminant.
7. The results of humidity cycling of ASW on the interdigitated electrode sensor brings into question whether surfaces contaminated with SSA ever can be considered truly dry in natural ambient conditions (in terms of corrosion being possible). Major phase transitions occurred at ~10%RH, attributed to a metastable hydrated Mg-Cl phase, and the ASW deposits remained significantly conductive down to <2% RH, even for 24 hours, likely due to fluid trapping. Humidity levels below <2%RH are rare in ambient outdoor environments.
8. Given the uncertainties associated with current time of wetness (TOW) determination methods and in light of these findings, the conservative assumption that, under conditions where SSA is present, electrolyte sufficient to enable corrosion is always present on steel surfaces may be most appropriate (i.e., TOW is unity). A simple alternative approach for dose-response models that utilize TOW as an input parameter is to account for a time above a critical relative

humidity where corrosion becomes considerable, which in this case was between 33% and 53% RH.

6 Future Work

As with all laboratory experiments, there are limitations regarding the direct application of the results presented to the natural environment, which were discussed in 4.2. Some of these differences include the expected chemistry between natural SSA and ASW, salt loading, the transient nature of RH and temperature and exposure time. Several areas of future work are suggested in this regard:

1. The results for artificial seawater bring into question whether mild steel surfaces contaminated with sea salt aerosol (SSA) ever can be considered dry in ambient marine environments. It is suggested that the interdigitated electrode sensing method developed in this work be utilized to examine the behavior of chemistries more representative of natural SSA under temperature conditions that emulate solar heating and nighttime cooling cycles. This could be accomplished by field deployment of the sensors utilized in this work to either collect SSA samples for subsequent laboratory interrogation or for a field-based study similar in nature to that presented in 2.1. Another knowledge gap is the effect of the presence of rust on the hygroscopic behavior of SSA chemistry. Establishment of the extent to which deliquesced brines persist on exposed surfaces would have impact on further assessment of the overall utility of the TOW parameter in outdoor marine environments.

2. Regarding the corrosion experiments presented in 4.1, the static contaminant loadings used were within the range reported for surfaces exposed at coastal marine sites, but they are not representative of the transient conditions witnessed in outdoor environments. In the outdoor environment, contaminant loading on

boldly exposed surfaces is subject to the competing effects of continuous aerosol deposition and wash-off by precipitation. Surfaces sheltered from the sky may witness continuous deposition of contaminants. One question of importance is, do the trends in attack morphology and corrosion loss as a function of RH reported in this work hold across the range of expected loading densities on outdoor surfaces? If this is the case, one potential utility of this is that RH could be utilized to tune the desired type and amount of attack in accelerated testing experiments.

3. In the same regard, the considerable differences in corrosion rate between 33 and 53% RH seen for NaCl and ASW contaminated steel were hypothesized to be due to the hygroscopic behavior of the corrosion chemistry that developed. If this is the case, such trends should hold across varying contaminant loadings, which could be explored as per above. A better understanding of the nature of the hygroscopic constituents that develop in the more complex case of natural seawater and SSA contaminants would allow for assessment of this hypothesis and the extent to which corrosion chemistry controls the humidity response of mild steel in marine environments. This understanding could lead to an informed establishment of critical humidity threshold for the corrosion of mild steel in marine atmospheres where SSA is the primary contaminant, which in turn could serve as alternative to current TOW-based relative humidity thresholds.

6.1 Related Research Avenues

In general there is great need for a more comprehensive understanding of the physical and chemical state of metallic surfaces exposed to the atmospheric environment and the relationship between surface state and corrosion response [1]. Such understanding is imperative for development of approaches that allow for improved quantitative prediction and laboratory emulation of atmospheric corrosion performance and behavior realized in actual service environments. Two areas enabled by the approach framework developed in this work or highlighted by the findings presented are discussed, which should have significant impact in this regard:

6.1.1 Effect of Electrolyte Geometry

Standardized laboratory salt fog tests designed to accelerate the corrosive effects of exposure to marine environments are heavily relied upon for materials development, product qualification and service life prediction. There is a large mismatch, however, between corrosion performance in these tests and that realized in service, making extrapolation to predict service life based on these tests unreliable. In response to this, there has been a push to better emulate conditions and damage realized during natural exposure conditions through replication of climatological phenomena, such as relative humidity and solar irradiation [2]. One condition that has received relatively little attention is that of the geometry of electrolyte that forms on surfaces in these tests. Recent work by Risteen and Schindelholz [3], using the inkjet instrument described in 4.2, demonstrated large discrepancies in corrosion rate and attack morphology of carbon steel due to differences in electrolyte geometry in the fog tests (macroscopic drops) and the natural marine environment (microscopic droplets from fine aerosols). These results and work by others [4, 5], suggest that accelerated testing has the potential to more accurately emulate natural degradation by control of electrolyte geometry. There are a number of unknowns, however, which must be addressed to translate these findings to engineering strategies including: (a) the underlying phenomena that cause these differences; (b) the universality of our findings in terms of conditions witnessed in accelerated testing and across other alloy systems; and (c) the extent to which electrolyte geometry can be controlled through aerosol size and deposition rate in accelerated tests.

6.1.2 Secondary Spreading

The studies in Chapter 4 highlighted and characterized a particular phenomenon whereby a fine alkaline film composed of small droplets (<10 μm diameter) spreads out from a salt deposit or droplet under which corrosion in atmospheric conditions is occurring. This film, termed the secondary spreading region, has been demonstrated to serve as an area for cathodic reduction of oxygen (which drives corrosion) and has been observed to occur on a wide range of alloy systems (e.g., Fe, Al, Cu, Mg) in association with aerosol deposits both in the lab and natural environments [6-9]. Importantly, as described in Chapter 3, there appears to be a strong correlation between the state of the catholyte on the surface under ASW and NaCl and the attack morphology that develops. This change in morphology is in line with the idea that the maximum pit size is controlled by ohmic drop between the cathodic and anodic sites and the cathodic current available to sustain a pit [10]. If areal coverage of secondary spreading relates to cathodic current, as has been suggested by others [6], minimizing this area would minimize the pit size and cause shallower pits. This along with the phenomenological knowledge base that has been built up on this subject serves as an excellent springboard to explore the following: (a) What is the interfacial mechanism that enables spreading? (b) To what extent does spreading affect corrosion rate and attack morphology and why? (c) If a clear relationship exists between spreading and corrosion response, can spreading be manipulated to control corrosion damage? A mechanistic understanding of secondary spreading and its effect on corrosion response will serve to inform corrosion models, identify avenues for control of attack during accelerated testing and open up potential means of mitigation through alloy modification or surface treatment.

6.2 References

1. National Research Council, *Research Opportunities in Corrosion Science and Engineering*. The National Academies Press: Washington D.C., 2011.
2. LeBozec, N.; Thierry, D., *Materials and Corrosion* 2010, *61* (10), 845-851.
3. Risteen, B.E.; Schindelholz, E.; Kelly, R. G. *ECS Transactions.*, in press.
4. Katayama, H.; *et al.*, *Corrosion Science* 2005, *47* (10), 2599-2606.
5. Muster, T. *et al.*; *Electrochimica Acta* 2011, *56* (4), 1866-1873.
6. Chen, Z. Y.; Persson, D.; Leygraf, C., *Corrosion Science* 2008, *50* (1), 111-23.
7. Chen, J.; *et al.*, *Corrosion Science* 2007, *49* (3), 1625-1634.
8. Jia, R.; Yan, C.; Wang, F., *Journal of Materials Science and Technology* 2009, 25 (2), 225-229.
9. Chen, Z. Y.; *et al.*, *Journal of the Electrochemical Society* 2005, *152* (9), 342-51.
10. Z. Y. Chen, F. Cui and R. G. Kelly, Journal of The Electrochemical Society 2008, 155, C360.